

Artificial Intelligence in Heavy-Ion Collisions:
bridging the gap between theory and experiments

Dissertation
zur Erlangung des Doktorgrades
der Naturwissenschaften

vorgelegt beim Fachbereich Physik
der Johann Wolfgang Goethe-Universität
in Frankfurt am Main

von

Manjunath Omana Kuttan
aus Kollam, Kerala, India

Frankfurt am Main, 2023
(D30)

vom Fachbereich Physik der
Johann Wolfgang Goethe - Universität als Dissertation angenommen.

Dekan: Prof. Dr. Roger Erb

Gutachter: Prof. Dr. Dr. h.c. Horst Stöcker, Prof. Dr. Dr. h.c. Marcus Bleicher

Datum der Disputation: 23.10.2023

To the loving memory of my father.

Diese Arbeit basiert auf folgenden Publikationen:

- Omana Kuttan, M., Steinheimer, J., Zhou, K., Redelbach, A., & Stoecker, H. (2020). A fast centrality-meter for heavy-ion collisions at the CBM experiment. *Physics Letters B*, 811, 135872.
- Omana Kuttan, M., Zhou, K., Steinheimer, J., Redelbach, A., & Stoecker, H. (2021). An equation-of-state-meter for CBM using PointNet. *Journal of High Energy Physics*, 2021(10), 1-25.
- Omana Kuttan, M., Motornenko, A., Steinheimer, J., Stoecker, H., Nara, Y., & Bleicher, M. (2022). A chiral mean-field equation-of-state in UrQMD: effects on the heavy ion compression stage. *The European Physical Journal C*, 82(5), 427.
- Omana Kuttan, M., Steinheimer, J., Zhou, K., & Stoecker, H. (2022). The QCD EoS of dense nuclear matter from Bayesian analysis of heavy ion collision data. *arXiv preprint arXiv:2211.11670*. (Submitted to Physical Review Letters)
- Omana Kuttan, M., Steinheimer, J., Zhou, K., Bleicher, M., & Stoecker, H. (2023). Model dependence of the number of participant nucleons and observable consequences in heavy-ion collisions. *arXiv preprint arXiv:2303.07919*. (Submitted to European Physical Journal C)
- Omana Kuttan, M., Steinheimer, J., Zhou, K., Redelbach, A., & Stoecker, H. (2021). Deep Learning Based Impact Parameter Determination for the CBM Experiment. *Particles*, 2021(4), 47-52.
- Omana Kuttan, M., Steinheimer, J., Zhou, K., Redelbach, A., & Stoecker, H. Extraction of global event features in heavy-ion collision experiments using PointNet. *Proceedings of FAIRness2022 -FAIR next generation scientists - 7th Edition Workshop (Paralia (Pieria, Greece) / 23 - 27 May 2022)*. (Accepted for publication in Proceedings of Science)
- Steinheimer, J., Omana Kuttan, M., Motornenko, A., Sorensen, A., Nara, Y., Koch, V., Bleicher, M. & Stoecker, H. (2023, June). Proton and Λ flow and the equation of state at high density. *European Physical Journal Web of Conferences* (Vol. 276, p. 01021).

Zusammenfassung

0.1 Das QCD-Phasendiagramm und Experimente zur Schwerionenkollision

Die Quantenchromodynamik ist die Theorie der starken Wechselwirkung, einer der fundamentalen Wechselwirkungen im Standardmodell der Teilchenphysik. Die Untersuchung der Eigenschaften von QCD-Materie unter verschiedenen thermodynamischen Bedingungen ist ein wichtiger Schwerpunkt der Forschung in der Kernphysik. Stark wechselwirkende Materie existiert als ein Gas aus wechselwirkenden Hadronen und ihren Resonanzen bei niedrigen Temperaturen und kleinen chemischen Potentialen. Durch Erhöhung der Temperatur und/oder des chemischen Potentials kann das Hadronengas in einen Zustand quasi-freier Quarks und Gluonen übergehen, das so genannte Quark-Gluon-Plasma (QGP). Gitter-Eich-Simulationen der QCD, bei kleinen baryo-chemischen Potentialen sagen einen kontinuierlichen Übergang von einem heißen Gas aus hadronischen Resonanzen zu einer Phase stark wechselwirkender Quarks und Gluonen, mit spontan gebrochener chiraler Symmetrie, voraus. In QCD Materie bei hoher netto Baryondichte werden mehrere interessante Eigenschaften, wie z.B. ein Phasenübergang erster Ordnung vom hadronischen Gas zum QGP oder ein kritischer Endpunkt, vermutet. Direkte Gitter-QCD-Simulationen sind hier, aufgrund des fermionischen 'Sign-problems' derzeit nicht möglich. Daher werden sowohl QCD-motivierte effektive Modelle in Verbindung mit direkten experimentellen Messungen verwendet, um nach einem Phasenübergang oder einem kritischen Endpunkt zu suchen.

Experimentell werden die Eigenschaften der QCD-Materie mit Hilfe von Schwerionenkollisionen oder Beobachtungsstudien von Verschmelzungen von Neutronensternen untersucht. Beide Systeme erzeugen stark wechselwirkende Materie mit hoher Temperatur und/oder Dichte. Das ultimative Ziel der Schwerionenkollisionsprogramme ist es, ein Phasendiagramm für QCD-Materie zu erstellen, das die Phasengrenzen, die Art der Übergänge an der Grenze und die kritischen Regionen aufzeigt. Derzeit liegt das Hauptaugenmerk auf Schwerionenkollisionen mit mittlerer Energie, die QCD-Materie bei hohen Baryondichten und Temperaturen erzeugen können.

Die experimentellen Messungen verschiedener Beobachtungsgrößen wie der kollektive Fluss, Teilchenzahlfuktuationen usw. werden mit aufwendigen Modellrechnungen verglichen, um

die physikalischen Grundlagen für die Entwicklung der, in den Kollisionen erzeugten, Materie zu ermitteln. Dieser Vergleich ist jedoch nicht ganz einfach. Experimentelle Daten müssen mehrere Verarbeitungsschritte durchlaufen, wie z.B. die Rekonstruktion von Spuren, die Identifizierung von Teilchen und die Auswahl der Zentralität, bevor verschiedene Beobachtungsgrößen extrahiert werden können. Die Modellrechnungen sollten die Phasenraumakzeptanz und die Detektoreffizienz des Experiments, wenigstens durch vereinfachte Akzeptanz- und Effizienzschritte oder ausgefeilte Detektorsimulationen, berücksichtigen um einen konsistenten Vergleich dieser experimentellen Observablen mit theoretischen Modellvorhersagen zu gewährleisten. Die Verarbeitungsalgorithmen können zusätzliche Unsicherheiten und Verzerrungen in die Daten einbringen, die die Ergebnisse der Analyse verfälschen können. Darüber hinaus verwenden solche Methoden iterative Algorithmen, die extrem langsam und unpraktisch für zukünftige Experimente, mit hoher Ereignisrate, sein können welche eine Online-Verarbeitung der experimentellen Daten erfordern. Darüber hinaus erschwert die Notwendigkeit kombinierter Schlussfolgerungen auf der Grundlage mehrerer Beobachtungsgrößen häufig den Analyseprozess.

Um diese Probleme zu lösen, werden neue Analysetechniken benötigt, um experimentelle Daten mit Modellvorhersagen zu vergleichen. Das Ziel dieser Arbeit ist es, neuartige Künstliche Intelligenz (KI)-basierte Methoden zu entwickeln, um diese Lücke zwischen Theorie und Experiment zu schließen. Das Hauptaugenmerk liegt dabei auf der Entwicklung von KI-Tools, die direkt mit den Ergebnissen von Detektoren arbeiten können, z.B. mit Teilchentreffern und -spuren, die bei Schwerionen-Kollisionsexperimenten mit mittlerer Energie gemessen werden. Zusätzlich zur KI, die direkt mit experimentellen Daten auf Detektorebene arbeitet, werden auch Methoden entwickelt um Modellvorhersagen für konventionelle Beobachtungsgrößen konsistent mit experimentellen Daten zu vergleichen. Als einzigartiges Experiment der nächsten Generation, das Kollisionen mittlerer Energie bei noch nie dagewesenen Intensitäten messen wird, wurde das CBM-Experiment bei FAIR als Beispiel verwendet, um die Fähigkeiten der entwickelten AI/DL-Modelle zu veranschaulichen.

Eine kurze Einführung in die QCD, Schwerionenkollisionen und KI für Schwerionenkollisionen findet sich in Kapitel 1. In Kapitel 2 werden die verschiedenen weltweiten Schwerionenprogramme vorgestellt, wobei der Schwerpunkt auf dem Physikprogramm an der FAIR-Beschleunigeranlage und dem CBM-Experiment liegt. Auch die experimentellen Herausforderungen im Zusammenhang mit der Analyse der Messdaten wurden in Kapitel 2 kurz erörtert.

0.2 Modelle für Schwerionen-Kollisionen

Kapitel 3 enthält eine detaillierte Diskussion über die verschiedenen Modelle zur Simulation von Schwerionenkollisionen bei mittleren Strahlenergien. Die Vorteile und Limitationen der verschiedenen Modelle wurden untersucht. Der Schwerpunkt lag darauf, zu verstehen, wie die verschiedenen Modelle die Zustandsgleichung (Equation of State, EoS) einbeziehen, die

die zeitliche Entwicklung des Systems bestimmt. Die Zustandsgleichung ist ein wesentlicher Input für theoretische Modelle von Schwerionenkollisionen, da sie die mikroskopischen und makroskopischen Eigenschaften des erzeugten Systems verknüpft. Die EoS liefert den Druck des Mediums für jede gegebene Energie- und Nettobaryonenzahldichte. Bei der hydrodynamischen Beschreibung von Kollisionen geht die EoS als zusätzliche Gleichung ein, und wird direkt zur Lösung der hydrodynamischen Bewegungsgleichungen verwendet. Dies gilt auch für das UrQMD-Hybridmodell, das aus einer hydrodynamischen Phase mit einer nicht-gleichgewichts Initialisierung und Ausfrierphase kombiniert. Im UrQMD-Hybridmodell ist der Einfluss der Zustandsgleichung jedoch auf die heiße und dichte Gleichgewichtsphase der Entwicklung beschränkt.

Die Einbindung einer nicht-trivialen Zustandsgleichung in mikroskopische Transportmodelle ist jedoch nicht einfach. Eine Methode zur konsistenten Einführung einer beliebigen EoS in das UrQMD-Transportmodell wird erstmals in dieser Arbeit vorgestellt. Nicht-triviale hadronische Wechselwirkungen können im UrQMD Transportmodell durch die Anpassung des Terms der potentiellen Energie, in der semi-klassischen Bewegungsgleichung der Quanten-Molekular-Dynamik (QMD) eingeführt werden. So kann eine beliebige Zustandsgleichung in den QMD-Teil von UrQMD implementiert werden, wenn die potentielle Energie pro Baryon für das Modell bekannt ist. Es wurde diese Methode verwendet, um das realistische CMF Modell in UrQMD zu implementieren und dessen Einfluss auf die Entwicklung der Eigenschaften der Materie, die bei der Kollision entsteht, zu untersuchen. Die Ergebnisse wurden auch mit hydrodynamischen Simulationen unter Verwendung der gleichen Zustandsgleichung verglichen, um die Zuverlässigkeit der Methode zu zeigen. Die zeitliche Entwicklung der Baryondichte zeigte eine gute Übereinstimmung mit den hydrodynamischen Simulationen, wenn in beiden Fällen die gleiche Zustandsgleichung verwendet wird. Gleichzeitig ist die Kompression stark von der verwendeten EoS abhängig. Dies deutet darauf hin, dass Beobachtungen, die auf die anfängliche Kompressionsphase der Schwerionenkollision und die maximal erreichte Kompression sensitiv sind, zur Untersuchung der EoS bei hohen Baryondichten verwendet werden können. Die Nicht-Gleichgewichtseffekte führen jedoch dazu, dass die Temperatur des Systems in UrQMD höher ist als die in hydrodynamischen Simulationen erhaltene. Dennoch bietet die Methode eine konsistente Behandlung der Zustandsgleichung während der gesamten Entwicklung des Systems. Sie kann verwendet werden, um die Auswirkungen einer EoS in der anfänglichen Kompressionsphase der Kollision bei niedrigen Energien zu untersuchen.

0.3 Künstliche Intelligenz für Schwerionenkollisionen

Die Grundprinzipien der KI und verschiedene KI-Methoden werden in Kapitel 4 vorgestellt. Die Grundprinzipien der Funktionsweise von Deep Learning (DL)-Modellen auf der Basis neuronaler Netzwerke werden dort auch eingeführt. Ein neuronales Netzwerk ist eine Architektur des maschinellen Lernens, die aus einer Sammlung miteinander verbundener Knoten, den Neuronen, besteht. Ein neuronales Netzwerk nimmt verschiedene Eingaben

auf und verarbeitet sie durch das miteinander verbundene Netzwerk von Neuronen, um eine Ausgabe zu erzeugen. Die grundlegende Funktionsweise eines Neurons, eines vollständig verbundenen neuronalen Netzwerks und eines neuronalen Faltungsnetzwerks (Convolution Neural Networks, CNN) wird ausführlich erläutert. CNNs sind spezialisierte neuronale Netzwerke, die für das Lernen aus Bilddaten optimiert sind. CNN-basierte Deep Learning-Modelle sind jedoch nicht für das Lernen aus experimentellen Detektordaten optimiert.

Die auf PointNet basierenden Modelle wurden als eine neuartige DL-Methode vorgestellt, die direkt auf Treffer-/Spurinformationen von in einem Detektor gemessenen Partikeln trainiert werden kann. In diesem Kapitel wurden die allgemeine Struktur der PointNet-Architektur und ihre Funktionsweise im Detail beschrieben. Das PointNet ist eine DL-Architektur, die auf das Lernen aus Punktwolkendaten spezialisiert ist. Punktwolken sind Sammlungen von ordnungsinvarianter Punkte im Raum. Die experimentellen Daten haben eine inhärente Punktwolkenstruktur (z.B. sind die Partikeltreffer in den Detektorebenen einfach eine Punktwolke der Trefferkoordinaten). Das PointNet-Modell verwendet 1-D-Faltungsoperationen, um ordnungsinvariante Merkmale pro Punkt zu extrahieren, die dann durch symmetrische Operationen wie 'Average Pooling', 'Max Pooling' usw. in eine globale Event-Eigenschaft umgewandelt werden. Die extrahierten Event-Eigenschaften werden dann in ein konventionelles neuronales Netzwerk eingespeist, um die Zielvariable zu regressieren oder zu klassifizieren. Als statistische Lernmethode zur Parameterschätzung werden in diesem Kapitel auch die Bayes'sche Inferenztechnik und ihre Funktionsprinzipien erläutert.

0.4 PointNet-basierte Ereignis-Charakterisierung

In Kapitel 5 werden die Ergebnisse mehrerer AI-Analysen vorgestellt. Das Kapitel beginnt mit einer vergleichenden Studie des Glauber MC-Modells und des UrQMD-Modells zur Bestimmung der Zentralitätseigenschaften von Schwerionenkollisionen. Das Glauber MC-Modell ist eine vereinfachte Beschreibung von Kollisionen, die in Experimenten verwendet wird, um Beobachtungsgrößen wie die Anzahl der geladenen Spuren auf die Zentralität der Kollision abzubilden. In dieser Studie wurde festgestellt, dass die Bestimmung der Zentralität und die geschätzten Fluktuationen von N_{part} für Au-Au-Kollisionen bei 1,23 AGeV unter starken Modellabhängigkeiten leiden. Die vereinfachte Glauber-MC-Beschreibung von Kollisionen, die in den Experimenten verwendet wird, um die gemessene Spurenmultiplikation mit dem Stoßparameter oder N_{part} in Beziehung zu setzen, sagt eine völlig andere N_{part} -Verteilung voraus als das auf der mikroskopischen Transporttheorie basierende UrQMD-Modell. Diese starke Modellabhängigkeit von N_{part} kann die Interpretation der Ergebnisse der experimentellen Analyse erschweren, wenn das verwendete N_{part} während der gesamten Analyse und dem abschließenden Modell-Daten-Vergleich nicht konsistent ist. Um diesen Effekt zu demonstrieren, wurde die Produktion von geladenen Pionen sowie die Rapiditäts-Spektren von Protonen und leichten Kernen bei $E_{lab} = 1,23A$ GeV untersucht und die Ergebnisse mit HADES- und STAR-Messungen verglichen. Es wurde gezeigt, dass

die Pionenmultiplizität pro Partizipant sehr empfindlich auf das Modell reagieren kann, das zur Schätzung der zugrundeliegenden N_{part} -Verteilung für eine bestimmte Zentralitätsklasse verwendet wird. Es wird vorgeschlagen, dass die Untersuchung von Observablen wie der Pionenmultiplizität als Funktion der Zentralität anstelle von N_{part} die explizite Modellabhängigkeit von N_{part} , die beim Vergleich experimenteller Daten mit Modellvorhersagen auftritt, teilweise vermeiden kann. Allerdings ist damit nicht garantiert, dass die experimentellen Daten und das zu vergleichende Modell eine ähnliche Verteilung von N_{part} aufweisen. Die Modellabhängigkeit von N_{part} hat auch messbare Konsequenzen für die beobachteten Rapiditäts-Verteilungen von freien Protonen und leichten Kernen. Auch hier zeigen vorläufige Daten des HADES-Experiments eine signifikante Verringerung der Protonenzahl dN/dy im Vergleich zu UrQMD, was mit einem deutlich kleineren N_{part} übereinstimmt, ein Effekt, der in den Daten des STAR-Experiments nicht beobachtet wurde. Offensichtlich ist das Verständnis dieser Widersprüche auch für die Interpretation von Beobachtungsgrößen wie der Pionenmultiplizität und Protonenzahlfluktuationen wichtig.

Die Methode, die für die Auswahl oder Charakterisierung von Ereignissen verwendet wird, sollte mit dem theoretischen Modell übereinstimmen, mit dem die Beobachtungswerte der ausgewählten Daten verglichen werden. In diesem Zusammenhang haben wir das Potenzial von PointNet-basierten DL-Methoden untersucht, um den Impaktparameter oder die Anzahl der beteiligten Nukleonen in einem Kollisionsereignis zu rekonstruieren. PointNet-basierte Modelle wurden trainiert, um den Impaktparameter von Kollisionen aus den Treffern und/oder der rekonstruierten Spur von Teilchen in 10 AGeV Au-Au-Kollisionen am CBM Experiment zu rekonstruieren. Das Ziel war es, diese Impaktparameter direkt aus den experimentellen Ergebnissen auf Detektorebene zu extrahieren. Daher wurde ein Datensatz erstellt, der den experimentellen Daten sehr ähnlich ist. Um dies zu erreichen, wurde die Ausgabe von UrQMD durch eine komplexe Pipeline geleitet, die aus einer GEANT-basierten CBM-Detektorsimulation besteht, die den Transport der Teilchen, die Digitalisierung der Treffer und die Ereignisrekonstruktion durchführt. Es wurde festgestellt, dass die PointNet-Modelle eine genaue Rekonstruktion der Impaktparameter im Bereich von 2-14 fm durchführen können. Ein Modell, das Treffer des MVD-Detektors und aus Treffern im MVD und STS rekonstruierte Spuren zur Vorhersage des Impakt-Parameters verwendet, hatte einen Validierungs-MSE von etwa $0,39 \text{ fm}^2$. Im Gegensatz zur konventionellen Glauber MC-basierten Zentralitätsauswahl, die nur eine erwartete Impact-Parameter-Verteilung für Ereignisse liefert, die zu einer bestimmten Zentralitätsklasse gehören, können die PointNet-Modelle eine genaue Impact-Parameter-Rekonstruktion auf der Basis einzelner Ereignisse durchführen. Die Idee der Rekonstruktion von Impaktparametern wurde auch auf das PANDA-Experiment bei FAIR ausgeweitet, das Antiprotonen-Kern-Kollisionen untersucht. Für Antiproton-Neon-Kollisionen bei $p_{lab} = 15 \text{ GeV}$ hatte ein Modell, das auf der Punktwolke des Impuls-Vier-Vektors und der Ladung der Endzustandsteilchen trainiert wurde, einen Validierungs-MSE von etwa 1 fm^2 . Es wurde auch eine Abhängigkeit der Leistung von der Systemgröße beobachtet, wobei die Vorhersagegenauigkeit mit abnehmender Systemgröße abnahm. Schließlich wurden auch PointNet-basierte Modelle entwickelt, um den N_{part} bei Kollisionen zu bestimmen. Es wurde festgestellt, dass

die Modelle auch eine genaue, ereignisweise N_{part} -Bestimmung für 10 A GeV Au-Au-Kollisionen im CBM-Experiment mit einer Validierungs-MAE von etwa 8,2 durchführen können. Für 1,23 AGeV Au-Au-Kollisionen am HADES-Experiment zeigten die PointNet-Modelle einen MAE von etwa 11,6. Dennoch liefern die PointNet-basierten Modelle Ereignis für Ereignis N_{part} , die mit einem theoretischen Modell übereinstimmen. Auf diese Weise kann man die inkonsistente Verwendung des von Glauber MC vorhergesagten N_{part} für die Ereignisauswahl vermeiden, wenn man experimentelle Daten mit einem theoretischen Modell wie UrQMD vergleicht. Man kann im Wesentlichen die Glauber MC-basierte Zentralitätsauswahl und Ereignischarakterisierung durch die überlegenen DL-Modelle ersetzen. Solche Modelle können auch in Experimenten zur Online-Analyse und Ereignischarakterisierung von Free-Streaming-Detektorausgaben verwendet werden.

0.5 AI-Methoden zur bestimmung der Zustandsgleichung bei hoher Dichte

Eines der Hauptziele der Schwerionenprogramme weltweit ist die Untersuchung der Zustandsgleichung von heißer und dichter QCD-Materie. Im letzten Teil der Arbeit haben wir verschiedene KI-Methoden zur Untersuchung der Zustandsgleichung bei hohen Baryonendichten diskutiert. Zunächst wurde eine Bayes'sche Inferenz durchgeführt, um die Dichteabhängigkeit der Zustandsgleichung anhand der verfügbaren experimentellen Messungen des elliptischen Flusses und der mittleren transversalen kinetischen Energie von Protonen mittlerer Geschwindigkeit in Kollisionen mit mittlerer Energie einzuschränken. In dieser Studie wurde das UrQMD-Modell verwendet, das um beliebige Potentiale (oder äquivalent dazu die EoSs) erweitert wurde. Gaußsche Emulations-Modelle wurden für das UrQMD-Modell trainiert, um ein schnelles MCMC-Sampling durchzuführen. Ein parametrisiertes dichteabhängiges Potenzial wird in das UrQMD-Modell eingeführt, das zum Trainieren der Gauß-Prozess-Modelle verwendet wird. Die Bayes'sche Inferenz wurde verwendet, um den gemeinsamen Posterior für die Parameter des Potentials zu konstruieren. Es wurde festgestellt, dass das ursprüngliche Potential gut aus den experimentellen Beobachtungsdaten von Schwerionenkollisionen rekonstruiert werden kann, die bereits aus experimentellen Messungen verfügbar sind. Die experimentellen Daten schränken die in unserer Methode rekonstruierte Zustandsgleichung für Dichten bis zu 4-facher Grundzustandsdichte n_0 ein. Jenseits von $3n_0$ hängt die Form des Potentials jedoch von der Wahl der verwendeten Beobachtungsdaten ab. Dies wird in der Abbildung 1 veranschaulicht, in der das Quadrat der Schallgeschwindigkeit, die mit Hilfe der Bayes'schen Inferenz extrahiert wurde, deutliche Unterschiede in Abhängigkeit von den zur Rekonstruktion verwendeten Daten aufweist. Die EoS, die unter Verwendung aller verfügbaren Datenpunkte (*MEAN (13 points)*) extrahiert wurde, stimmt gut mit den Einschränkungen aus der Verschmelzung von Neutronensternen mit einer steifen Zustandsgleichung für Dichten bis zu $4n_0$ und ohne Phasenübergang überein. Wenn jedoch nur ein reduzierter Datensatz von 13 Datenpunkte verwendet wird, zeigt die extrahierte Schallgeschwindigkeit einen drastischen Abfall, der

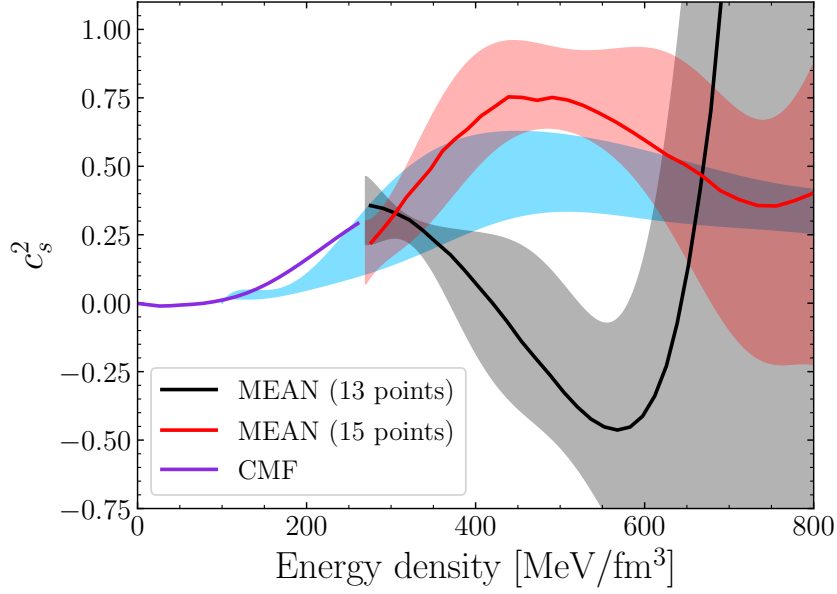


Figure 1: Quadrat der Schallgeschwindigkeit c_s^2 , bei $T = 0$, als Funktion der Energiedichte. Das c_s^2 für die MEAN EoS, die aus allen Datenpunkten extrahiert wurde, ist in rot dargestellt, wohingegen das nur aus 13 Datenpunkten extrahierte in schwarz dargestellt ist. Das Ergebnis aus astrophysikalischen Beobachtungen sind als blaues Band dargestellt. Für Energiedichten bis zu $270 \text{ MeV}/\text{fm}^3$ ist die Schallgeschwindigkeit aus dem CMF als violette Kurve aufgetragen. Die Unsicherheitsbänder entsprechen einem Intervall der wahrscheinlichsten 68% aller abgeleiteten Potenzialkurven.

mit einem starken Phasenübergang erster Ordnung bei hohen Dichten übereinstimmt. Es gibt eine Diskrepanz in den experimentellen Messungen von $\langle m_T \rangle - m_0$ und v_2 bei einer Kollisionsenergie von $\approx 4 \text{ GeV}$. Dies könnte auf große Unsicherheiten in den Messungen hinweisen oder auf die Unfähigkeit des zugrundeliegenden Modells, die Messwerte mit einer gegebenen Zustandsgleichung simultan zu beschreiben. Es ist zu beachten, dass die Daten aus verschiedenen Experimenten stammen und über unterschiedliche Zeiträume hinweg durchgeführt wurden. Die Unterschiede in der Akzeptanz, der Auflösung, der Statistik und sogar in den Analysemethoden der experimentellen Daten machen es uns schwer, die genauen Quellen dieser Effekte zu bestimmen.

Die Bayes'sche Inferenz kann die QCD EoS mit hoher Dichte einschränken, indem sie experimentelle Daten zu v_2 und $\langle m_T \rangle - m_0$ von Protonen verwendet. Eine solche Analyse auf der Grundlage von HIC-Daten kann die Eigenschaften der dichten QCD-Materie aus Neutronensternbeobachtungen verifizieren und ergänzt astrophysikalische Studien, um die Zustandsgleichung bei endlicher Temperatur und ihre Abhängigkeit von der Symmetrienergie einzuschränken. Vollständig schlüssige Aussagen über die EoS jenseits der Dichte $3n_0$ erfordern jedoch hochwertigere Daten im gesamten Strahlenergiebereich von 2-10 GeV, die hoffentlich durch das Programm von STAR-FXT am RHIC, das bevorstehende CBM-

Experiment an FAIR und zukünftige Experimente an HIAF und NICA bereitgestellt werden.

Schließlich wurde gezeigt, dass die PointNet-basierten Modelle auch zur Identifizierung der Zustandsgleichung im CBM-Experiment verwendet werden können. PointNet-basierte Modelle wurden trainiert, um eine Phasenübergangs-EoS von einer Crossover-EoS anhand der rekonstruierten Spurinformatoren im CBM-Experiment zu unterscheiden. Die Modelle waren in der Lage, eine fast perfekte Vorhersagegenauigkeit zu erreichen. Trotz der Unsicherheiten aufgrund der begrenzten Detektorakzeptanz und der Verzerrungen in den Rekonstruktionsalgorithmen war das PointNet-basierte Modell in der Lage, die Merkmale zu erlernen, die die zugrunde liegende Physik der Kollision genau identifizieren können. Das PointNet-Modell konnte eine Genauigkeit von über 96 % bei der Klassifizierung von Phasenübergangsereignissen von Crossover-Ereignissen erreichen, wenn es mit realistischen experimentellen Einschränkungen der Detektorauflösung und -akzeptanz trainiert und getestet wurde. Das Modell erwies sich auch als robust gegenüber einigen Änderungen der Modellparameter. Kurz gesagt, dies demonstriert die Flexibilität von PointNet-basierten Modellen bei der Untersuchung von Schwerionenkollisionen. Das PointNet-basierte Modell kann nicht nur die geometrischen Merkmale des Ereignisses, wie den Stoßparameter oder den N_{part} , identifizieren, sondern auch abstrakte physikalische Merkmale, wie die EoS, direkt aus den Detektorergebnissen extrahieren.

Kurzum, in dieser Arbeit wurden verschiedene Techniken der künstlichen Intelligenz entwickelt, um Schwerionenkollisionen bei hoher Baryondichte zu untersuchen. Die Bayes'sche Analyse zur Einschränkung der EoS bei hoher Dichte deutet darauf hin, dass die Flussbeobachtungen tatsächlich wertvolle Informationen enthalten, die die EoS von Kernmaterie mit hoher Dichte eng eingrenzen können. Wir haben auch PointNet-basierte DL-Modelle entwickelt, die sehr komplexe universelle Ereignismerkmale aus grundlegenden Ereignisinformatoren extrahieren können, die aus Schwerionenkollisionsexperimenten verfügbar sind. Mit Hilfe von PointNet-basierten Modellen ist es nun möglich, die Impaktparameter und N_{part} in Schwerionen-Kollisionsexperimenten Ereignis für Ereignis genau zu extrahieren. PointNet-basierte Modelle sind sogar in der Lage, Ereignisse anhand von sehr abstrakten Ereignismerkmalen zu klassifizieren, wie z.B. der EoS, die während der heißen und dichten Phase der Kollision vorhanden war, d.h. ob ein Phasenübergang vorhanden war oder nicht. Die Verwendung von experimentellen Daten wie z.B. Teilchenspuren in diesen Modellen kann mögliche Verzerrungen in den Daten beseitigen, die in späteren Phasen der Datenverarbeitung auftreten können. Die Punktwolkendarstellung der Daten erfordert nur eine minimale Vorverarbeitung, bevor sie in das DL-Modell eingespeist wird. Dadurch kann das Modell im Experiment für eine schnelle Online-Analyse der experimentellen Daten verwendet werden. Aufgrund ihrer Fähigkeit, globale Merkmale in den Eingabedaten zu identifizieren, können PointNet-basierte Modelle auch leicht angepasst werden, um jedes andere globale Ereignismerkmal von Schwerionenkollisionen zu analysieren. Obwohl sich die in dieser Arbeit entwickelten PointNet-basierten Modelle auf die Anwendung im CBM-Experiment konzentriert haben, können die Modelle auch leicht für die Anwendung in anderen Experimenten erweitert werden.

Contents

Zusammenfassung	vii
0.1 Das QCD-Phasendiagramm und Experimente zur Schwerionenkollision . . .	vii
0.2 Modelle für Schwerionen-Kollisionen	viii
0.3 Künstliche Intelligenz für Schwerionenkollisionen	ix
0.4 PointNet-basierte Ereignis-Charakterisierung	x
0.5 AI-Methoden zur bestimmung der Zustandsgleichung bei hoher Dichte	xii
1 Introduction	1
1.1 Quantum chromodynamics	1
1.2 Heavy-ion collisions	3
1.3 The Phase diagram of QCD	4
1.4 Theoretical models for heavy-ion collisions	6
1.5 Artificial intelligence for heavy-ion collisions	7
2 Heavy-ion collision experiments	9
2.1 Physics at FAIR	11
2.1.1 HADES	14
2.1.2 The CBM detector	15
2.2 Other major experiments	16
2.2.1 NA61/ SHINE	16
2.2.2 ALICE	16
2.2.3 STAR	17
2.3 Challenges in the analysis of experimental data	17
3 Models for heavy-ion collisions	19
3.1 The UrQMD (cascade) model	20
3.1.1 Coarse grained UrQMD	21
3.2 Hydrodynamics	22
3.3 UrQMD- hybrid	23
3.4 UrQMD with potential interactions	25
3.5 Density dependent EoS in UrQMD	26

3.5.1	The CMF EoS in UrQMD	27
3.5.2	Results on the evolution of bulk properties	28
4	Artificial intelligence for heavy-ion collisions	39
4.1	Machine learning and deep learning	39
4.1.1	Artificial neural networks	40
4.1.2	Convolution Neural Networks	44
4.2	Learning from experimental data with PointNet	46
4.3	Bayesian Inference	48
4.3.1	The Metropolis algorithm	48
5	AI based analysis of heavy-ion collision data	51
5.1	The Glauber MC model based event selection	52
5.1.1	Glauber MC based centrality selection in HADES	53
5.1.2	Glauber MC vs UrQMD: N_{part} and b distributions	58
5.1.3	Pion production at 1.23 AGeV	62
5.1.4	Protons and light nuclei at 1.23 AGeV	67
5.2	PointNet based event characterisation in experiments	69
5.2.1	Impact parameter determination in the CBM experiment	70
5.2.2	Impact parameter determination in the PANDA experiment	84
5.2.3	N_{part} determination in HADES and CBM experiments	85
5.3	Bayesian inference of dense matter EoS	87
5.3.1	Closure tests	96
5.3.2	Results based on experimental data	99
5.4	PointNet based EoS classification in the CBM experiment	107
5.4.1	Performance of the models	111
5.4.2	Dependence on model parameters	114
5.4.3	Interpreting the PointNet model	118
6	Summary	123
6.1	Outlook	127
A	Equations of state	129
A.1	The hadron resonance gas model	129
A.2	The chiral mean field model	129
	Bibliography	133
	Acknowledgements	157
	Curriculum vitae	159

List of Figures

1	Schallgeschwindigkeit zum Quadrat c_s^2 , bei $T = 0$, als Funktion der Energiedichte	xiii
1.1	The conjectured phase diagram of QCD.	5
2.1	The proposed FAIR accelerator complex.	12
3.1	UrQMD cascade: four-volumes at different T and ρ	22
3.2	Nuclear potential U , the field energy per baryon E_{field}/A and its derivative as a function of the baryon density n_B for three different potentials	29
3.3	CMF in UrQMD: four-volumes at different temperatures and densities . . .	31
3.4	Time evolution of the baryon density	32
3.5	Time evolution of average temperature	34
3.6	Time evolution of pressure	35
3.7	Expansion trajectories in the temperature-baryon density plane	36
3.8	Entropy production per baryon as a function of beam energy	37
4.1	Structure of a neuron.	41
4.2	The convolution operation	45
4.3	General structure of the PointNet model.	47
5.1	Glauber MC vs UrQMD: N_{part} - b distributions.	55
5.2	Glauber MC fit to UrQMD data	57
5.3	Glauber MC vs UrQMD cascade: 5% Centrality bins.	59
5.4	Mean and standard deviation of the impact parameter distributions.	60
5.5	Mean and standard deviation of the number of participants distribution. .	61
5.6	N_{part} distributions for 0-10% and 0-40 % centrality classes.	63
5.7	Charged pion multiplicity per participant as a function of N_{part}	65
5.8	Charged pion multiplicity as a function of centrality.	66
5.9	Rapidity distributions of free protons and light nuclei	69
5.10	Charged particle track multiplicity as a function of impact parameter . . .	71
5.11	General structure of the joint alignment networks.	74
5.12	General structure of M -hits, S -hits and MS -tracks models.	75
5.13	Structure of the model HT -combi.	76

5.14	Relative precision of DL models as a function of impact parameter.	78
5.15	Mean error of the predictions as a function of the impact parameter.	79
5.16	Distribution of predicted impact parameters using <i>MS-tracks</i>	79
5.17	Mean error in predictions as a function of centrality.	80
5.18	Difference of the mean track multiplicity (ΔM) as a function of centrality.	81
5.19	Difference in the mean of the error distributions as a function of centrality	82
5.20	Performance of the N_{part} determination model in the HADES experiment .	86
5.21	Performance of the N_{part} determination model in the CBM experiment . .	86
5.22	The EoSs used in training the Gaussian process models	91
5.23	v_2 and $\langle m_T \rangle - m_0$ for 50 random EoSs from the training data	92
5.24	Performance of GP models in predicting v_2 at different beam energies . . .	93
5.25	Performance of the GP models in predicting $\langle m_T \rangle - m_0$ for 5 different beam energies	94
5.26	Distribution of the potential $V(n_B)$ at different densities	96
5.27	Probability density of the posterior constructed in the closure tests	97
5.28	Prior- posterior comparison for the closure test	98
5.29	Probability density of the posterior constructed from experimental data . .	100
5.30	Prior-posterior comparison for experimental inference	101
5.31	v_2 and $\langle m_T \rangle - m_0$ values from UrQMD using MEAN and MAP EoS	102
5.32	Slope of the directed flow, dv_1/dy , of protons for MEAN and MAP EoSs .	103
5.33	Speed of sound squared c_s^2 , at $T = 0$, as a function of energy density	104
5.34	Probability density of the posterior extracted without $\langle m_T \rangle - m_0$ of the two highest beam energies	105
5.35	Differential elliptic flow of protons for MEAN and MAP EoSs at 1.23 <i>AGeV</i>	107
5.36	The equations of state, along an isentropic trajectory	109
5.37	Validation accuracy of PointNet models as a function of the number of events per input.	112
5.38	Variation in the testing accuracy of the PointNet models	115
5.39	Fraction of the medium below the freeze-out energy density at the beginning of hydrodynamics	116
5.40	Distributions of mean transverse momentum and elliptical flow for crossover and first order phase transitions.	118
5.41	Most important feature distribution and output of convolution for feature 104.	119
5.42	Distribution of track multiplicity difference.	120
A.1	The CMF equation of state for different values of constant entropy per baryon (S/A)	131

List of Tables

5.1	Pion yields for elementary collisions at 1.23 AGeV	68
5.2	Training and testing datasets for PointNet-based impact parameter determination in the CBM experiment.	73
5.3	Performance metrics for the PointNet based models trained for impact parameter determination in the CBM experiment	77
5.4	Performance change of the <i>M-hits</i> model without the alignment networks. .	83
5.5	Observables used in Bayesian inference	89
5.6	Means (μ) and standard deviations (σ) of the Gaussian priors	95

Chapter 1

Introduction

The search for a coherent description of the matter and radiation that constitute the universe, consistent at all scales of length and energy, is a fascinating, yet unresolved, fundamental problem in physics. Towards the latter half the last century, attempts by physicists around the world to develop such a description resulted in the development of the *Standard Model* of particle physics, which describes three of the four fundamental interactions (except the gravitational interaction). The standard model identifies quarks, leptons and gauge bosons as the fundamental particles in the universe. There exist six different types of quarks (up, down, charm, strange, top, bottom) and their antiparticles. The up, charm and top quarks have an electric charge of $+2/3$, while the down, strange and bottom quarks have an electric charge of $-1/3$. There are also six different leptons (electron, muon, tau and their associated neutrinos) and their antiparticles. The electron, muon and tau particles have an electric charge of -1 , while the neutrinos have no charge. The gauge bosons are the force carriers with the W^{+-} and Z^0 mediating the weak interaction, the photon mediating the electromagnetic interaction and the gluon mediating the strong interaction. Besides their electric charge, quarks also carry a colour charge. There are three different colour charges: red, blue and green. The quarks interact via the exchange of colour charge, mediated by gluons which themselves carry colour charge. Only combinations of all three colours, or colour-anti-colour quarks, form colour-neutral stable hadrons found in nature. The interactions between quarks and gluons are described by Quantum Chromodynamics (QCD), the theory of strong interaction.

1.1 Quantum chromodynamics

Quantum chromodynamics is a non-Abelian gauge theory of colour charge based on the $SU(3)$ symmetry group. The QCD Lagrangian is given by:

$$L = -\frac{1}{4} \sum_a G_{\mu\nu}^a G_a^{\mu\nu} + \sum_k \bar{\Psi}_k \left(i\gamma^\mu \partial_\mu - g\gamma^\mu \sum_a A_\mu^a \frac{\lambda^a}{2} - m_k \right) \Psi_k. \quad (1.1)$$

The $G_{\alpha}^{\mu\nu}$ in the first term of the Lagrangian is the gluon field strength tensor which has the form

$$G_a^{\mu\nu} = \partial^{\mu} A_{\nu}^a - \partial^{\nu} A_{\mu}^a - g f^{abc} A_{\mu}^b A_{\nu}^c. \quad (1.2)$$

where g is the strong coupling constant, A_{μ}^a are the gluon fields and f^{abc} are the structure constants. The index $a = 1 - 8$ denotes the colour of the gluons and the last term in eq. 1.2 incorporates the self interaction of gluons due to their non-zero colour charge. The second term in the Lagrangian describes the interaction between quarks and gluons as well as the self interaction of the quarks where Ψ_k are the quark fields with the index $k = u, d, c, s, t, b$ representing the flavour of the quarks, γ^{μ} are the Dirac matrices and λ^a are the Gell-Mann matrices, which are the generators of the SU(3) symmetry group.

One of the interesting features of QCD is the running coupling constant

$$g(Q^2) = \frac{16\pi^2}{(11 - \frac{2}{3}N_f) \ln(Q^2/\Lambda_{QCD}^2)} \quad (1.3)$$

where Q^2 is the four-momentum transferred, $\Lambda_{QCD} \approx 0.2$ GeV is the QCD scale parameter and N_f is the number of quark flavours.

For large values of Q^2 or small distances, the coupling strength becomes extremely small and the quarks can behave as "free" particles. This property of the strong interaction is called "asymptotic freedom", the discovery for which David Gross, Frank Wilczek and David Politzer were awarded the 2004 Nobel Prize in Physics. Perturbative methods can be used to make quantitative predictions of QCD at extremely high energies due to the weak coupling strengths. On the other hand, at small values of Q^2 the coupling strength becomes extremely large. This leads to the property called "confinement", which prevents the existence of isolated quarks in nature. At large coupling strengths, it becomes energetically more favourable to create a quark-antiquark pair than to separate a quark from a hadron. At intermediate and large couplings, perturbative methods cannot be used and complex numerical methods become necessary.

Lattice QCD is one such method in which different actions are evaluated on a numerical grid using Monte Carlo methods. In lattice QCD, the quark fields are defined at discrete points in space-time (lattice sites), while the gluon fields are represented on the links connecting neighbouring lattice sites. Although a powerful technique for studying the non-perturbative regime of QCD, lattice simulations require enormous computational resources, which currently limits their practical applications to non-dynamical systems.

There are several effective models for QCD that simplify the problem by dealing directly with hadronic degrees of freedom. These models assume the existence of hadrons and construct an effective Lagrangian that can reproduce some fundamental symmetries and interactions of the QCD Lagrangian. Although their applicability is limited to a certain region of QCD, effective models provide valuable information about the structure and properties of strongly interacting matter.

1.2 Heavy-ion collisions

The study of the properties of QCD matter under different thermodynamic conditions is one of the most exciting directions in QCD physics. In the laboratory, such systems can be created for short periods of time by colliding large nuclei such as Au, U, Ag, Pb, etc. at relativistic energies [1–3]. In Heavy-Ion Collisions (HIC), the initial kinetic energy of the nucleons is converted to heat and compressional energy, creating a hot and/or dense QCD fireball. The fireball then rapidly expands under its own pressure and gradually cools down to produce the dilute gas of hadrons that is ultimately measured in experiments. The experiments explore the properties of QCD matter at different temperatures and densities by varying the collision energy and system size. High energy collisions tend to rapidly heat the system to a very high temperature but the net baryon densities achieved are lower as the nucleons are not stopped to create a thermalised system. On the other hand, intermediate or low energy collisions produce fireballs with relatively low temperatures but high baryon densities.

The intermediate energy collisions of heavy nuclei are of particular interest because they offer the possibility of compressing nuclear matter to many times the nuclear saturation density, which is otherwise expected to occur only in neutron stars, core collapse supernovae and neutron star mergers. Early fundamental studies on the theoretical mechanisms for the production of highly compressed nuclear matter in ion-ion collisions, mainly based on nuclear shock waves [4–8] were complemented by the first generation of relativistic nuclear collision experiments worldwide. Of particular interest are the plastic ball [9] and streamer chamber [10] experiments at BEVALAC [11], Lawrence Berkeley National Laboratory, which studied collisions in the range ≈ 100 A MeV to 2 A GeV. The plastic ball and streamer chamber experiments were the first to make full 4π measurements of the final state particles produced in nucleus-nucleus collisions. The experiments collected a wealth of data that observed the predicted compression effects and collective flow of particles in nucleus-nucleus collisions [12–16]. The exciting results spurred many more investigations into the properties of hot and dense nuclear matter via relativistic and ultra-relativistic nucleus-nucleus collisions. BEVALAC was complemented by a number of heavy-ion experiments at GSI (UNILAC, SIS-18), BNL (AGS, RHIC) and CERN (PS, SPS) around the world. The fixed target experiments at these facilities were/are used to study the properties of highly compressed nuclear matter. While these facilities have been instrumental in the growth of experimental heavy-ion physics, accurate determination of the fundamental properties of nuclear matter, such as the Equation of State (EoS), requires precise measurements and large statistics that were not technologically feasible at the time. Such measurements are expected to be provided by several proposed and existing fixed target experiments worldwide. In chapter 2 some of the major heavy-ion collision experiments are discussed in detail, with emphasis on the heavy-ion physics programme at the Facility for Antiproton and Ion Research (FAIR), which is a major focus of this work.

1.3 The Phase diagram of QCD

The predictions from lattice QCD, perturbative QCD and effective models are used to construct a conjectured phase diagram of QCD bulk matter, as shown in figure 1.1. Different phases of QCD matter, their boundaries and different particle accelerators probing different regions of the phase diagram are illustrated in terms of temperature T and baryon chemical potential μ_B in figure 1.1. The QCD phase diagram has several interesting features that are being studied by the heavy-ion programmes around the world.

1. *Deconfinement transition.* At low temperatures and low chemical potentials, matter exists as a gas of interacting hadrons and their resonances. This gas is mainly composed of pions. By increasing the temperature and/or the chemical potential, the hadron gas could transition to a state of quasi-free quarks and gluons called the Quark Gluon Plasma (QGP) [17–21]. Lattice QCD calculations suggest that the transition from hadron gas to QGP is a smooth crossover at vanishing baryon chemical potential and high temperature [22–25]. This is similar to the thermodynamic condition that existed in the early universe. A first-order phase transition is conjectured at lower temperatures and moderate baryon densities [26]. The search for signals of a first-order phase transition and a possible critical endpoint of the first-order phase transition are the main goals of the current heavy-ion experiments.
2. *Chiral symmetry restoration.* In the limit of massless quarks, QCD is invariant under the interchange of left- and right-handed quarks. Adding a mass term to the Lagrangian explicitly breaks this chiral symmetry. However, the masses of the u, d and s quarks are very small and the breaking of the symmetry is very weak. Therefore, the chiral symmetry is often considered to be approximate. If the chiral symmetry is approximate or exact, there should be degenerate parity partners for the hadronic states. However, no such partners are observed. Therefore, chiral symmetry is most likely broken spontaneously in vacuum, during which the Lagrangian remains symmetric with respect to chiral transformations, while the true ground state of the theory is not. At high temperatures and/or chemical potentials, the chiral symmetry of QCD matter is expected to be restored. The chiral and deconfinement transitions are expected to occur at almost the same temperature [27]. However, this may not be the case for QCD matter at finite chemical potential. Identifying the signals of a chiral transition is another exciting goal for heavy-ion collision experiments.
3. *Nuclear Liquid-Gas Transition.* Ordinary nuclear matter (the nuclear liquid) exists at a baryon chemical potential of about 923 MeV and a temperature of about 0 MeV. When the temperature of this system is increased by a few MeVs, part of the nuclear liquid evaporates, emitting nucleons, light nuclei and other fragments. Alternatively, if the density is reduced below the nuclear saturation density, the nucleus is fragmented into droplets. As the temperature is increased and the density reduced, a mixed phase of the nuclear droplets and the gas of the emitted particles is formed. At vanishing chemical potentials, nuclear matter exists in a "gaseous"

1.3. THE PHASE DIAGRAM OF QCD

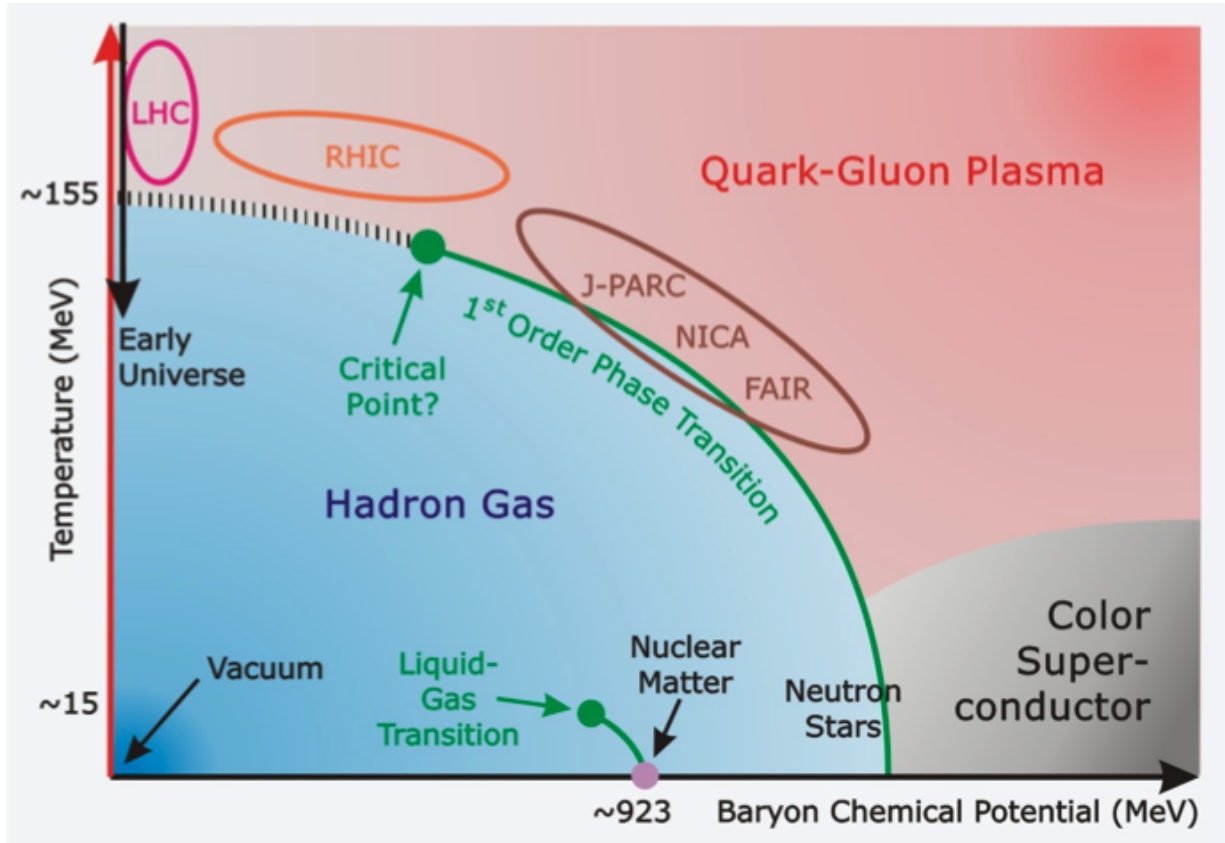


Figure 1.1: The conjectured phase diagram of QCD. The smooth crossover transition at vanishing chemical potential is shown as the vertical dashed lines, while the following solid green line represents the conjectured first-order phase transition. The region of the phase diagram probed by heavy-ion collisions at different accelerators is also shown. Figure taken from the GSI website [28].

phase of nucleons. At low temperatures, this transition from nuclear liquid to gas is a first-order phase transition associated with a latent heat of vaporisation for the nuclear liquid. The transition becomes weaker as the temperature is increased and finally ends in a second order critical point at $T \approx 15\text{-}20$ MeV and $\mu_B \approx 923$ MeV. The nuclear liquid-gas phase transition has been studied in several nuclear experiments and is a well-established region of the phase diagram [29, 30].

4. *Quarkyonic matter.* It is also suggested that at high baryon chemical potentials a new phase of matter exists between the deconfined QGP and the confined hadronic phase. This confined phase, which behaves like a gas of quarks at high baryon density, is known as the quarkyonic phase [31]. A triple point is also proposed where hadronic matter, Quark Gluon Plasma and quarkyonic matter would coexist. Note that in the figure 1.1 the quarkyonic phase is not labelled.

5. *Colour superconductor.* At asymptotically large chemical potentials and low temperatures, QCD matter could behave in a similar way to electrical superconductors in condensed matter physics. The quarks could form Cooper pairs to exhibit colour superconductivity, similar to the superconductivity in metals that arises from the condensation of electron Cooper pairs [32,33]. Experiments cannot currently achieve the densities required to produce a colour superconducting phase. However, such matter is expected to be found in compact stellar structures such as neutron stars.

1.4 Theoretical models for heavy-ion collisions

One of the main objectives of heavy-ion collision experiments is to map the QCD phase diagram by studying the final state particles measured by particle detectors. The experimental observables are compared with the predictions of theoretical models to infer the properties of the hot and/or dense matter produced in heavy-ion collisions. This is particularly true for the high net-baryon density region of the phase diagram, i.e. at large chemical potential, where direct lattice QCD simulations are currently not possible due to the fermionic sign problem [34]. In this regime, QCD motivated effective models as well as direct experimental evidence are employed to search for structures in the QCD phase diagram, such as a conjectured first-order phase transition and a corresponding critical endpoint [35–37].

The space-time evolution of heavy-ion collisions can be broadly divided into three distinct phases. In the initial pre-equilibrium phase, the projectile and target nuclei collide and the nucleons begin to interact with each other, both elastically and inelastically, creating a hot dense "fireball". Once the system has had sufficient time to interact, a phase of thermal equilibrium could be reached. In the equilibrium phase, the fireball expands and exhibits collective behaviour. Finally, the system becomes dilute and is no longer in chemical or thermal equilibrium. The final interactions of the hadrons before the freeze-out take place in this decoupled phase.

Depending on how each of these stages is implemented, there are several dynamical models for heavy-ion collisions.

1. *Transport models.* Models based on relativistic transport theory explicitly calculate the entire evolution of each microscopic degree of freedom, from the initial pre-equilibrium state to the final freeze-out [38]. There are two main approaches to solving the transport equations.
 - (a) Boltzmann-Uehling-Uhlenbeck (BUU) type approaches, which propagate the one-body phase space density under a mean field [39].
 - (b) Quantum Molecular Dynamics (QMD) type approaches that propagate the position and momenta of nucleons under an n-body Hamiltonian [40–46].

One of the main challenges in modelling heavy-ion reactions using transport theory

is to describe the transition between the hadronic and partonic phases. Transport models also require the cross section values for all processes as input, since all microscopic scatterings are treated explicitly. Therefore, the cross sections must be calculated analytically if experimental data are not available.

2. *Relativistic hydrodynamics.* Assuming that the system is in thermal equilibrium throughout the evolution, a macroscopic ideal hydrodynamical description can be used to model heavy-ion collisions [47]. However, this is only partially true for the intermediate stage where the system is sufficiently dense. This limits the applicability of hydrodynamics during the early and very late stages of evolution. The equilibrium assumption can be relaxed by introducing viscosity into the model. Nevertheless, hydrodynamical models can implement the transition from the hadronic phase to the quark gluon plasma by providing an appropriate equation of state.
3. *Hybrid models.* The hybrid micro+macro models for heavy-ion collisions use a microscopic description for the initial and final phases of the collision, while a macroscopic, hydrodynamic description is applied to the intermediate dense phase [48]. This combined approach to modelling the evolution is popularly known as the "standard model for heavy-ion collisions". Using hydrodynamics only for the dense phase evolution allows hybrid models to include different QCD transitions without using the equilibrium description to model the non-equilibrium dynamics during the interpenetration and final dilute phase. One of the challenges of a hybrid description is that the switching time from a transport model to hydrodynamics and vice versa is not well defined. The choice of starting and stopping time of the hydrodynamic evolution can significantly influence the final result.

Chapter 3 contains detailed discussions of different dynamical models for heavy-ion collisions, which are extensively used in the studies presented in the following chapters. In particular, a new method to consistently describe the entire evolution of the system within a QMD-type transport model is presented.

1.5 Artificial intelligence for heavy-ion collisions

The final state spectra measured by particle detectors in heavy-ion collision experiments carry information about the properties and dynamics of the matter created in the collision. However, due to the transient and stochastic nature of heavy-ion collisions, extracting the relevant physics signals from observables based on final state spectra is not straightforward. Traditional methods for analysing heavy-ion collision data require large-scale model comparisons and multi-parameter model fits to multiple observables sensitive to a physics phenomenon. The huge computational cost of Monte Carlo simulations is the main challenge associated with such investigations. In addition, the limited phase space coverage and the limited positional and temporal resolution of the detectors affect the quality of the collected data. Furthermore, different pre-processing and analysis algorithms used

for event characterisation and selection may introduce unanticipated biases into the data. Conventional observables that perform well in ideal model simulations could have reduced sensitivity in the presence of these experimental effects.

The main objective of this work is to investigate novel Artificial Intelligence (AI) based analysis techniques that could overcome the aforementioned limitations of conventional physics analyses. Artificial intelligence is a branch of computer science that deals with the development of techniques to emulate "intelligence" in machines, thereby giving them the ability to make decisions with minimal human intervention. Over the past few decades, there have been tremendous advances in hardware technology for high performance computing, particularly with Graphics Processing Units (GPUs). The advances in GPU technology and the availability of large amounts of data have made it possible to develop extremely complex, data-centric Artificial intelligence methods for solving a multitude of problems. A formal introduction to the basic concepts of data-centric AI methods is presented in chapter 4.

The success of AI in solving several computer science problems has motivated the high energy physics and nuclear physics community to explore AI as a novel tool for both experimental and theoretical analysis. The present work explores AI methods for connecting heavy-ion theory to experiment, with a particular emphasis on the experiments at FAIR. The heavy-ion experiments at FAIR will study the QCD phase structure at high net-baryon densities. The unique experimental and theoretical challenges posed by FAIR make it an ideal testbed to investigate the capabilities of AI in heavy-ion physics.

In order to avoid bias in the data due to the pre-processing algorithms used by the experiments and to speed up the analysis process, it is ideal to use AI methods that directly process detector-level information. However, there are several challenges in processing detector level information using conventional AI methods. These issues and proposed solutions are discussed in chapter 4. Note that conventional statistical inference methods are also considered in the context of AI in this thesis, although they use different modelling approaches than those used by modern AI methods. The basic principles of such a method based on Bayesian statistics is also presented in chapter 4.

Before introducing the AI methods for the analysis of experimental data, the limitations of a conventional simplified Glauber MC model [49,50] for collisions are presented in chapter 5. The Glauber MC model is often used for event selection in the experiments. The Glauber MC model is compared with a transport model to shed light on the uncertainties and ambiguities arising from the inconsistent use of different models to analyse experimental data. Various AI based solutions to avoid such ambiguities in experimental results are then presented in chapter 5. AI models that can accurately extract the underlying physics of the collisions are also presented. In addition to AI methods working directly on detector level information, a statistical learning technique is applied to experimental data to infer the physics as described by a theoretical model for heavy-ion collisions. Such an analysis is also presented in chapter 5. Finally, the results of the work are summarised in chapter 6.

Chapter 2

Heavy-ion collision experiments

Experimental research in high energy/nuclear physics was revolutionised by the discovery of particle accelerators. Today, particle accelerators are one of the fundamental tools for experimental research in high energy/nuclear physics. By accelerating and colliding heavy nuclei such as Au, U, Pb, etc. at velocities close to the speed of light, QCD matter of extremely high temperature and density is produced in the laboratory, which can be studied using particle detectors that measure the final state charged particles produced in the collision.

The earliest particle accelerators used a static electric field to accelerate charged particles such as an electron or a proton. However, the maximum energy that particles could achieve in such electrostatic accelerators was limited by their breakdown voltage, which was the maximum possible acceleration voltage. This was overcome by electrodynamic accelerators, which use time-varying electromagnetic fields to accelerate particles. Electrodynamic accelerators can be broadly categorised into linear and circular accelerators. Linear accelerators use dynamic electric fields to accelerate particles in a straight line, using an array of cavities that switch their electric polarities as the particle passes through, so that the particle is accelerated from one cavity to the next until it reaches the target. The main limitation of linear accelerators is that the maximum kinetic energy achieved by the particle depends on the length of the accelerator. This was overcome by the discovery of the cyclotron, for which Ernest O. Lawrence was awarded the Nobel Prize in Physics (1939). In a cyclotron, a particle accelerated by an electric field follows a curved path as it passes through a static magnetic field. In a linear accelerator, the spacing between the gaps of the cavities must be increased to account for the increasing speed of the particle, so that the particle always experiences an accelerating voltage when it is at the gap. In a cyclotron, however, as the particle follows an outward spiral trajectory, the same gap can be reused and the increasing distance the particle has to travel before reaching the gap again compensates for the increasing speed. Thus the particle reaches the gap at the same point in the voltage cycle each time, accelerating the particle further.

The principle of cyclotron can be extended to accelerate particles in a fixed closed loop. To ensure that the accelerated particle follows the fixed closed trajectory, the magnetic field strength is increased as the kinetic energy of the particle increases. Such accelerators, in which the magnetic field is synchronised with the increase in particle energy, are known as synchrotrons. Several of the world's most powerful particle accelerators are synchrotrons. The Large Hadron Collider (LHC) and the Super Proton Synchrotron (SPS) at CERN, the Relativistic Heavy Ion Collider (RHIC) at Brookhaven National Laboratory, and the Schwerionensynchrotron-18 (SIS-18) at GSI are the major synchrotrons currently performing nucleus-nucleus collisions at relativistic and ultrarelativistic energies.

The LHC, which began its first operational run in 2009, is the largest accelerator at CERN with a circumference of about 27 km. The LHC has performed proton-proton (p-p), proton-nucleus (p-A) and nucleus-nucleus (A-A) collisions at incredibly high beam energies of several TeV. Recently, in its *Run-3*, the LHC operated at record collision energies of 13.6 TeV for p-p collisions and $\sqrt{s_{NN}} = 5.36$ TeV for lead-lead (Pb-Pb) collisions [51]. The LHC is home to four major experiments: ALICE, CMS, ATLAS and LHCb. ALICE, which stands for A Large Ion Collider Experiment, is an experiment dedicated to heavy-ion physics. Although CMS, ATLAS and LHCb focus mainly on p-p collisions, they also collect heavy-ion data for a limited part of the run.

The Super Proton Synchrotron (SPS) is the second largest synchrotron in operation at CERN. The SPS has a circumference of about 7 km and accelerates protons up to 450 GeV and heavy-ions in the intermediate energy range ($E_{lab} \approx 20 - 160A$ GeV). Experiments such as NA-49, NA-60 and NA-45/ CERES have collected data in this intermediate energy range [52–56]. The SPS is currently operating as the final injector for the LHC and also provides beams for several fixed target experiments such as NA-61/ SHINE, NA-62 and NA-58/ COMPASS.

RHIC operates at intermediate collision energies and is home to four heavy-ion experiments: STAR, PHENIX, BRAHMS and PHOBOS. All experiments except STAR are now decommissioned and PHENIX is being upgraded to the sPHENIX detector. In 2011, RHIC completed data collection for the first phase of its Beam Energy Scan (BES) programme with STAR, which aims to explore the phase diagram by varying the beam energies. In addition to the data already collected at beam energies of $\sqrt{s_{NN}} = 62, 130$ and 200 GeV, data were collected at collision energies of $\sqrt{s_{NN}} = 7.7- 39$ GeV during the BES-I [57,58]. In 2021, the RHIC also concluded the BES-II programme in which high luminosity Gold-Gold (Au-Au) data was collected for energies $\sqrt{s_{NN}} = 9.8, 7.3, 5.75, 4.59$ and 3.85 GeV [59]. The STAR experiment also has a fixed target programme to extend the range of BES-II to lower beam energies ($\sqrt{s_{NN}} \lesssim 7$ GeV) [60].

The Alternating Gradient Synchrotron (AGS), which is the predecessor to RHIC, currently operates as the pre-accelerator of RHIC. The AGS has a circumference of about 800 m. The AGS has performed several experiments in the energy range $E_{lab} \approx 2 - 11A$ GeV [61–63].

The SIS-18 at GSI carries out fixed target experiments at lower energies of $1 - 2A$ GeV

[64–69]. The synchrotron has a maximum magnetic rigidity of 18 Tm and a circumference of 216 m. The SIS-18 is currently being upgraded to serve as an injector for the future SIS-100 accelerator. SIS-100 is the heavy-ion synchrotron under construction at the Facility for Antiproton and Ion Research (FAIR) [70, 71].

The heavy-ion collision programmes such as BES at RHIC, CBM at GSI/ FAIR, NA61/ SHINE at CERN, HIAF in China, NICA in Russia and J-PARC-HI in Japan aim to explore the phase diagram of nearly isospin symmetric QCD matter at high baryon densities and temperatures. The matter produced in these collisions is expected to have temperatures between 50 and more than 250 MeV and densities several times the ground state density of nuclear matter. The experiments will mainly focus on exploring the nature of the transition of QCD matter from a confined hadronic phase to a phase where chiral symmetry is restored and quarks are eventually deconfined.

The terrestrial experiments are complemented by astrophysical observations of Binary Neutron Star Mergers (BNSM) and supernova explosions which create (isospin asymmetric) matter of high densities and temperatures up to 50 MeV [72]. The cold neutron star matter, similar to the matter formed in heavy-ion collisions, is dynamically compressed and heated in binary neutron star mergers. The gravitational waves produced during the mergers are then measured by ultra-sensitive gravitational wave detectors to infer the properties of the hot, compressed neutron star matter [73–76].

While the systems created in such different scenarios vary in size over many orders of magnitude, they share a common unknown and defining property, the equation of state of dense nuclear matter. The equation of state is an input to theoretical models of heavy-ion collisions. It combines the microscopic and macroscopic properties of the created system and provides the pressure of the medium for any given energy and net baryon number density. Various types of QCD transitions are implemented in theoretical models via the equation of state. Extracting the equation of state and its properties, such as phase transitions or softest points, has been a defining challenge for many experimental and theoretical programmes over the last decade.

In the following, we discuss some of the major heavy-ion experiments, their physics goals and detectors with focus on the experiments at FAIR. Part of the contents in this chapter are based on [77–80].

2.1 Physics at FAIR

FAIR is an international research facility under construction next to GSI in Darmstadt, Germany [82–84]. A schematic diagram of the proposed FAIR accelerator complex is shown in figure 2.1. The heart of the facility is the SIS-100 synchrotron, which will be able to provide ion beams of unprecedented intensity for all the natural elements of the periodic table, as well as antiprotons. The existing linear accelerator UNILAC (120 m long) and the SIS-18 synchrotron at GSI will pre-accelerate the heavy-ion beams for the SIS-100

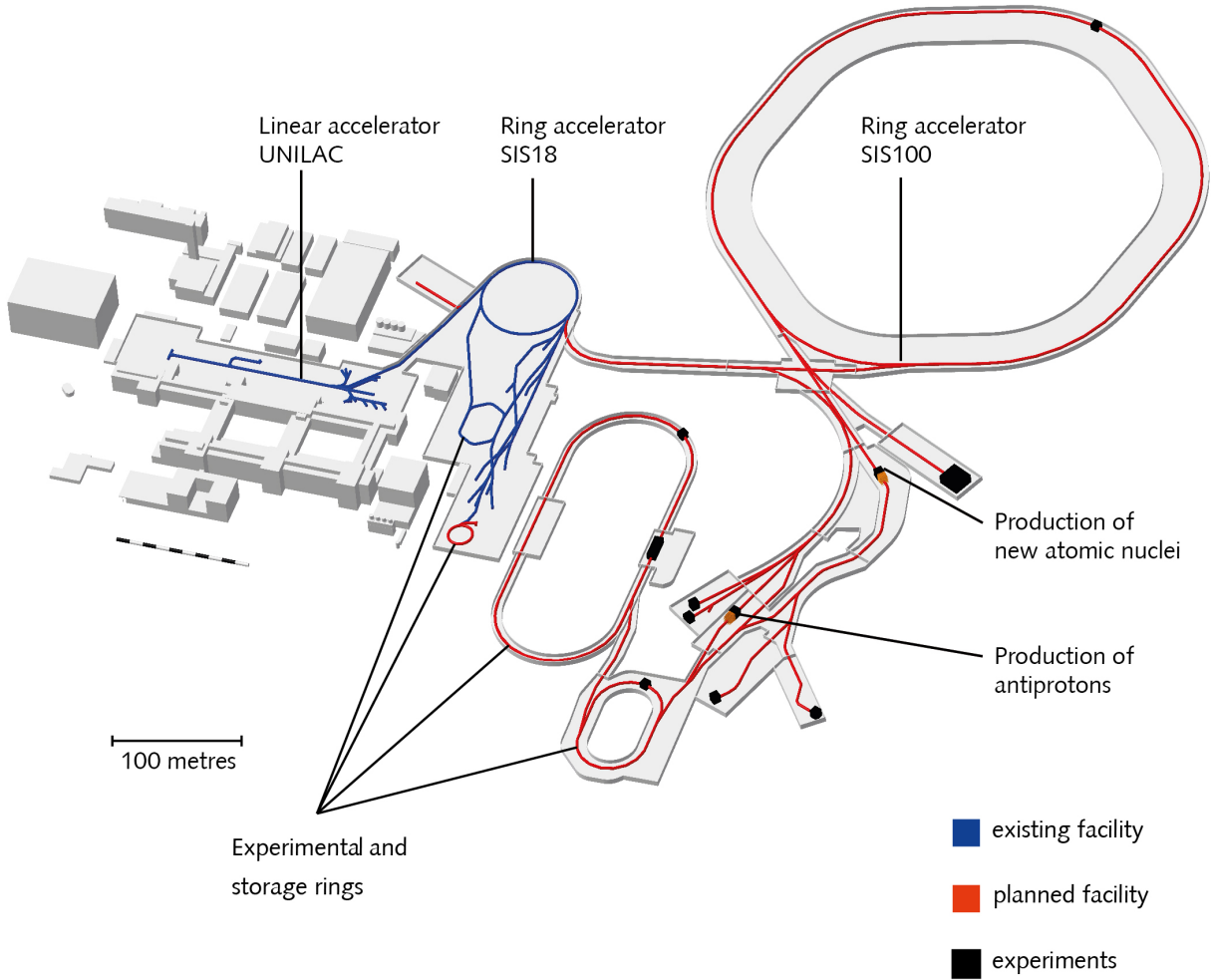


Figure 2.1: The proposed FAIR accelerator complex. The existing accelerators UNILAC and SIS-18 (shown in blue) will act as injectors and pre-accelerators for SIS-100. The accelerated beams from SIS-100 will then be directed to the experimental cavities for use in fixed target experiments or for the production of secondary particles. Figure taken from the GSI website [81].

accelerator. A new proton linear accelerator (LINAC) will be built in front of SIS-18 to provide the high-intensity proton beam required for antiproton production. The SIS-100 has a circumference of about 1.1 km and a maximum magnetic rigidity of 100 Tm. The SIS-100 is capable of producing proton beams of energy up to $E_{lab} \approx 29A\text{GeV}$, calcium beams up to $E_{lab} \approx 14A\text{GeV}$ and gold and uranium beams up to $E_{lab} \approx 11A\text{GeV}$ [85]. The SIS-100 will produce extremely high intensity protons and heavy-ions at intermediate beam energies. The proton beam at 29 GeV will have an intensity of about 2.5×10^{13} protons/cycle, while the uranium U^{92+} at 10 GeV will have an intensity of about 4×10^{10}

ions/cycle [71].

The accelerated beams from the SIS-100 either go directly to the experimental caves, where different fixed target experiments are performed, or to the production targets for antiproton or radioactive nuclei. The Superconducting Fragment Separator (Super-FRS) will then be used to provide spatially separated isotopic beams of the radioactive ions [86]. A Collector Ring (CR) will be used to cool the antiproton or radioactive ion beams, and an accumulator ring (RESR) will accumulate the antiprotons as well as decelerate the radioactive nuclei. The beam will then enter the New Experimental Storage Ring (NESR), which will house several antiproton and ion experiments. The NESR will also further cool the beams for use in the Facility for Low energy Antiproton and Ion Research (FLAIR) [87]. FLAIR will carry out studies with very low energy antimatter beams. There is also a High Energy Storage Ring (HESR), which will accelerate and store antiproton beams up to 15 GeV [88].

The experimental programme at FAIR comprises four main directions:

1. *APPA*. The Atomic, Plasma Physics and Applications (APPA) collaboration will investigate a wide range of topics from biophysics and materials research to plasma physics [89]. Using proton and heavy-ion beams, biophysicists at APPA will investigate new techniques for cancer treatment and imaging. APPA will also study the effects of radiation damage on the human body and on electronic equipment in space. Such studies of how cells react to cosmic radiation would be useful for our future missions to nearby planets and into space. Materials scientists at APPA will also study the structure of the Earth's interior by bombarding minerals in high-pressure cells with high-energy ions. This will mimic conditions in the Earth's interior. Studying the properties of bulk matter in the high density plasma state and testing the theory of quantum electrodynamics for extremely strong electromagnetic fields are other major goals of the APPA collaboration.
2. *CBM*. The Compressed Baryonic Matter (CBM) experiment [85, 90–93] is the dedicated heavy-ion collision experiment at FAIR. In its first phase, the CBM experiment will study the properties of highly compressed baryonic matter using high-energy nucleus-nucleus collisions with beam energies from 2 to 10 AGeV at the SIS-100 accelerator. The physics goals of the CBM experiment are to study the equation of state of nuclear matter at densities similar to neutron star cores, to search for the conjectured phase transition and its critical endpoint, to study the in-medium properties of hadrons and to search for exotic objects such as multi strange hypernuclei. The CBM experiment will study observables sensitive to the early and dense phases of fireball evolution. This includes precise measurements of short-lived vector mesons (ρ , ϕ and ω) decaying into di-lepton pairs, multi strange hyperons (λ , Ξ and Ω), direct photons, charmed mesons (D , λ_c and J/ψ), collective flow and particle number fluctuations. However, extremely high interaction rates are required to study some of these probes, which have very small cross sections (for charmed particles) or small branching fractions (for di-leptons). The experimental challenge of CBM is therefore to develop state-of-the-art, radiation-hard detectors capable of precise and

fast measurements of these rare probes at unprecedented interaction rates, and to develop analysis methods to efficiently process the collected data in real time.

3. *NUSTAR*. The NUclear Structure Astrophysics and Reactions collaboration, abbreviated NUSTAR, focuses on experiments to study the properties of exotic nuclei [94]. A key element of the NUSTAR experiments is the Super-FRS, which separates different exotic nuclei produced in the collision of the primary ion beam with a target. The cooling and storage rings of the FAIR facility allow the rare nuclei produced to be reused in the experiments without additional beam time. The experiments at NUSTAR are crucial for understanding the formation and evolution of stellar matter and the properties of rare nuclei created in violent astrophysical phenomena.
4. \bar{P} ANDA. The antiProton ANnihilations at DArmstadt (\bar{P} ANDA) [95] collaboration will study antiproton-proton and antiproton-nucleus reactions up to 15 GeV/c. The high-intensity, cooled antiproton beams provided by the HESR will be collided with a proton or nuclear target to perform various exciting studies in hadron physics. The \bar{P} ANDA will perform precision studies on the bound states of QCD. This includes charmonium, D-meson and baryon spectroscopy and the search for gluonic excitations. The high-intensity antiproton beam will also enable the \bar{P} ANDA experiment to study the in-medium modifications of hadrons in the charm sector, to study nuclear structure in the framework of generalised parton distributions and to search for new states of Λ hypernuclei.

2.1.1 HADES

The High Acceptance Di-Electron Spectrometer (HADES) is a versatile detector currently operating at the SIS-18 accelerator at GSI. The primary goal of HADES is to study in-medium modifications of hadrons in hot and dense nuclear matter. HADES will primarily measure the di-electron decays of light vector mesons such as ρ , ϕ and ω . The lifetimes of these short-lived particles are similar to the duration of the compression phase of collisions at SIS-18 energies. In addition, the di-electron decay channels are not affected by the strong interaction. Thus, accurate measurements of vector meson decays can be used to study the properties of matter during the compression phase of the system.

The HADES detector has an almost complete azimuthal acceptance and a polar angle acceptance of 18- 85°. The detector consists of six identical detection sections defined by a six-coil superconducting magnet that produces a toroidal magnetic field. A Ring Imaging CHerenkov (RICH) detector is placed after the target for electron identification. The momentum of the hadrons is reconstructed using the two sets of Multi-wire Mini Drift Chambers (MDC) placed before and after the magnets. Behind the MDCs are the Resistive Plate Chambers (RPC) covering the polar angles 18- 45° and the scintillator Time of Flight (TOF) detector covering the polar angles 45- 85°. The MDC together with the TOF and RPCs are used for hadron identification. A START detector is placed in front of the target to measure reaction times, and the signal from the START detector is used to define a

minimum bias trigger.

HADES currently measures nucleus-nucleus collisions in the beam energy range of 1- 2 AGeV. Over the years, HADES has already collected large amounts of data for p + p [96,97], p + Nb [98,99], C + C [65,100,101], Ar + KCl [102–104] and Au-Au [105–107] reactions at different beam energies. In the future, HADES will also be operated at low SIS-100 energies.

2.1.2 The CBM detector

The CBM is a fixed target experiment that can be configured for both electron-hadron and muon-hadron measurements. The CBM detector is designed for fast and precise measurements of hadrons, muons and electrons produced in nucleus-nucleus collisions. The experiment will use advanced radiation-hard detectors with self-triggered readout electronics to achieve the desired performance. A microstrip detector based Silicon Tracking System (STS) [108,109], which reconstructs the momenta and tracks of charged particles, is one of the key components of the CBM experiment. The STS consists of 8 equidistant planar detector stations placed 30-100 cm behind the target. The STS provides a single hit resolution of $25 \mu\text{m}$ and a momentum resolution of 1% . The CMOS pixel based Micro Vertex Detector (MVD) [109] is designed to reconstruct open charm decays with a secondary vertex resolution of $50 \mu\text{m}$ and has an excellent position resolution of $3.5 - 6 \mu\text{m}$. The MVD consists of 4 layers of Monolithic Active Pixel Sensors (MAPS) located 5-20 cm behind the target. The MVD is placed together with the STS in the gap of a superconducting dipole magnet with a magnetic field integral of 1 Tm. A Ring Imaging CHerenkov (RICH) [110] detector is used to identify electrons from decay of low mass vector meson decay while high energy electrons and positrons are identified using the Transition Radiation Detector (TRD). RPC based time of flight measurements are used to identify hadrons [111] and Projectile Spectator Detector (PSD) will be used for centrality and event plane determination.¹ The collisions will produce up to 1000 charged particles at a maximum interaction rate of 10 MHz. This will produce 1 Tbytes/s of raw data. The data will then be processed using a First Level Event Selector (FLES) [112], which performs online particle tracking, event reconstruction and event selection. It is interesting to note that a full system CBM test setup called mCBM has been built at the SIS18 facility of GSI/FAIR. As this setup provides additional high-rate detector tests in nucleus-nucleus collisions under realistic experimental conditions, it can be used to test the present analysis also at lower energies than at the full CBM detector.

An important feature of the CBM experiment is the very high event and trigger rate, which allows the detection of rare particles as well as the study of observables that require large event samples, such as higher order fluctuations and correlation functions. To take full advantage of these properties of the CBM detector, new analysis techniques are needed

¹These detector systems form the basis of the electron-hadron configuration considered in the rest of this thesis.

that allow the ultrafast analysis of the continuous stream of events produced at the detector.

2.2 Other major experiments

There are several major heavy-ion collision experiments currently operating and collecting data around the world. In this section we briefly describe some of these experiments at RHIC, LHC and SPS. A short description of the physics goals of each experiment and its detector is given. Note that the detectors described below have undergone several upgrades over the years of data collection. Only the basic detector components and geometry are presented here.

2.2.1 NA61/ SHINE

The NA61 experiment [113], also known as the SPS Heavy Ion and Neutrino Experiment (SHINE), is the successor to the NA49 experiment at the SPS, CERN. The NA49 measured strong signals for the minimum collision energy threshold for the production of deconfined matter to be around 30 AGeV for Pb-Pb, known as the onset of deconfinement [55]. NA61 performs a 2-D scan in collision energy and size of the colliding nuclei to study the energy dependence of the onset of deconfinement and to search for a critical endpoint in the QCD phase diagram [114]. Proton-proton and various nucleus-nucleus collisions in the beam energy range 13- 150 AGeV are studied by the SHINE experiment. The NA61 detector is a large acceptance hadron spectrometer consisting mainly of Time Projection Chambers (TPC), TOF detectors and a PSD. Two TPCs, known as Vertex TPCs (VTPCs), are placed inside superconducting magnets behind the target. Behind the VTPCs, the two Main TPCs (MTPCs) are placed symmetrically on either side of the beamline. Behind the MTPCs are two TOF walls, one on each side of the beamline. Finally, the PSD, a forward calorimeter used to estimate the centrality of collisions, is placed at the very end.

2.2.2 ALICE

ALICE [115–117] is a heavy-ion experiment at the LHC that studies the physics of strongly interacting matter at extreme temperatures and energy densities. ALICE measures heavy-ion collisions at beam energies of several TeV. The ALICE detector is designed to accurately reconstruct the hadrons, electrons, muons and photons produced in the heavy-ion collisions at the LHC. The ALICE detector has dimensions of $16 \times 16 \times 26 \text{ m}^3$ and weighs about 1000 tonnes. The main part of the detector is the inner barrel, which contains the Inner Tracking System (ITS), the transition radiation detector, the time projection chamber, the time of flight detector, the PHOTon Spectrometer (PHOS), the Electromagnetic Calorimeter (EMCal) and the High Momentum Particle Identification Detector (HMPID). All these detectors are housed in a solenoid magnet. The ITS and the TPC are the main tracking detectors for ALICE. The multigap RPC-based TOF is used for intermediate momentum particle identification. The TRD is used for electron identification and charged particle

tracking. The HMPID, PHOS and EMCal will identify hadrons at intermediate momenta. Other major ALICE sub-detectors include a Photon Multiplicity Detector (PMD) and a silicon Forward Multiplicity Detector (FMD) measuring photons and charged particles at $|\eta| \approx 3$, a Zero Degree Calorimeter (ZDC) for centrality estimation and a muon spectrometer.

2.2.3 STAR

The Solenoid Tracker At RHIC (STAR) was built at RHIC to study the properties of strongly interacting matter at high energy densities [21, 60, 118]. The physics goals of the experiment include studying the properties of the fireball produced in the collision, observing the disappearance of QGP formation, searching for signatures of a phase transition and the critical point. The STAR detector consists of several sub-detector systems for specific tasks [119]. The heart of the detector are the TPCs, which are used for charged particle tracking and particle identification by measuring the dE/dx . Surrounding the TPCs are TOF detectors, which help in particle identification for high momenta particles. A plastic scintillator based event plane detector has recently been incorporated into the STAR detector for improved event plane determination. A recent upgrade of the forward calorimeter system, consisting of a forward tracking system, a hadron calorimeter and an electromagnetic calorimeter, has been carried out to improve the detection capabilities of the detector for neutral pions, photons, leading hadrons, electrons and jets in the pseudorapidity range $2.5 < \eta < 4$ [120].

2.3 Challenges in the analysis of experimental data

Experiments reconstruct a collision event by measuring the position, momentum, charge and mass of the particles produced in the collision using a variety of particle detectors. However, the detection efficiency, dead time and phase space coverage of the detectors make these measurements noisy and incomplete. In addition, the efficiency of event reconstruction is ultimately limited by the position, momentum and time resolution of the detectors. Additional uncertainties are introduced by the algorithms used to process the detector data. The ultimate goal is then to trace back the physics embedded in this partial, noisy information recorded by the experiments by comparing various observables such as flow coefficients, baryon number fluctuations, etc. with the predictions of theoretical models [121]. Although these observables have proven useful for studying the properties and dynamics of matter produced in heavy-ion collisions, experimental effects can significantly reduce the sensitivity of these observables. This requires the development of novel methods to analyse and characterise heavy-ion collision data. Such methods should not only be accurate and robust in the presence of experimental uncertainties, but also fast and flexible enough to be used in the next generation of high-luminosity experiments without the need for dedicated, expensive computational resources. In this thesis, we will focus on the development of such methods using AI techniques. As an ambitious experiment that

will study heavy-ion collisions at unprecedented intensities, the CBM experiment requires fast and accurate analysis methods to deal with the large amounts of data collected in the experiment in real time. Therefore, we will use the future FAIR experiments, in particular the CBM experiment, as an example and baseline to develop and test the performance of various AI methods.

Chapter 3

Models for heavy-ion collisions

The main focus of heavy-ion programmes in laboratories and astrophysical data from neutron star radii and binary neutron star mergers is to constrain the properties of hot and dense QCD matter. Experiments compare observables such as collective flow, particle yields, multiplicity fluctuations and correlations etc. with theoretical model predictions to infer the underlying equation of state and its properties [1, 8, 122–124]. However, at intermediate beam energies, the predictions for these observables are strongly model-dependent due to the lack of first-principles calculations.

The equation of state, which is an essential component of theoretical models, drives the evolution of the system created in the collision. Various types of QCD transition are also incorporated into theoretical models via the EoS. However, in order to extract the EoS from experimental data, model simulations are required that can incorporate different possible equations of state. Such models can be based on a microscopic description such as UrQMD, a macroscopic fluid dynamic description or a combined micro+macro description for the evolution of the system. In order to draw reliable and consistent conclusions about the equation of state and its properties by comparing experimental data with model simulations, it is therefore important to systematically analyse how different theoretical models treat collisions and the resulting differences in model predictions. In this chapter we introduce different dynamical models for heavy-ion collisions, with emphasis on how these models incorporate the equation of state to model the evolution of the system. In particular, a method for the consistent introduction of arbitrary EoS within a microscopic transport simulation is also presented in this chapter.

Part of the results and model descriptions presented in this chapter are based on [79, 125–127].

3.1 The UrQMD (cascade) model

Early microscopic transport approaches to describe nucleus-nucleus collisions were mainly based on the Vlasov-Uehling-Uhlenbeck (VUU) theory [39]. The time evolution of the single particle distribution function $f(r, p, t)$ in the VUU model is given by

$$\begin{aligned} \frac{\partial f}{\partial t} + \mathbf{v} \cdot \frac{\partial f}{\partial \mathbf{r}} - \nabla U \cdot \frac{\partial f}{\partial \mathbf{p}} = & - \int \frac{d^3 p_2 d^3 p'_1 d^3 p'_2}{(2\pi)^6} \sigma v_{12} \left[f f_2 (1 - f'_1) (1 - f'_2) \right. \\ & \left. - f'_1 f'_2 (1 - f) (1 - f_2) \right] \delta^3 \left(p + p_2 - p'_1 - p'_2 \right). \end{aligned} \quad (3.1)$$

The VUU based models include single particle dynamics in a mean field but don't include n-body interactions which are essential to describe mechanisms such as fragment formation and multifragmentation [128]. This was addressed by the QMD models [40–44] which included n-body correlations as they solved Hamilton's equations of motion for n particles in a mean field.

In equation 3.1, neglecting the real part of the retarded self-energy and approximating the Pauli blocking factor to 1, gives the Boltzman equation. Most of the modern transport models for heavy-ion collisions are based on an effective solution of the Boltzman equation, which describes the time evolution of the distribution function of different particle species by a collision integral [129].

UrQMD [45,46] is a microscopic non-equilibrium N-body transport model based on an effective solution of the relativistic Boltzman equation, augmented by a QMD part. UrQMD initialises the projectile and target nucleons using a Wood-Saxon distribution

$$\rho(r) = \frac{\rho_0}{1 + \exp\left(\frac{r-R}{a}\right)}, \quad (3.2)$$

where R is the radius parameter, ρ_0 is the charge density at the center and a is the diffuseness parameter. The sampled nucleons also have a randomly chosen Fermi momentum between 0 and P_F^{max} , where

$$P_F^{max} = \hbar c (3\pi^2 \rho)^{\frac{1}{3}}. \quad (3.3)$$

UrQMD is based on the covariant propagation of hadrons and their resonances on straight trajectories. In its default setup, the model corresponds to a hadronic cascade and can be readily used to describe the final state spectra of hadrons over a wide range of beam energies. The hadron interactions are determined based on the geometric interpretation of the cross section. The transverse separation between each particle pair (d_{ij}) is calculated at the point of closest approach, and the particles are considered to undergo a collision if the geometric area defined by (d_{ij}) is smaller than the total cross section (σ_{tot}^{ab}) for the particle species involved, i.e.,

$$i.e., \pi d_{ij}^2 \leq \sigma_{tot}^{ab}. \quad (3.4)$$

3.1. THE URQMD (CASCADE) MODEL

The σ_{tot}^{ab} here depends on the center of mass energy of the pair as well as the species of particles involved (a, b). Particle production in this model occurs via resonance decays or string excitation and fragmentation. The decomposition of the collisions into elastic or inelastic collisions, subsequent particle production and decays are then performed according to their respective cross sections, which are taken either from experimental h-h data [130] if available, or from effective parameterisation based on phase space considerations and continuations of known cross sections, i.e. by the additive quark model. In UrQMD, any nucleon that has undergone at least one elastic or inelastic interaction during its evolution is considered to be a participant nucleon, i.e. to have undergone a collision.

The UrQMD model in the cascade mode has an equilibrium state that is equivalent to the HRG model description of QCD matter [131]. Since only elastic scattering and resonance excitations occur in the cascade mode of UrQMD, the HRG is a good approximation for the effective EoS of the model. More details on the HRG model can be found in the appendix A.1. It is the cascade mode that is commonly used to calculate the initial compression phase in the prevalent hybrid models of heavy-ion collisions [132].

Note that the UrQMD cascade does not include potential interactions. UrQMD with potential interactions will be discussed later in this chapter.

3.1.1 Coarse grained UrQMD

It is interesting to study the macroscopic properties such as the local energy densities or the temperature reached in the system during the evolution dictated by the microscopic transport theory. This allows a systematic comparison of the evolution of the system in microscopic models with that in macroscopic models. In the microscopic transport treatment, the equivalent expectation values for the local energy and baryon number densities can be calculated by a coarse graining procedure [133]. The calculations are performed on a space-time grid, where the total energy and baryon density in a given cell can be calculated as the sum of the energy and net baryon charge of the participants in that volume. These quantities are averaged over a large number of events of a given beam energy and centrality. To further extract the thermodynamic quantities such as temperature, pressure and entropy density, a mapping to the effective equation of state used is performed.

The temperatures and densities extracted from UrQMD cascade simulations by this coarse-graining procedure are demonstrated in Figure 3.1, which shows the space-time volume ("four-volume") spent by the system at different temperatures and densities as simulated by the UrQMD cascade model for Au-Au collisions at beam energies of 1.23- 10 AGeV. The HRG EoS is used in this case to extract the temperature of the cell. The results shown are based on 1000 events with impact parameter less than 3.4 fm. Note that this beam energy range will be investigated by the upcoming CBM experiment at FAIR. As expected, higher temperatures and densities are achieved as the collision energy is increased. At 1.23 AGeV, a large four-volume reaches temperatures of 50-80 MeV and densities up to $2.5 \rho_0$, and at 10 AGeV this rises to about 80- 130 MeV in temperature and $2- 5 \rho_0$ in density. At

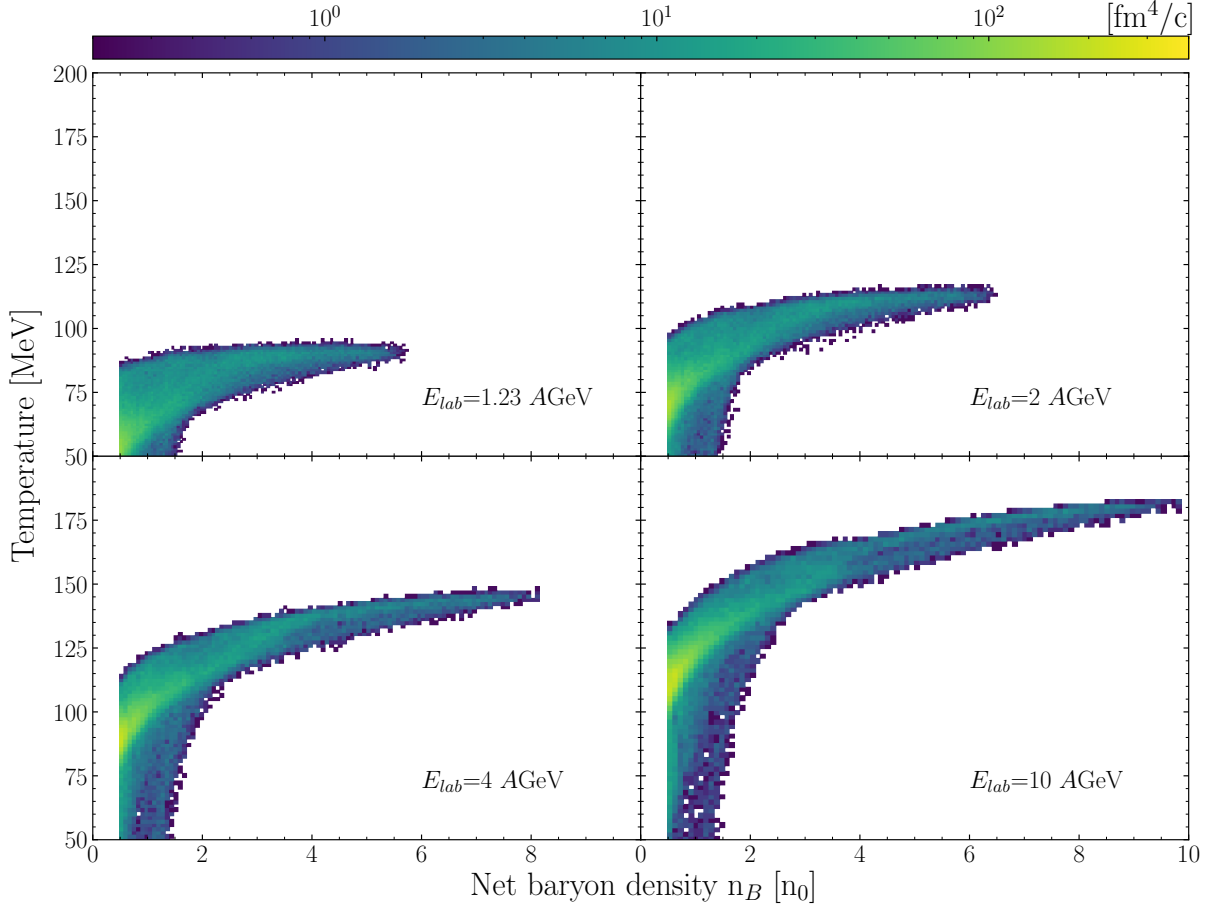


Figure 3.1: UrQMD cascade: space-time volume (four-volume) spent by the system at different T and ρ . The temperature and densities achieved in central Au-Au collisions at beam energies 1.23, 2, 4, 10 AGeV are shown. Space-time cells with $\Delta x=1$ fm and $\Delta t=0.25$ fm have been used for coarse graining. The results are from 1000 UrQMD events for each collision energy.

1.23 AGeV, the maximum density reached is around $6 n_0$ and at 10 AGeV, this increases to about $10 n_0$. Clearly, the beams at FAIR will be able to produce QCD matter with very high baryon densities and moderate temperatures, which can then be studied with detectors such as CBM or HADES, and UrQMD provides a reasonable and physically motivated scenario for nucleus-nucleus collisions at FAIR beam energies.

3.2 Hydrodynamics

The full 3+1D evolution of a heavy-ion collision can be simulated by (ideal) relativistic hydrodynamics. The hydrodynamic initial state is given by two counter streaming Lorenz-contracted Wood-Saxon distributions of baryon charge n_{WS} (and corresponding energy

density) representing the two colliding (cold) nuclei:

$$n_{WS} = \gamma_{CM} \frac{n_0}{1 + \exp\left(\frac{\Delta r - R}{a}\right)}. \quad (3.5)$$

Here, γ_{CM} is defined by the collision energy in the center of mass (CM) frame. Δr is the distance from the nucleus center and is Lorentz contracted along the z -axis. The parameters of the WS distribution are the nuclear saturation density n_0 , the nuclear radius R and the surface thickness a . This initialisation procedure allows a hydrodynamic treatment of both the early entropy production and the expansion stages, which is important for low collision energies where the interpenetration times are of the same order of magnitude as the lifetime of the system. In this work, for hydrodynamic simulations of Au-Au collisions, $R = 6.6$ fm and $a = 0.5$ fm are used.

The equations of motion for hydrodynamics describe the conservation of energy and momentum given by

$$\partial_\mu T^{\mu\nu} = 0, \quad (3.6)$$

as well as the conservation of the baryon four current

$$\partial_\mu j^\mu = 0. \quad (3.7)$$

In this work the SHASTA algorithm [134, 135] is used for the flux-corrected relativistic numerical solution of the above equations. The equations are solved on a $200 \times 200 \times 200$ Cartesian grid with a cell size of $0.2 \times 0.2 \times 0.2$ fm³ and the time step is set to $\delta t = 0.4 \times 0.2 = 0.08$ fm/ c . To complete this set of hydrodynamic equations, an equation of state is necessary. The EoS can be treated as a free input to the equations, provided by a table, using only the constraints of strangeness-neutral $n_S = 0$ matter with a charge to baryon fraction of $n_Q/n_B = 0.4$.

3.3 UrQMD- hybrid

The hybrid, micro+macro models are known as the 'Standard Model of ultra-relativistic heavy-ion collisions'. In these hybrid models, the dynamical evolution of the collisions is divided into roughly three phases [47, 48, 136–145]. The reaction begins with an initial non-equilibrium phase in which the kinetic energy of the two incoming nuclei loses a fraction of its longitudinal momentum, producing a pre-equilibrium fireball. This phase is usually described by string models or QCD-inspired non-equilibrium approaches, e.g. via a colour glass condensate model or quantum kinetic theory [146–153]. Due to its violent non-equilibrium nature, this phase of the reaction is generally independent of the equation of state. After this energy deposition and a sufficient equilibration time, the near-equilibrium evolution can be described by (viscous) hydrodynamic or transport theoretical approaches.

Here an equation of state and transport properties of the medium can be included in the simulations. Finally, once the system has hadronised, hadronic rescattering and the final freeze-out phase occur [138, 154]. As described above, in this approach the EoS enters the well-defined equilibrium phase, in contrast to the hydrodynamic approach where the pre-equilibrium early-stage dynamics are also influenced by the EoS.

The hybrid version of UrQMD [48] uses the microscopic UrQMD model for the initial and final phases of evolution and a hydrodynamic intermediate phase for the hot, dense phase. The UrQMD model, as described in section 3.1, is used to generate realistic initial states of the collision at high baryon density. The subsequent hydrodynamic evolution models the intermediate hot and dense stage during which the system may undergo a phase transition [132]. The hydrodynamic evolution begins once the Lorentz contracted nuclei have passed through each other. This time (t_{start}) is given in natural units by

$$t_{start} = 2R\sqrt{\frac{2m}{E_{lab}}} \quad (3.8)$$

where R is the radius of the nuclei, m is the mass of the nucleon and E_{lab} is the kinetic energy of the beam. At this point, the UrQMD particle list is transformed into an initial distribution of the energy-momentum and net baryon number densities required for the subsequent hydrodynamic evolution. The necessary smoothing of the density is achieved by treating each hadron from UrQMD as a three-dimensional Gaussian distribution of its energy-momentum and baryon number. It should be noted that this initial state will give reasonable event-by-event fluctuations for the initial eccentricities and is also independent of the equation of state used for the fluid dynamical evolution. Any effect of the EoS will therefore be confined to the expansion phase. The SHASTA [135, 155] algorithm is then used for the 3+1D ideal fluid dynamical evolution on a Cartesian grid with $\Delta x = 0.2$ fm spacing and a grid size of 200^3 cells.

The hydrodynamic evolution will continue until the energy density in all cells falls below a freeze-out energy density (ϵ), whereupon the evolution will stop. The default value for ϵ is five times the nuclear ground state energy density (ϵ_0), but it can be freely adjusted. More details on the motivation behind the chosen values for t_{start} and ϵ are discussed in [48, 132]. Particles are then generated from an iso-energy density hypersurface created throughout the time evolution. The density that defines this particlization hypersurface is the value of $n\epsilon_0$ defined above. The sampling of particles is done using the well-known Cooper-Frye formula

$$E \frac{dN}{d^3p} = \int_{\sigma} f(x, p) p^{\mu} d\sigma_{\mu} \quad (3.9)$$

where $f(x, p)$ is the boosted Fermi or Bose distribution and $d\sigma_{\mu}$ is the freeze-out hypersurface element. Here the global conservation of baryon number, charge and strangeness is strictly observed. The particles are then transferred to UrQMD, where hadronic cascade calculations take place. Important final state effects such as hadronic rescattering and resonance decays are performed at this stage.

The challenge with the hybrid approach is that many features not related to the EoS, such as microscopic properties, unknown transport parameters or boundary conditions, are not well constrained. This 'standard picture' is only well justified at very high beam energies, i.e. when the initial interpenetration time of the incoming nuclei is very short and can be well separated from the subsequent expansion. This is generally found to be the case of heavy-ion collisions above $\sqrt{s_{NN}} \approx 15$ GeV (corresponding to $E_{\text{lab}} \gtrsim 100A\text{GeV}$), where mainly the energy of the incoming nuclei is stopped while the baryon number of the participant nuclei is observed far from mid-rapidity. At much lower beam energies, the interpenetration time can last as long or even longer than the expansion phase. In such a scenario, a large fraction of the baryon number is stopped in the central collision region and a system of high baryon density is created around mid-rapidity.

The lower beam energies are exactly what is needed to study the EoS at the highest baryon densities. This also means that the initial compression phase cannot be separated from the expansion phase, and the observables will therefore also depend on the equation of state in the initial compression phase. This will be particularly true in the presence of a phase transition. It is therefore necessary to study the effects of the EoS on the initial compression at lower beam energies and also to develop new methods to describe the dynamical evolution of such a system. To achieve both of the above, a consistent treatment of the equation of state throughout the collision is necessary.

3.4 UrQMD with potential interactions

Extending the equations of motion in transport models to non-trivial hadronic interactions, and hence to any possible equation of state, is not straightforward. Early on, a non-relativistic QMD approach [41] was developed to include a density-dependent Skyrme interaction [156]. Here, in the QMD part of the UrQMD model, the change of momenta of the baryons, due to a density dependent potential, is calculated using the non-relativistic equations of motion

$$\dot{\mathbf{r}}_i = \frac{\partial \langle \mathbf{H} \rangle}{\partial \mathbf{p}_i}, \quad \dot{\mathbf{p}}_i = -\frac{\partial \langle \mathbf{H} \rangle}{\partial \mathbf{r}_i}. \quad (3.10)$$

Here $\mathbf{H} = \sum_i H_i$ is the total Hamiltonian of the system, including the kinetic energy and the total potential energy. $\mathbf{V} = \sum_i V_i \equiv \sum_i V(n_B(r_i))$. The Hamiltonian of each baryon, $H_i = E_i^{\text{kin}} + V_i$, consists of the kinetic energy and the mean field potential energy $V_i = E_{\text{field}}/A$ of the baryon i . The mean field potential energy per baryon can be related to a density dependent single particle energy:

$$U_i(n_B) = \frac{\partial (n_B \cdot V_i(n_B))}{\partial n_B}. \quad (3.11)$$

In the Skyrme UrQMD approach [41, 45, 156] the density dependence of the single particle energy for all baryons is given by a simple form:

$$U_{\text{Skyrme}}(n_B) = \alpha(n_B/n_0) + \beta(n_B/n_0)^\gamma. \quad (3.12)$$

Two of the three parameters (α , β and γ) are usually constrained by the nuclear matter saturation density and binding energy, while the remaining unconstrained property is the nuclear incompressibility, which defines the so-called stiffness of the EoS.

Such a single free parameter approach to describe the equation of state of dense QCD matter has a significant shortcoming: the equation of state for densities above nuclear saturation is fixed by parameters defined solely at the saturation density. A similar problem arises when a purely nuclear relativistic mean field model is implemented in QMD [157,158], although such an approach also allows the inclusion of additional degrees of freedom and thus a more complex phase structure. Recently, another idea has been proposed, where additional terms are added to the equation (3.12), which allow the description of non-trivial features such as a phase transition in the potential [159]. However, this density functional approach suffers from a serious problem characteristic of the Skyrme potential: the speed of sound of this EoS eventually becomes superluminal at large baryon densities, even at $T = 0$. Below we introduce a different way to replace the limited Skyrme potential by a more realistic density dependent equation of state. This method was presented in [125,127].

3.5 Density dependent EoS in UrQMD

The density-dependent EoS is realised by an effective density-dependent potential entering the non-relativistic QMD [1, 40, 160] equations of motion, given by eq. 3.10. Once the mean field potential is known, the change in momentum of each baryon can be calculated according to Hamilton's equations of motion as

$$\dot{\mathbf{p}}_i = -\frac{\partial H}{\partial \mathbf{r}_i} = -\frac{\partial V(n_B)}{\partial n_B} \cdot \frac{\partial n_B(\mathbf{r}_i)}{\partial \mathbf{r}_i}. \quad (3.13)$$

Besides the derivative of the mean field potential energy, only the local density and its gradient for each baryon are necessary to calculate the momentum change.¹ This is calculated by assuming that each particle can be treated as a Gaussian wave packet [41, 45]. With such an assumption, the local interaction baryon density $n_B(r_i)$ at the location \mathbf{r}_i of the i -th particle in the computational frame is:

$$n_B(r_i) = \left(\frac{\alpha}{\pi}\right)^{3/2} \sum_{j, j \neq i} B_j \exp(-\alpha(\mathbf{r}_i - \mathbf{r}_j)^2), \quad (3.14)$$

where $\alpha = \frac{1}{2L^2}$, with $L = \sqrt{2}$ fm, is the effective range of the interaction. The summation runs over all baryons, B_j is the baryon charge of the j -th baryon.

¹Ignoring a possible momentum dependence of the potential.

For simplicity, it is assumed that the mean field potential for all baryon types is the same as for nucleons in the QMD implementation. This model also assumes that only baryons are directly affected by the potential interaction. This simplification can be supported by the fact that at the beam energies under consideration, the EoS is dominated by the contribution of baryons. The equations of motion are solved given the potential energy V , which is related to the pressure and thus to the EoS in a straightforward way [161].

$$P(n_B) = P_{\text{id}}(n_B) + \int_0^{n_B} n' \frac{\partial U(n')}{\partial n'} dn' \quad (3.15)$$

Here $P_{\text{id}}(n_B)$ is the pressure of an ideal Fermi gas of baryons and $U(n_B) = \frac{\partial(n_B \cdot V(n_B))}{\partial n_B}$ is the single particle potential.

In this framework one can study the effect of a density dependent EoS on the evolution of the system, consistently within UrQMD. To do so, first, a realistic Chiral Mean Field (CMF) EoS is implemented in the QMD part of UrQMD.

3.5.1 The CMF EoS in UrQMD

The Chiral Mean Field model [162–164] is an approach to describing QCD thermodynamics for a wide range of temperatures and densities. The effective degrees of freedom of the CMF model include a complete list of known hadrons, as well as the three light quark flavours plus a gluon contribution. The phase diagram of the CMF model contains three critical regions: the nuclear liquid-vapour phase transition, the chiral symmetry restoration, and the transition to quark matter [164]. The model predicts two first-order phase transitions. The first is associated with the nuclear liquid-vapour phase transition at $n_B \sim n_0$. The second one appears at about four times the normal nuclear density $4n_0$ due to the chiral symmetry restoration. However, this chiral transition shows only a small latent heat and the critical endpoint of this transition occurs already at $T_{\text{CP}} \approx 17$ MeV.

Regarding its phase structure, the CMF model has several attractive features:

1. A nuclear incompressibility compatible with experimental observations.
2. A stiff supersaturation nuclear equation of state required to explain astrophysical observations.
3. A "softening" of the equation of state at even higher densities due to the slow approach to the high density limit of a free gas of three quark flavours.

More details on the CMF model can be found in the Appendix A.2.

In the CMF model the single nucleon potential is given by the interactions with the chiral and repulsive mean fields. At $T = 0$ in the CMF model it can be calculated from the self-energy of the nucleons as

$$U_{\text{CMF}} = m_N^* - m_N^{\text{vac}} - \mu_N^* + \mu_N, \quad (3.16)$$

where m_N^{vac} and μ_N are the vacuum mass and chemical potential of the nucleon calculated only from the charge constraints, and m_N^* and μ_N^* are the corresponding effective nucleon mass and effective chemical potential generated by the interactions with the scalar and vector mean fields. These quantities are described in detail in appendix A.2.

To set the stage, the CMF potential U_{CMF} is shown in panel (a) of Fig. 3.2, where we contrast the CMF single-particle potential U_{CMF} , as a function of baryon density n_B in units of the ground-state baryon density, with two different Skyrme potentials U_{Sky} (resulting in different equations of state). We show the chiral mean field EoS (solid orange line) compared with the well-known hard Skyrme potential (dotted red line) and the soft Skyrme potential (dotted green line).

To implement the CMF EoS in the QMD part of the UrQMD model, we essentially need to calculate the effective field energy per baryon of any given model, which can then be used in the QMD equations of motion. In the CMF model, the nucleon interaction is described relativistically via scalar and vector mean fields, which are not present in UrQMD. Moreover, the CMF model is not restricted to nucleons only, so the single-nucleon potential U_{CMF} as defined in eq. (3.16) is not suitable for calculating the relevant mean-field potential needed for the equations of motion. Fortunately, the effective field energy per baryon E_{field}/A calculated from the CMF model can be used, i.e. the relevant quantity that enters the equations of motion:

$$V_{CMF} = E_{\text{field}}/A = E_{CMF}/A - E_{FFG}/A, \quad (3.17)$$

where E_{CMF}/A is the total energy per baryon at $T = 0$ from the CMF model and E_{FFG}/A is the energy per baryon from a free non-interacting Fermi gas. The resulting effective field energy per baryon as a function of baryon density from the CMF model is shown as a solid line in panel (b) of figure 3.2, again compared with the known curves from the hard and soft Skyrme EoS. Finally, panel (c) of figure 3.2 shows the derivative of the field energy per nucleon with respect to the baryon density as a function of the baryon density n_B in units of the ground-state baryon density for the three different potentials.

It can be observed that the CMF-EoS shows a behaviour similar to the soft Skyrme potential for subsaturation (up to saturation) density, then becomes even stiffer than the hard Skyrme potential and finally shows a significant softening compared to the hard Skyrme, which essentially becomes superluminal at large densities. At about four times the nuclear saturation density, the CMF-EoS shows a small kink in the derivative of the field energy per baryon due to the weak chiral phase transition at $T = 0$. Since this transition is very weak, we do not expect it to have a significant effect on the dynamical evolution, especially at finite temperatures where the kink will be smeared out by the thermal energy.

3.5.2 Results on the evolution of bulk properties

We now have two approaches, hydrodynamics and microscopic transport, to study the effects of a density dependent EoS on the evolution of the bulk properties of the system.

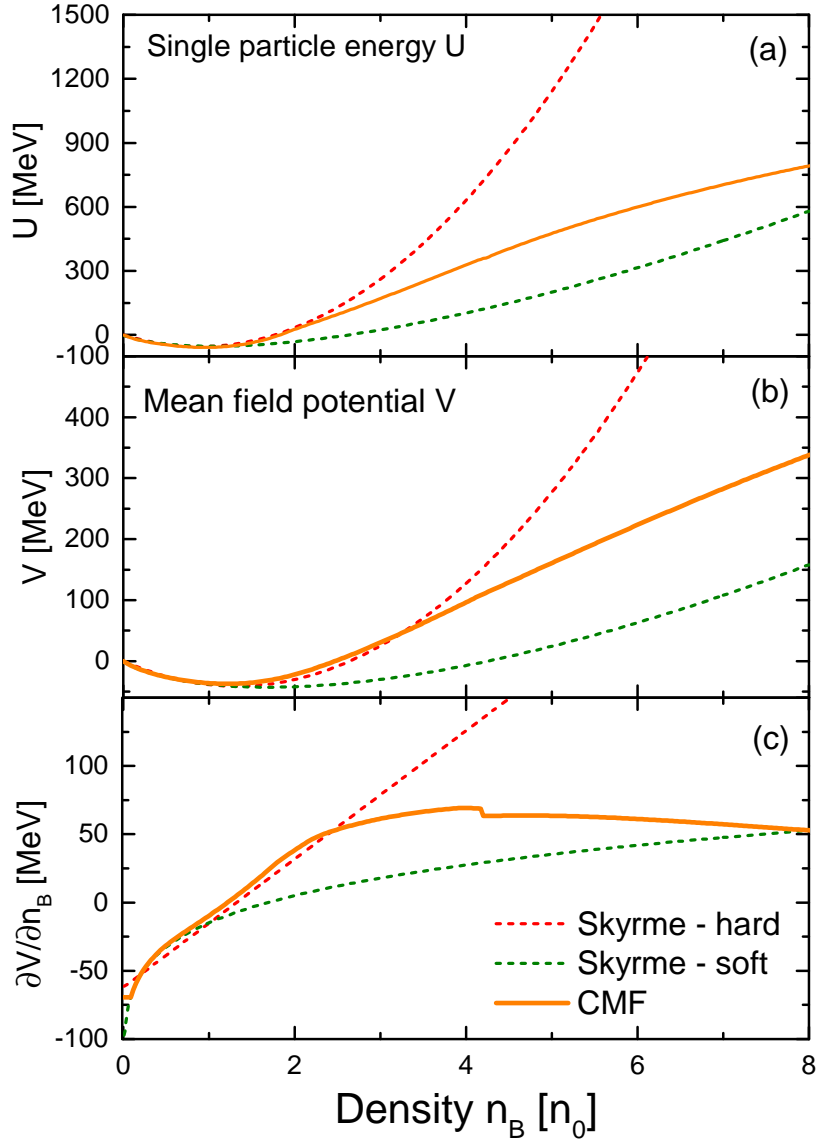


Figure 3.2: (a) Single particle potential U as a function of the baryon density n_B in units of the ground-state baryon density for three different potentials (resulting in different equations of state). (b) The resulting field energy per baryon E_{field}/A for the three different equations of state. (c) The derivative of the field energy per nucleon with respect to the baryon density as a function of the baryon density ρ_B in units of the ground state baryon density for three different potentials. The kink at around $4 n_0$ is the chiral phase transition. We show the chiral mean field EoS (solid orange line) compared to the well-known hard Skyrme potential (dotted red line) and the soft Skyrme potential (dotted green line).

In the hydrodynamic model, the expected properties of the matter at different beam energies can be extracted in a straightforward way. Here, only a single event per beam energy with an impact parameter $b = 2$ fm is sufficient to average the thermodynamic properties in the central volume (a cubic volume of length $l = 2$ fm) of central Au+Au collisions at different beam energies. The local energy density and the net baryon density are propagated explicitly in the hydrodynamic framework, and quantities such as temperature, pressure and entropy density can be related directly and unambiguously to these volume-averaged densities via the equation of state.

In the UrQMD model, the macroscopic quantities such as energy densities and baryon densities can be calculated via the coarse-graining procedure discussed in section 3.1.1. Here, the coarse graining is performed using 1000 events with impact parameter less than 3.4 fm. The mapping of energy density and baryon density to quantities such as temperature, pressure or entropy is done using either the HRG-EoS (for the UrQMD cascade simulations) or the CMF-EoS (for the corresponding CMF-UrQMD simulation). Note that this procedure assumes that the system is close to local equilibrium, which is not necessarily the case in the UrQMD transport model, especially at very early and late times. Thus the extracted values for temperature, pressure and entropy density can (and as we will see later will) vary due to deviations from equilibrium.

We first look at the space-time volume spent by the system at different temperatures and densities for the UrQMD simulations with the CMF equation of state. This is shown in figure 3.3. A similar plot for the UrQMD cascade model with HRG EoS used for mapping has already been presented in figure 3.1. It can be seen that in both cases the temperatures reached in the system are similar. However, at any given beam energy, the densities achieved with the CMF EoS are lower than with the UrQMD cascade. At 10 AGeV the maximum density of a cell is about 7 times the saturation density (n_0) for UrQMD with CMF EoS, while this is close to $10 n_0$ for the UrQMD cascade with HRG EoS for mapping. This suggests a strong EoS dependence of the maximum density achieved.

This is further explored by comparing the time evolution of the baryon density in the central volume² of the reaction for central Au+Au reactions at $E_{\text{lab}} = 1.23, 2.0, 4.0, 6.0, 10.0$ A GeV (from left to right). This is shown in Fig. 3.4. The solid lines show the results of the coarse-grained UrQMD simulations, the dashed lines show the results of the one-fluid 3+1-dimensional hydrodynamic calculations for the same systems and energies. The green lines show the results using the HRG-EoS in hydro and for the coarse-grained conversion of (ε, ρ_B) to the thermodynamic quantities, while the red lines show the results for the CMF-EoS. The time evolution of the baryon density in figure 3.4 clearly shows that the full hydrodynamic simulation and the transport simulation with the CMF-EoS give almost identical results up to the highest beam energies. Only for the beam energy $E_{\text{lab}} = 10.0$ A GeV the transport simulation gives a smaller compression due to the effect of transparency, which cannot be described in a 1-fluid simulation (although it is known that 3-fluid models can reproduce this effect). In the case of the HRG-EoS in hydro compared to the cascade

²To study the evolution in the central volume, a cube of length 2 fm is considered for coarse graining.

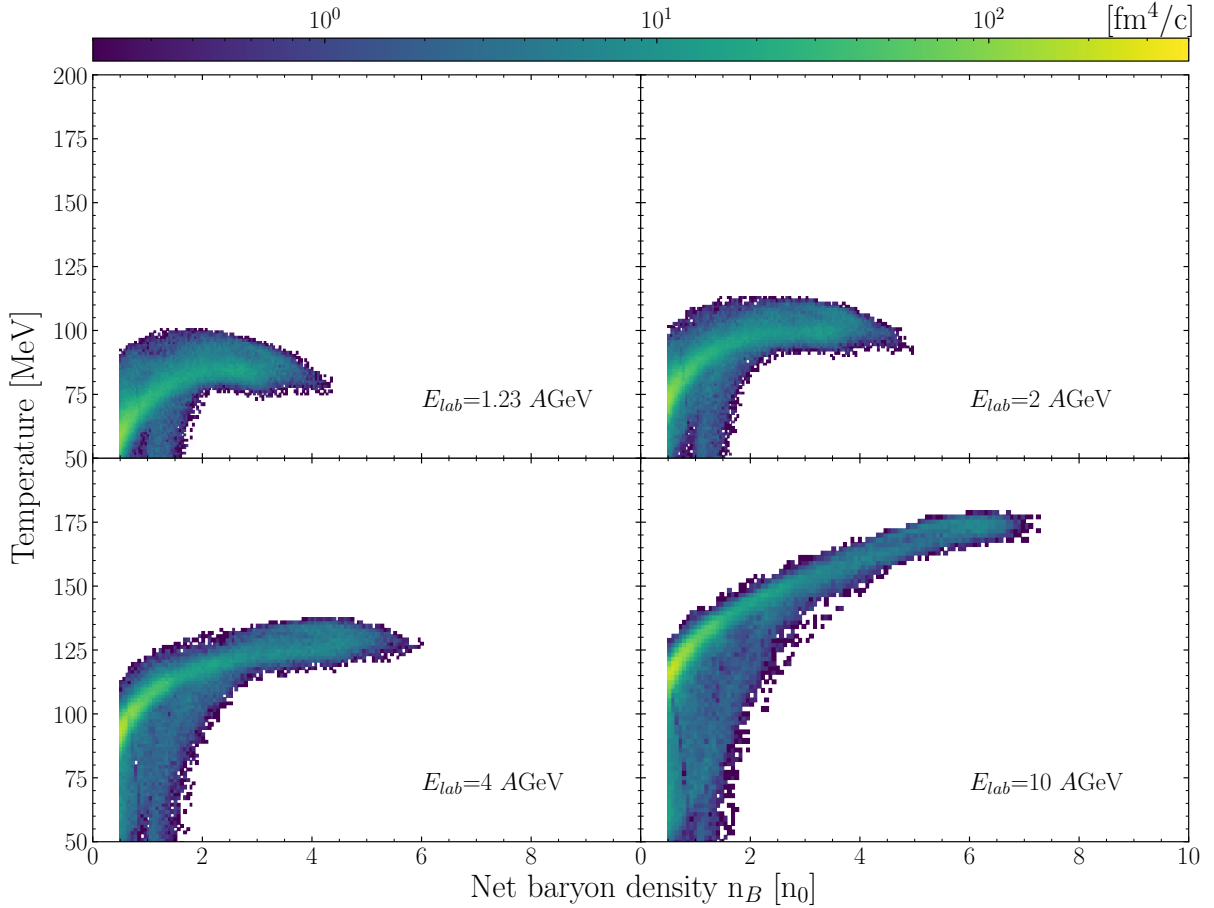


Figure 3.3: CMF in UrQMD: time-integrated space-time volume (four-volume) spent by the system at different temperatures and densities. The temperatures and densities achieved in central Au-Au collisions at beam energies 1.23, 2, 4, 10 AGeV are shown. The results are obtained from 1000 UrQMD events for each collision energy. Space-time cells with $\Delta x=1$ fm and $\Delta t=0.2$ fm have been used for coarse graining. Note that the temperatures shown here are not explicitly propagated, but extracted by mapping to an effective EoS where equilibrium is assumed. In the early stages of the collision, when the system is far from equilibrium, this mapping may therefore be inaccurate.

model, the agreement of the density evolution is not as exact, but still comparable. This is to be expected, as the EoS is not introduced explicitly in the cascade mode, but only implicitly through the set of degrees of freedom. The fact that the transport model and the hydrodynamic model agree so well on compression is not a trivial result, but clearly shows that the maximum compression achieved, for low beam energies where transparency can be neglected, depends to a first order on the work to be done against the pressure of the compressed system. The compression achieved varies drastically, by almost a factor of 2, between the two equations of state used. This finding has important consequences,

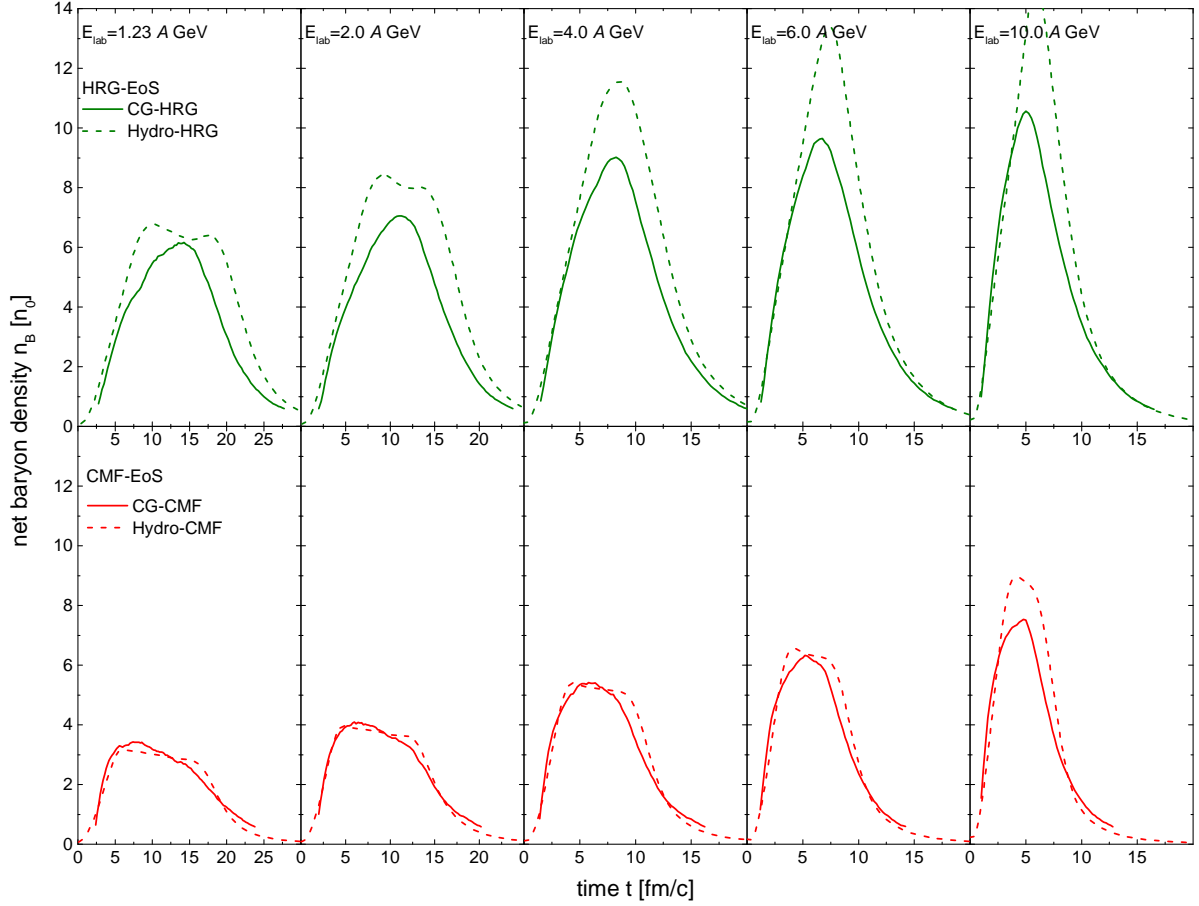


Figure 3.4: Time evolution of the baryon density in the central volume of the reaction for central Au+Au reactions at $E_{\text{lab}} = 1.23, 2.0, 4.0, 6.0, 10.0A$ GeV (from left to right). The solid lines show the results of coarse-grained UrQMD simulations and the dashed line shows the results of one-fluid (3+1) dimensional hydrodynamic calculations for the same systems and energies. The green lines in the top row are calculated using the hadron resonance gas EoS in hydro and for the conversion from (ε, ρ_B) to the thermodynamic quantities, while the red lines in the bottom row show the results for the CMF EoS. The 'CG-HRG' is from UrQMD cascade simulations with HRG EoS used for mapping to thermodynamic quantities, while the 'CG-CMF' is from UrQMD with potential interactions where the CMF potential was used for both simulations and mapping to thermodynamic quantities. The 'Hydro-HRG' and 'Hydro-CMF' are from fluid dynamic simulations with HRG and CMF EoS respectively.

since it means that any observable sensitive to the maximum compression achieved in these collisions would be a very good and almost model-independent messenger for the equation

of state of dense QCD matter.

Figure 3.5 shows the time evolution of the equilibrium temperature in the central volume of the same reactions. The colours and line styles are the same as in figure 3.4. When comparing the (equilibrium) temperature, the differences between the hydro and transport approaches are more obvious. Especially at very early times, the temperature in the coarse-grained transport simulations is significantly higher than in the hydro simulation. This can be understood as an effect of the non-equilibrium state of the microscopic transport, which is then mapped to an equilibrium temperature. The effect of the non-equilibrium is not observed in the baryon density which is explicitly propagated and conserved in both approaches but in the temperature which is implicitly inferred. Nevertheless, after a few fm/c, even in the non-equilibrium approach, the temperatures obtained agree within 5-10 MeV. In particular, the HRG simulations also give a systematically higher temperature, but the increase compared to the CMF is only in the order of 10 MeV.

Much of the compression, as well as the subsequent expansion of the system, depends strongly on the pressure reached in the initial phase. As we have seen, a higher pressure in the EoS (harder EoS) leads to lower densities. On the other hand, the amount of radial as well as directed and elliptic flow produced depends on the pressure that drives the expansion stage. In figure 3.6 we show the time evolution of the pressure in units of the ground state energy density in the central cell of the reaction for central Au+Au reactions at $E_{\text{lab}} = 1.23, 2.0, 4.0, 6.0, 10.0A$ GeV (from left to right). The solid lines show the results of coarse-grained UrQMD simulations and the dashed line shows the results of one-fluid (3+1) dimensional hydrodynamics calculations for the same systems and energies. The green lines show the results using the HRG-EoS, while the red lines show the results using the CMF-EoS. Again, the extraction of the pressure from the local densities (ε, n_B) is straightforward in the hydro model, while for the coarse grained approach we assume local equilibrium and isotropic pressure, which allows us to read the effective pressure from the EoS table as described above.

Most notably is that the maximum pressure is reached at different times, depending on the equation of state used. This is due to the fact that the maximum density is also reached at different times, as shown in figure 3.4. This different time dependence of the pressure evolution is likely to have significant consequences on observables such as the collective flow.

The expansion dynamics of the studied systems can also be represented in the $T-n_B$ phase diagram. Therefore, we examine the expansion trajectories along the time evolution in the central cell in Fig. 3.7 in the temperature-baryon density plane for central Au+Au reactions at $E_{\text{lab}} = 1.23, 2.0, 4.0, 6.0, 10.0A$ GeV (from left to right). The solid lines show the results of coarse-grained UrQMD simulations and the dashed line shows the results of one-fluid (3+1) dimensional hydrodynamics calculations for the same systems and energies. The green lines show the results using the HRG-EoS for the conversion from (ε, n_B) to the thermodynamic quantities, while the red lines show the results for the CMF-EoS. Note that for this comparison we start the trajectories at the point of maximum compression, after

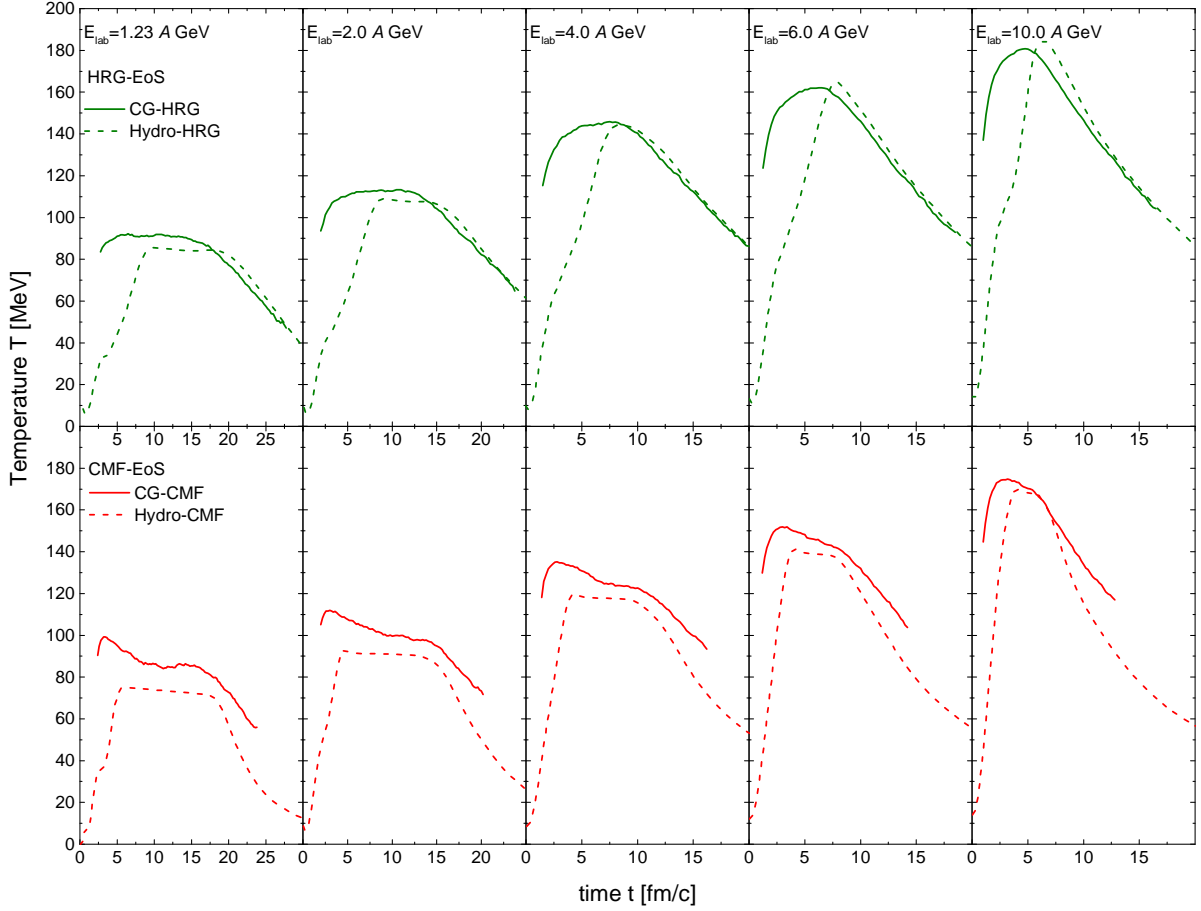


Figure 3.5: Time evolution of the average temperature in the central volume of the reaction for central Au+Au reactions at $E_{\text{lab}} = 1.23, 2.0, 4.0, 6.0, 10.0 A$ GeV (from left to right). The solid lines show the results of coarse-grained UrQMD simulations and the dashed line shows the results of one-fluid (3+1) dimensional hydrodynamic calculations for the same systems and energies. The green lines in the top row are calculated using the hadron resonance gas EoS in hydro and for the conversion from (ε, ρ_B) to the thermodynamic quantities, while the red lines in the bottom row show the results for the CMF EoS. The 'CG-HRG' is from UrQMD cascade simulations with HRG EoS used for mapping to thermodynamic quantities, while the 'CG-CMF' is from UrQMD with potential interactions where the CMF potential was used for both simulations and mapping to thermodynamic quantities. The 'Hydro-HRG' and 'Hydro-CMF' are from fluid dynamic simulations with HRG and CMF EoS respectively. In the coarse-graining procedure, only the participants are used for averaging, so the temperature appears to 'jump' to a finite value.

which they follow lines of constant entropy per baryon in the case of ideal hydrodynamics.

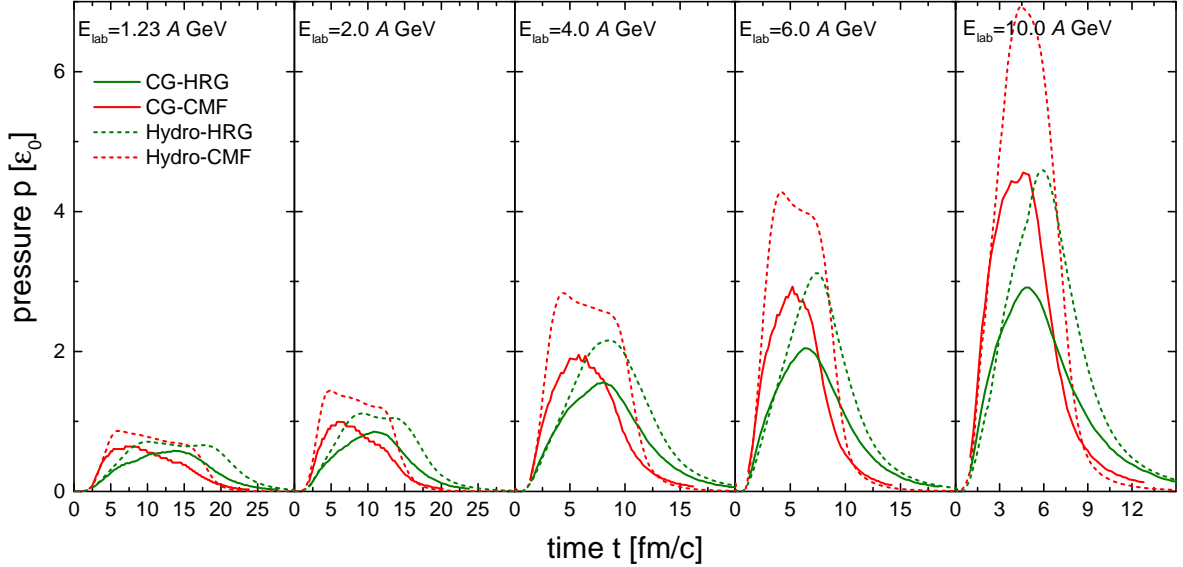


Figure 3.6: Time evolution of pressure in units of the ground state energy density in the central cell of the reaction for central Au+Au reactions at $E_{\text{lab}} = 1.23, 2.0, 4.0, 6.0, 10.0$ A GeV (from left to right). The solid lines show the results of coarse-grained UrQMD simulations and the dashed line shows the results of one-fluid (3+1) dimensional hydrodynamic calculations for the same systems and energies. The green lines show the results using the hadron resonance gas EoS to convert (ε, ρ_B) into the thermodynamic quantities, while the red lines show the results for the CMF EoS. The 'CG-HRG' is from UrQMD cascade simulations with HRG EoS used for mapping to thermodynamic quantities, while the 'CG-CMF' is from UrQMD with potential interactions where the CMF potential was used for both simulations and mapping to thermodynamic quantities. The 'Hydro-HRG' and 'Hydro-CMF' are from fluid dynamic simulations with HRG and CMF EoS respectively.

The most significant difference is that the HRG curves start at a much higher density. On the other hand, the trajectories become very close at lower densities. This means that by the time the systems reach freeze-out, at $n_B \leq n_0$, the thermodynamic conditions are very similar for the different models and equations of state.

As already shown in Fig. 3.7, the expansion in both the hydro and transport models follows approximately the same isentropic trajectories. However, we expect the final entropy per baryon to be different in the two approaches, since the microscopic transport has a finite viscosity (shear and bulk) and the system is at best in partial chemical equilibrium.

To complete the comparison, Fig. 3.8 shows the entropy production per baryon as a function of beam energy for central Au+Au reactions in the energy range from $E_{\text{lab}} = 1.23$ A GeV to 10 A GeV. The lines denote calculations using the coarse-grained UrQMD model with CMF-EoS (solid red line), the 3+1D one-fluid hydrodynamics calculation (dotted red

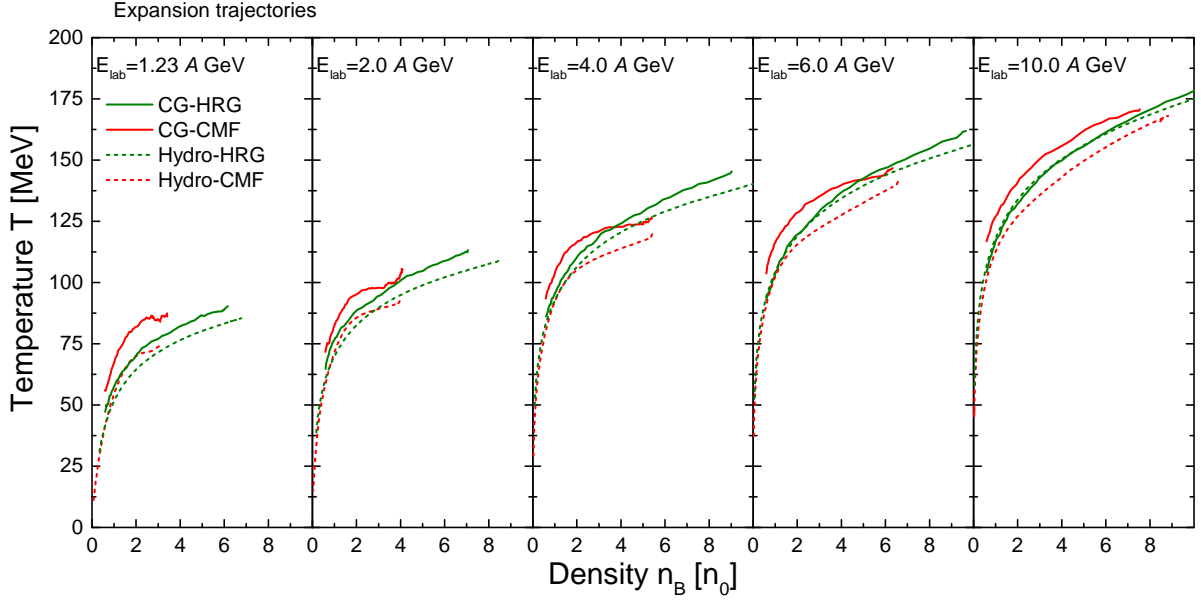


Figure 3.7: Expansion trajectories (along the time evolution in the central cell) in the temperature-baryon density plane for central Au+Au reactions at $E_{\text{lab}} = 1.23, 2.0, 4.0, 6.0, 10.0A$ GeV (from left to right). The solid lines show the results of coarse-grained UrQMD simulations and the dashed line shows the results of one-fluid (3+1) dimensional hydrodynamic calculations for the same systems and energies. The green lines show the results using the hadron resonance gas EoS for the conversion from (ε, n_B) to the thermodynamic quantities, while the red lines show the results for the CMF EoS. The 'CG-HRG' is from UrQMD cascade simulations with HRG EoS used for mapping to thermodynamic quantities, while the 'CG-CMF' is from UrQMD with potential interactions where the CMF potential was used for both simulations and mapping to thermodynamic quantities. The 'Hydro-HRG' and 'Hydro-CMF' are from fluid dynamic simulations with HRG and CMF EoS respectively.

line) and the one-dimensional relativistic shock model, i.e. the Taub adiabat (dashed grey line). For both the hydrodynamics and UrQMD coarse-grained simulations, the entropy was extracted implicitly from the CMF model, as described above for the temperature, knowing the local energy and baryon densities. In the hydro simulation, S/A as a function of time is essentially a constant throughout the expansion phase. In the transport simulation it shows only a slight increase. Here we compare the values of S/A at the end of the expansion, i.e. when the density falls below $n_B = n_0$. The full 3+1D ideal hydrodynamic simulation produces almost exactly the same entropy per baryon as the analytical 1-D shock solution (Taub adiabat). In general, the entropy per baryon is smaller in the hydrodynamic case than in the non-equilibrium transport which is expected. The difference between these two scenarios grows with increasing energy which is also expected from the increasing transparency that leaves a smaller baryon number in the centre of the collision

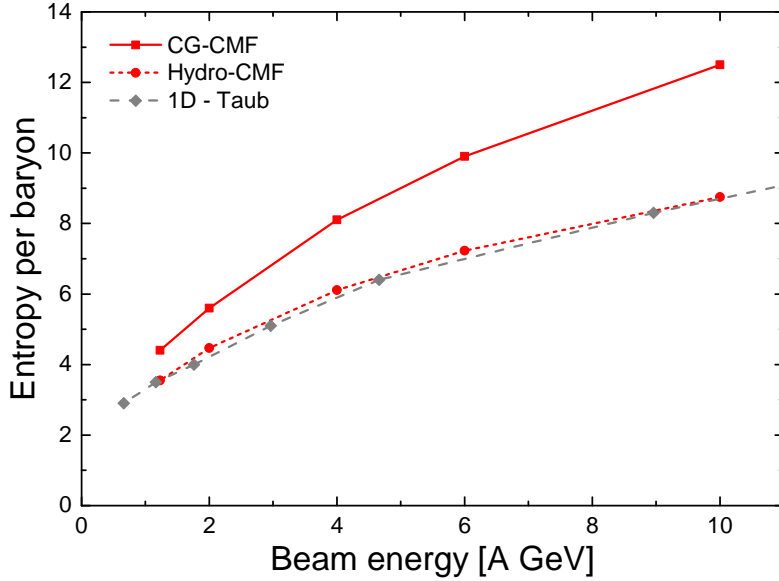


Figure 3.8: Entropy production per baryon as a function of beam energy for central Au+Au reactions in the energy range from $E_{\text{lab}} = 1.23A$ GeV to $10A$ GeV. The lines denote calculations using the coarse-grained UrQMD model with CMF EoS (solid red line), a one-fluid hydrodynamics calculation (dotted red line) and the the semi-analytic relativistic stationary 1D Taub adiabat solution (dashed grey line).

zone. Furthermore, it is known that at late times the system can only be described as being in partial chemical equilibrium. Mapping such a system onto an equilibrium EoS to calculate the entropy per baryon will yield larger values of the effective (equilibrium) S/A .

In summary, for low beam energies $E_{\text{lab}} \leq 6A$ GeV, the bulk density evolution in this new description agrees very well with a relativistic 1-fluid simulation with the same equation of state. The effective temperature from the UrQMD simulation is slightly increased compared to the ideal hydrodynamic model due to non-equilibrium effects. Our results highlight the importance of the equation of state for the initial compression phase in low-energy nuclear collisions and provide a method for introducing it in a consistent manner. This new method now allows us to study the effect of different possible equations of state within the microscopic transport approach. This method can be easily extended to include a strong first-order phase transition. This consistent description of the whole collision, which does not require ad hoc matching of different phases, will allow us to study possible observable signals of this transition in heavy-ion collisions. Nevertheless, this is a non-relativistic model and it is assumed that the EoS is dominated by its density dependence, i.e. fermions, and that the effective potentials governing the interactions have only a weak explicit temperature dependence. A hybrid approach, such as UrQMD-hybrid, would be more appropriate if a relativistic treatment of the collisions or explicit temperature dependence of EoS were to be included.

Chapter 4

Artificial intelligence for heavy-ion collisions

In the previous chapters we have discussed in detail the various theoretical and experimental challenges involved in studying heavy-ion collisions at high baryon densities. We have introduced different theoretical models for heavy-ion collisions and also presented a new method to consistently describe the entire evolution of the system within the UrQMD model. The experimental challenge in the analysis of heavy-ion collision data is to infer the properties of hot, dense QCD matter from collision events reconstructed using conventional algorithms that process data from detectors with limited acceptance and space-time resolution. In this chapter, we will discuss several novel methods based on artificial intelligence that could be used to address these challenges. Some of the methods presented in this chapter are based on [77–80, 165]. In particular, the focus is on the development of AI methods that can work directly on raw detector level information, such as particle hits/tracks, to extract the underlying properties of the collision as described by a theoretical model. The goal is to develop data-driven methods that can consistently and accurately analyse experimental data. However, we first introduce the basic concepts and principles of AI.

4.1 Machine learning and deep learning

The terms Machine Learning (ML) and Deep Learning (DL) are often used interchangeably in the broader context of AI. However, machine learning refers to a broad class of AI methods that build mathematical models from data, enabling a machine to "learn" to perform various tasks without explicit instructions.

Depending on the nature of the training data, machine learning techniques can be broadly divided into supervised and unsupervised learning. Supervised learning techniques rely on labelled data to learn how to perform a task. Here, the labels refer to the target variable

that the model needs to learn. For example, if the task is to identify images of cats from dogs, the labels are 'cat' and 'dog' for each image in the dataset. Such problems can be further classified as follows

1. Classification: In a classification problem, the variable to be predicted is categorical in nature, e.g. distinguishing the images of cats from those of dogs.
2. Regression: In a regression problem, the model predicts a continuous variable, e.g. predicting the future price of a stock.

On the other hand, unsupervised learning techniques identify hidden patterns in unlabelled data. These include methods such as clustering, where the model groups similar data points together, and anomaly detection, which identifies outliers in the data.

Deep learning [166] is a subset of machine learning inspired by the way information is processed in biological systems. It uses multi-layer Artificial Neural Networks (ANN) to learn higher dimensional correlations in the data. This enables the computer to find better solutions to complex problems that traditional ML techniques cannot.

With access to unprecedented amounts of data and computing power in recent years, ML and DL models have been found to outperform traditional algorithms for various tasks. DeepFace [167], a face recognition system from Facebook, Google's AlphaGo [168], a DL program that plays the board game Go, AlphaFold [169], which accurately predicts protein structures, and ChatGPT [170], a language model capable of having realistic conversations with the user, are just a few examples that demonstrate the recent progress in the field and the diverse applications of ML/DL models.

4.1.1 Artificial neural networks

An artificial neural network is a machine learning architecture that consists of a collection of interconnected nodes called neurons. The functioning of neurons in artificial neural networks is analogous to the functioning of biological neurons in our brain. The connections between different neurons and the activation of different neurons in the brain in response to different sensory inputs determine our thoughts and actions. Similarly, a neural network takes different inputs and processes them through the interconnected network of neurons to produce an output.

A neuron

The structure of an artificial neuron is illustrated in the figure 4.1. A neuron in an ANN is a mathematical object that takes several inputs $\{x_1, x_2, \dots, x_n\}$, to which weights $\{w_1, w_2, \dots, w_n\}$ can be assigned and a bias term b . A neuron simply performs a non-linear transformation of the sum of the weighted inputs and the bias term to produce the output

$$y = f \left(b + \sum_{i=1}^n x_i w_i \right). \quad (4.1)$$

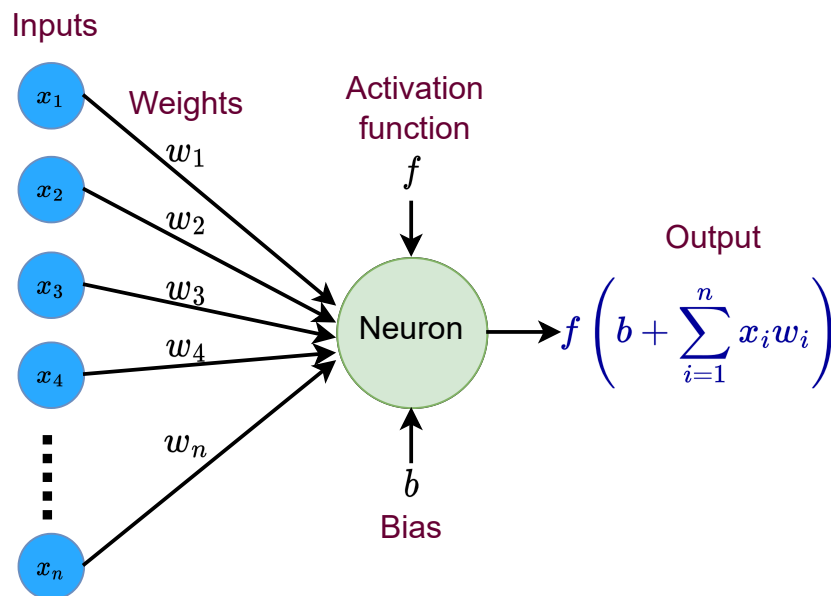


Figure 4.1: Structure of a neuron. A neuron maps the weighted sum of its inputs x_i and bias b to an output using a non-linear activation function f .

The non-linear mapping function f is called the activation function of the neuron. Some examples of commonly used activation functions are

1. ReLU: ReLU stands for Rectified Linear Unit. It has the functional form

$$f(X) = \max(0, X) \quad (4.2)$$

where $X = b + \sum_{i=1}^n x_i w_i$ is the input to the activation function. Evidently, relu simply squashes negative inputs to zero.

2. Sigmoid: The functional form of the sigmoid activation function is

$$f(X) = \frac{1}{1 + e^{-X}}. \quad (4.3)$$

The sigmoid activation function restricts the output to the range $(0,1)$.

3. Tanh: This activation function has the form

$$f(X) = \frac{e^X - e^{-X}}{e^X + e^{-X}}. \quad (4.4)$$

The output of tanh is in the range $(-1,1)$.

4. Softmax: The softmax activation function takes a vector of numbers and converts it to a vector of probabilities. It is given by

$$f(\mathbf{z})_j = \frac{e^{z_j}}{\sum_{k=1}^n e^{z_k}} \quad (4.5)$$

where $j = 1, \dots, n$ and $\mathbf{z} = (z_1, z_2, \dots, z_n)$. The softmax takes the exponent of each element in the vector and normalises it by the sum of the exponents of all the elements. Each element of the softmax output vector will be in the range $(0,1)$ and their sum will be unity. Therefore, the output vector can be interpreted as probabilities.

Neural networks as function approximators

Broadly speaking, supervised machine learning techniques learn a function that can map the given input data D to the desired output O . In terms of probabilities, the machine has to model the probability distribution $P(O|D)$. This mapping can be modelled with an interconnected network of neurons. A neural network consists of several layers of neurons. A layer of neurons consists of several neurons that process the same set of inputs, but with different weights. Each neural network has an input layer, which takes the input data, and an output layer, which provides the final, desired prediction. The layers of neurons between the input and output layers that process the input data are called hidden layers. In such networks, each neuron in a layer is connected to every other neuron in the next layer, and the input data is processed successively through different layers, with the output of each neuron becoming the input to the neurons in the next layer. These networks are therefore called fully connected feed-forward neural networks. Depending on the number of layers in the network, the networks are referred to as shallow neural networks or Deep Neural Networks (DNNs). A shallow neural network consists of a single hidden layer, while deep neural networks are constructed with multiple hidden layers that process the data.

The universal function approximation theorem [171–174] tells us that a neural network with a sufficient number of neurons ("width of the network") or a sufficient number of layers ("depth of the network") can approximate any continuous function when given appropriate weights. Note that the theorem only states the ability of neural networks to approximate functions. It does not tell us how to find the appropriate weights for the neurons that will approximate the desired function. This is where cost functions and optimisation algorithms come in.

Optimising the network

In supervised learning, building a model involves two stages: training and testing. The entire dataset is randomly divided into the training and test datasets. During the training stage, the model iterates through the labelled training data to iteratively update the weights so that the error in the predictions is minimised. Finally, the performance of the trained

model is evaluated on the unseen test data. The functions used to quantify the error in the predictions are known as the cost function or loss function. The most commonly used loss functions are

1. *MSE*: *MSE* stands for Mean Squared Error. *MSE* is the average of the square of the difference between the true and predicted values. It is given by

$$MSE = \frac{1}{n} \sum_{i=1}^N (y_i^{true} - y_i^{pred})^2 \quad (4.6)$$

where y_i^{true} and y_i^{pred} are the true and predicted labels respectively.

2. *MAE*: *MAE* stands for Mean Absolute Error. *MAE* is calculated as the average of the absolute value of the differences between the true and predicted values. It is given by

$$MAE = \frac{1}{n} \sum_{i=1}^N |y_i^{true} - y_i^{pred}|. \quad (4.7)$$

It can be seen that *MSE* would severely penalise small errors compared to *MAE* as *MSE* takes into account the square of the error. Therefore, *MAE* is more appropriate when the training data contains outliers.

3. Cross Entropy (CE): Cross entropy is a common choice of cost function for classification problems. If we consider a multi-class classification problem and the model predicts the output probabilities for different classes, the cross entropy loss for a single data point is calculated as

$$CE = - \sum_{i=1}^c y_i \ln(y_i^{pred}) \quad (4.8)$$

where y_i is the truth label for class i and y_i^{pred} is the predicted probability for the true class of the datapoint. The cross-entropy loss penalises errors in predicting the true class. Usually the loss is averaged over several data points.

The prediction error estimated by the cost function is processed by algorithms known as optimisers to update the weights of the network. Optimisers make small changes to the current value of the weights such that the new weights would result in a lower loss (as given by the loss function). A very simple but commonly used optimiser algorithm is gradient descent. It is based on the idea that the direction opposite to the gradient is the direction of steepest descent. The gradient descent algorithm calculates the gradient of the cost function with respect to the model parameters (weights and bias) and uses it to update the model parameters $\theta = (\theta_1 \dots \theta_n)$ as follows

$$\theta = \theta - \alpha \nabla J(\theta) \quad (4.9)$$

where α is the learning rate, which controls the size of the update. One of the disadvantages of gradient descent is that the gradients are computed for the entire training dataset, causing the convergence to a solution to be extremely slow. This would also result in large memory requirements to compute the gradient for a large dataset. There are several variations of gradient descent that address these issues. A stochastic gradient descent algorithm updates the parameters after each training sample. Although this method solves the memory problem, the frequent updates can lead to a large variance in the model parameters. As a result, convergence to a minimum is difficult, even though the model is close to one. This is solved in the mini-batch gradient descent algorithm, where the parameters are updated after gradient evaluation on mini-batches of data. There are also many other gradient based optimisation algorithms such as ADAM [175], Adagrad [176], Adadelata [177], RMSprop etc. which are commonly used to solve ML problems. An overview of gradient based optimisation techniques can be found in [178].

While there are several methods for updating weights based on gradients, the computation of the gradients themselves for the nodes in the hidden layers is not straightforward and can be extremely slow if not done carefully. Back-propagation algorithms [179] are used to efficiently compute the gradients of model parameters in deep neural networks. As the name suggests, back-propagation algorithms start from the output layer, compute the gradient of the cost function, and propagate the error in the output back to the nodes in the hidden layer to compute their gradients.

We now have all the ingredients to properly train a neural network. If we have enough training samples, we can design and optimise DNNs to solve the problem at hand. So far we have only discussed Fully Connected Neural Networks (FCNN), which take only a 1-dimensional vector as input. In reality, the data available to us is often high-dimensional, for example in the form of images. An image is a 2-dimensional array of pixels (3-dimensional if colour is also considered), where each entry represents the intensity of a particular pixel. FCNNs are not designed to work with this type of data. Images contain strong spatial correlations or symmetries that cannot be efficiently extracted by a Fully Connected Neural Network. In addition, the images need to be converted into a 1-dimensional vector before a FCNN can process them. This does not scale well for large images.

4.1.2 Convolution Neural Networks

Convolution Neural Networks (CNN) are a type of DNN designed to learn efficiently from image data. The core of CNNs is the convolution operation shown in figure 4.2. The convolution operation involves a convolution kernel sliding through an image to extract a feature map. A kernel is a 2-dimensional weight map that performs a dot product with the pixel values in the image. As the kernel completes a pass through the entire image, we obtain a feature map. By defining different kernels, several different feature maps can be extracted. These extracted feature maps are usually processed by pooling layers that perform operations such as addition (sum pooling), averaging (average pooling), and taking the maximum value (max pooling) to summarise the extracted features and reduce

4.1. MACHINE LEARNING AND DEEP LEARNING

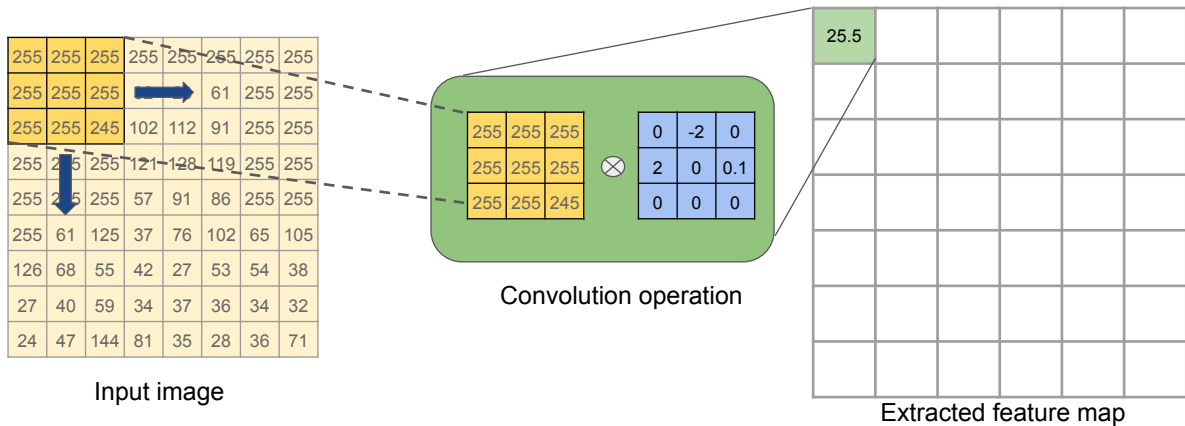


Figure 4.2: The convolution operation. A convolution kernel slides through the input image and calculates dot products to extract the features from the image. Several such kernels can be defined to extract different feature maps from the input image. The convolution operation can also be applied to the extracted feature maps.

dimensionality. Multiple layers of convolutions can be defined to further extract even abstract feature maps from already extracted feature maps. Finally, the extracted features are usually fed into an FCNN to obtain the final output. The FCNN works on these extracted features to regress or classify the input image.

CNNs are a good choice of algorithm for extracting correlations from image-like heavy-ion collision data, i.e. data provided in the form of equally spaced multidimensional histograms [180, 181]. However, histogramming of data can lead to loss of information. Furthermore, converting the raw detector output into a histogram of different observables would require several stages of data processing. As mentioned above, these processing and analysis algorithms can introduce unwanted biases into the data. In addition, experiments such as CBM require online analysis of the collected data, which can be slowed down significantly by the use of conventional iterative pre-processing and analysis algorithms.

Therefore, our goal is to train DL models directly on minimally processed experimental output, such as information from discrete reconstructed tracks of particles in a collision event. One of the main problems in training CNN-based deep learning models on detector output is the sparse nature of the detector data. Consider a particle detector that records the coordinates of the particles that pass through it. This hit information from an event can be stored as a 3-dimensional histogram of particle coordinates (x,y,z) . The data is now a three-dimensional array containing an "image-like" representation of the detector output. However, most of the bins in such a histogram will not contain any hits. Modern particle detectors with excellent positional resolution would further increase the size and sparsity of these arrays. Processing such extremely sparse arrays with CNNs would require huge amounts of memory and computing power. In addition, extending such a represen-

tation to include more features of a hit, such as the time of the hit or the amplitude of the signal produced by the hit in the sensor, would require the inclusion of additional dimensions, making it even more sparse. CNNs are not efficient at learning from sparse, high-dimensional detector data.

One solution to these problems is to use a point cloud representation of the data. Point clouds are collections of unordered points in space. A point cloud of hits from an event is a dense representation of the detector data in the form of an unordered list, where each element is the set of coordinates of a hit. This can be stored in the form of a two-dimensional array where each row stores a hit and each column stores an attribute of the hit (e.g. x-coordinate). This representation solves the sparsity problem associated with an image-like representation, as we only store the locations of hits, not the entire representation of the detector volume. Furthermore, it is possible to add more features to a hit by simply adding another column to this array. This makes point clouds ideal for representing high-dimensional data.

4.2 Learning from experimental data with PointNet

PointNet is a deep learning architecture optimised for learning from point cloud data [182]. One of the key features of the PointNet model is that it can learn to be invariant to the order of the input points. The PointNet architecture can be extremely useful in nuclear and particle physics experiments, where most sensor or detector data has the geometric structure of point clouds. PointNet can be used to train deep learning models that take as input raw experimental data such as hits or the reconstructed tracks of particles. Here, the predictions are independent of the order of the particle tracks or hits.

However, the lack of inherent order in the point cloud representation makes it difficult to train CNN-based DL models using point cloud data. The PointNet is a modification of the regular CNN that is designed to respect the order invariance in the data, allowing us to train DL models directly on the point cloud data. Figure 4.3 illustrates the general operation of the PointNet architecture with an example of an input point cloud of particle hits. The PointNet model consists of the following 2 components to achieve order invariance in the predictions, unlike regular CNNs:

1. Convolution kernels of size $1 \times N$, where N is the number of columns in the input point cloud array. The advantage of using $1 \times N$ kernels is that only single point (hit) features are extracted, as the kernel can only span one row at a time. Similar kernels are used in all hidden layers to ensure that the features extracted even in the last convolution layer are order invariant.
2. Symmetric functions to extract global features. The single point feature maps extracted by the $1 \times N$ kernels are converted into global feature maps of the entire point cloud by passing each feature map produced by the last convolution layer through an order invariant, symmetric function such as average pooling or max pooling. The

4.2. LEARNING FROM EXPERIMENTAL DATA WITH POINTNET

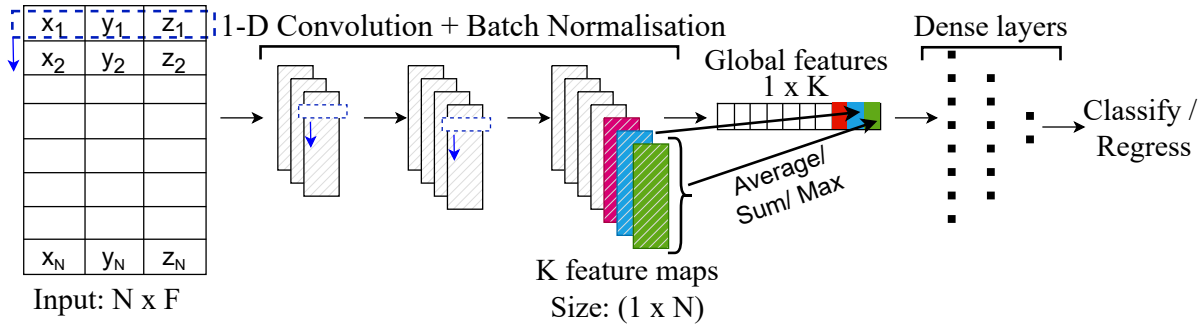


Figure 4.3: General structure of the PointNet model. The input point cloud is a list of coordinates of particle hits in a detector plane. The convolution kernels (blue rectangles) are of size 1 to extract order-invariant feature maps. The extracted feature maps are later converted into a global feature of the point cloud using a symmetric function such as max pooling, sum pooling, average pooling, etc. All convolution layers are followed by batch normalisation layers.

output of these symmetric functions in the PointNet model can be interpreted as a global feature of the point cloud (collision event).

These global features are then passed through a fully connected neural network to classify or regress our target quantity. The original implementation of PointNet also includes "mini-PointNets" that learn matrices that can transform the input point cloud ("input transformation network") or the feature point cloud ("feature transformation network") in a way that allows PointNet to respect the symmetries involved. These "mini-PointNets" have the same structure as the PointNet described in figure 4.3, except for the input and output. When used as an input transformation network, the input has dimensions $N \times F$, where N is the maximum number of hits or tracks expected in a point cloud and F is the number of input attributes of each hit or track (e.g. $F=3$ if the model uses the x, y, z coordinates of all hits as input features). The alignment network then learns an $F \times F$ matrix. Similarly, if the network is used as a feature transformation network, the input has dimensions $N \times K$, where K is the number of feature maps produced by the convolution layer preceding the feature transformation network. In this case, the network learns a $K \times K$ matrix to transform the feature maps. Finally, these transformations are applied to the input or feature point cloud before the next 1-D convolution is applied.

The ability to extract order-invariant, global event features that also respect the symmetries in the data directly from a dense representation of experimental data makes PointNet an ideal choice for training DL models on detector output.

4.3 Bayesian Inference

Bayesian inference is a statistical learning technique based on the Bayes' theorem. According to Bayes' theorem, if we have a hypothesis \mathbf{H} , the probability that the hypothesis is true after we encounter evidence \mathbf{E} is proportional to

$$P(\mathbf{H}|\mathbf{E}) \propto P(\mathbf{E}|\mathbf{H})P(\mathbf{H}). \quad (4.10)$$

Where $P(\mathbf{H})$ is the prior distribution for the hypothesis, which encodes the probability that the hypothesis is true before encountering the evidence. The $P(\mathbf{E}|\mathbf{H})$ is the likelihood, which describes how well the hypothesis describes the evidence. Finally, $P(\mathbf{H}|\mathbf{E})$ is the desired posterior, which encodes the updated knowledge about the hypothesis after encountering the experimental evidence \mathbf{E} .

As discussed earlier, the underlying physics of heavy-ion collisions, as described by a theoretical model, is often extracted by comparing model predictions for different observables with measured data. Bayesian inference can be very useful for this purpose. Bayesian inference can quantitatively extract the model parameters that can describe the experimental measurements. If we need to constrain the parameters of a simulation model and have several measurements or observations that can be used to test the validity of a given parameter set, the posterior distribution for the parameters can be constructed using Markov Chain Monte Carlo (MCMC) methods.

4.3.1 The Metropolis algorithm

The Metropolis algorithm [183] is a popular MCMC algorithm used in Bayesian inference problems to draw samples from the posterior distribution. The distribution of the generated samples becomes closer to the posterior distribution as more and more samples are drawn. Metropolis sampling can be performed if we know a function g that is proportional to the probability density from which we want to draw samples. In our case, we already know from eq.4.10 that the posterior probability is proportional to the likelihood weighted by the prior. Therefore, we can use the Metropolis algorithm to sample from the posterior in the following steps:

1. Choose an arbitrary sample x_t and an arbitrary proposal density $P(x_{t+1}|x_t)$. $P(x_{t+1}|x_t)$ is the probability density for the next sample x_{t+1} given the current sample x_t . This probability is usually assumed to be a Gaussian distribution around x_t .
2. Sample a candidate y for x_{t+1} from the proposal density.
3. Calculate the ratio $\alpha = \frac{g(y)}{g(x_t)}$.
4. Generate a uniform random number r between 0 and 1.

Reject candidate y if $r > \alpha$. Set $x_{t+1} = x_t$.

Accept candidate y if $r \leq \alpha$. Set $x_{t+1} = y$.

5. Repeat steps 2-4 until enough samples have been accepted.

The Metropolis algorithm uses the current sample to create a candidate, and rejects or accepts the candidate depending on its probability density relative to the current sample. As the iteration proceeds, more and more samples are drawn from regions of higher probability density, creating a population that converges to the desired probability distribution. However, some of the initial samples may still be from a low probability region and may not represent the posterior distribution we are interested in. Therefore, in practice, a "burn-in" period is set to discard several initial samples.

Here we have discussed the simple Metropolis algorithm for MCMC sampling. There are several advanced variations of the Metropolis algorithm that are faster and more efficient at converging to the desired distribution. The DE-Metropolis algorithm [184] uses previously generated samples from different MCMC chains to construct the proposal distribution, while another variant called DE-Metropolis(Z) [185] uses previous samples from the same chain to construct the proposal distribution. Since the MCMC chains converge to the desired posterior, using the history of these chains to construct the probability density of the next sample actually increases the acceptance ratio α , which in turn leads to faster convergence.

Chapter 5

AI based analysis of heavy-ion collision data

As discussed in earlier chapters, a model-to-data comparison of conventional observables such as particle yields, fluctuations, collective flow, etc. is carried out to determine the fundamental properties of the strongly interacting matter produced in the collision, such as the equation of state or the transport coefficients. However, any inconsistency in the analysis chain, especially at stages such as event selection, for which experiments use simplified models, would introduce huge uncertainties in the final, extracted results. In addition, the sensitivity of conventional observables may be substantially reduced by the experimental effects. Nevertheless, model-data comparison is an inevitable step in extracting the physics of hot and dense QCD matter. In this chapter we present several AI methods that can accurately infer the underlying physics, as described by a theoretical model, from experimental data and potentially bridge this gap between models and experiments.

Artificial intelligence-based methods are a popular analytical tool in fundamental physics research. In particular, ML and DL techniques have been widely used by the particle/heavy-ion physics community to study jets and their substructures [186–193], to search for exotic particles [194], for ultrafast simulations [195–198], to search for new physics [199–201] and for various tasks such as particle identification, tracking, event reconstruction and extraction of various physical and theoretical quantities [180,202–214]. Furthermore, the Bayesian inference technique has been applied to extract the transport coefficients [215,216] and the EoS [217] of QCD matter at high temperatures. However, there have been very few studies related to the use of ML or Bayesian techniques for high baryon density QCD. Moreover, most of the existing DL techniques for the analysis of heavy-ion collision data require heavily processed experimental output. The drawbacks of such an approach have been discussed elsewhere. In this chapter we present the various applications of the PointNet based DL models and Bayesian inference in the analysis of heavy-ion collision data.

Before exploring the possibilities of DL methods, it would be interesting to examine the

conventional techniques for experimental analysis and their limitations. The conventional observables used in the analysis of heavy-ion collision data often depend strongly on the size of the interaction volume, which varies from event to event with the number of participant nucleons (N_{part}) or the impact parameter (b) of the collision. Both b and N_{part} are not directly measured by the experiments. Observables such as the charged track multiplicity N_{ch} or the number of hits in a detector N_{hits} are used as proxies to determine b and N_{part} . This is performed using simplified models such as the Glauber MC model. The selection of events based on collision centrality and interaction volume is often the first step in experimental analysis. We therefore begin with a detailed study of the Glauber MC model. The Glauber MC model is compared with the UrQMD cascade transport model, and the uncertainties introduced into experimental analyses by the use of Glauber MC-based event selection are studied.

The AI methods and the results presented in this chapter are based on [77–80, 125–127, 165, 218].

5.1 The Glauber MC model based event selection

The Glauber MC model is a simplified description of heavy-ion collisions based on the optical interpretation of the initial interpenetration phase. The Glauber MC treats the collision as a collection of instantaneous, independent inelastic binary scatterings of nucleons traveling on straight trajectories. In this model, the collision participants are determined solely from the transverse overlap of the nuclei, and both energy and baryon number deposition occur instantaneously along the beam axis. The model description and the results presented in this section are based on [126].

The Glauber Monte Carlo (MC) is a simple model that is often used to relate the experimentally measured N_{ch} to the b and N_{part} of the collision. At LHC or RHIC beam energies, the Glauber MC provides a reliable approximation of the initial state of a heavy-ion collision to characterize events based on collision centrality. However, at low and intermediate beam energies ($\sqrt{s_{NN}} \lesssim 5\text{-}10$ GeV), several assumptions of the model become questionable. At these energies, the dynamics of the nuclei during the interpenetration and compression phases are relevant to the modelling of the collision. Early hydrodynamic simulations even showed a complete disintegration of the spectator fragments due to the compression wave generated, even in peripheral collisions [7]. Recent studies with transport model simulations [219] as well as a hydro-hybrid model [220], show a strong interaction between the stopped and compressed system and the spectators, leading to the large directed flow observed at low beam energies (see e.g. [2, 221–224]). The Glauber MC model does not take this effect into account. Furthermore, the Glauber MC model neglects the elastic interactions between the nucleons when mapping N_{part} onto the measured particle spectra. For collision energies of $\sqrt{s_{NN}} \lesssim 3$ GeV, where the elementary nucleon-nucleon elastic cross section σ_{el}^{NN} and the nucleon-nucleon inelastic cross section σ_{inel}^{NN} are nearly equal, this assumption is no longer valid. Nucleons undergoing only elastic interactions during the

initial compression and subsequent expansion phases will have a significant contribution to the final state spectra. Despite these inconsistencies, the Glauber MC model is used to fit the experimental data using several parameters with little physical interpretation, which are then used to estimate the centrality, the interaction volume and its fluctuations. Therefore, at low collision energies, it is important to systematically test the Glauber MC model against transport models to which the experimental data are compared.

In particular, Au-Au collisions at 1.23 A GeV are analysed, as this data was recently collected by the HADES collaboration at the SIS-18 accelerator at GSI. The Glauber MC model is used by HADES to characterise event centrality [225]¹. In addition to HADES, the STAR collaboration at BNL's RHIC has recently measured Au-Au collisions at an intermediate energy of $\sqrt{s_{NN}} = 3$ GeV. It was shown that the strong model dependence of the volume fluctuations leads to large uncertainties in the analysis of higher order proton cumulants [106, 226]. In this context, the present study will be useful not only for HADES or STAR, but also for all future HIC experiments at intermediate energies, to understand the implications of a Glauber MC-based centrality selection for the analysis of data at intermediate collision energies.

5.1.1 Glauber MC based centrality selection in HADES

In order to study in detail the differences between Glauber MC and the fully dynamic UrQMD model, a Glauber MC based centrality selection is implemented for 1.23 AGeV Au-Au collisions at HADES .

Initialisation of the nuclei. In the Glauber MC model, sampling of the positions of the nucleons in both projectile and target nuclei is performed similarly to the UrQMD model, using a two-parameter Fermi (Wood-Saxon) distribution as the nuclear charge density function². The distribution is given by

$$\rho(r) = \frac{\rho_0}{1 + \exp\left(\frac{r-R}{a}\right)}, \quad (5.1)$$

where ρ_0 is the charge density at the center, R is the radius parameter and a is the diffuseness parameter. Following the values used in [225] for a gold nucleus, we set $\rho_0=1$, R=6.554 and a=0.523. The radial component (r) of the positions of the nucleons is sampled with probability

$$P(r) \propto r^2 \rho(r). \quad (5.2)$$

¹More precisely, the HADES centrality is based on the sum of the number of hits detected by the TOF and RPC detectors, which is not identical to the number of reconstructed charged tracks at mid-rapidity. However, it has been shown in the Glauber MC study [225] that both quantities are strongly correlated and both give the same results for the mean number of participants as well as the impact parameter, while using the number of hits gives a better resolution. For simplicity, we use only the number of charged tracks and assume that all our conclusions also apply to the centrality determination with the number of tracks in the TOF and RPC detectors.

²Note that both the Glauber MC and UrQMD models assume the same distribution for protons and neutrons and do not include 2-particle or short-range correlations inside the nucleus.

The azimuthal (ϕ) and polar (θ) components of the positions of the nucleons are sampled from uniform probability distributions. A sampled nucleon is re-sampled if there is already another nucleon within a distance of less than $d_{min} = 0.9$ fm. This is to prevent the nuclei from overlapping.

The impact parameters (b) of the collisions are taken from the probability distribution

$$P(b) \propto b db . \quad (5.3)$$

The sampled impact parameters are in the range 0 to b_{max} , where b_{max} is set to be greater than the sum of the radii of the projectile and target. The projectile and target nuclei are positioned such that the distance between their centre of masses in the transverse plane is the sampled impact parameter.

The collision process. The Glauber MC also treats the binary collision process via a geometric interpretation of the cross section. However, unlike UrQMD which uses the total cross section, Glauber MC only considers the inelastic cross section to define collisions. A nucleon pair is marked as participant if the transverse distance between them (d_{ij}) is less than their radii, defined by the nucleon-nucleon inelastic cross section.

$$i.e. \pi d_{ij}^2 \leq \sigma_{inel}^{NN} . \quad (5.4)$$

The value of σ_{inel}^{NN} is set to 23.8 mb based on [225]. In this way, all nucleons from either the projectile or the target that have undergone at least one inelastic collision are counted as "participant nucleons", regardless of how many collisions they would actually undergo in a transport model such as UrQMD. In figure 5.1, the N_{part} distributions for Au-Au collisions at 1.23 AGeV predicted by Glauber MC are compared with the distributions given by the UrQMD transport model. The top and middle panels show the Glauber MC results, while the bottom panel shows the UrQMD results. For any given impact parameter, the maximum N_{part} given by Glauber MC is smaller than the maximum N_{part} given by UrQMD. For very central collisions ($b < 3$ fm), the N_{part} distribution from Glauber MC has a large variance compared to UrQMD. However, for intermediate and peripheral collisions ($b > 3$ fm) the N_{part} distribution from UrQMD has a very large variance compared to the Glauber MC distribution.

As mentioned above, Glauber MC neglects the elastic interactions, while UrQMD considers both elastic and inelastic nucleon-nucleon interactions when modelling N_{part} . This assumption is only reasonable at high beam energies, where most of the newly produced particles contribute to the measured particle multiplicity and is not a valid assumption for the SIS-18 energies.

To study the effect of including elastic interactions in Glauber MC, we also used the total p-p cross section value from UrQMD (47.8 mb) at 1.23 AGeV as input to the Glauber MC collision criteria (eq. 5.4) instead of just the inelastic cross section. The resulting N_{part} distribution is shown in the middle panel of Fig. 5.1. It is found that the inclusion of elastic interactions increases the maximum N_{part} reached in very central collisions in the Glauber

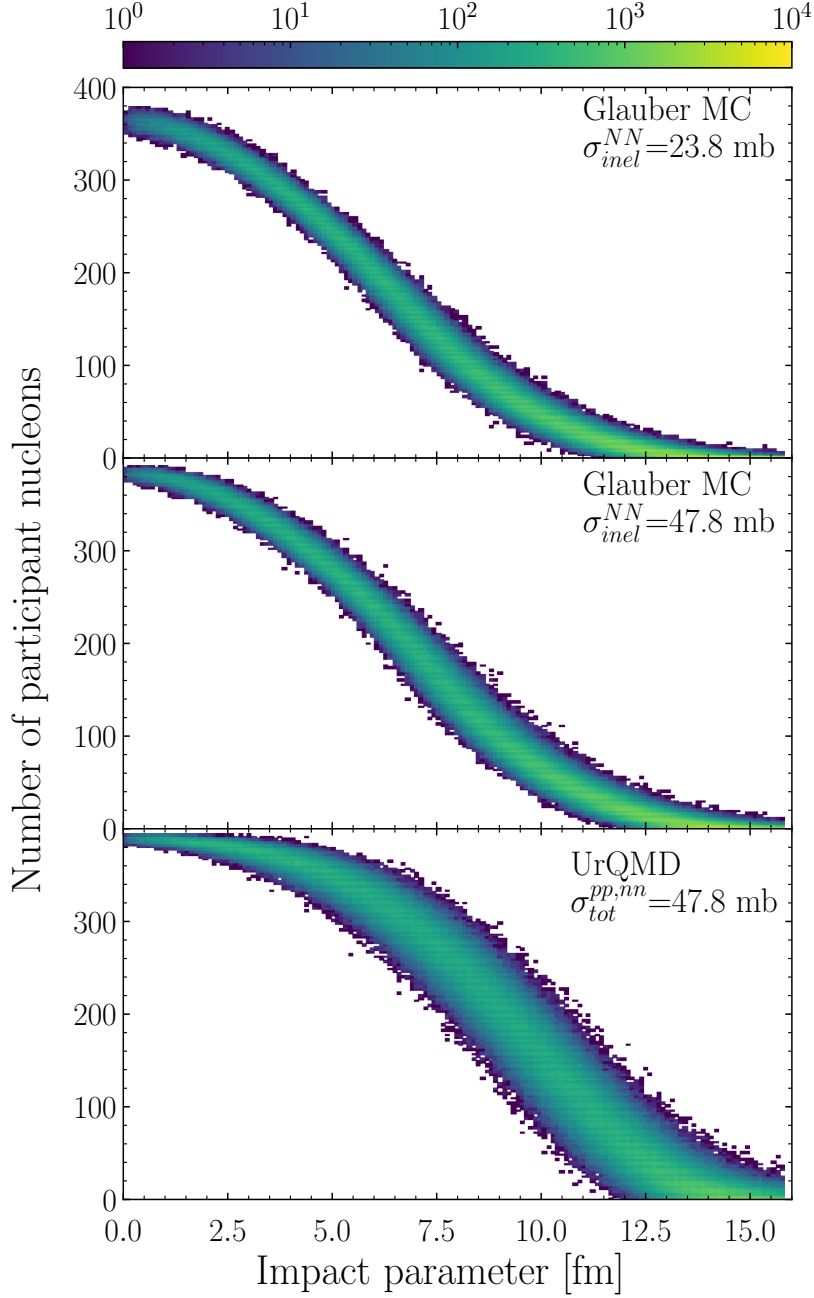


Figure 5.1: N_{part} vs b distributions. The top and middle panels show the results from the Glauber MC model with $\sigma_{inel}^{NN} = 23.8$ and 47.8 mb respectively, while the bottom panel shows the N_{part} distribution from UrQMD cascade simulations. The N_{part} distribution from Glauber MC when the total proton-proton or neutron-neutron cross section used by UrQMD (47.8 mb) at 1.23 AGeV is used as the input cross section to Glauber MC is shown in the middle panel. It can be seen that Glauber MC and UrQMD predict different distributions for N_{part} , even when elastic collisions are taken into account in Glauber MC. Each distribution is generated from 7.5×10^5 events.

MC model. The maximum N_{part} achieved by Glauber MC for any given collision parameter is now close to the UrQMD values. However, the overall width of the distribution has not changed and is still very different and much narrower than the UrQMD results.

Mapping N_{part} to observables. The next step in Glauber MC is to map the number N_{part} to experimental observables, usually the measured charged particle multiplicity N_{ch} . It is interesting to see how these differences in N_{part} manifest themselves when mapped to observables such as the charged track multiplicity. Experimental analyses typically map the Glauber MC generated N_{part} to the measured charged track multiplicity.

Based on the assumption of the "wounded nucleon" model that the $\langle N_{ch} \rangle$ is proportional to $\langle N_{part} \rangle$, the number of charged particles per participant (n) can be sampled from a Negative Binomial probability Distribution (NBD)

$$P(n) = \frac{\Gamma(n+k)(\mu/k)^n}{\Gamma(n+1)\Gamma(k)(\mu/(k+1))^{n+k}} . \quad (5.5)$$

where the values of μ and k are chosen so that the sampled N_{ch} distribution fits the experimental data. They are later used to sample the number of charged tracks produced by each participant nucleon in the event.

For a consistent comparison between the models, the UrQMD distribution is assumed to be the "measured" distribution and the Glauber MC generated N_{part} is mapped to the UrQMD distribution of charged tracks within the HADES acceptance, i.e., between 18-85° polar angle. The UrQMD data to which the Glauber model is fitted consists of 600,000 events, each with at least one inelastic collision. The result of the fit is shown in figure 5.2. The NBD parameters are fitted to minimise the deviation from the UrQMD "data" for both central and mid-central collisions (number of tracks >90). The Glauber MC fit shown in figure 5.2 used $\mu=0.4$ and $k=30$ for the NBD sampling. For central events, the Glauber MC fit agrees reasonably well with the UrQMD data, i.e. events with number of tracks >110. However, for extremely central events, the Glauber MC fit overestimates the number of events by an order of magnitude. The Glauber MC fit also underestimates the number of charged tracks for intermediate collisions ($25 < \text{number of tracks} < 110$) and overestimates it again for extremely peripheral collisions (number of tracks <10).

In practice, experiments often fold this multiplicity distribution with additional efficiency functions. These functions are said to take into account multiplicity dependent uncertainties and other non-linear effects in the data, which would usually result in an improved fit. However, introducing more parameters of little physical significance to improve the Glauber MC fit would only marginally change the volume fluctuations in the Glauber model. Therefore, such corrections are not implemented in the present work. The fit results simply indicate that a simplified Glauber MC model cannot provide as accurate a description of collisions as a dynamical model such as UrQMD.

For ease of reading, we will refer to the true UrQMD N_{ch} distribution within the HADES acceptance (figure 5.2, red curve) as "UrQMD- N_{ch} " and the Glauber fit to the UrQMD

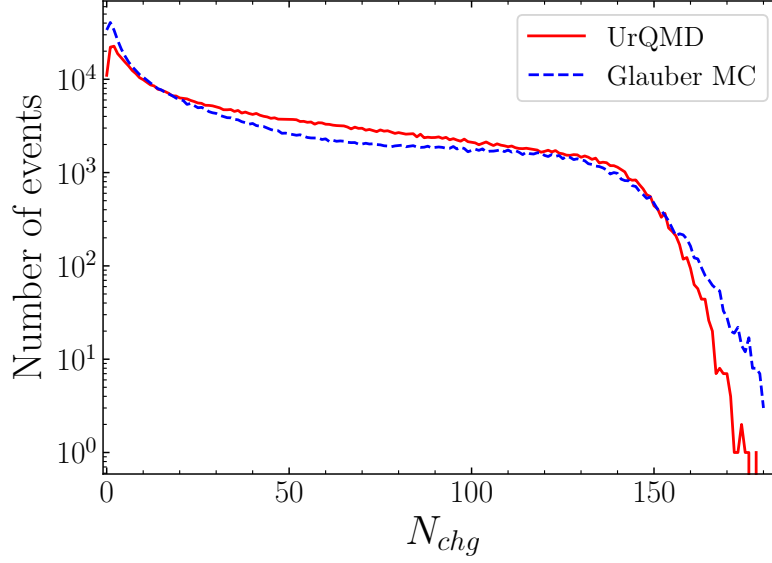


Figure 5.2: Glauber fit to UrQMD cascade data. The solid red curve is the UrQMD charged track multiplicity N_{ch} within the HADES acceptance angles (18- 85 °), for Au-Au collisions at 1.23 AGeV. The distribution is generated from 6×10^5 inelastic events. The dashed blue curve is the Glauber MC fit to the UrQMD data. The fit is generated from 6×10^5 inelastic events with $\mu= 0.4$ and $k= 30$ for eq. 5.5. The Glauber MC N_{ch} fits the UrQMD data reasonably well for central collisions $N_{ch} > 110$, but underestimates the number of events for intermediate collisions ($25 < N_{ch} < 110$) and overestimates it again for extremely peripheral collisions ($N_{ch} < 10$).

N_{ch} distribution within the HADES acceptance (figure 5.2, blue curve) as "Glauber- N_{ch} ".

Defining centrality classes. The final, important and potentially problematic step is to define centrality percentiles on the Glauber MC sampled N_{ch} distribution and then calculate the mean impact parameter and mean number of participants for a centrality class from this Glauber model.

The centrality C for events with $N_{ch} = n$ is defined as the fraction of the total cross section (σ_{tot}) given by

$$C = \frac{1}{\sigma_{tot}} \int_n^{N_{ch}^{max}} \frac{d\sigma}{dN_{ch}} dN_{ch} . \quad (5.6)$$

It follows that sharp cuts in N_{ch} , based on their percentile score, can be used to define centrality classes. For any given centrality class, the mean impact parameter $\langle b \rangle$ and the mean number of participants $\langle N_{part} \rangle$ can be calculated from the Glauber MC events. This definition of centrality based on cuts in N_{ch} is then applied to the experimental data to separate events based on collision centrality, and these values of $\langle b \rangle$ and $\langle N_{part} \rangle$ are then

used as the expected average impact parameter $\langle b \rangle$ and number of participants $\langle N_{part} \rangle$ for the centrality class. Thus, all events in the experimental data within a range of N_{chg} are grouped together and only the expected values of $\langle b \rangle$ and $\langle N_{part} \rangle$ are known for all events in the centrality class. This is a drastic difference to N-body models such as UrQMD, which can provide the impact parameter and the number of nucleons involved in collisions on an event-by-event basis.

In figure 5.3, centrality bins of 5%, defined as sharp cuts in two different N_{ch} distributions, are visualised. In the top panel, the centrality classes are defined using the Glauber MC fit to the UrQMD– N_{ch} distribution within the HADES detector acceptance (Glauber– N_{ch}), while in the bottom panel the centrality classes are defined directly on the UrQMD N_{ch} distribution within the HADES detector acceptance (UrQMD– N_{ch}). It can be seen that the class boundaries defined in the two cases are slightly different, as the Glauber MC fit to the UrQMD data is not perfect.

The collision centrality as defined by the two models, Glauber MC and UrQMD, can now be used to understand the model dependence of volume fluctuations. Furthermore, the Glauber MC predictions can be compared to the ground truth or "measured" distribution, which in our case is the UrQMD data to which Glauber MC is fitted. In this way, the biases introduced by the use of a Glauber based centrality selection in the experimental analyses can be investigated.

5.1.2 Glauber MC vs UrQMD: N_{part} and b distributions

The N_{ch} cuts shown in figure 5.3 can be used to compare the impact parameter b and N_{part} distributions in the UrQMD and in the Glauber MC for different centrality classes. This is shown in figures 5.4 and 5.5 where the following three cases are compared.

1. N_{part} and b are taken from Glauber MC for centrality classes defined with the Glauber N_{ch} distribution. These blue curves are referred to as "Glauber MC" in figures 5.4 and 5.5.
2. N_{part} and b are taken from UrQMD and the centrality classes are defined with the true UrQMD N_{ch} distribution. These red curves are referred to as "UrQMD" in figures 5.4 and 5.5.
3. N_{part} and b are taken from UrQMD, but for N_{ch} bins defined from the Glauber MC fit to the UrQMD distribution. These green curves are referred to as "Glauber, Ur- b " and "Glauber, Ur- N_{part} " in figures 5.4 and 5.5. They represent the underlying b and N_{part} distributions in the model that is fit to obtain the Glauber MC centrality classes.

The $\langle b \rangle$ and σ_b curves compared in figure 5.4 show that both Glauber MC and UrQMD give similar impact parameter distributions for any given centrality class when the impact parameter of an event is consistently taken from the same model as that used to define the centrality classes. However, the means of the impact parameter distributions

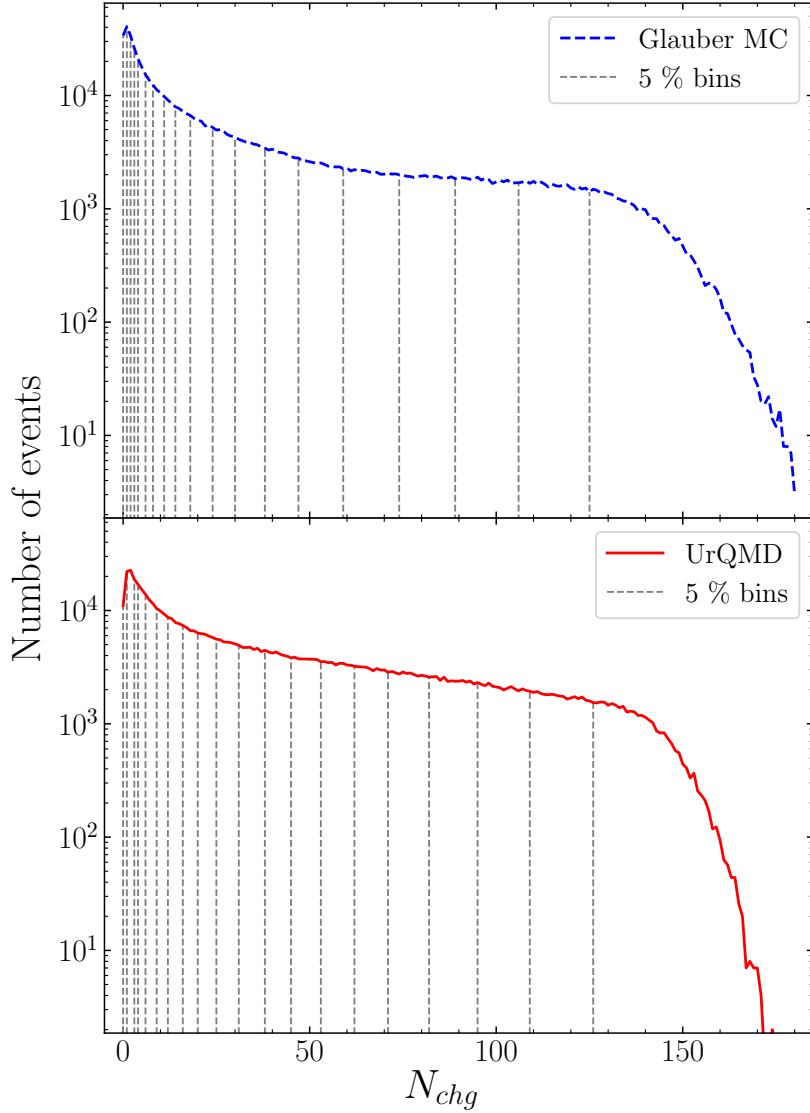


Figure 5.3: 5% Centrality bins. The centrality bins defined on the Glauber fit to the UrQMD– N_{ch} distribution (cascade) are shown in the top panel, while the centrality bins defined directly on the UrQMD– N_{ch} distribution are shown in the bottom panel. The vertical lines represent the bin boundaries. The Glauber fit strongly overestimates extremely peripheral and extremely central collisions and underestimates the intermediate collisions compared to UrQMD data. As a result the bin boundaries differ in the two cases.

extracted from UrQMD using centrality classes defined by the fitted Glauber– N_{ch} distribution (dashed green curve) differ from the true impact parameter values from UrQMD (solid red curve). This is because the Glauber MC fit to the UrQMD multiplicity distribution had large deviations, especially for intermediate and peripheral collisions, and as

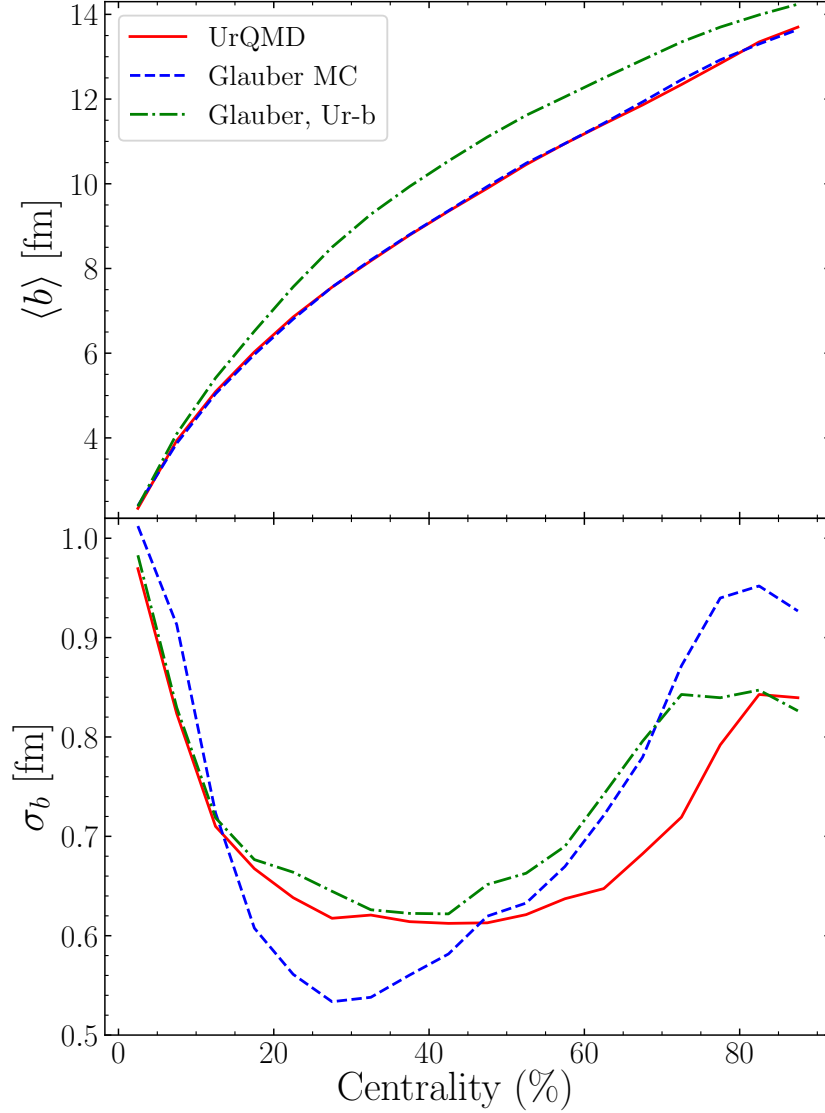


Figure 5.4: Mean and standard deviation of the impact parameter distributions. The top panel shows the mean ($\langle b \rangle$) and the bottom panel the standard deviation (σ_b) of the impact parameter distributions for different centrality classes. The dashed blue curve shows the $\langle b \rangle$ and σ_b from the Glauber MC fit for centrality classes defined on the Glauber N_{ch} distribution. The $\langle b \rangle$ and σ_b defined on the UrQMD– N_{ch} distribution are shown as the solid red curve. The dot-dashed green curve (Glauber, Ur-b) is the $\langle b \rangle$ and σ_b taken from UrQMD for centrality bins defined from the Glauber MC fit N_{ch} distribution.

a result the N_{ch} cuts defining any given centrality class in the Glauber– N_{ch} distribution would differ from the cuts defined directly on the UrQMD– N_{ch} distribution. The standard deviation of the impact parameter distributions for all centralities looks similar in all three

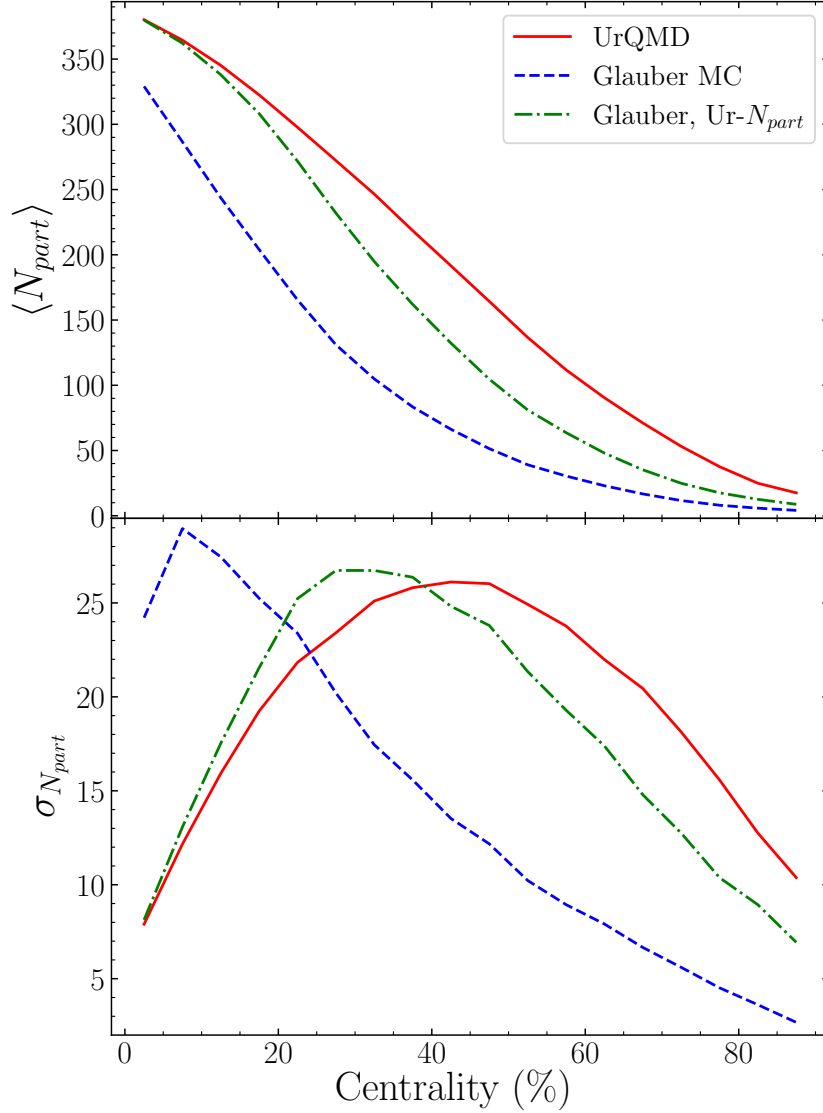


Figure 5.5: Mean and standard deviation of the number of participants distribution. The top panel shows the mean ($\langle N_{part} \rangle$) of the distributions of the number of participants, while the bottom panel shows the standard deviation ($\sigma_{N_{part}}$) of the distributions of the number of participants. The dashed blue line shows the $\langle N_{part} \rangle$ and $\sigma_{N_{part}}$ from Glauber MC for centrality classes defined on the Glauber- N_{ch} distribution. The $\langle N_{part} \rangle$ and $\sigma_{N_{part}}$ from UrQMD for centrality classes defined on the UrQMD- N_{ch} distribution is shown as the solid red curve. The dot-dashed green curve (Glauber, Ur- N_{part}) shows the $\langle N_{part} \rangle$ and $\sigma_{N_{part}}$ from UrQMD for centrality classes defined on the Glauber- N_{ch} distribution.

cases. For any given centrality class, there is only a difference of about 0.1 fm between the three scenarios.

However, as shown in figure 5.5, the results for the three scenarios differ drastically when it comes to the N_{part} distributions. For all centrality classes, there is a huge difference in the number of participants between the Glauber MC and UrQMD models, even when the centrality classes are defined consistently using the corresponding model data. There is a difference of up to a factor of ≈ 2 between the $\langle N_{part} \rangle$ from Glauber MC for centrality classes defined on the Glauber- N_{ch} distribution and the $\langle N_{part} \rangle$ from UrQMD for centrality classes defined on the UrQMD- N_{ch} distribution. A significant difference is also observed between the Glauber MC and UrQMD N_{part} distributions when centrality classes defined using the Glauber MC- N_{ch} are used. The centrality dependence of the variance of the N_{part} distributions also differs drastically between these three cases. The Glauber MC N_{part} distributions have the largest standard deviation $\sigma_{N_{part}}$ of about 30, for most central collisions (about 0-10 %) as defined by the Glauber N_{ch} distribution. On the other hand, the UrQMD N_{part} distributions have their lowest variance for the most central collisions (as defined by the UrQMD- N_{ch} distribution), with a difference of a factor of ≈ 2 . The UrQMD N_{part} distributions have the largest variance for mid-central collisions (about 40-45 %).

The differences between the N_{part} distributions for the two models suggest that N_{part} (and its fluctuations) are strongly model dependent, at least for beam energies $\sqrt{s_{NN}} \lesssim 5$ -10 GeV. Different models can produce similar N_{ch} distributions even if the underlying N_{part} distributions are completely different. The drastic differences in the N_{part} distributions given by the two models are well illustrated in figure 5.6, where the N_{part} distributions of Glauber MC and UrQMD are plotted for 0-10 % (top panel) and 0-40 % (bottom panel) centrality classes. For the 0-10 % centrality class, the N_{part} distribution from UrQMD for centrality classes defined on the UrQMD- N_{ch} distribution peaks at about 380, while the N_{part} distribution from Glauber MC for centrality classes defined on the Glauber- N_{ch} distribution does not show a clear maximum at all. The Glauber MC N_{part} distribution has a huge variance and contains events with very small N_{part} even for the 0-10 % centrality class. For the 0-40 % centrality class, the UrQMD N_{part} distribution peaks at about 385, while the Glauber N_{part} distribution peaks at about 100. This is about a factor of 4 lower than the UrQMD value! When centrality classes defined on the Glauber N_{ch} distribution are applied to the UrQMD data to select events, the resulting N_{part} distributions are close to the UrQMD N_{part} distributions for centrality classes defined on the UrQMD- N_{ch} distribution. This important finding has strong implications for the volume fluctuations and their correlations, and is relevant for the extraction of proton fluctuations for the HADES experiment and also in the STAR-BES energy range. This is a direct consequence of secondary particle scattering and the contribution of elastic scattering to the finally observed protons.

5.1.3 Pion production at 1.23 AGeV

Having established the strong model dependence of the volume fluctuations at beam energies $\sqrt{s_{NN}} \lesssim 5$ -10 GeV, it is worth investigating how this might affect the experimental analyses. HADES has recently published the centrality dependence of charged pion pro-

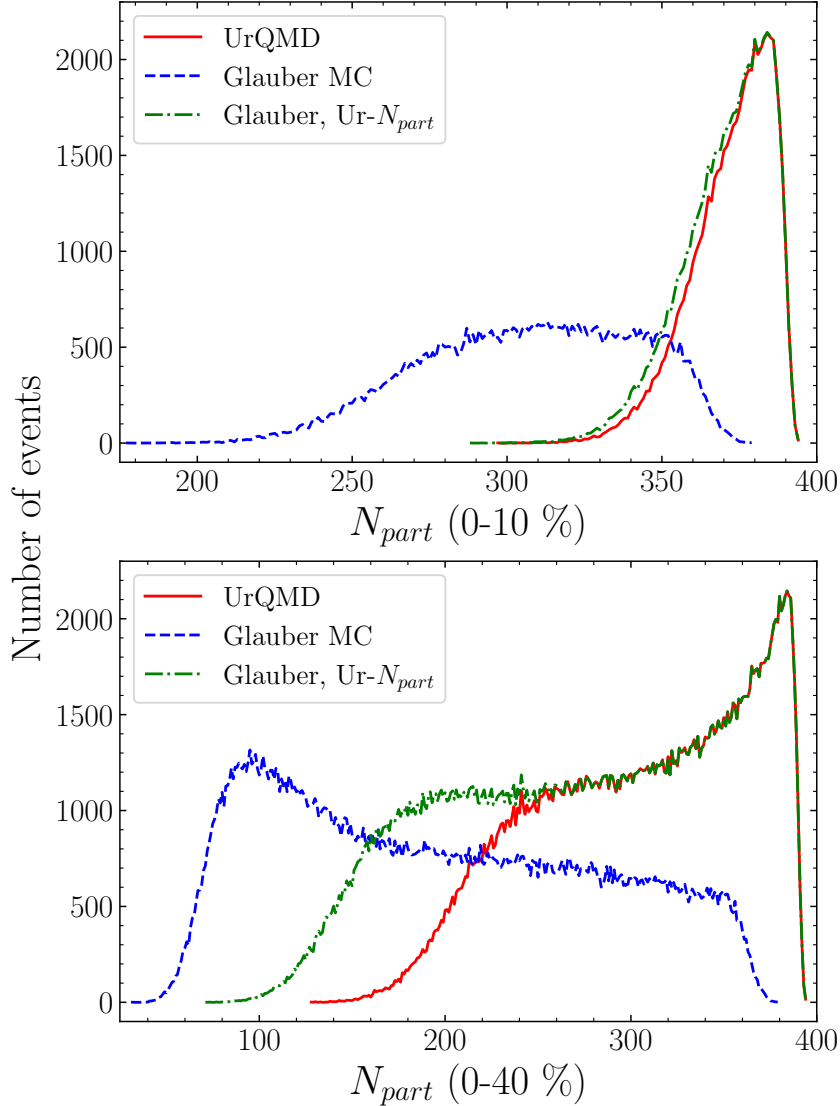


Figure 5.6: N_{part} distributions for 0-10% (top panel) and 0-40 % (bottom panel) centrality classes. The N_{part} distribution from Glauber MC for centrality classes defined on the Glauber- N_{ch} distribution is shown as the dashed blue curve, while the N_{part} distribution from UrQMD for centrality classes defined on the UrQMD- N_{ch} distribution is shown as the solid red curve. The dot-dashed green curve (Glauber, Ur- N_{part}) shows the N_{part} from UrQMD for centrality classes defined on the Glauber- N_{ch} distribution.

duction measured at a beam energy of 1.23 AGeV and the comparison with transport model simulations [227]. It was found that the measured pion yields were significantly lower than the predictions of several theoretical models such as GiBUU, SMASH, PHSD, IQMD and PHQMD. Apart from the introduction of explicit density dependent production

cross sections, few ideas have been put forward to explain this discrepancy [228].

In this section, the charged pion production in 1.23 AGeV Au-Au collisions is investigated within the framework of UrQMD cascade and the results are presented. The centrality and the N_{part} dependence of the pion yields are reported for different methods used to determine them, and the results are compared with the HADES measurements.

In figure 5.7 the charged pion multiplicity per participant predicted by UrQMD is plotted as a function of $\langle N_{part} \rangle$ for different centrality selection methods. The values for $\langle N_{part} \rangle$ and $\langle \pi \rangle$ used in figure 5.7 are from 10% centrality bins for the different models. The last 4 points in all curves and HADES data in figure 5.7 therefore correspond to results from centrality bins 30-40%, 20-30%, 10-20%, 0-10% respectively. It is clear that since different models predict different N_{part} distributions for any given centrality class, the results vary drastically depending on our choice of model for centrality selection and $\langle N_{part} \rangle$ estimation. When the Glauber MC model is used for both centrality selection and $\langle N_{part} \rangle$ estimation, the resulting pion multiplicity per participant from UrQMD is larger than the HADES measurements for any given centrality (blue curve). However, when the UrQMD model is used both to select the centrality and to estimate the $\langle N_{part} \rangle$, the resulting pion multiplicity per participant from UrQMD is smaller than the HADES measurements for mid-central and peripheral collisions (red curve) and larger than the HADES data for the most central collisions (0-10 %). There is a large difference in $\langle N_{part} \rangle$ for each of these centrality classes for the two models, making $\langle N_{part} \rangle$ an unreliable quantity for comparing experimental observations such as particle yields with model predictions.

Due to the ambiguities associated with $\langle N_{part} \rangle$, it is not advisable to examine the pion multiplicity as a function of $\langle N_{part} \rangle$. Instead, the multiplicities can be studied as a function of the centrality, which is consistently defined by a percentile of N_{ch} from either a Glauber MC fit or directly from the model simulation. The charged pion multiplicities from UrQMD are plotted as a function of centrality in figure 5.8. In the figure, the UrQMD results for centrality classes defined from the UrQMD- N_{ch} distribution are plotted in red ("UrQMD bins"), while the UrQMD results for the Glauber- N_{ch} based centrality selection are plotted in blue ("Glauber bins"). If the Glauber MC fit to the UrQMD- N_{ch} distribution was perfect, both the "Glauber bins" and "UrQMD bins" curves would have looked identical. It can be seen that UrQMD predicts significantly larger pion multiplicities for all centrality classes than what is measured by HADES in this case. The results are similar to the predictions of other theoretical models, as shown in [227].

The main source of uncertainty when comparing experimental observations with theoretical models is the assumption that events with similar centrality have similar underlying N_{part} distributions. However, for any given centrality class, the underlying N_{part} distribution or volume fluctuations depend strongly on the model used. For example, the N_{part} distribution given by the Glauber MC model for any given centrality class can be completely different from the N_{part} distribution given by UrQMD, even though the Glauber MC was fitted to the UrQMD- N_{ch} distribution. It may be possible to fit the Glauber MC model to an experimental or theoretical N_{ch} distribution. However, this does not guarantee that the

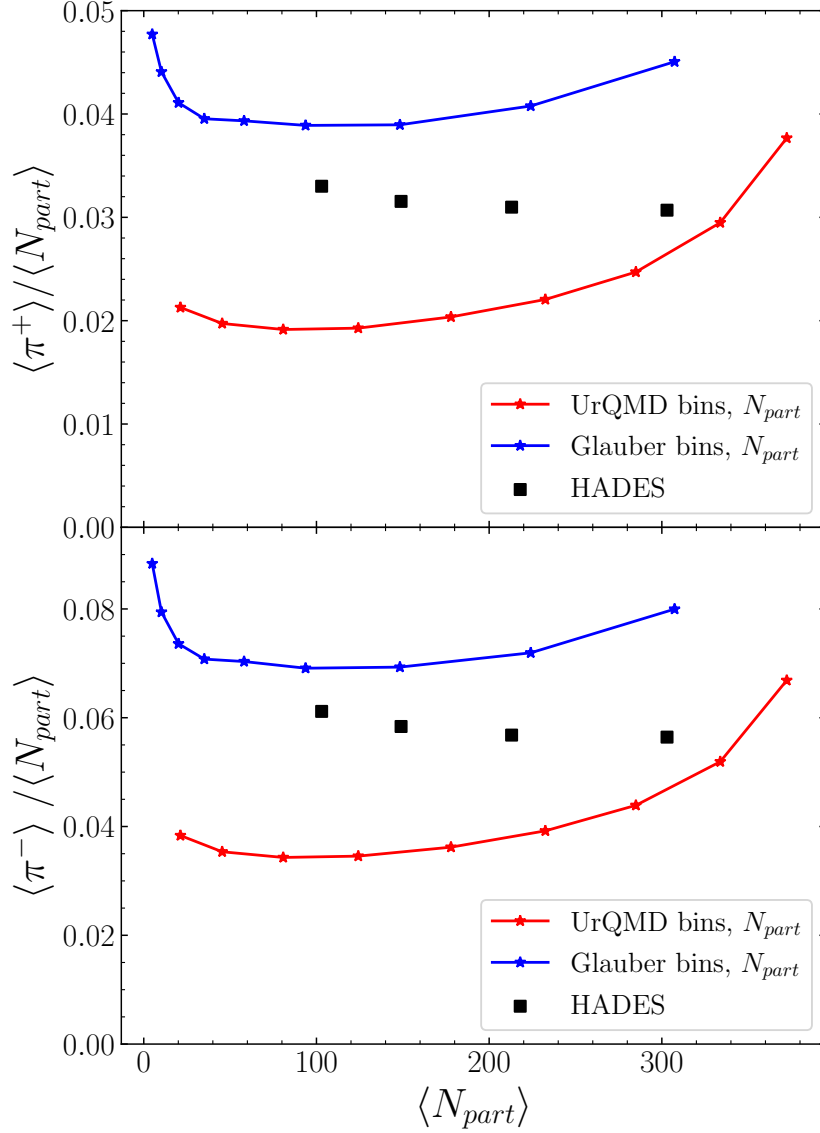


Figure 5.7: Charged pion multiplicity per participant from UrQMD cascade simulations as a function of N_{part} . The red curve (UrQMD bins, N_{part}) shows the results for centrality classes defined on UrQMD data with N_{part} also taken from UrQMD. The pion multiplicity from UrQMD for centrality bins and the number of participants defined by Glauber MC are shown in blue (Glauber bins, N_{part}). The HADES results [227] are shown as black squares. The large difference between the blue and red curves arises from the strong model dependency of N_{part} .

N_{part} distribution extracted from a Glauber MC for a centrality class and the true N_{part} distribution are similar. To demonstrate the uncertainty this introduces into the analysis, the events are now sampled so that the N_{part} distribution is similar to that predicted by

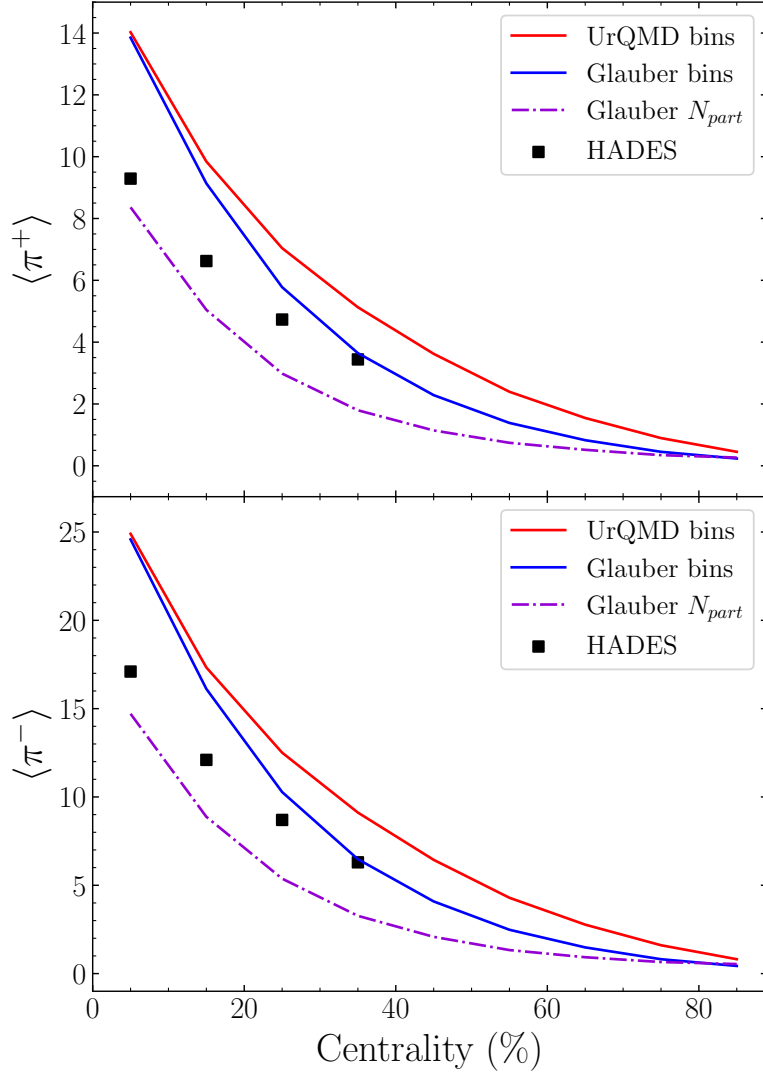


Figure 5.8: Charged pion multiplicity as a function of centrality. The plots show the $\langle \pi^+ \rangle$ and $\langle \pi^- \rangle$ multiplicities from UrQMD cascade and HADES. The results from UrQMD for Glauber- N_{ch} based centrality selections are shown as the blue curve, while the results from UrQMD for UrQMD- N_{ch} based centrality selections are shown as the red curve. The black squares are the HADES measurements [227]. The dot-dashed violet curve shows the pion multiplicities from UrQMD when the events are sampled to have N_{part} distribution similar to the Glauber MC predictions for any given centrality class. Unlike N_{part} , "centrality" is less model dependent quantity for model to data comparison of observables such as pion multiplicities although this does not assure that the Glauber MC correctly predicts the underlying N_{part} distribution of a centrality class (as evidenced by the difference between red and violet curves).

the Glauber MC for any given centrality class. The results are shown as the dot-dashed violet curves in figure 5.8. It can be seen that the predicted pion multiplicities are now lower than the HADES data, in contrast to the UrQMD– N_{ch} based event selection which predicted more pions than the HADES observations. The strong centrality dependence in the deviation from the HADES data is also reduced in this case. This shows that if the assumption of the underlying N_{part} distribution is incorrect, or at least not fully consistent, this can lead to large uncertainties in the predicted pion multiplicities. When the model predictions are compared with the measured data, this could then lead to incorrect or inconsistent conclusions.

Influence of elementary cross sections

The Glauber MC and UrQMD differ in their treatment of collisions and this definitely leads to discrepancies in the number of participant nucleons for the two models. In addition, significant model uncertainties also arise from the treatment of elementary cross sections at SIS-18 energies. It may be the case that experimental data for some reaction channels are not available or that the experimental data contain large uncertainties. These would then lead to large uncertainties in the calculated yields for the particle species involved. To study the systematic uncertainties arising from the choice of these cross section values, we consider two different cases in UrQMD for p-n cross sections, where the cross sections are assumed to be known for all but one reaction channel:

Case A: The $p+n \rightarrow p+n^*$ cross section is considered unknown. The cross section for this channel is chosen so that the total collision cross section matches the measured values.

Case B: The total elastic cross section ($p+n \rightarrow p+n$) is considered unknown. The cross sections for all other reaction channels including $p+n \rightarrow p+n^*$ are considered known and fixed. The cross section for this channel is chosen so that the total collision cross section matches the measured values.

The pion yields for different elementary collisions at 1.23 AGeV for the two cases above are tabulated in table 5.1. A significant difference in the charged pion multiplicities is observed between the two different cases. The difference is mainly due to the p+n collisions and case A produces about 15% more charged pions per participant than case B. This very high uncertainty in the treatment of the elementary cross sections can therefore also lead to very significant effects on the final state multiplicities at SIS 18 energies.

5.1.4 Protons and light nuclei at 1.23 AGeV

The unreliability of N_{part} due to its model dependence and its consequences for experimental analyses at SIS-18 beam energies have been established in the previous section. Nevertheless, at these beam energies, experiments may indeed be able to use the measurements to check the consistency of the underlying N_{part} . The total baryon number in the

Table 5.1: Pion yields for elementary collisions at 1.23 AGeV. The second part of the table shows the average π^+, π^- yields over different collisions (p+n, p+p, n+n, n+p), total π and π^{chg}/N_{part} , for the two cases.

Case	Collision	π^+	π^-	N_{inel}/N_{tot}
A	p+n	0.262	0.259	0.429
B	p+n	0.174	0.173	0.356
A	p+p	0.814	0.011	0.569
B	p+p	0.809	0.001	0.601
A	n+n	0.012	0.828	0.547
B	n+n	0.003	0.812	0.604
	π_{avg}^+	π_{avg}^-	π_{chg}/N_{part}	π_{tot}
A	0.337	0.339	0.338	1.090
B	0.290	0.290	0.290	1.010

system is conserved and at these energies, rarely any baryon-antibaryon pairs are produced. Therefore, by measuring the protons and light nuclei, the number of baryons involved could be measured directly. Since the current experiments, which measure only charged particles cannot detect the free neutrons N_n , the experiments can ultimately measure the $N_{part} - N_n$.

Both the HADES and STAR experiments have published the data (albeit preliminary) on the rapidity distribution of the free protons and baryons in light nuclei. These can be compared with our UrQMD simulations, which have been extended to include a coalescence mechanism to describe the production of light nuclei [229]. The comparison between the UrQMD simulations and the experimental data for the 0 – 10% most central ($b < 4.7$ fm) collisions is shown in figure 5.9. The left panel shows the comparison to STAR measurements at $E_{lab} = 3$ AGeV, while the right panel is the comparison to HADES measurements at $E_{lab} = 1.23$ AGeV. It is clear that the light nuclei make a significant contribution to the total baryon number. It can also be seen that the UrQMD model gives a very good description of all the STAR rapidity distributions, except at rapidities close to the fragmentation region. The sum of all measured baryons in this case is $N_{part} - N_n \approx 220$. The HADES data, on the other hand, show a clear suppression of proton and deuteron rapidity spectra compared to the model simulation, and the $N_{part} - N_n$ in this case is ≈ 190 . Adding the number of neutrons, the total N_{part} in HADES is surprisingly in agreement with the number of participants in the Glauber model. However, the total N_{part} given by UrQMD for both cases is consistent with the UrQMD N_{part} discussed earlier. In the case of HADES, the significant reduction in N_{part} is also consistent with the significant reduction in the measured proton dN/dy compared to UrQMD. Interestingly, such an effect is not seen in the STAR data, and the measurements are consistent with UrQMD predictions.

There are several possible reasons for this observed discrepancy between experiments and between experiments and simulations. It could be that some of the protons are not detected due to the different acceptance of STAR and HADES, or that there is a systematic

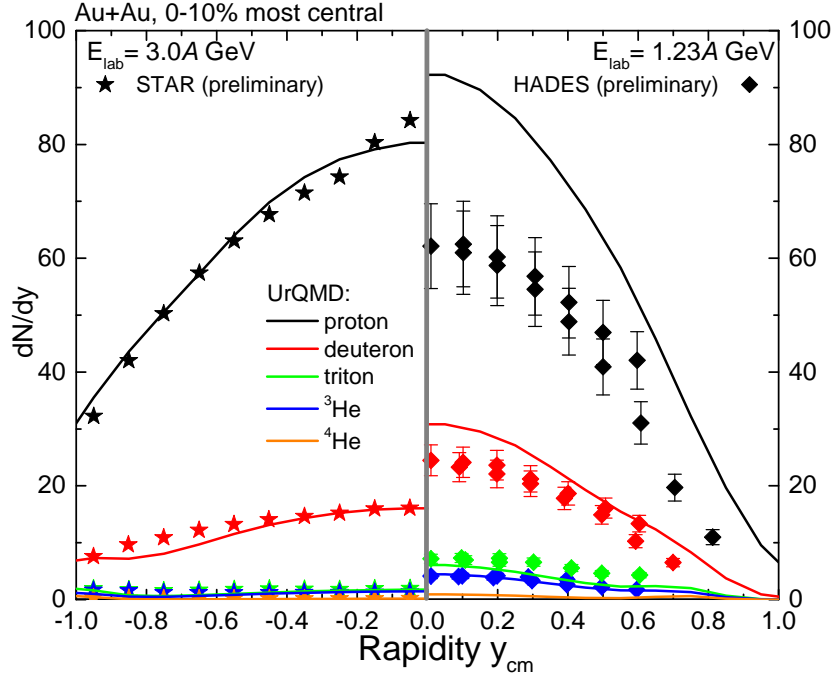


Figure 5.9: Rapidity distributions of free protons and light nuclei in the most central collisions of Au-Au nuclei at $E_{lab} = 1.23$ and 3 A GeV. The simulations are from the UrQMD cascade model plus coalescence and are shown as solid lines. The simulations are compared with the preliminary data from the two respective experiments STAR [230] (left, stars) and HADES [231, 232] (right, diamonds), shown as symbols. The beam rapidity in this frame for STAR is $y_{beam} \approx 1.05$ and for HADES is $y_{beam} \approx 0.75$. The simulations reproduce the STAR data well. However, the HADES data show significantly fewer protons and light nuclei at all rapidities. The sum of all participating baryons minus the free neutrons is ≈ 220 for both cases in UrQMD, while for HADES it is ≈ 190 .

incompatibility in the centrality determination of either experiment. It could also be due to a large change in the underlying physics modelled by the transport description. Understanding these inconsistencies is also important for the interpretation of observables such as pion multiplicity and proton number fluctuations. A possible solution to this problem is to measure N_{part} explicitly in experiments, using detectors such as a zero degree calorimeter, and then compare the model results for events with the same N_{part} distribution. It would also be interesting to investigate whether N_{part} can be accurately extracted from models such as UrQMD using artificial intelligence techniques.

5.2 PointNet based event characterisation in experiments

We will first use the PointNet architecture to develop DL models that can characterise collision events in experiments. We have already seen how event selection based on simplified

models fail to accurately model the underlying N_{part} and how this in turn leads to large uncertainties in the results of physics analyses. The method used for event selection or characterisation should be consistent with the theoretical model to which the observables of the selected data are compared. Moreover, an accurate determination of the initial volume of the system is very important for the analysis of fluctuations [233, 234] and correlations, and thus for the search for observables sensitive to a possible phase transition or critical point. This requires novel methods that can accurately characterise events based on collision centrality or interaction volume. In future experiments such as CBM, a method that can quickly determine the centrality of an event, before any information about the particles produced is known, would be very important for a first step in event selection. Such fast, accurate analysis methods that can be applied directly to detector data would be a first step towards overcoming the challenges associated with the extremely high event rates of the CBM experiment. The results presented in this section are based on [77, 78, 80, 218].

5.2.1 Impact parameter determination in the CBM experiment

The impact parameter is an essential quantity for understanding the event geometry and analysing the collected data. Although most theoretical calculations require the impact parameter as an input, it is not directly measurable in experiments. Typically, final state observables such as the mid-rapidity charged particle multiplicity and the number and energy of the spectator fragments are used to determine the centrality of a collision, from which the impact parameter is then estimated. For the CBM experiment, this was done using a Monte Carlo Glauber (MC-Glauber) model. These estimators are then used to group events into different centrality classes based on the centrality percentile [235]. Note that the Glauber MC cannot determine the impact parameter or number of participants of an individual event, but only provides the likely distribution of impact parameters within a given centrality class.

While conventional methods of centrality determination, based on connecting the number of charged tracks in an event with its centrality [235], can be useful for a broad grouping of events, they lack the ability to perform accurate impact parameter determination of individual events. This is illustrated in figure 5.10, where the track multiplicity of the charged particles is plotted as a function of the impact parameter. For a given track multiplicity there is a wide range of possible impact parameters. This spread in track multiplicity is greatest for the most interesting central events. Similarly, for the most peripheral events, a given track multiplicity could correspond to a wide range of impact parameters. Accurate determination of impact parameters on an event-by-event basis is therefore not a trivial task that can be accomplished on the basis of a single variable such as track multiplicity. It requires modelling of other known and unknown correlations in the experimental data to the impact parameter. Furthermore, next generation experiments such as CBM require online event analysis methods, which is only possible with minimal pre-processing of the raw experimental data. This makes PointNet based DL models an efficient candidate for event-by-event impact parameter determination in CBM.

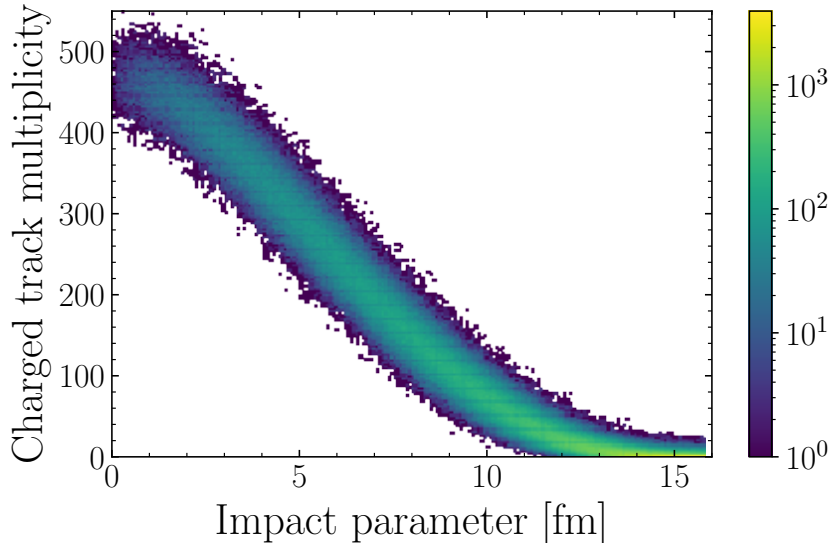


Figure 5.10: Histogram of the charged particle track multiplicity as a function of impact parameter. The distribution is generated using the 10^6 minimum bias Au-Au collision events at 10 AGeV generated using UrQMD cascade model+ CbmRoot [236] detector simulation. Conventional methods for event selection based on charged track multiplicity can only perform a broad grouping of events, as there exists a wide range of impact parameters for any given track multiplicity.

Machine learning approaches have previously been proposed as a method for determining impact parameters in heavy-ion collisions. Feed-forward networks used with event generator output have been shown to outperform conventional methods in [237–239]. Other studies [240–242] have used neural networks or conventional machine learning methods to determine the impact parameter in real experimental data. However, these studies used shallow neural networks or traditional machine learning models trained directly on the output of event generators such as the Quantum Molecular Dynamics (QMD), Isospin Quantum Molecular Dynamics (IQMD), Classical Molecular Dynamics (CMD) or UrQMD model [40, 44, 243–246]. Experimental constraints were only taken into account by simple filters based on detector acceptance or event selection criteria. Such simplifications do not take into account the uncertainties in the data introduced by detector efficiency or resolution and do not reflect the real output of a detector setup. The observables used in the previous studies are only available after several stages of processing, such as track reconstruction, particle identification and efficiency corrections. Although models based on these inputs are easier to interpret, their main shortcoming is that any bias or constraints in the processing algorithms would also add to the uncertainty of the predictions. Furthermore, in order to judge the computational efficiency of such models, they need to be used in a more realistic setup that closely mimics the actual data processing in the corresponding experiment.

Finally, an important motivation for using PointNet with direct detector output information is the flexibility of the networks output. If the analysis of the impact parameter can be done within such a model, the desired observable could easily be replaced by other possible observables of interest and event properties such as collective flow or the appearance of exotic particles.

Preparing training and testing data

The microscopic relativistic N-body hadron transport model UrQMD 3.4 (cascade) is chosen as the event generator for the present study. These generated UrQMD events then serve as input to the subsequent CbmRoot [236] detector simulation framework, which performs event-by-event transport of all particles of each event through the detector subsystems. The standard macros in CbmRoot are used to perform particle transport, detector response and event reconstruction. The default detector geometry for the electron-hadron configuration (sis100_electron) is simulated using the Geant3 software [247]. Since UrQMD does not include weak or electromagnetic decays of the produced hadrons, these are performed within the Geant3 package. The present analysis includes only those particles that produce hits in the two main silicon detectors (STS and MVD).³

With the current simulation setup, four different datasets, labelled *Train* and *Test1-Test3*, of Au+Au collisions at 10 AGeV are generated for this study. The DL models were trained using the dataset *Train*, which contains 10^5 events with impact parameters ranging from 0 to 16 fm, sampled from a uniform b distribution. The datasets *Test1*, *Test2* and *Test3* were used to quantify the performance of the trained models. The first testing set *Test1* contains 18 subsets, each comprising 500 events with a different but fixed impact parameter ranging from 0 to 16 fm. The datasets *Test2* and *Test3* contain 10^6 and 10^5 events respectively with impact parameters sampled from a bdb distribution (i.e. the probability of an impact parameter b is proportional to b , from 0 to 16 fm). Thus, *Test2* and *Test3* contain impact parameter distributions that are different from the training set, which is important for meaningful validation of the models. In addition, *Test3* uses a modified physics scenario, which will be explained later.

The features of all the datasets are presented in the table 5.2.

Models

In this study, we have developed four PointNet based models that learn from different types of detector output, such as hits and tracks of particles, as features to determine the impact parameter of each collision. A point in the point cloud is therefore defined by the attributes of a hit or a track. In this study, the models were trained using 75% of the events in the dataset *Train* with the MSE as the loss function. The remaining 25% of events were

³Although the CbmRoot can perform the full detector simulation according to the experimental specifications, it does not include a realistic simulation of different backgrounds, which may lead to additional noise. However, for the sake of simplicity, this is not considered in this study.

5.2. POINTNET BASED EVENT CHARACTERISATION IN EXPERIMENTS

Dataset	# events	impact parameter [fm]	impact parameter distribution
<i>Train</i>	10^5	0-16	uniform
<i>Test1</i>	18×500	0.5 - 16	constant
<i>Test2</i>	10^6	0-16	<i>bdb</i>
<i>Test3</i>	10^5	0-16	<i>bdb</i>

Table 5.2: Datasets used in the study. The last column defines the impact parameter distribution of the events. The training dataset has a uniform impact parameter distribution, while a constant or *bdb* distribution is used in the testing datasets.

used for validation. Other metrics such as MAE and coefficient of determination (R^2) were used to select the best model for further analysis. If y_{true} , y_{pred} and $\langle y_{true} \rangle$ are the true impact parameter, the DL predictions and the mean of the true values respectively, the coefficient of determination is calculated as

$$R^2 = 1 - \frac{\sum (y_{true} - y_{pred})^2}{\sum (y_{true} - \langle y_{true} \rangle)^2 + \epsilon} \quad (5.7)$$

where the second term is the fraction of the variance unexplained by the predictions and ϵ is a small positive number to prevent division by zero. The sums run over all validation events.

The training of the models requires the tuning of several hyperparameters to achieve the best performance. We started with network structures similar to the original PointNet implementation and then tuned different hyperparameters using a trial and error method until optimal performance, as defined by MSE, MAE and R^2 , was observed.

All models in this study used ReLU activation units and the Adam optimiser (learning rate = 0.00001). The convolution layers were always followed by batch normalisation layers. The convolution operations (1-D) used kernels of size 1 to ensure that the local features of individual points were separately segregated. Dropout layers with a dropout probability of 0.5 were used after each dense layer in the models to control overfitting. The models use a common structure for input and feature transformation networks (I_{trans} and F_{trans}) as shown in figure 5.11. When used for input transformation, the network has input dimensions $N \times F$, where N is the maximum number of hits or tracks (depending on the model) in the data and F is the number of input attributes per point. For the feature transformation network, the input dimensions are $N \times K$, where K is the number of feature maps produced by the previous convolution layer. The input passes through a series of convolution and batch normalisation layers to perform order-independent feature extraction before aggregating global features using an average pooling layer. The global features are then regressed using a deep neural network to output F^2 (or K^2) numbers, which act as transformation matrices. The overall structure of the models is also similar to the alignment networks. The features extracted after the input and feature transformations

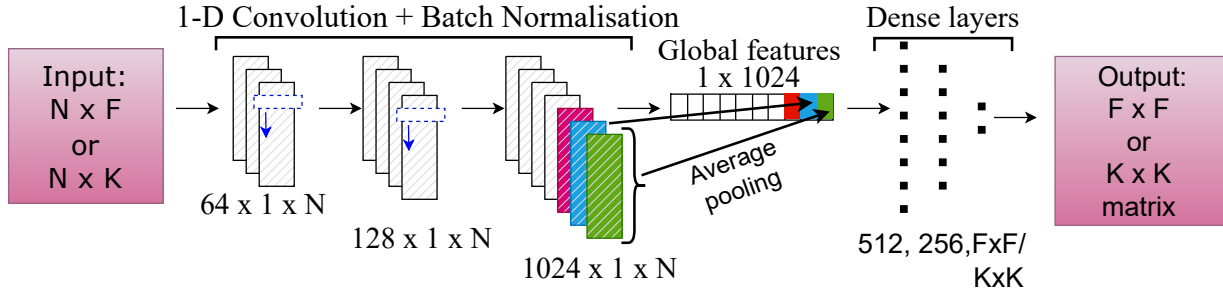


Figure 5.11: General structure of the joint alignment networks. This network is used as the input and feature transformation networks in all models. All convolution layers are followed by batch normalisation layers. The convolution kernels (blue rectangles) have a size of 1. When used as an input transformation network, the input has dimensions $N \times F$, where N is the maximum number of hits or tracks expected in an event and F is the number of input attributes of each hit or track (for example: $F=3$ if the model uses the x, y, z coordinates of all hits as an input feature). The alignment network then learns an $F \times F$ matrix. Similarly, if the network is used as a feature transformation network, the input has dimensions $N \times K$, where K is the number of feature maps produced by the convolution layer preceding the feature transformation network.

also use an average pooling layer to collect global features and then finally find the impact parameter from these features using a DNN.

The models developed in this study, their network architecture and hyperparameters are briefly described below.

Model-1 (M-hits): This model (*M-hits*) uses the x, y, z position of the hits of particles in the MVD detector as input attributes. Since our inputs are merely hits in the detector planes, this model can perform the impact parameter determination prior to track finding and fitting. Since the PointNet architecture requires a fixed input size, the event with the maximum number of hits ($N_{max} = 1995$) in the training dataset is used as a reference to set the input dimensions ($N \times F$) to 1995×3 . Any event with a smaller number of hits will have the remaining rows filled with zero. When the maximum number of hits in the test datasets exceeded 1995, hits were randomly dropped to fit the input dimensions. Note that in principle the input size could be extended to include the exponential tail of the N_{charge} distribution, but this would also increase the computation time.

The model architecture of *M-hits* is illustrated in figure 5.12. The input transformation network (figure. 5.11) learns to generate a 3×3 matrix ($F \times F$) that transforms the three-dimensional points in the input space. This network uses three convolution layers which produce 64, 128 and 1024 feature maps respectively. The transformed input passes through forward network 1, which consists of 2 convolution layers, each producing 64 feature maps. This data is then transformed by a 64×64 matrix ($K \times K$) learned by the feature transformation network (figure. 5.11) with three convolution layers (64, 128 and 1024 feature

5.2. POINTNET BASED EVENT CHARACTERISATION IN EXPERIMENTS

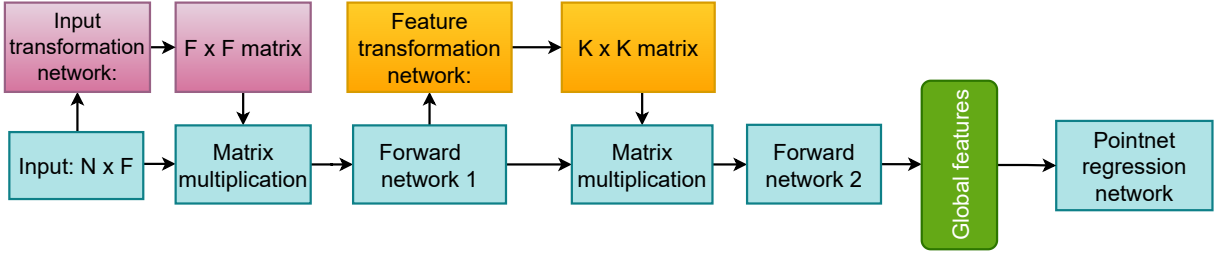


Figure 5.12: General structure of *M-hits*, *S-hits* and *MS-tracks* models. The main difference between the models is the input shape, which depends on the maximum number of hits or tracks expected in an event (N) and the number of attributes considered for each hit or track (F). This changes the dimensions of the input transformation matrix accordingly. The dimensions of the feature transformation matrix ($K \times K$) are equal to the number of feature maps extracted by the last convolution layer of the forward network 1.

maps). The data then passes through a series of 3 convolution layers (forward network 2) with 128, 256 and 512 feature maps respectively. Finally, the global features are collected using an average pooling function with a pool size of 1995. This separates 512 global features of the event which are passed to the point cloud regression network consisting of a three layer neural network with 256, 128 and 1 neuron respectively.

Model-2 (S-hits): This model uses the x, y, z coordinates of hits in the STS detector planes. Similar to the *M-hits* model, *S-hits* does not require tracking to be performed before the impact parameter can be reconstructed. The structure is similar to the *M-hits* model, the only difference being the input shape. The maximum number of hits present in an event in the training data was 9820. Therefore, the input dimensions ($N \times F$) were set to 9820×3 , with provisions similar to *M-hits* to overcome smaller or larger numbers of hits in the testing data.

Model-3 (MS-tracks): The *MS-tracks* model uses the features of the tracks reconstructed from the hits in both MVD and STS to predict the impact parameter. Therefore, this model can only be used to estimate the impact parameter after track reconstruction. In this model, the x, y, z coordinates, $dx/dz, dy/dz$ and charge-to-momentum ratio (q/p) of the tracks of the particles in the first and last plane of the tracks are the attributes of a point in the 12-dimensional point cloud. Therefore, the input dimensions are 560×12 ($N \times F$), where 560 is the maximum number of tracks present in an event from the training data. Events with fewer tracks are filled with rows of zeros to maintain the same input dimensionality.

The basic structure of the data flow in this model is also similar to that of the *M-hits* model. An input transformation network with a similar structure to the one in the *M-hits* model learns the 12×12 alignment matrix. The forward network 1 consists of 2 convolution layers, each producing 128 feature maps. The features extracted from the forward network 1 are transformed by a 128×128 matrix ($K \times K$). The matrix is learned by the alignment

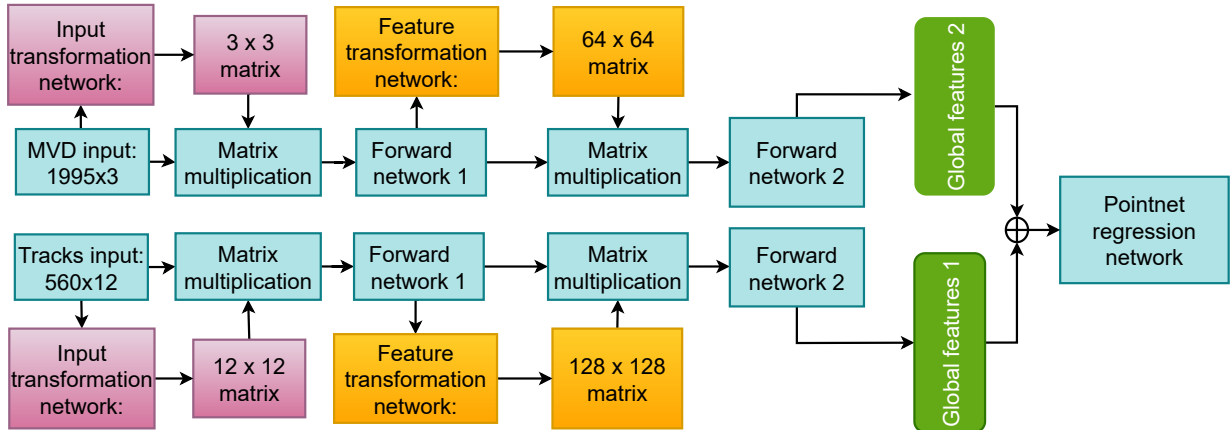


Figure 5.13: Structure of the model *HT-combi*. The model is a combination of *M-hits* and *MS-tracks*. Both models extract the global features independently and are then concatenated before being fed into a regression network.

network with 3 convolutional layers (128, 256 and 1024 feature maps). The extracted features then pass through a forward network 2 similar to the *M-hits* model. Then an average pooling layer (pool size = 560) segregates the global features and feeds them to a regression network similar to *M-hits*.

Model- 4 (HT-combi): This model learns from the combination of both hit and track information used by *M-hits* and *MS-tracks* respectively. It uses the hits from MVD together with tracks reconstructed from hits in MVD and STS to determine the impact parameter of an event. It takes the MVD hits with dimensions 1995×3 and the MVD + STS tracks with dimensions 560×12 .

In this model, two separate networks similar to *M-hits* and *MS-tracks* run in parallel to perform input transformation, feature transformation and global feature extraction. Finally, the global features are concatenated and fed into the regression network with 512, 256, 128 and 1 neurons respectively. The model structure is shown in figure 5.13.

Performance of the PointNet models

The DL models were trained via backpropagation until the validation MSE (loss) started to saturate or diverge from the training loss. The MAE and coefficient of determination of the validation dataset were also considered before choosing the final weights for the model. The trained models were then tested on the datasets *Test1*, *Test2* and *Test3* to evaluate their performance. Details of the final models are tabulated in the table 5.3. All models achieved a R^2 value of about 0.98 upon training. It can be seen that increasing the complexity (# param.) increases the training time required for the model to converge to an optimal solution. Nevertheless, all models eventually achieve similar values for MSE, MAE and R^2 , with the *MS-tracks* and *HT-combi* models achieving a slightly better R^2

5.2. POINTNET BASED EVENT CHARACTERISATION IN EXPERIMENTS

Model	Epochs	# param- eters	MSE	MAE	R^2	Events/s
M-hits	128	$3 \cdot 10^6$	0.43	0.51	0.979	660
S hits	354	$3 \cdot 10^6$	0.47	0.54	0.976	159
MS tracks	372	$6 \cdot 10^6$	0.40	0.50	0.981	1092
HT-combi	484	$10 \cdot 10^6$	0.39	0.49	0.981	435

Table 5.3: Main features of the trained DL models. An epoch is defined as a single training pass through the entire training dataset. The number of parameters (# param.) refers to the weights, biases and kernels of the model, together with non-trainable parameters that define the structure of the network. This number roughly corresponds to the complexity of the model. The MSE, MAE and R^2 are for the validation data. The last column gives an estimate for the speed of execution of the model on a GPU card.

value.

To study the speed of the DL models, 10000 events from the dataset *Test2* were tested on a Nvidia Geforce RTX 2080 Ti with 12 GB of GPU memory. The *MS-tracks* model was found to be the fastest with a prediction speed of about 1092 events/second, while the *S-hits* model was the slowest with a speed of about 159 events/second. However, the *MS-tracks* can only be deployed after track reconstruction, which means that some sort of pre-processing is required, which takes up computational time. It should also be noted that the models have not been optimised for speed. It is possible to improve the speed of the models by reducing the complexity of the models, by modifying the input dimensions to make the best use of the available resources, or by using more advanced GPUs. Nevertheless, the current speed is promising for online analysis of data when run in parallel on multiple GPUs. In addition, the advantage of a more complex model, as in our study, is that it can be used for other analysis tasks that can then be performed at a similar speed.

As a basic reference for the performance of our DL models, we will use a much simpler polynomial fit that can also perform event-by-event predictions from the track multiplicity of the event. This model (*Polyfit*) uses a third-order polynomial fit to the track multiplicity as a function of the impact parameter to determine the impact parameter

$$b = a_0 + a_1 \times x + a_2 \times x^2 + a_3 \times x^3 \quad (5.8)$$

where b and x are the impact parameter and the number of charged tracks, respectively. The fit yields the following parameters

$$a_0 = 14.28; \quad a_1 = -7.01 \times 10^{-2}; \quad a_2 = 2.13 \times 10^{-4}; \quad a_3 = -2.70 \times 10^{-7}.$$

To quantify the precision of DL models, we first look at the spread of DL predictions for a fixed input impact parameter. The relative precision in the predictions of DL models can be calculated as σ_{err}/b_{true} , where σ_{err} is the standard deviation of the distribution of the

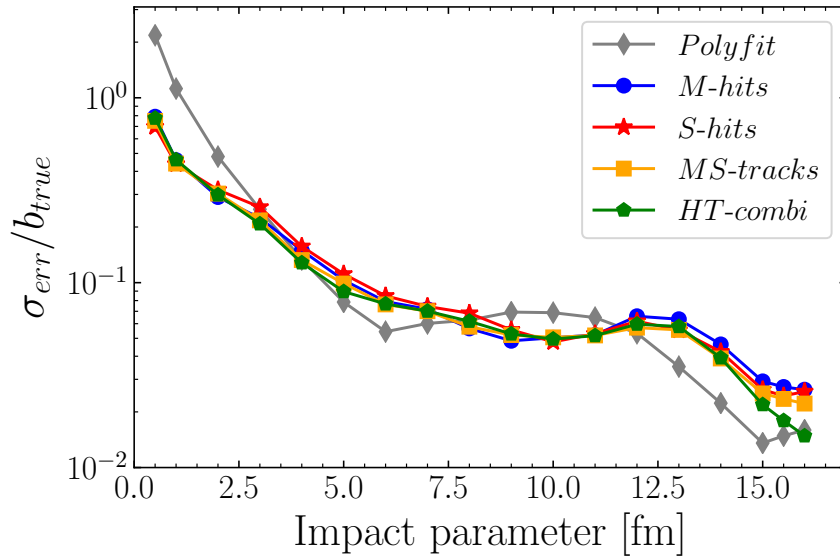


Figure 5.14: Relative precision of DL models as a function of impact parameter. The results of the *Polyfit* model (grey) are also plotted to benchmark the performance of the DL models. The events used are from the *Test1* dataset (Au-Au collisions at 10 AGeV from UrQMD cascade + CbmRoot) and the predictions are for a fixed impact parameter.

prediction error ($true - predicted$) and b_{true} is the true impact parameter. The relative precision of the predictions is plotted as a function of the impact parameter for different DL models and the *Polyfit* model in figure 5.14. It can be seen that the simple model fails for the most central collisions ($b < 2$ fm), with the relative precision increasing up to 200 %, while the DL models have a better precision in comparison. At 0.5 fm, the worst relative precision observed in the DL models was about 79 %, and this dropped below 50 % for events with impact parameters of 1 fm or more. For events of 3 - 16 fm, the spread of predictions from DL models and the polynomial fit model are similar.

However, the standard deviation of the error in predictions only quantifies the precision of the model. Predictions can only be considered both accurate and precise if the error distributions have a mean close to zero and an acceptable precision. Figure 5.15 shows the mean error of the predictions as a function of the impact parameter for *Test1*. The polynomial fit model has a poor accuracy compared to the DL models, despite its comparable precision for mid-central and peripheral events. The DL models have a mean error between -0.33 and 0.22 fm for events with an impact parameter of 2-14 fm, while the mean for the *Polyfit* model varies between -0.7 and 0.4 fm. For events in the range 5-14 fm, the *HT-combi* and *Polyfit* models offer relative precision of 4-9 % and 2-8 % respectively. Despite their similar precision (for 5-14 fm), *HT-combi* yields more accurate predictions, with a mean error of -0.33 to 0.13 fm, while the polynomial fit has mean errors ranging from -0.7 to 0.4 fm.

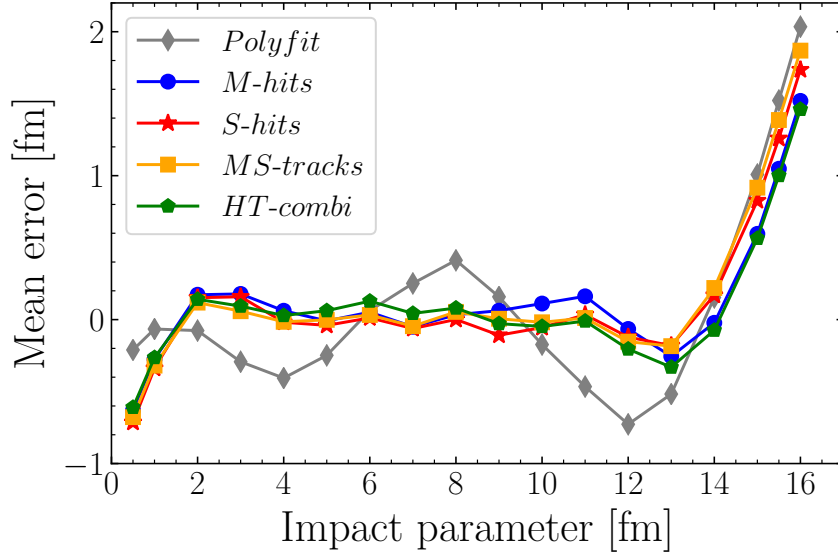


Figure 5.15: Mean error of the predictions as a function of the impact parameter. The events used are from the dataset *Test1* (Au-Au collisions at 10 AGeV from UrQMD cascade + CbmRoot) and the predictions are for a fixed impact parameter. The error bars are smaller than the symbol size.

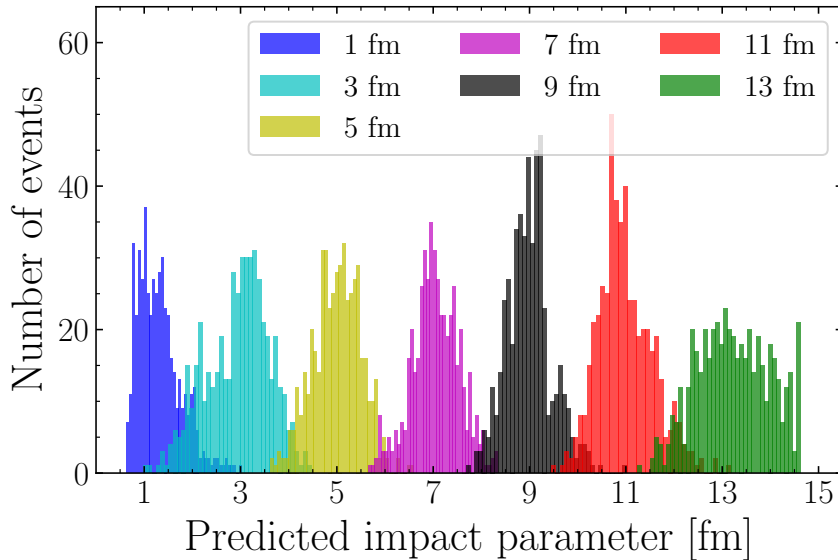


Figure 5.16: Distribution of predicted impact parameters using *MS-tracks*. For a given fixed impact parameter, 500 Au-Au collision events at 10 AGeV generated from UrQMD cascade + CbmRoot were used.

In figure 5.16, the predictions of the *MS-tracks* model for different values of impact

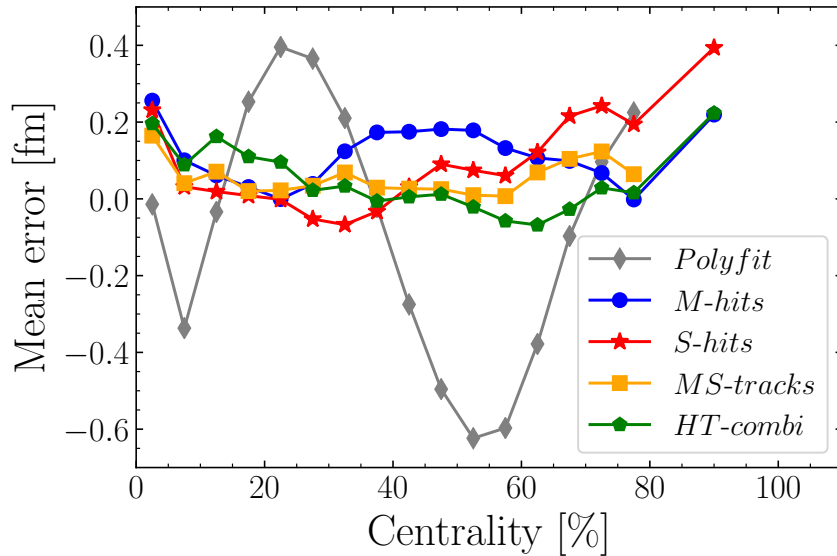


Figure 5.17: Mean error in predictions as a function of centrality. The dataset *Test2* (Au-Au minimum bias collisions at 10 AGeV from UrQMD cascade + CbmRoot) is used, in which peripheral events are more likely to occur. The track multiplicity is used for centrality binning. The points at 90 % centrality are results from events with no reconstructed tracks. Therefore, the *Polyfit* and *MS-Tracks* models have no data point at 90 % centrality. In addition, it can be seen that the *Polyfit* is highly fluctuating and unreliable for event-by-event determination of impact parameters.

parameters are visualised. It can be seen that the predictions for all impact parameters are all centred around the true value. All these results indicate that the DL models use more information than just the number of charged tracks to determine the impact parameter.

In an actual collision experiment, the probability of having events with an impact parameter (b) is proportional to the impact parameter, which gives a different distribution of impact parameters than those used in the *Train* dataset: i.e. peripheral events are more likely. To study the performance of the DL models in such a scenario, the dataset *Test2* was used to predict the impact parameter for different centrality classes with a bin width of 5%. The mean prediction error is plotted as a function of centrality in figure 5.17. The DL models have a mean error close to zero for most of the centrality classes, while there are large fluctuations in the simple polynomial model. Another interesting factor is that the number of events that have at least 1 hit in the MVD detector but no tracks reconstructed (using MVD and STS hits) was about 10% of *Test2*. These are “empty” events for the track multiplicity based method. However, the DL models can use hits to make predictions about the impact parameter of these events, although the error is large compared to their predictions for central and mid-central events.

The accuracy of the reconstructed impact parameter of an event may depend on how accu-

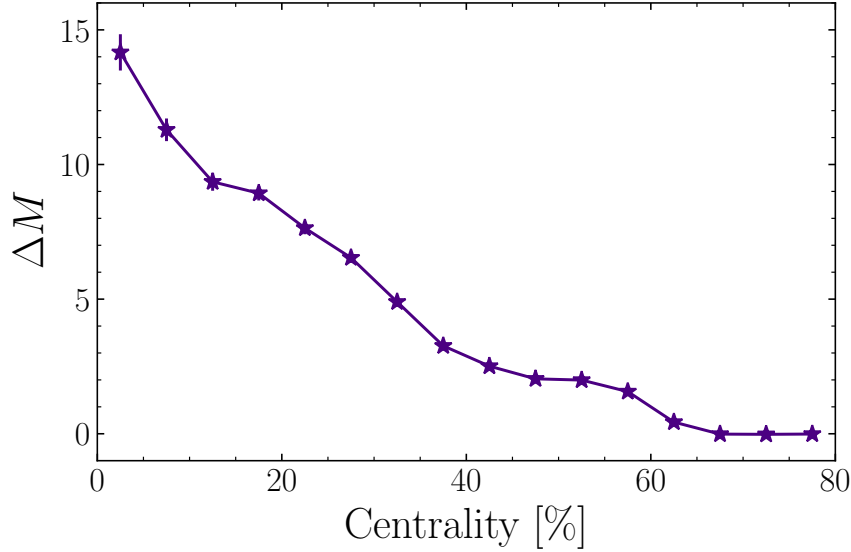


Figure 5.18: Difference of the mean track multiplicity for the datasets *Test3* and *Test2* (ΔM) as a function of centrality. Both datasets contain minimum bias Au-Au events at 10 AGeV from UrQMD cascade + CbmRoot. However, the Δ baryon absorption cross section was reduced by a factor of 2 from their default value to generate *Test3*. The change in pion cross section in *Test3* is expected to be more pronounced in central collisions, leading to a larger number of charged tracks.

rately the simulation model can describe the outcome of individual events. This introduces a bias in the predictions from the choice of event generation model. The dependence of the DL predictions on the physics model is investigated by predicting the events from a separate dataset that introduces different physics (*Test3*) on the DL model trained on the dataset *Train*. To generate *Test3*, the final charged particle multiplicity in the tested events was modified by increasing the pion production cross section in UrQMD. To do this, the Δ baryon absorption cross section in the UrQMD model was reduced by a factor of 2, resulting in increased pion production, especially for central collisions. The increased number of pions is reflected in the difference in the mean charged track multiplicity (ΔM) for events in *Test3* and *Test2*, for a given centrality, as shown in figure 5.18. There is a difference of about 14 tracks for most central events, and it is reduced to less than 3 for peripheral collisions. This change in the physics translates into a shift in the mean of the error distributions (μ_{err}^{shift}), given by

$$\mu_{err}^{shift} = \sqrt{(\mu_{errT3} - \mu_{errT2})^2} \quad (5.9)$$

where μ_{errT3} and μ_{errT2} are the mean prediction errors for datasets *Test3* and *Test2* respectively. This shift in mean is plotted as a function of centrality in figure 5.19. It is observed that the DL models show a shift in the mean of up to 0.32 fm, while the polynomial fit shows a shift of up to 0.53 fm. As expected, the shift is more pronounced for

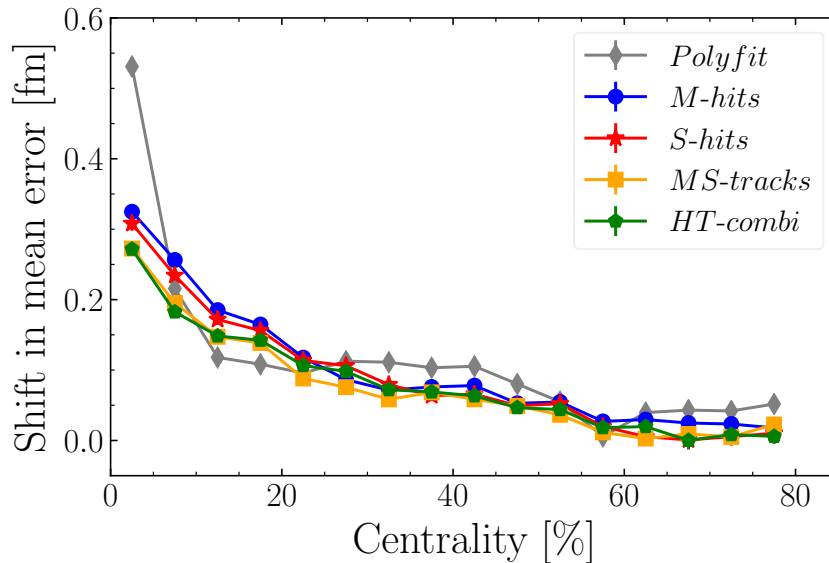


Figure 5.19: Difference in the mean of the error distributions for the datasets *Test3* and *Test2* as a function of centrality. Both datasets contain minimum bias Au-Au events at 10 AGeV from UrQMD cascade + CbmRoot. However, unlike the training dataset and *Test2*, the Δ baryon absorption cross section was reduced by a factor of 2 from their default value to generate *Test3*. The resulting increase in pion production in central events leads to a systematic underprediction of the impact parameter in *Test3*. However, the DL models appear to be less model dependent than the polynomial fit.

central collisions. This means that the DL network learns more information about the event features independent of the event multiplicity than the *Polyfit* and is thus less model dependent than a simple fit. The *MS-tracks* and *HT-combi* models show a slightly better robustness to the physics modification compared to the *M-hits* and *S-hits* models. The track multiplicity of the event is definitely an important feature with a strong correlation with the impact parameter. However, because DL models learn other information in the data in addition to track multiplicity, they tend to be more robust than the polynomial fit model, which essentially depends only on track multiplicity.

The joint alignment networks used in the study are a straightforward application of these networks in [182]. The intuition behind the use of these networks is to allow the DL models to learn certain transformations in the data that can better reveal the correlations in the data for the subsequent convolution layers. The same idea of input transformations can be extended to the feature space. The learned features could be transformed before being fed to the next convolution layer. If there are some correlations that are highlighted by the transformation, the model could benefit from the transformation. We tested the change in performance of the *M-hits* model without the alignment networks. The results are tabulated in 5.4. It can be seen that the performance is only marginally improved when both alignment networks are used. When only the feature transformation network

5.2. POINTNET BASED EVENT CHARACTERISATION IN EXPERIMENTS

Model	MSE	MAE	R^2	Epoch
original <i>M-hits</i>	0.4290	0.5123	0.9789	128
without I_{trans} & F_{trans}	0.4378	0.5196	0.9784	455
without F_{trans}	0.4304	0.5137	0.9788	172

Table 5.4: Performance change of the *M-hits* model without the alignment networks. I_{trans} and F_{trans} are the input and feature transformation networks respectively. The MSE, MAE and R^2 are for the validation data. The last column shows the number of training epochs the model needed to converge to its best performance.

was removed, the validation loss was slightly better than when both alignment networks were removed. Although the performance improvement is marginal, it should be noted that the models without the alignment networks tend to overfit more compared to the original *M-hits* model. This was observed in the difference between their training and validation loss. The use of an alignment network also gives more stability in the training, avoiding sudden fluctuations in the validation loss. In addition, the model converges faster when using alignment networks.

In this study, we have shown that pointnet based DL models can be used to accurately determine the impact parameter in the CBM experiment. The use of input data with minimal pre-processing and the high processing speed of DL models make them an ideal candidate for online event selection. It is also interesting to note that all four types of models (*M-hits*, *S-hits*, *MS-tracks* and *HT-combi*) lead to essentially comparable precision in the determination of the underlying impact parameter. In fact, track-based modelling shows only slightly better performance in evaluating validation data. The DL models are found to be a reliable tool for impact parameter determination for impact parameters in the range of 2-14 fm. Events with an impact parameter less than 2 fm represent only a very small fraction of the total events in an experiment. Nevertheless, the predictions are still better than the prediction from the polynomial fit, which fails for most central events. The deep learning models show superior performance compared to a simple model based only on track multiplicity. However, all methods for estimating the impact parameter will have a bias in the predictions obtained from the physics models used to generate the data. This is also true for Glauber based estimation. In addition, the training data used in this DL study with the UrQMD model and the CBM detector simulation may not perfectly represent the real data. This model bias can be estimated for DL models by comparing the predictions of a model on different event generator data. This bias could also be minimised by using events from multiple event generators in the training samples. However, by using a DL model trained on UrQMD data (or any other model) for event selection when the data need to be compared with UrQMD predictions (or the corresponding model), we can avoid the additional biases and uncertainties introduced into the analyses by using inconsistent simplified models such as Glauber MC for event selection.

The PointNet-based models presented in this study use information such as particle tracks

and hits, which is available immediately during data collection in any heavy-ion collision experiment. The developed model architectures can also be adapted to other heavy-ion collision experiments, e.g. ALICE at the LHC or HADES at the SIS18. Here the model can be used and studied with real data. In fact, these methods are not limited to nucleus-nucleus collisions and the PointNet models can be extended to reconstruct the centrality in p-nucleus collisions as well.

5.2.2 Impact parameter determination in the $\bar{\text{P}}\text{ANDA}$ experiment

The production of hyperon-antihyperon pairs in antiproton-nucleus collisions close to their threshold has been proposed to study the hyperon and antihyperon potentials in nuclei [248–250]. Using the high-intensity antiproton beams at FAIR, the $\bar{\text{P}}\text{ANDA}$ detector will be able to study the $\Lambda - \bar{\Lambda}$ production in \bar{p} -N collisions. This provides a unique opportunity to study the in-medium effects of baryons (antibaryons) in nuclei. However, the production probability for $\Lambda - \bar{\Lambda}$ pair production depends strongly on the collision impact parameter.

Therefore, a method to determine the collision impact parameter is needed to analyse the data collected by the $\bar{\text{P}}\text{ANDA}$ detector. In Alexander Greiners master thesis [218] at HIM and GU- Mainz, the PointNet-based models for impact parameter estimation at CBM were adapted to determine the impact parameter in $\bar{p} - Ne$ collisions.

The study investigated the system size dependence of the performance of the PointNet based models for impact parameters estimation. The models were trained on a 5-dimensional point cloud of the charge, components of the momentum and the mass of the final state particles. It was found that when the models were trained on the UrQMD output for Au-Au collisions at $E_{lab}=10$ AGeV, the MSE in the predictions was about 0.18 fm^2 , while the MSE increased to 0.67 fm^2 for Ne-Ne collisions at the same energy. For $\bar{p} - Ne$ collisions at $p_{lab}=15$ GeV the performance increased further to an MSE of about 0.87 fm^2 . It was also found that when the detection efficiencies for different particle species were taken into account in the simulations, the models trained on $\bar{p} - Ne$ collisions at $p_{lab}=15$ GeV had a prediction MSE of about 0.97 fm^2 .

It is evident that the accuracy of the predictions decreases with decreasing system size. This is to be expected since the final state particles produced in $\bar{p} - Ne$ collisions are smaller than the final state particles produced in Au-Au collisions by a factor of ≈ 10 . The PointNet model has to rely on the information contained in the small number of particles produced to infer the impact parameter. Nevertheless, an MSE of about 1 fm^2 can still be useful for the $\bar{\text{P}}\text{ANDA}$ experiment, as there is currently no other method that can predict the event-by-event impact parameter with this accuracy.

The PointNet based DL models are thus an excellent choice of algorithm for the analysis of experimental data. The models developed for impact parameter determination can be easily adapted for other tasks as well.

5.2.3 N_{part} determination in HADES and CBM experiments

In this subsection we explore the potential of PointNet based models to determine the number of participant nucleons in the HADES and the CBM experiments. A model that can provide event-by-event N_{part} consistent with the theoretical models used in the experimental analysis can replace the Glauber MC based N_{part} estimation. In this way, the same theoretical model can be used consistently throughout the analysis of experimental data. This mitigates the biases introduced by "mixing" models with different physical assumptions in the analysis chain.

In this study, we train two PointNet based models, one each for the CBM (with 10 AGeV data) and HADES (with 1.23 AGeV data) experiments, using the data generated by the UrQMD cascade model. For each of the beam energies $E_{lab} = 1.23$ and 10 AGeV, 10^5 Au-Au collisions (with uniform collision parameter distribution) were generated, 75% of which were used to train the models and the remaining 25% to test the models. As a proof of concept study, we consider a simple setup to mimic detector acceptance, where an angular acceptance cut is applied to the UrQMD output. The HADES acceptance cut of 18- 85° polar angle is applied to the 1.23 GeV data, while the CBM acceptance cut of 2- 25° polar angle is applied to the 10 GeV data. Both models are trained on the four-momentum point cloud of all charged particles within the acceptance cut. In this way we can investigate the performance of PointNet based models in determining the N_{part} of collisions at FAIR experiments.

The two models trained in this work share an identical network architecture. A simple PointNet model without the joint alignment networks was used in this study. The input point cloud passes through three layers of 1-D convolution, producing 128, 256 and 512 feature maps respectively. The extracted 512 feature maps are converted into 512 global features of the point cloud by average pooling. Finally, the global features were regressed to output N_{part} using a fully connected network with two hidden layers (256, 128). The ReLU activation function was used throughout the network. Batch normalisation layers were used after each convolution layer, and dropout layers (dropout probability=0.5) were used after each layer in the dense neural network.

The model trained on 1.23 AGeV data with HADES acceptance achieved a validation MAE of about 11.6 and R^2 of 0.98 after 158 epochs. The test results for this model are visualised in figure 5.20. It can be seen that the predictions are centred around the true value. However, for any given N_{part} , the distribution of predictions has large tails. This means that while the predictions are accurate most of the time, occasionally there can be large errors in the predictions. Note that very few particles are produced at this energy, and the measured particles may not contain enough correlations to accurately extract the underlying N_{part} . On the other hand, the model trained on 10 AGeV data with CBM acceptance cut shows a superior performance. The model achieved a validation MAE of about 8.2 and a R^2 value of about 0.99 after 39 epochs of training. The predictions of this model for different values of N_{part} are shown in figure 5.21. Compared to the previous

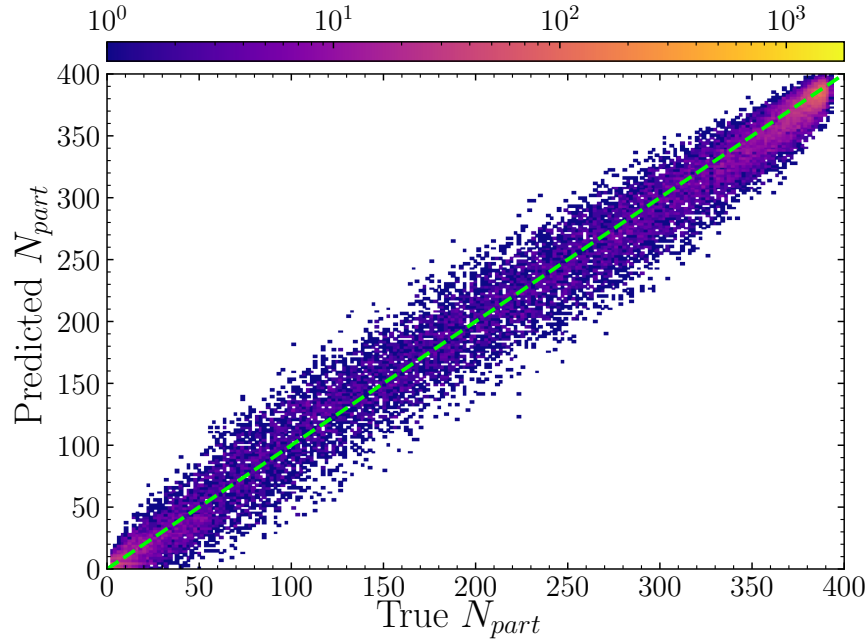


Figure 5.20: Performance of the PointNet based N_{part} determination model in the HADES experiment. The results are from 25000 Au-Au testing events at 1.23 AGeV with uniform impact parameter distribution. The colour indicates the number of collision events. The dashed green line shows the true $N_{part} = \text{predicted } N_{part}$ curve.

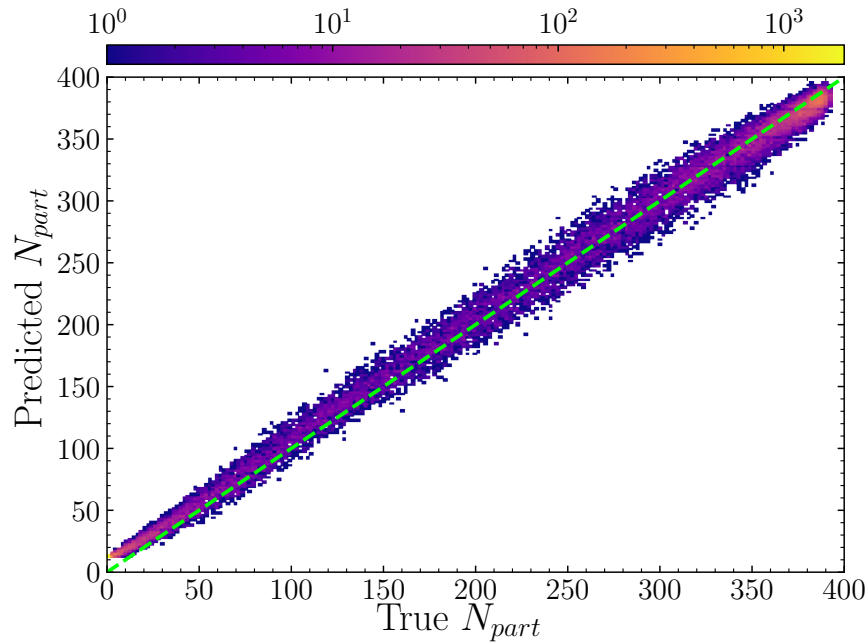


Figure 5.21: Performance of the PointNet based N_{part} determination model in the HADES experiment. The model was trained and tested on 10 AGeV Au-Au collisions. The results shown are from 25000 testing events. The colour indicates the number of collision events.

model, the distributions here are much narrower and centred around the true value for most N_{part} values.

In short, the PointNet based models can perform accurate N_{part} estimation in SIS-100 energies. Although the performance of the model in SIS-18 energies is not as good as the performance in SIS-100 energies, the DL models can serve as an alternative to GlauberMC based N_{part} estimation. Note that the model can also be further tuned and trained on a larger dataset to improve performance.

The PointNet based impact parameter and N_{part} estimation models are an excellent solution to quickly process, characterise and analyse the experimental data in a CBM experiment. It should be noted that the actual performance of the N_{part} determination model may vary due to experimental effects. This can only be investigated by replacing the simple angular acceptance filter in the data preparation pipeline with a dedicated detector simulation. Nevertheless, the analyses demonstrate the flexibility of PointNet-based models and serves as an example of how a generalised analysis of experimental data can be performed using DL methods.

5.3 Bayesian inference of dense matter EoS

We will now see how AI methods can be used to extract the underlying physics of collisions from experimental data. The results presented in this section are based on [165]. Extracting the EoS of QCD matter from experimental data is an extremely challenging but fundamental goal for heavy-ion collision programmes around the world. Bayesian constraints on the EoS at high temperatures ($> 160\text{MeV}$) and vanishing net baryon densities, based on RHIC and LHC data, suggest an EoS consistent with lattice QCD calculations [217]. However, at high baryon densities, where only effective model calculations are possible, precise experimental measurements are limited. Although various signals have been proposed to probe the high-density EoS over the last decades [1, 8, 122–124], a conclusive picture has not yet emerged due to the lack of systematic studies that consistently and quantitatively relate all possible signals to an underlying dynamical description of the system. We apply AI methods to fill this gap and extract the EoS of dense QCD matter from experimental data. Here we use available experimental measurements to constrain the density dependence of the EoS of nuclear matter.

This work presents a Bayesian method to quantitatively constrain the high net baryon density EoS from the existing data of intermediate energy heavy-ion collisions. A recent study attempted such an analysis using a rough, piecewise constant speed of sound parameterisation of the high density EoS [251]. This study uses a more flexible parameterisation of the density dependence of the EoS in a model that can consistently incorporate this density dependent EoS and then make direct predictions for various observables.

The model

To be able to quantify the high-density EoS, we first need a model that allows us to incorporate the density-dependent EoS in a consistent way and then to make direct predictions for different observables. The standard hybrid models for heavy-ion collisions usually include a hydrodynamic phase where different EoSs are easily accommodated [48, 252, 253]. However, the initial state as well as the particlization procedures used in these models introduce ambiguities [254], especially at moderate and low energies where the compression phase dominates the flow observables. Thus, the determination of the EoS at high baryonic density is a challenging task when using these hybrid approaches. Therefore, a different approach is taken in this work, where the dynamic evolution of heavy-ion collisions is fully described by the microscopic UrQMD model, extended by a density dependent EoS. The model has already been described in section 3.5. This approach describes the whole system evolution consistently within one model.

Remember that in this model the density dependent EoS enters the models through a density dependent potential and this potential U or potential energy V is directly related to the EoS by eq. 3.15. Therefore the terms equation of state and potential energy are used interchangeably in this section.

Parameterisation of the EoS

In order to constrain the EoS from data, a robust and flexible parameterisation of the density dependence of the potential energy is required, which is capable of constructing physical EoSs. For densities below twice the nuclear saturation density (n_0), the EoS is reasonably constrained by QCD chiral effective field theory (EFT) calculations [255, 256], nuclear incompressibility [257], flow measurements at moderate beam energies [1, 3, 258, 259] and Bayesian analysis of both neutron star observations and low energy heavy-ion collisions [260]. This work focuses on the high density EoS, in particular the range $2n_0$ - $6n_0$, which is not yet well understood. Therefore, the potential energy $V(n_B)$ is fixed for densities up to $2n_0$ using the Chiral Mean Field (CMF) model fit to nuclear matter properties and flow data in the low beam energy region [161]. For densities above $2n_0$, the potential energy per baryon V is parameterised by a seventh degree polynomial:

$$V(n_B) = \sum_{i=1}^7 \theta_i \left(\frac{n_B}{n_0} - 2 \right)^i + h \quad (5.10)$$

where $h = -22.07$ MeV to ensure that the potential energy is a continuous function at $2n_0$.

The data

The parameters θ_i and thus the EoS are constrained by Bayesian inference using the elliptic flow v_2 [61, 68, 105, 261–264] and the mean transverse kinetic energy $\langle m_T \rangle - m_0$ [265–267] of mid rapidity protons in Au-Au collisions at beam energy $\sqrt{s_{NN}} \approx 2 - 10$ GeV. The

5.3. BAYESIAN INFERENCE OF DENSE MATTER EOS

Observable	$\sqrt{s_{\text{NN}}}$ [GeV]	Centrality
v_2	2.24, 2.32, 2.4, 2.42, 2.51, 3.0, 3.32, 3.84, 4.23, 4.72	mid-central
$\langle m_T \rangle - m_0$	3.83, 4.29, 6.27, 7.7, 8.86	central

Table 5.5: Observables used in the study. The experimental data consist of v_2 at 10 different energies [61, 68, 105, 261–264] and $\langle m_T \rangle - m_0$ at 5 different energies [265–267].

experimental measurements of v_2 and $\langle m_T \rangle - m_0$ are from mid-central collisions and central collisions respectively. The observables used for Bayesian inference are summarised in the table 5.5. Important, sensitive observables such as the directed flow [122, 268] are finally used to cross-check the EoS extracted in this way.

To calculate these observables from the UrQMD model, similar cuts in rapidity and centrality are applied.

The v_2 is calculated from the UrQMD data as

$$v_2 = \left\langle \frac{P_x^2 - P_y^2}{P_x^2 + P_y^2} \right\rangle \quad (5.11)$$

where the momenta are defined with respect to the reaction plane of the model. At low beam energies, event plane or cumulant methods are usually not used to extract the elliptical and directed flow due to the significant interactions between the spectator and the participant region, resulting in negative elliptic flow and strong directed flow. For a more detailed discussion of the flow correlations at SIS18 energies, refer to [269]. Experiments in this energy range usually have dedicated detectors to determine the actual reaction plane of the collisions. In this analysis we also calculate the flow with respect to the reaction plane. In this way, non-flow effects, e.g. from multi-baryon correlations not related to the collective flow, are not included in the analysis.

Both v_2 and $\langle m_T \rangle - m_0$ are calculated for protons at mid-rapidity ($|y/y_b| < 0.1$, where y_b is the beam rapidity in the center of mass frame). For a given EoS, to calculate v_2 and $\langle m_T \rangle - m_0$ with errors similar to the experimental error, 12000 mid-central ($5 < b < 8.3$ fm) and 1000 central collision events ($0 < b < 3.4$ fm) respectively, are used.

The choice of proton observables (as a proxy for baryons) is motivated by the fact that interesting features in the EoS at high baryon densities and moderate temperatures are dominated by the interactions between baryons and protons, which are the most abundant hadron species for the beam energies considered in this work. At the beam energies considered, the dynamics is dominated by the baryons and the pions 'feel' the effect of the density dependent potential only indirectly, e.g. through the baryonic resonance decays. The elliptic flow was chosen because of the large number of high-precision measurements with relatively small systematic uncertainties. On the other hand, the transverse kinetic energy measurements are only available for a few beam energies. However, the transverse kinetic energy can be calculated with a precision similar to the experimental data using

fewer events (about 1000 events). This makes the transverse kinetic energy measurements a good choice of observable in addition to v_2 for constraining the EoS.

Fast emulators of UrQMD for likelihood estimation

The objective of Bayesian inference is to construct the joint posterior distribution for the 7 polynomial coefficients $\boldsymbol{\theta} = \{\theta_1, \theta_2, \dots, \theta_7\}$ based on the experimental data $\mathbf{D} = \{v_2^{exp}, \langle m_T \rangle^{exp} - m_0\}$ using the Bayes theorem, given by

$$P(\boldsymbol{\theta}|\mathbf{D}) \propto P(\mathbf{D}|\boldsymbol{\theta})P(\boldsymbol{\theta}). \quad (5.12)$$

Here, $P(\boldsymbol{\theta})$ is the prior distribution that encodes our prior knowledge about the parameters, while $P(\mathbf{D}|\boldsymbol{\theta})$ is the likelihood for a given set of parameters, which determines how well the parameters describe the observed data. Finally, $P(\boldsymbol{\theta}|\mathbf{D})$ is the desired posterior, which encodes the updated knowledge about the parameters $\boldsymbol{\theta}$ after encountering the experimental evidence \mathbf{D} .

The likelihood is given by

$$\ln P(\mathbf{D}|\boldsymbol{\theta}) = -\frac{1}{2} \sum_i \left[\frac{(x_i^\boldsymbol{\theta} - d_i)^2}{\sigma_i^2} + (\ln(2\pi\sigma_i^2)) \right] \quad (5.13)$$

where i is the number of observations used for inference, which in this case is 15 (10 values of v_2 and 5 values of $\langle m_T \rangle^{exp} - m_0$). Here d_i and $x_i^\boldsymbol{\theta}$ are the measured data and the model prediction for parameter set $\boldsymbol{\theta}$ respectively for i^{th} observable. The uncertainty term includes both experimental and model prediction uncertainties.

$$\sigma_i^2 = \sigma_{i,exp}^2 + \sigma_{i,GP}^2. \quad (5.14)$$

To evaluate the likelihood for a parameter set, the v_2 and $\langle m_T \rangle - m_0$ observables must be calculated by UrQMD. The MCMC method then constructs the posterior distribution by exploring the high-dimensional parameter space based on numerous such likelihood evaluations. This requires numerous computationally intensive UrQMD simulations, which would require unfeasible computational resources. Therefore, Gaussian Process (GP) models, a non-parametric statistical model, are trained as fast surrogate emulators for the UrQMD model to interpolate simulation results in the parameter space [215, 217, 270, 271].

The Gaussian process models used in this study take the 7 polynomial coefficients as input and predict the v_2 or $\langle m_T \rangle - m_0$ observables. Figure 5.22 shows a set of example curves randomly generated using the polynomial parameterisation of the EoS. Such EoSs are used as input to UrQMD to calculate the v_2 and $\langle m_T \rangle - m_0$ observables. To avoid unrealistic EoSs in the training data, several constraints are applied to the potential functions for densities $2 - 8 n_0$. A lower limit of about -40 MeV is set for the value of the potential to prevent the formation of a second bound state, while the upper limit is set to be at most 50

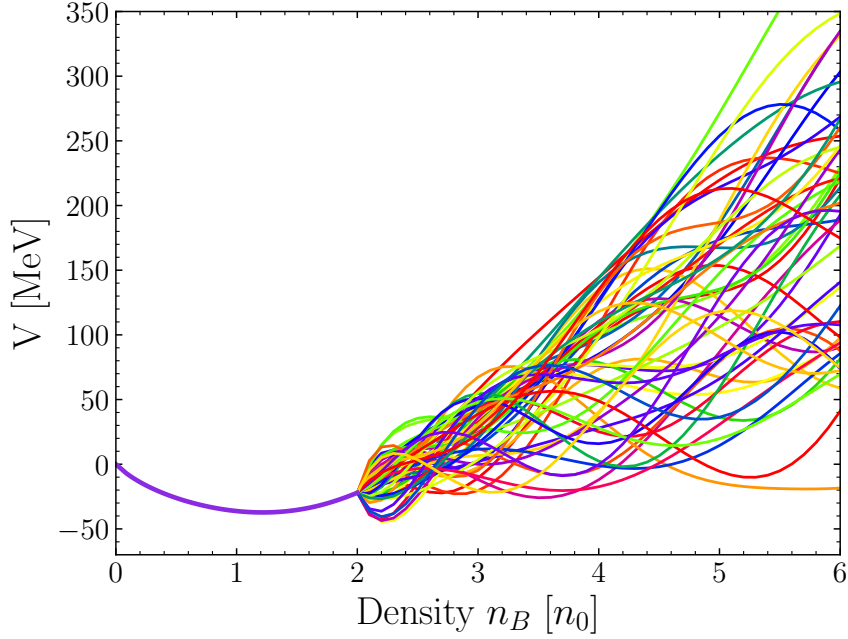


Figure 5.22: Visualisation of some of the EoSs used in training the Gaussian process models. The purple line up to $2 n_0$ is the CMF EoS and the lines starting from $2n_0$ are the different polynomial EoS. The CMF and polynomial EoS are forced to match at $2n_0$. The plot shows the flexibility of the polynomial parameterisation in constructing different EoSs.

MeV higher than the value of a hard Skyrme EoS at any given density to avoid superluminal EoSs. Furthermore, the potentials generated to train the GP models are constrained to have a derivative dV/dn_B approximately within $[-350, 450]$ MeV/ n_0 for densities $2 - 8 n_0$ to prevent the potential from fluctuating too much. Note that these constraints are only used to generate the training data for the GP models and are not applied during the MCMC sampling.

The simulated v_2 and $\langle m_T \rangle - m_0$ values for several random EoSs used to train the GP models are shown in figure 5.23. It is clear from the figure that our training data is diverse enough to cover a wide range of values for v_2 and $\langle m_T \rangle - m_0$ around the experimental observations.

The GP emulators are trained on a set of 200 different parameter sets, each with a different high density EoS, and the performance of these models is then validated on another 50 input parameter sets. 15 different GP models are trained, each one predicting one of the observables (v_2 for 10 collision energies + $\langle m_T \rangle - m_0$ for 5 collision energies). The trained GP models can be evaluated by comparing the GP predictions with the "true" results of the UrQMD simulations. The performance of the GP models in predicting the v_2 and $\langle m_T \rangle - m_0$ observables for 50 different EoSs in the validation dataset are shown in figures 5.24 and 5.25 respectively. As evident from these plots, the GP models can accurately

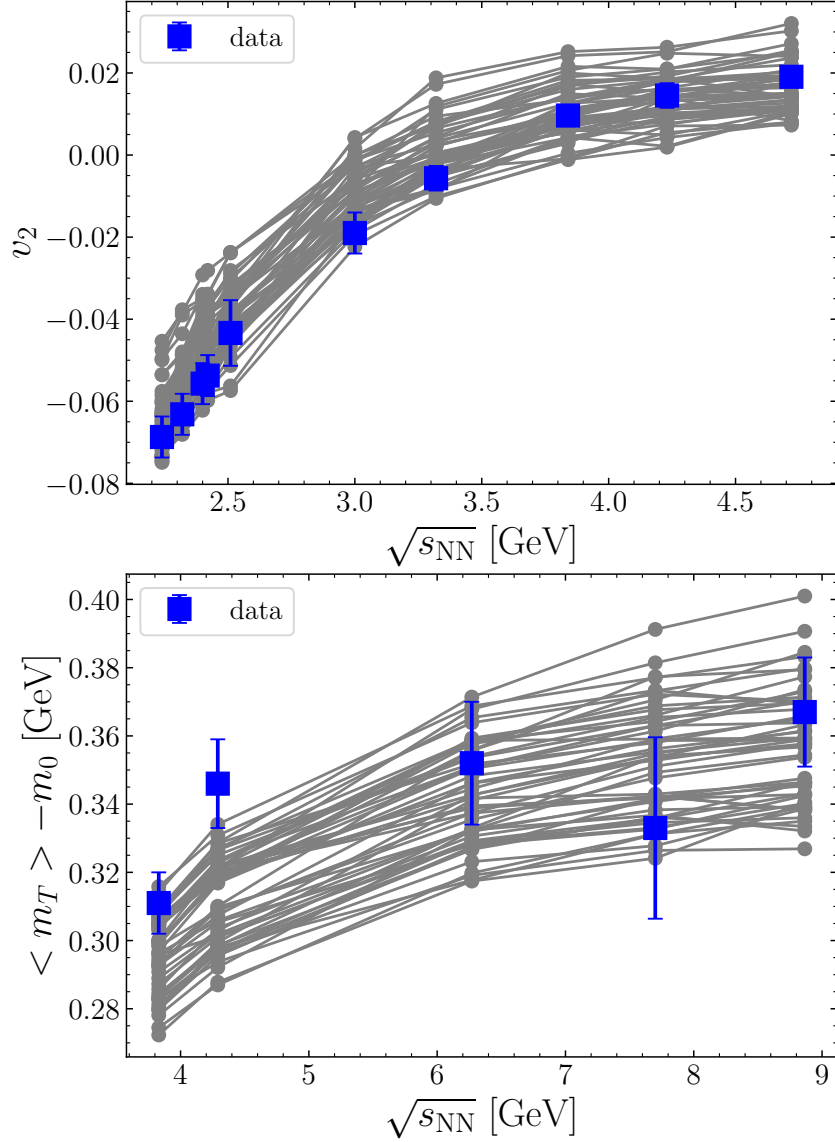


Figure 5.23: Visualisation of v_2 and $\langle m_T \rangle - m_0$ of protons at mid rapidity for 50 random EoSs from the training data generated using UrQMD model with density dependent potential. The v_2 is from mid-central collisions while $\langle m_T \rangle - m_0$ data is from central collisions and $m_T = \sqrt{m_0^2 + p_t^2}$. The top plot is the v_2 and the bottom plot is the $\langle m_T \rangle - m_0$ as a function of $\sqrt{s_{NN}}$. The experimental data are shown in blue squares, while the grey lines are from the training EoSs.

predict the simulated observables given the polynomial coefficients. Therefore, the GP models can be used as fast emulators of UrQMD during MCMC sampling.

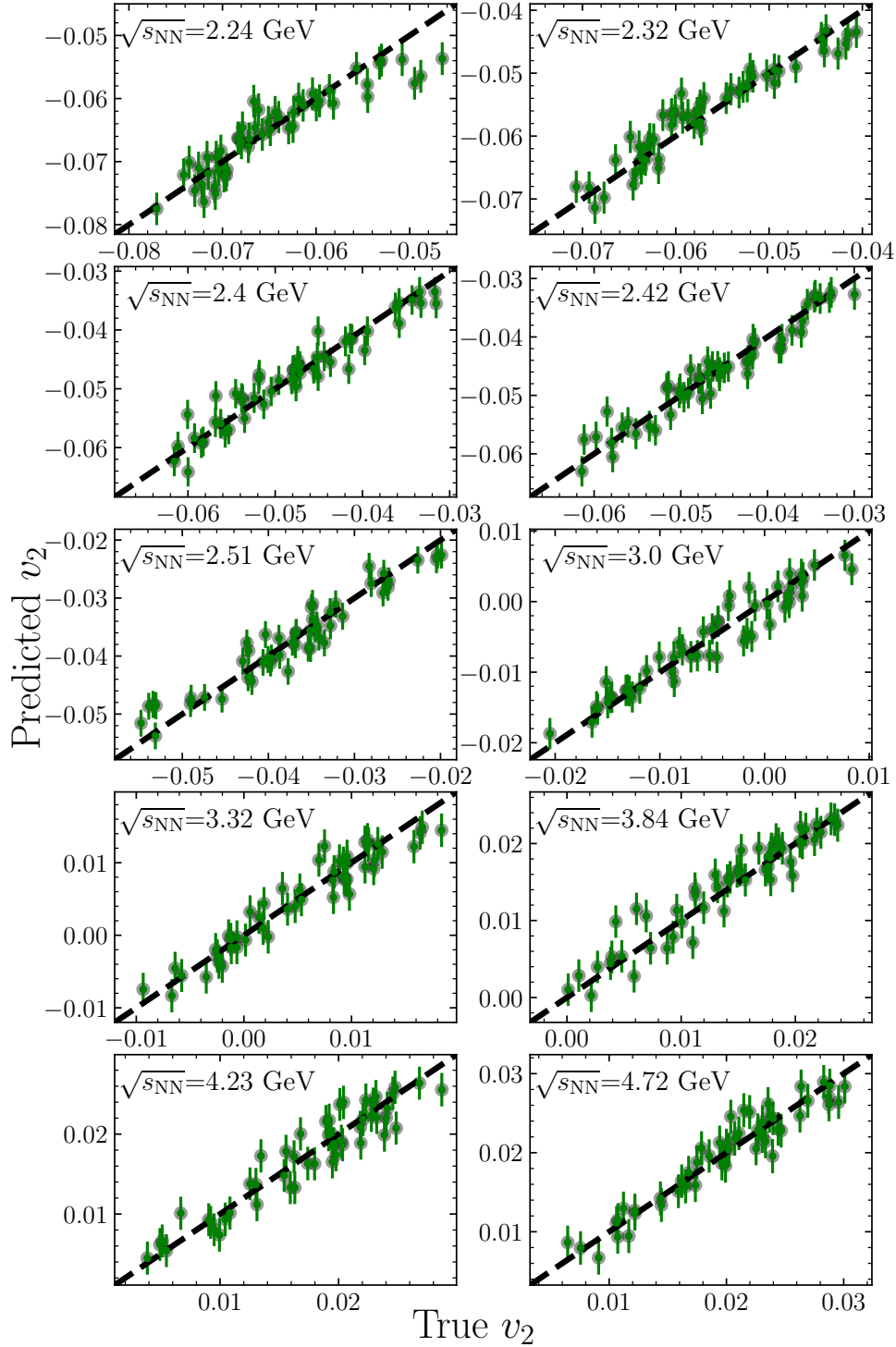


Figure 5.24: Performance of Gaussian process models in predicting v_2 at different collision energies. The predictions for 50 different EoSs in the validation dataset are shown in green, while the error bar is the standard deviation of the prediction given by the GP model. The black dashed line shows vertical scale = horizontal scale. The true v_2 values are from UrQMD simulations with density dependent potentials.

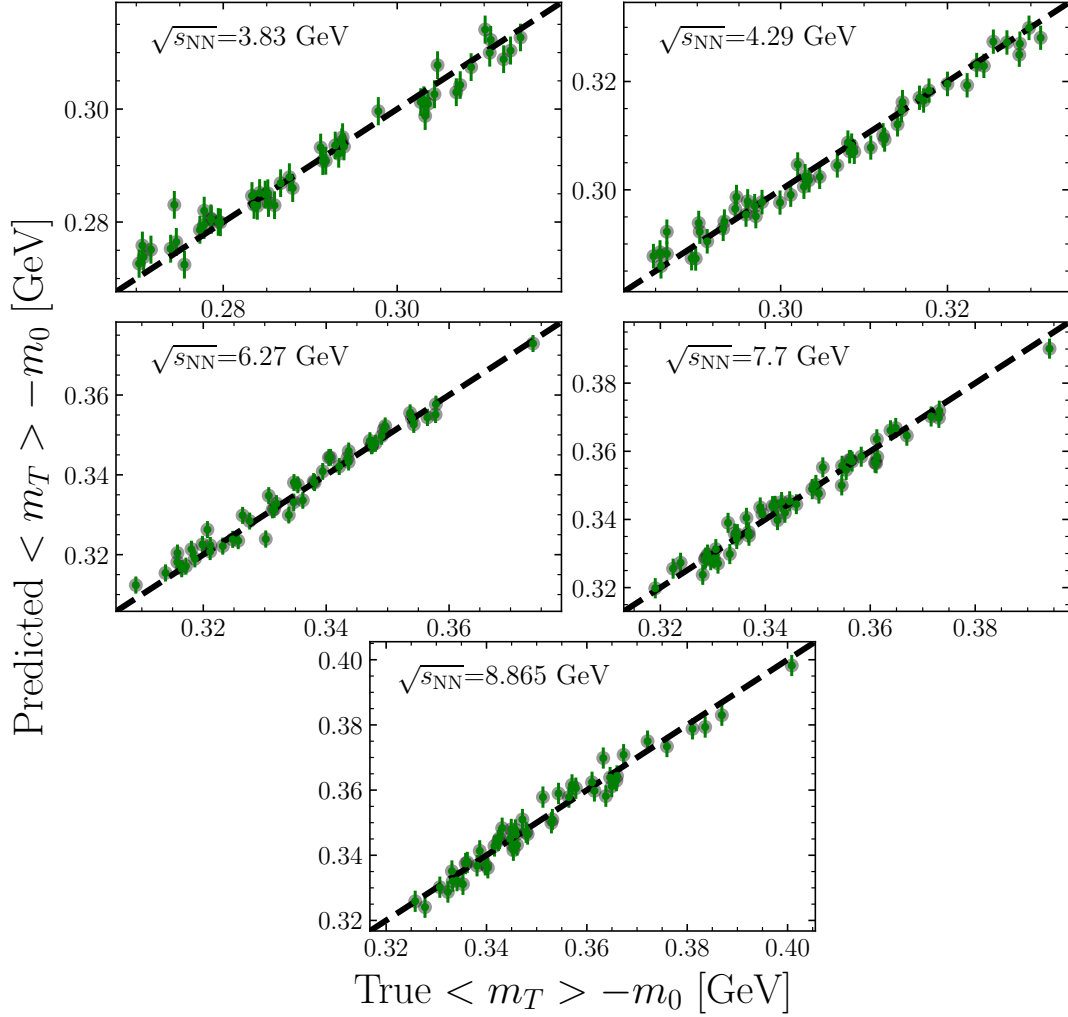


Figure 5.25: Performance of the Gaussian process models in predicting the $\langle m_T \rangle - m_0$ for 5 different collision energies. The predictions are shown in green. The black dashed line shows vertical scale = horizontal scale. The true $\langle m_T \rangle - m_0$ values are from UrQMD simulations with density dependent potentials.

The prior

The final component necessary for Bayesian inference is the prior probability distribution for the polynomial coefficients. Technically, the priors of the parameters θ_i are chosen as gaussian distributions whose means and variances are estimated from the randomly sampled EoSs, under physical constraints, used in the training of the gaussian process emulators. These constraints were introduced to ensure numerically stable results when training the GP models. In order to produce such a robust training dataset, various physics constraints were applied, as discussed above. These constraints eliminate some of the highly fluctuating and superluminal EoSs from the training data.

5.3. BAYESIAN INFERENCE OF DENSE MATTER EOS

	θ_1	θ_2	θ_3	θ_4	θ_5	θ_6	θ_7
μ	77.5	-78.7	65.4	-25.96	5.52	-0.6	0.03
σ	150	450	450	225	55	7	0.3

Table 5.6: Means (μ) and standard deviations (σ) of the Gaussian priors for the seven polynomial coefficients (θ_i).

To ensure that the prior in the analysis is broad enough to reflect an a priori high degree of uncertainty (i.e. without introducing bias), the mean and width of the distributions in the GP training constraint were also used in the prior. However, the polynomial coefficients θ_i resulting from these constraints, which are used to construct the prior distributions for Bayesian inference, are then sampled independently and are therefore not correlated as they would be in GP model training. As a result, the priors for Bayesian inference are much broader than the distributions used for GP model training. The means and standard deviations of the Gaussian priors for the polynomial coefficients are shown in the table 5.6.

Regarding the prior for Bayesian inference, it is important to note that a prior based only on the GP training constraints could also be a good starting point for parameter estimation, but it is not necessary. The physics constraints can disfavour the acausal range for the parameters. However, we use this range only as a soft constraint in the prior, as we use the mean and width of each coefficient independently, so the prior is not constrained by the correlations between the coefficients from the GP training set. This results in inferred potentials that may be outside the training range for the GP models. In fact, the range of physically constrained potentials used to train the GP models is only a small fraction of the prior distribution of potentials at any given density, as shown in figure 5.26. Here the prior distributions of the potential V at four different densities (grey lines) are compared with the range of the potentials used in training the GP models.

It is true that the predictions of GP models may not be reliable for potentials very far from their training range. However, in this case the prediction uncertainty given by the GP models ($\sigma_{i,GP}$) will also be very high. This would then result in a very low likelihood, as the uncertainty term takes into account the uncertainty in the experiment as well as in the GP predictions (see eq. 5.14). Thus, the GP training data can be considered as the lower bound of the "effective prior" seen by the MCMC for Bayesian inference, and it is possible for the MCMC to sample potentials outside this range if the evidence demands.

The prior is used together with the trained GP emulator, experimental observations and the likelihood function for MCMC sampling using the DeMetropolisZ [185, 272] algorithm from PyMC v4.0 [273]. All posterior distributions presented in this study are generated by 4 different MCMC chains. Each chain generates 25000 samples after 10000 tuning steps.

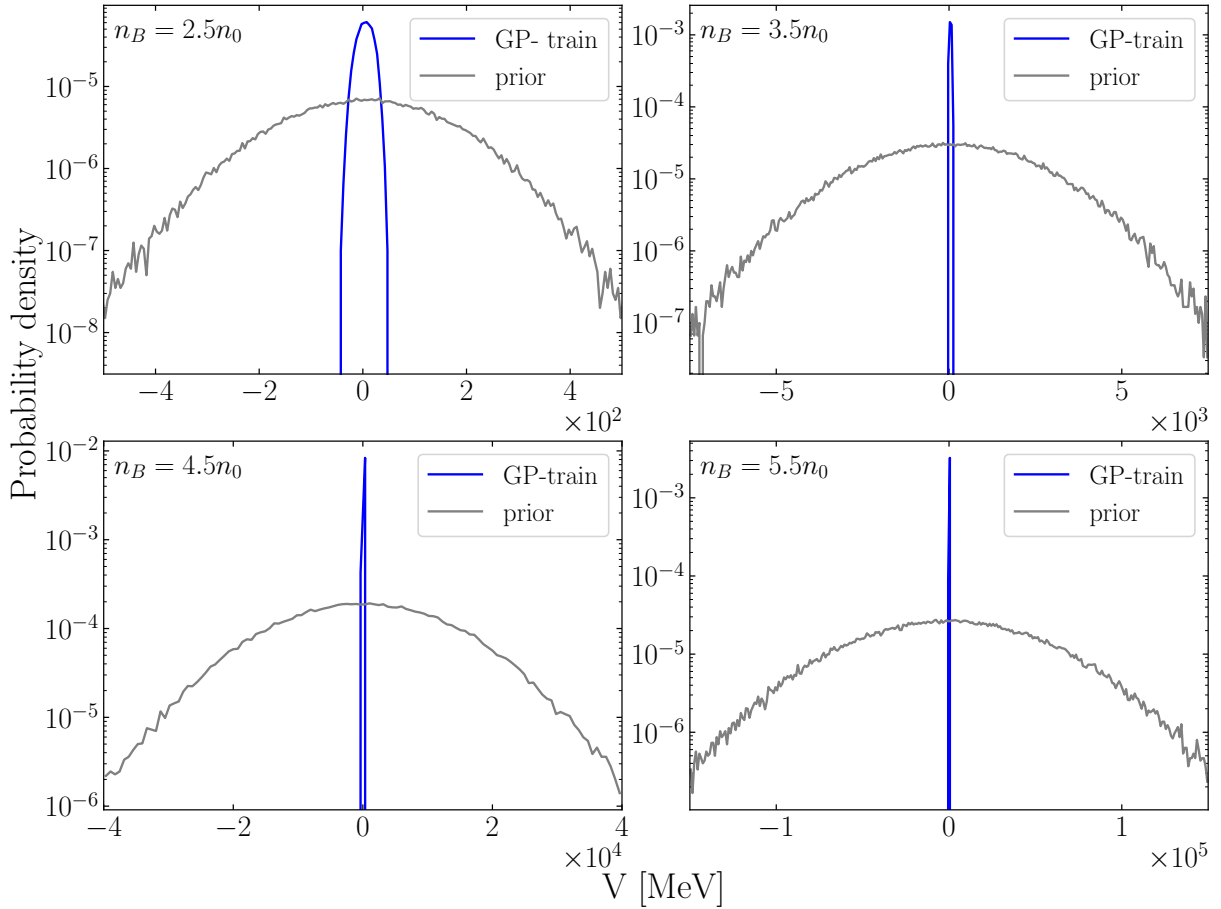


Figure 5.26: Distribution of the potential $V(n_B)$ at four different values of the baryon density. Compared are the prior used in Bayesian inference (grey lines) and the distributions of the constrained potentials used in training the GP models (blue lines).

5.3.1 Closure tests

In order to verify the performance of the Bayesian inference method and its sensitivity to experimental data, two closure tests are performed.

The first test involves constructing the posterior using v_2 and $\langle m_T \rangle - m_0$, simulated with the experimental uncertainties from UrQMD for a specific but randomly chosen EoS. The inference results are then compared with the known ‘ground-truth’. The first column of figure 5.27 shows the posterior constructed for two random input potentials. The black curves in the plot are the ‘ground-truth’ input potentials, while the coloured contours represent the reconstructed probability density for a given value of the potential $V(n_b)$. In addition to the posterior distribution of the potential, two specific estimates of the ‘ground-truth’ potential are highlighted in the figure. These are the Maximum A Posteriori (MAP) estimate, which represents the mode of the posterior distribution as evaluated by

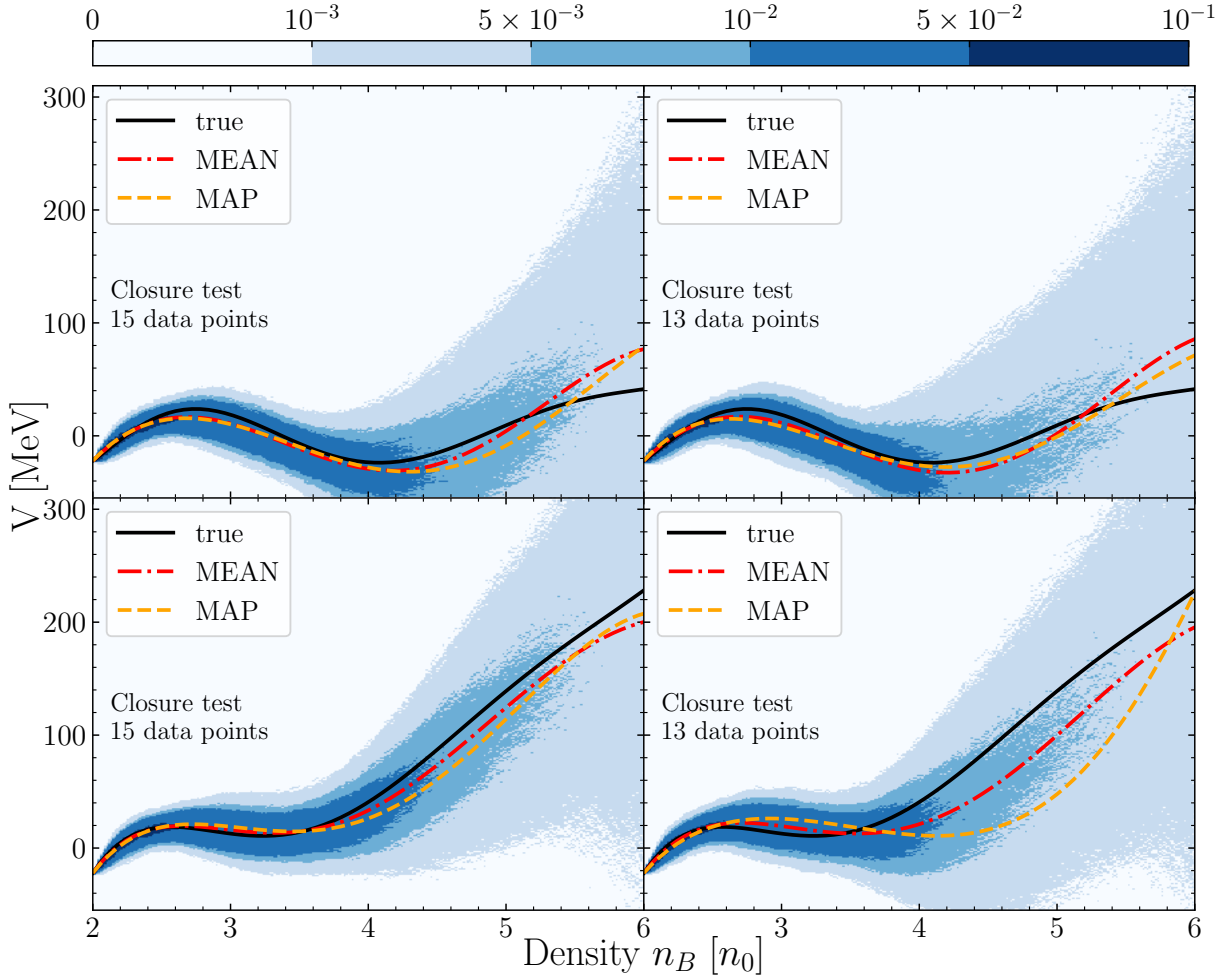


Figure 5.27: Visualisation of the posterior constructed in the closure tests. The colour represents the probability for the potential at a given density. The "ground truth EoS" used to generate the observations is plotted as a black solid line. The red dot-dashed and orange dashed curves are the MEAN and MAP EoS for the posterior. Each row in the figure corresponds to the posterior for a random ground-truth EoS. The plots in the first column show the posterior constructed using all 15 observables. The posterior constructed using 13 observables is shown in the second column. The $\langle m_T \rangle - m_0$ values for $\sqrt{s_{\text{NN}}} = 3.83$ and 4.29 GeV were removed in the test results shown in the second column.

MCMC, and the 'MEAN' estimate, which is calculated by averaging the values of the sampled potentials at different densities. Although it is not necessary that the optimisation converges to the true mode of the posterior, the "MAP EoS" is a quantitative estimate of a most likely EoS that satisfies the constraints imposed by the experimental observations. A comparison of the MAP and MEAN curves with the 'ground truth' shows that the reconstruction results from Bayesian inference are centred around the 'ground truth' EoS and that the sampling is indeed converging to the true posterior. From the distribution

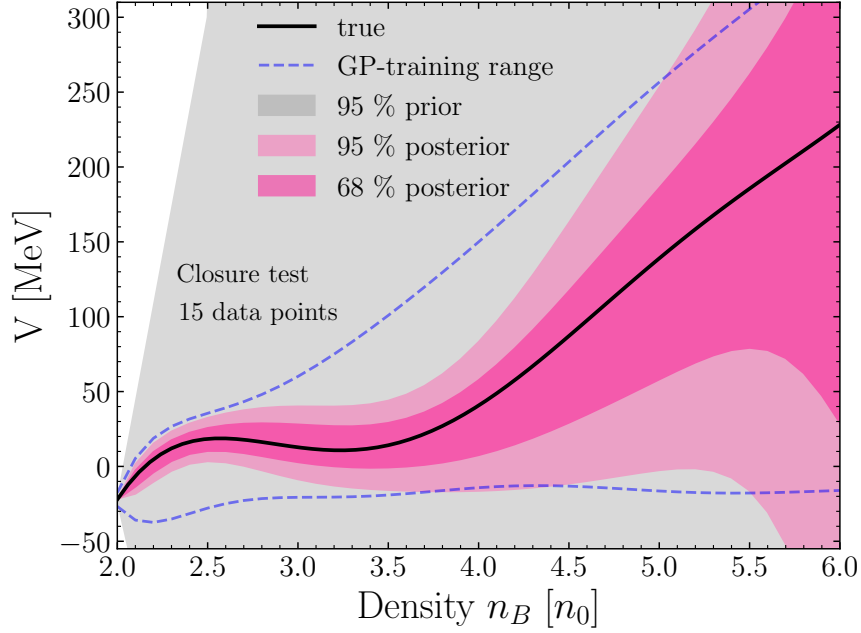


Figure 5.28: Comparison of the prior and posterior distributions for a random input potential. The ground truth potential is shown as the black curve. The confidence intervals for the posterior are shown in various shades of pink, while the grey band corresponds to the 95 % confidence interval for the prior. The training range for the GP models is shown in the dashed blue curve for reference.

of the posterior it can be seen that the EoS are well constrained in the closure tests for densities up to $4 n_0$, and for densities $4-6 n_0$ the posterior distributions have large variance. However, the mean potentials closely follow the true potential. The tests show that the Bayesian inference technique can constrain the high-density EoS well using v_2 and $\langle m_T \rangle - m_0$ values for beam energies $\sqrt{s_{\text{NN}}} = 2-10$ GeV, provided that all experimental observables are simulated consistently.

It is also important to understand how much information is gained from the data that has already been put into the Bayesian inference in the form of a prior. This requires a comparison of the prior and posterior distributions. However, as shown in figure 5.26, the actual prior distribution used is extremely broad. Nevertheless, we have visualised the prior and posterior distributions (95% and 68 % confidence intervals), together with the GP training range (blue dashed lines), for one of the potentials in the above closure test, in a single plot in figure 5.28. As can be seen, the actual prior is much broader than the posterior for the closure test with the simulated data. Indeed, there is a significant gain in information possible with the observables used in the study.

The second closure test is performed to determine the sensitivity of the inference to the choice of observations. Hence, the procedure is similar to the previous test, except that the $\langle m_T \rangle - m_0$ values for $\sqrt{s_{\text{NN}}} = 3.83$ and 4.29 GeV are not used in this test to estimate

the posterior. The results of this test are shown in the second column of figure 5.27. When these two data points are excluded, the agreement of the ‘ground-truth’ EoS with the MAP and MEAN estimates decreases significantly for densities greater than $4n_0$. This indicates that these data points are indeed critical for constraining the EoS at higher densities. When the two data points are removed from the observations, the MEAN and MAP EoSs extracted in this case may not always accurately represent the ground truth. In the first example (figure 5.27, top right plot) the MEAN and MAP EoSs are close to the ground truth for densities up to $5 n_0$. However, in the second example (figure 5.27, bottom right plot), the MAP and MEAN EoS deviate from the ground truth for densities above $3.5 n_0$. Nevertheless, the overall trend of the MEAN and MAP EoSs and the posterior distribution don’t change drastically even if the $\langle m_T \rangle - m_0$ values for $\sqrt{s_{\text{NN}}} = 3.83$ and 4.29 GeV are not used in the inference procedure. This is an indication that if the observations are consistent with each other, removing a few observations from the evidence wouldn’t affect the extracted posterior distribution, although it could lead to a larger variance in the posterior distribution.

5.3.2 Results based on experimental data

The results of sampling the posteriors by using experimental data, for the two cases, with and without the $\langle m_T \rangle - m_0$ values at $\sqrt{s_{\text{NN}}} = 3.83$ and 4.29 GeV, are shown in figure 5.29. The confidence intervals for the posterior distribution are compared with the prior distribution for the two cases in figure 5.30. The upper panel in both figures corresponds to using 15 experimental data points while the lower panel shows the results without the two $\langle m_T \rangle - m_0$ values. The data as used in this work constrain the EoS well for densities from $2n_0$ to $4n_0$. However, beyond $4n_0$ the sampled potentials have a large uncertainty and the variance is significantly larger for the posterior extracted from 13 data points. Beyond densities of about $3n_0$, the posterior extracted using 13 data points differs significantly from the posterior extracted using all 15 points. A softening of the EoS, consistent with a phase transition, can be observed in the extracted posterior and the MEAN and MAP curves for densities $3\text{--}5 n_0$ when only 13 data points are used for inference, while a stiff EoS, without any softening is observed when all 15 data points are used for inference. This is quite different from our closure tests, where the extracted MAP and MEAN curves did not depend strongly on the choice of data points used. This suggests a possible tension within the data in the context of the model used.

To understand this significant deviation that occurs when only two data points are removed, the MAP and MEAN EoS resulting from the two scenarios are implemented in the UrQMD model to calculate the v_2 and the $\langle m_T \rangle - m_0$ values, which are then compared to the experimental data used to constrain them. Figure 5.31 shows that the MAP and MEAN curves agree better with the experimental observations for the v_2 values at higher energies when only 13 data points are used. At the same time, using all data points results in larger $\langle m_T \rangle - m_0$ values for both the MAP and MEAN curves. The model encounters a tension between the $\langle m_T \rangle - m_0$ and the v_2 data. This tension may be either due to a real tension

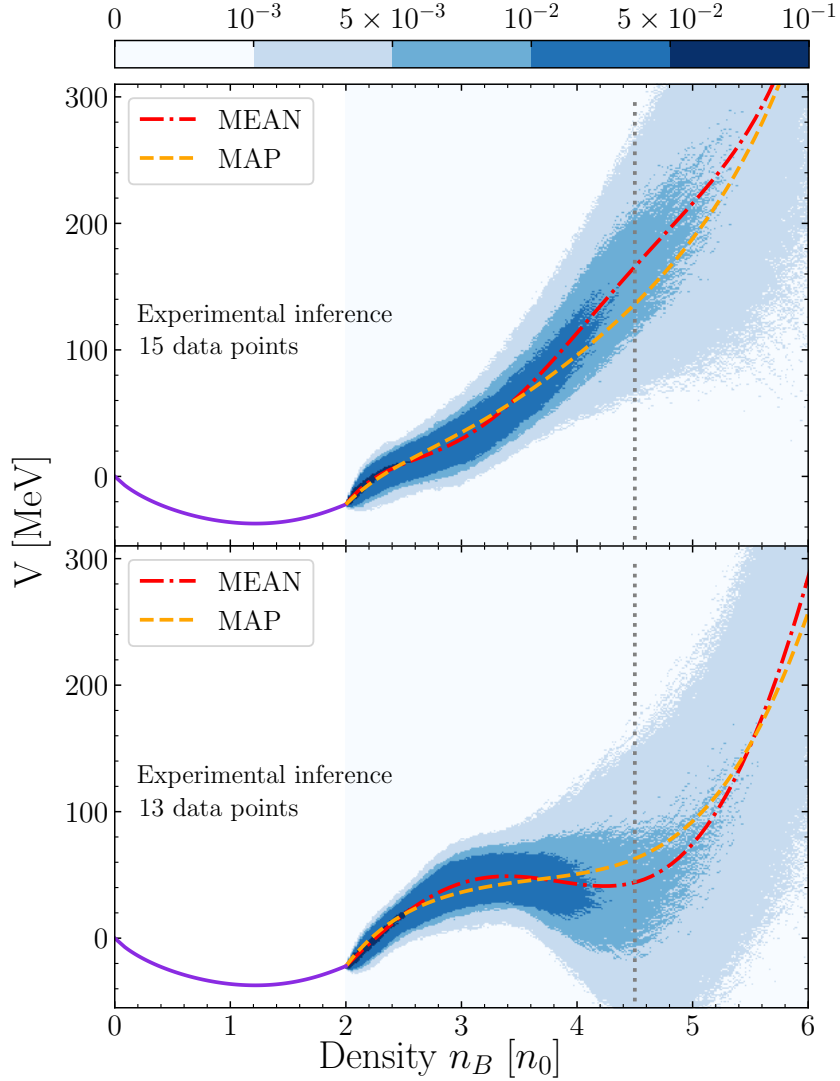


Figure 5.29: Posterior distribution for the EoS inferred from experimental observations of v_2 and $\langle m_T \rangle - m_0$ of protons at mid-rapidity. The top figure is the posterior using all 15 data points, while the bottom figure is obtained from 13 data points only, without using the $\langle m_T \rangle - m_0$ values for $\sqrt{s_{\text{NN}}} = 3.83$ and 4.29 GeV. The MEAN and MAP EoSs in both cases are shown as red dot-dashed and orange dashed curves respectively. The vertical grey line shows the highest average central compression achieved in collisions at $\sqrt{s_{\text{NN}}} = 9$ GeV. The CMF EoS is shown in violet for densities below $2n_0$. For densities above $3n_0$, the extracted EoSs and posteriors are strongly dependent on the choice of observables. The MEAN and MAP EoSs and the posterior extracted using only 13 data points show a softening for densities $3-5n_0$, while the MEAN and MAP EoSs and the posterior extracted using 15 data points reveal a stiff EOS.

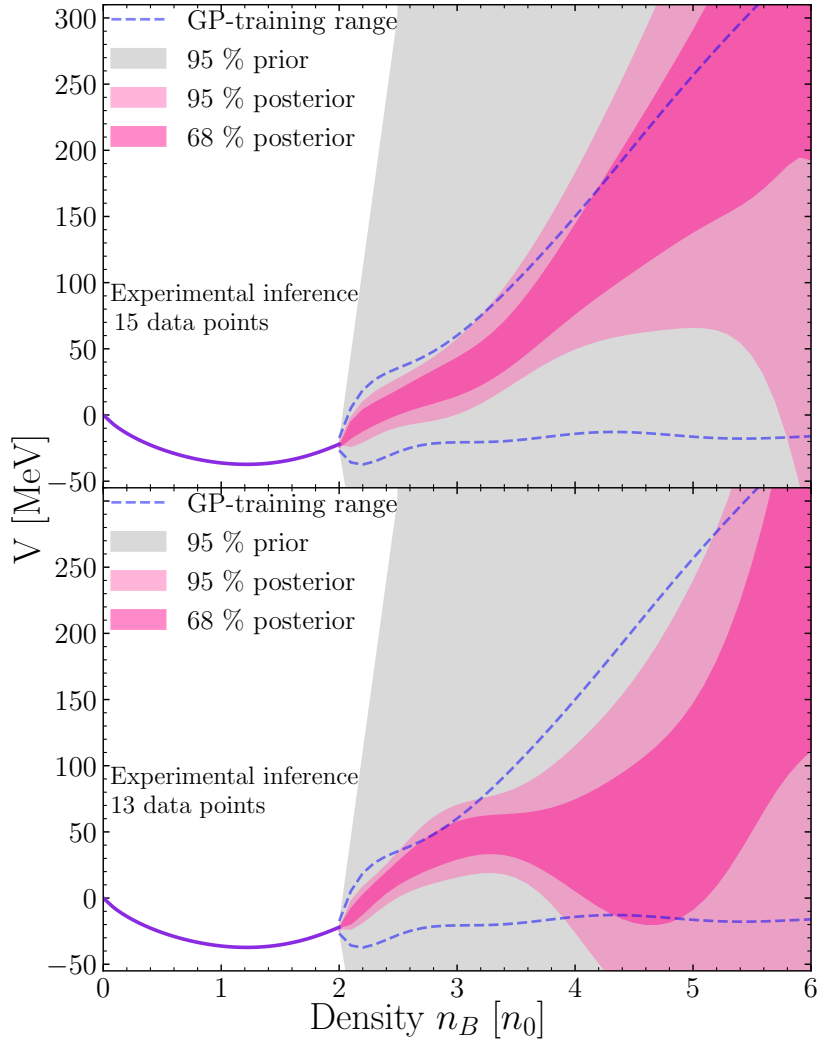


Figure 5.30: Comparing the prior with the posterior constructed from experimental observations. The ground truth potential is shown as the black curve. Confidence intervals for the posterior are shown in various shades of pink, while the grey band corresponds to the 95 % confidence interval for the prior. The training range for the GP models is shown as the dashed blue curve for reference. The CMF EoS is shown in violet for densities below $2n_0$. The top panel shows the result when 15 data points are used, while the bottom panel shows the results when only 13 observations are used in the inference. In both cases, the broad prior is tightly constrained by the data for densities up to $4n_0$. However, the posterior shows dramatic differences depending on the choice of observables. When only 13 observables are used for inference, the extracted posterior suggests a softening of the EoS for densities between 3 and $5n_0$. However, when all 15 observables are used for inference, the posterior indicates a stiff EoS. In this density range, there is a significant difference in the upper and lower bounds of the confidence intervals in the two cases.

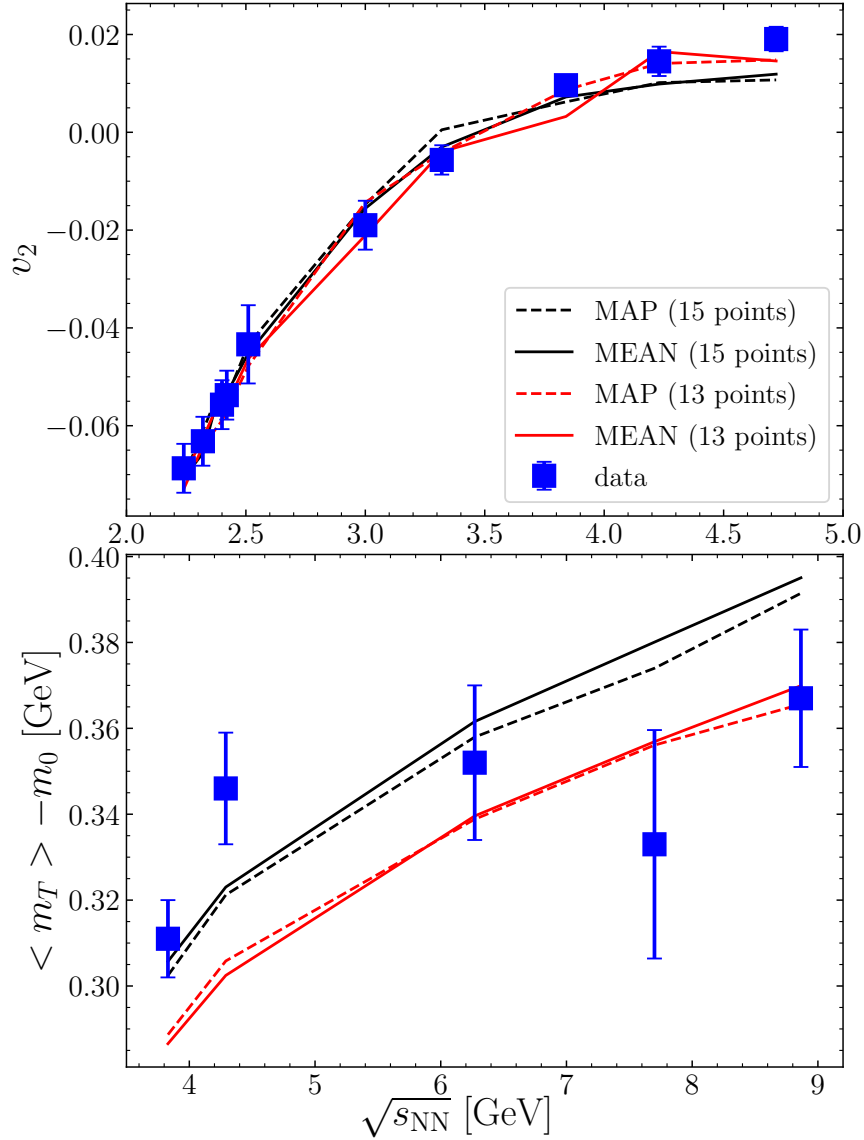


Figure 5.31: v_2 and $\langle m_T \rangle - m_0$ values of mid rapidity protons from UrQMD using the MEAN and MAP EoSs as extracted from the measured data. The observables for the MEAN and MAP EoSs extracted using all 15 data points are shown as solid and dashed black lines respectively, while those generated using only the 13 data points (without the first two $\langle m_T \rangle - m_0$ points) are shown as solid and dashed red lines respectively. The experimental data are shown as blue squares. If the two $\langle m_T \rangle - m_0$ data points at low energies are removed, the model fits the $\langle m_T \rangle - m_0$ values at high energies, leading to an overall decrease in the $\langle m_T \rangle - m_0$ values and a better fit to the large v_2 observations at higher energies. This is consistent with the softening observed in the corresponding extracted EoSs. However, when the all data points are included in the inference, the model fits to the $\langle m_T \rangle - m_0$ observations at low energies, which has relatively smaller error bars, leading to an overall increase in the $\langle m_T \rangle - m_0$ values, which is only consistent with a stiff EoS that gives relatively small v_2 for the highest beam energies shown.

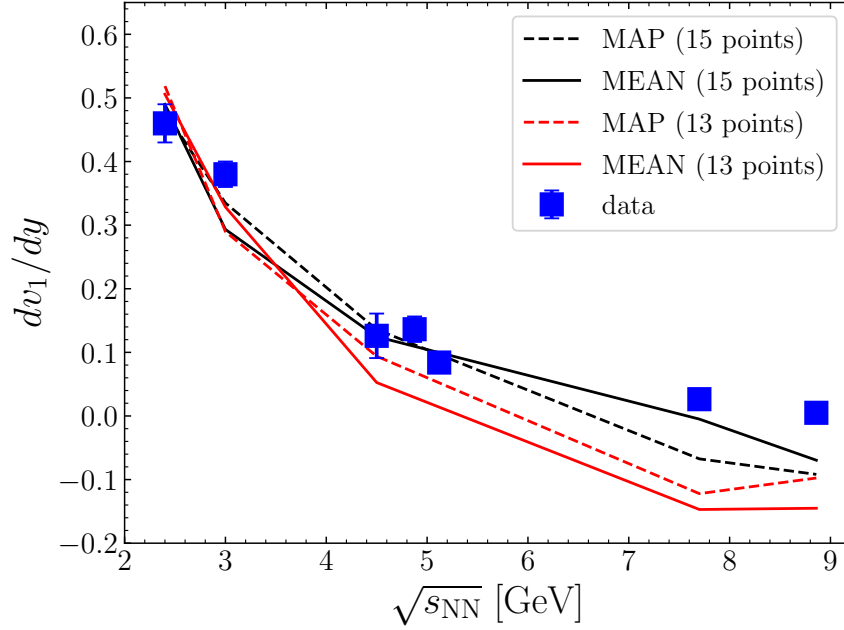


Figure 5.32: Slope of the directed flow, dv_1/dy , of protons at mid rapidity. The observables for the MEAN and MAP EoSs extracted using all 15 data points are shown as solid and dashed black lines respectively, while those generated using only the 13 data points are shown as solid and dashed red lines respectively. The experimental data [105, 224, 263, 264, 274–277] are shown as blue squares. The change in sign of the slope of the directed flow has been shown to be a signal of a first order phase transition [121, 221, 222]. This behaviour is clearly observed in the EoSs extracted using 13 data points for $\sqrt{s_{\text{NN}}} > 6$ GeV. On the other hand, the EoSs extracted using all 15 data points show much larger values for the slope of the directed flow for $\sqrt{s_{\text{NN}}} > 6$ GeV and are in better agreement with the data.

within the experimental data or due to a shortcoming of the theoretical model used to simulate both the $\langle m_T \rangle - m_0$ and the v_2 data at high beam energies for a given equation of state. It should also be noted that at higher beam energies the contributions of the mesonic degrees of freedom to the equation of state become more dominant, which may require an explicitly temperature dependent equation of state.

The extracted EoS can be tested using different observables such as differential flow measurements or different flow coefficients. The slope of the directed flow dv_1/dy at mid rapidity are calculated using the reconstructed MEAN and MAP EoSs. The results, together with the available experimental data, are shown in figure 5.32. The dv_1/dy prediction is in good agreement with the experimental data, especially at the higher energies, for the MEAN EoS extracted from all 15 data points. The reconstructed EoSs are consistent with the dv_1/dy data, although it was not used to constrain the EoSs. A notable difference between the extracted EoSs can be seen at high energies. For the EoSs extracted using 13 data points, the slope of the directed flow decreases and becomes negative for $\sqrt{s_{\text{NN}}} \gtrsim 6$

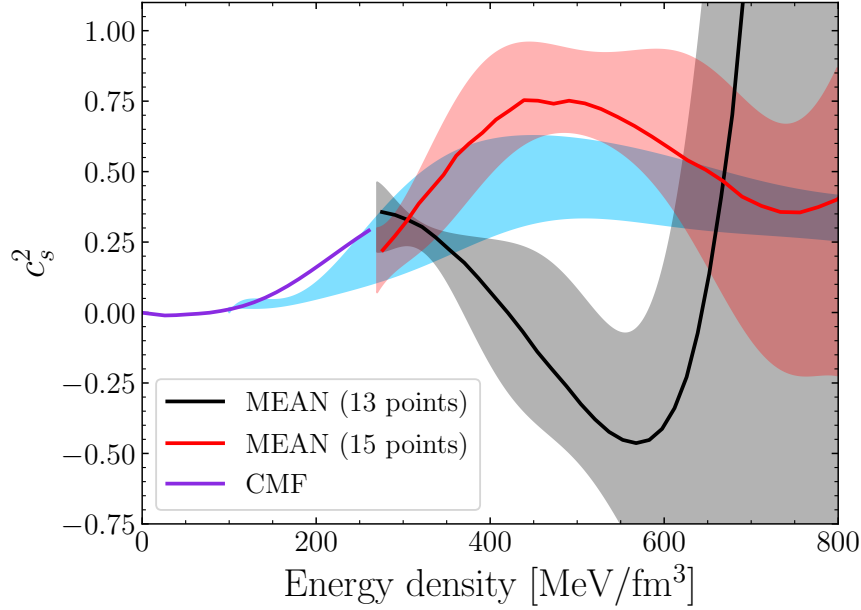


Figure 5.33: Speed of sound squared c_s^2 , at $T = 0$, as a function of energy density. The c_s^2 for the MEAN EoS extracted from all data points are shown in red, and those extracted from only 13 data points are shown in black. For energy densities up to 270 MeV/fm³, the speed of sound from CMF is plotted as the violet curve. The uncertainty bands correspond to a 68% credibility interval from the derived potential curves. The constraints from astrophysical observations [278] are shown as a blue band. It is interesting to note that despite the different isospin fractions in nuclear matter and neutron star matter, both the EoS for nuclear matter extracted from all 15 data points and the EoS for neutron star matter extracted from astrophysical constraints exhibit a broad peak structure for the speed of sound squared.

GeV. This has been shown to be a signal of a first order phase transition [121, 221, 222] and is consistent with the softening of these EoSs for densities 3-5 n_0 . However, in this case the predicted slope deviates from the data for $\sqrt{s_{NN}} \gtrsim 6$ GeV in this case. On the other hand, the EoSs extracted using all 15 data points do not show this clear change in sign at high energies and are in better agreement with the data.

To relate the extracted high-density EoS to constraints from astrophysical observations, the squared speed of sound (c_s^2) at $T = 0$ for the MEAN EoSs is shown as a function of energy density in figure 5.33, together with a contour representing the constraints from recent Binary Neutron Star Merger (BNSM) observations [278].⁴ The speed of sound, as a derivative of the pressure, is very sensitive to even small variations in the potential energy. The c_s^2 values estimated from all data points show overall agreement with the c_s^2

⁴Note that although the two systems have different isospin fractions, the effect of isospin composition is likely to be small at large densities

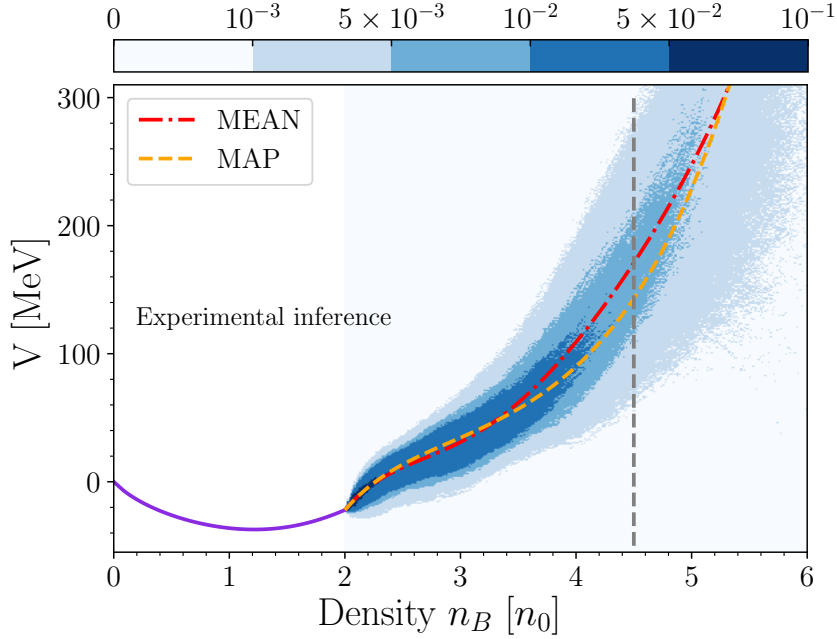


Figure 5.34: The probability density functions of the extracted posterior as a function of density, for a scenario where the $\langle m_T \rangle - m_0$ of the two highest beam energies is removed from the analysis. The extracted MEAN and MAP EoSs are shown as red dot-dashed and orange dashed curves respectively. It is clear that removing the two data points doesn't make much difference to the constructed posterior. The posterior is similar to that extracted with these two points included in the evidence (figure 5.29, top plot).

constraints from astrophysical observations, predicting a rather stiff equation of state at least up to $4n_0$. In particular, both the astrophysical constraints (see also [279]) and the EoS inference in the present work give a broad peak structure for c_s^2 . This is compatible with recent FRG [280] and conformality [281] analyses. However, if only the 13 data points are used, the extracted speed of sound shows a drastic drop, consistent with a strong first order phase transition at high densities [8, 122]. This is consistent with the softening phenomenon observed for $\langle m_T \rangle - m_0$ data shown in figure. 5.31. To give an estimate of the uncertainty in the speed of sound, we have calculated the speeds of sound for 100000 potentials that lie within the 68% credibility interval of the coefficients, but excluding those that lead to acausal equations of state for densities below $4.5 n_0$.

Sensitivity to high beam energies

To check whether it is really the two low energy $\langle m_T \rangle - m_0$ data points that are most relevant to the inference, the Bayesian inference was carried out after removing the $\langle m_T \rangle - m_0$ data points at the two highest beam energies. It was found that the resulting constraints were less sensitive to the removal of data points from higher beam energies (or higher densities). This can be seen in figure 5.34, which shows the probability density functions

of the extracted posterior as a function of density, for a scenario where the mean $\langle m_T \rangle - m_0$ of the two highest beam energies (7.7 GeV and 8.865 GeV) is removed from the analysis. The resulting potential is very similar to that with the two points, supporting our statement of less sensitivity to the data at the highest beam energies. It is therefore clear that the constraints on the EoS are very sensitive to the two data points at low beam energies and much less sensitive to the high energy points, within the beam energy range currently under consideration.

Differential spectra

The extracted EoS can be further tested with various observables from heavy-ion collisions. Several recent works have investigated other different observables sensitive to the equation of state [219, 282–284] (e.g. pion HBT, dilepton production, net proton fluctuations). In the current work we focus on the integrated values of the mean transverse momentum and the elliptic flow, since these can be calculated with a limited number of simulated events. The main limiting factor for our analysis is the computational effort required to simulate the different observables for the different equations of state needed to train the gaussian process emulator. Of course, once the EoS is constrained, many observables can be predicted and compared for many beam energies and system sizes.

In addition to the directed flow shown earlier, a comparison with recently published HADES data on the differential elliptic flow in Au-Au collisions at $E_{\text{lab}} = 1.23A$ GeV [224] is presented here. This comparison of the two different MEAN EoS to HADES data is shown in figure 5.35. As can be seen, the extracted EoSs reproduce the p_T dependence well up to a proton momentum of 1 GeV. Beyond this range, the model slightly overestimates the elliptic flow compared to the HADES data. The reason for this is probably a small momentum dependence of the potential interaction, which is not taken into account in the present approach. However, it is important to note that the integrated elliptic flow is only sensitive to the flow around the maximum of the proton p_T distribution, which roughly corresponds to p_T between 300 and 400 MeV.

This study has demonstrated how much information about the EoS of dense nuclear matter can be obtained from the available experimental data. To constrain the EoS further, more data are needed. We will now explore how DL methods can be used in future experiments (in particular the CBM experiment) to extract this information directly from the experimental data. It should also be noted that although the model used in the Bayesian inference allowed us to study the influence of the EoS on the initial state, it was a non-relativistic model without explicit temperature dependence for the EoS, which would be relevant at higher beam energies. Therefore, in the next study, we use the hybrid UrQMD model, which addresses these issues, and show how the EoS can be inferred from a different simulation model. Furthermore, this will also allow us to illustrate how the DL-based methods can be easily adapted and trained on a different model (in contrast to the impact parameter estimation model, which was trained using transport simulations).

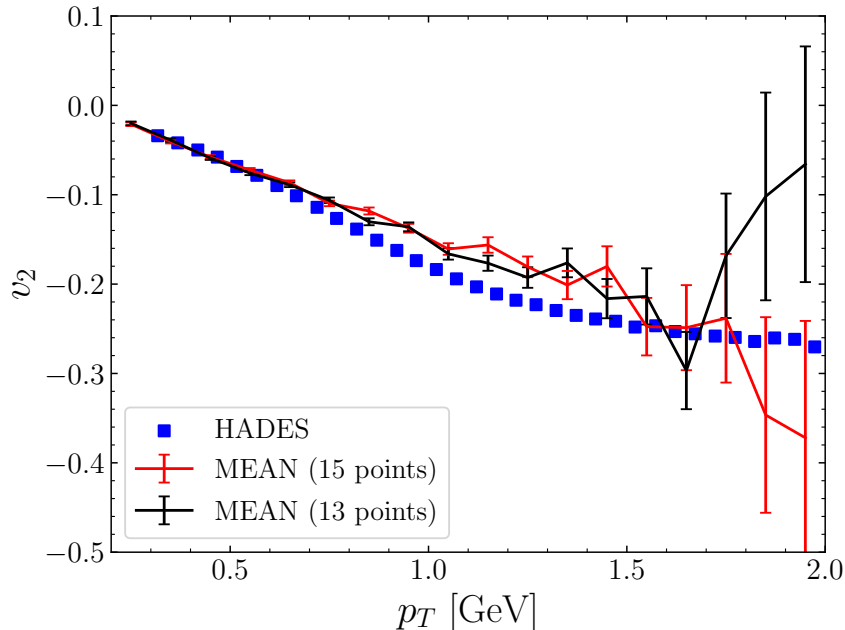


Figure 5.35: Differential elliptic flow of protons for mid-central collisions of AuAu at $E_{\text{lab}} = 1.23A$ GeV. The HADES data are compared with simulations using the two different MEAN equations of state.

5.4 PointNet based EoS classification in the CBM experiment

The CBM experiment will study the least explored high density intermediate temperature region of the phase diagram, where conjectured interesting structures such as the appearance of a phase transition or a critical endpoint are likely to be located (if they exist!). In the CBM experiment, the incoming data stream from the detector is processed by various algorithms to perform event reconstruction [285], particle identification and event selection [112] before various physics analyses can be performed. Events reconstructed and selected by these algorithms are used to calculate observables such as anisotropic flow and particle multiplicity fluctuations sensitive to a phase transition [121]. Multi-parameter fits of the model simulations to the experimental data for these observables are currently used in experiments to search for phase transitions and to calculate the bulk properties of the QCD medium. Bayesian analysis methods have been proposed as a method to fit the parameters to these observables [215, 217, 286] and we have already seen how Bayesian inference could be performed to extract the EoS of dense nuclear matter.

An alternative approach to identify the appearance of a phase transition in QCD matter is based on deep learning techniques. Such DL techniques are considered as so-called end-to-end approaches, where the DL model itself determines the interesting features of the data and performs a classification task on these features. In [180], convolution neural networks

were trained on pion spectra (p_t, ϕ) from hydrodynamic simulations to classify the EoS of a possible QCD transition. The study performed on the hydrodynamic output showed an average prediction accuracy of more than 95%. A follow-up study was presented in [214], where a hadronic cascade model was used after the hydrodynamic evolution in the simulations to achieve a realistic freeze-out and to include the effect of having a finite number of measurable particles in single events. The hadronic cascade "after-burner" introduces uncertainties in the final state spectra due to resonance decays and hadron rescatterings. This results in discrete particle spectra with dominant event-by-event fluctuations, in contrast to the smooth spectra produced by pure hydrodynamic simulations. DL methods are reliable and accurate for the identification of QCD transitions in heavy-ion collisions. However, as reported in [214], the performance depends largely on the fluctuations in the final state spectra. Therefore, if such a DL-based EoS-meter is to be used on the direct output of a heavy-ion experiment, a comprehensive analysis of the response of the DL model to additional uncertainties introduced by e.g. the detector resolution, the acceptance region and the efficiency of the reconstruction algorithms is necessary. The model should not only be robust to these constraints, but also meet the performance in terms of accuracy and speed as demanded by the experiment.

In this study, the effects of experimental uncertainties and detector effects on the predictions of DL models for classifying QCD transitions at the CBM experiment are investigated. DL methods for classifying EoSs involving different types of transitions in the CBM experiment a. The DL models are trained on data similar to an experimental output using a comprehensive data preparation pipeline that includes detector simulation and reconstruction algorithms. Having established the superior performance of PointNet based models in using detector output to characterise the impact parameter and the number of participants in collision events, we now investigate the ability of similar models to identify the EoS of QCD transitions from raw experimental output. We also study the performance of PointNet based models at different situations of detector resolution and acceptance, and evaluate the dependence of prediction accuracy on collision centrality and simulation model parameters.

Preparing the data

To generate the training data for the DL analysis, this study uses the hybrid mode [48] of UrQMD 3.4 to simulate heavy-ion collision events with and without phase transition. We use two distinctly different equations of state for training and validation. One based on a Maxwell construction between a bag model quark gluon EoS and a gas of pions and nucleons [135, 155] to simulate the first-order phase transition scenario. The second EoS is called the Chiral Mean Field hadron-quark EoS [163], which describes a smooth crossover transition as predicted by lattice QCD. To investigate the model results for an unknown EoS, we also use a hadron resonance gas equation of state based on a free gas of hadrons according to the known hadronic resonances from the particle data group [287]. The three equations of state along trajectories of constant entropy per baryon, as expected for heavy-

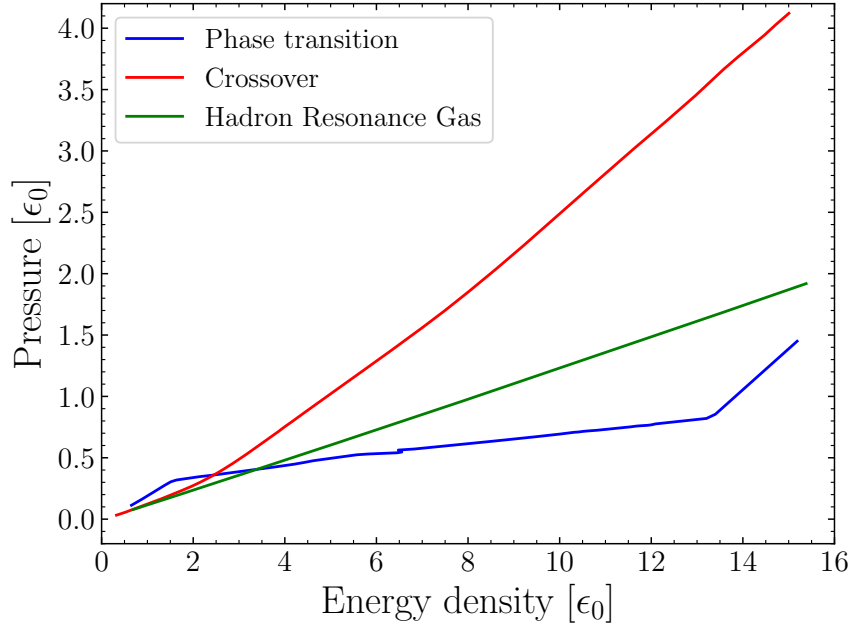


Figure 5.36: The equations of state, along an isentropic trajectory, for the first order phase transition, crossover and hadron resonance gas as included in the UrQMD hybrid simulations. The pressure of the medium for a central cell is plotted as a function of its energy density in a central Au-Au collision at 10 AGeV in the lab frame. The phase transition and crossover EoS are used to train the models, while the hadron gas EoS is only used to test the performance of the models on an EoS which it was not trained on.

ion collisions at $E_{\text{lab}} = 10$ AGeV, are visualised in figure 5.36. While the crossover EoS is the stiffest and the phase transition the softest equation of state, the HRG lies between these two extreme cases.

The main objective of the study is to develop a DL model that uses information similar to the experimental output of the CBM experiment, without any significant analysis chain. Furthermore, our study will analyse the effects of experimental constraints on the performance of this model. Therefore, an accurate modelling of the experimental condition is necessary. The CbmRoot [236] package is used to transport the final state particles from UrQMD through the CBM detector simulation. CbmRoot uses GEANT3 [247] to simulate the electromagnetic and weak interactions as well as the decays of the particles passing through the detector. The hits in the detector are then digitised to mimic the detector resolution and finally these digitised hit positions are used to reconstruct the tracks using a Kalman filter based algorithm [285]. The standard CbmRoot macros are used for transport simulation, digitisation and track reconstruction. As a result, we obtain realistic event-wise output from the detector simulation, which can now be used as input for the DL analysis.

It is also important to note that CbmRoot can perform the full detector simulation ac-

ording to the experimental specifications. However, the default setup does not include a realistic simulation of different backgrounds, which may lead to additional noise and potentially weaken the discrimination performance. In the actual experimental data acquisition, the quasi real-time processing of free-streaming detector data requires an additional step of event building, i.e. the identification of clusters of detector hits that are sufficiently close in time and space. After the event building step, separate events are technically defined and can be processed, also in the approach of this analysis. It is interesting to note that the process of event building could also be improved by using PointNet based models for event characterisation.

The present study was performed on a set of Au+Au collisions at a beam energy of 10 AGeV in the laboratory frame. As mentioned above, the dataset for this study was generated using the UrQMD hybrid model and the CbmRoot package. It consists of 30000 training events and 10000 validation events each for the crossover and first-order phase transition equations of state with a uniform impact parameter (b) distribution from 0 to 7 fm. To study the effects of experimental uncertainties and constraints on the performance of the DL models, the PointNet model was trained on different outputs:

1. First, the final state output (*Dataset 1*), i.e. the particle information directly from the UrQMD model without any acceptance cuts. This dataset contains essentially the full event information and has not been transported through the detector simulation.
2. Second, the final state output within the CBM detector acceptance (*Dataset 2*). This dataset contains final state particles from the UrQMD model within the CBM acceptance range of 2-25° polar angles. This corresponds to a hypothetical, ideal detector output that detects all particles within its acceptance with infinite resolution.
3. Finally, the CbmRoot simulated data (*Dataset 3*), i.e. the final state output of UrQMD, is passed through CbmRoot. This dataset consists of the reconstructed tracks from the digitised particle hits in the simulated CBM detector.

Network architecture

The network architecture used in this study is similar to that used to train the PointNet based models for N_{part} determination. The PointNet based models accept the point cloud in the form of a 2D array where each row is a point (i.e. a track in the event) in the point cloud and each column is an attribute of the point/track. This array is then processed using symmetric, order-invariant operations to extract global features, which are then passed through a fully connected deep neural network to identify the EoS that produced the given point cloud.

The input point cloud is passed through three 1-D convolution layers to extract 128, 256 and 512 feature maps respectively. Batch normalisation layers are present between each convolution layer. An average pooling layer then extracts one global feature of the point cloud from each of the 512 feature maps generated by the final convolution layer. The 512

global features are the input to a 3-layer fully connected deep neural network with 256, 128 and 2 neurons respectively. Batch normalisation and dropout layers (with dropout probability 0.5) are present between each DNN layer. All layers except the final layer use the ReLU activation function. A softmax activation is used on the final layer to classify the EoS. The models use the Adam optimiser with a learning rate of 10^{-5} and categorical cross entropy as the loss function. The models were trained until the network began to overfit the data and the best model in terms of validation accuracy and loss was selected for further analysis.

The network structure and other training parameters were fine-tuned through trial and error to achieve the best performance on the final output (*Dataset 1*). The same network architecture and hyperparameters (but with different input dimensions depending on the dataset) were then used to train the experimental effects model (*Dataset 2,3*). In this way, it was possible to study the response of the same DL network to different experimental constraints.

5.4.1 Performance of the models

As mentioned above, three different input data scenarios were investigated in this study. In the first case (*Dataset 1*), the input for training was the event-by-event list of four-momenta of all particles from UrQMD. The input data has the dimensions $N \times 4$, where N is the maximum number of particles present in an event. Events with fewer particles are filled with zeros to maintain the same input dimensions. In this scenario, the trained PointNet model achieved a validation accuracy of 77.2% for the correct event-wise classification between crossover and phase transition EoS. This accuracy can be improved by combining multiple events to form the input. This was done by randomly selecting K events, i.e. all rows (without replacement) in that event, from the event-by-event lists (along with rows filled with zeros) and concatenating them to create a longer list with dimensions $(K \times N) \times 4$. Note that the combined events are randomly selected from $b=0-7$ fm. A validation accuracy of 99.7% was achieved by the model when the input was the combined data of 15 events, as can be seen in figure 5.37. The model learns a set of unique observables to classify the underlying EoS and the boundaries of these observables for both classes are accurately learned with a combined dataset.

In the second case, the training input was the four-momentum of particles from UrQMD that were within the CBM detector acceptance. Particles outside the CBM acceptance range of a polar angle of $2-25^\circ$ were removed from the events. The validation accuracy in this case was reduced to about 72.2% for the event-by-event input, and the model was able to achieve an accuracy of 99.5% by combining 20 events for the input.

The decrease in accuracy is understandable. Providing the PointNet with only a shortened or partial list of particles increases the difficulty of learning the observables capable of classifying the EoS. The DL model therefore needs a few more events to achieve a classification

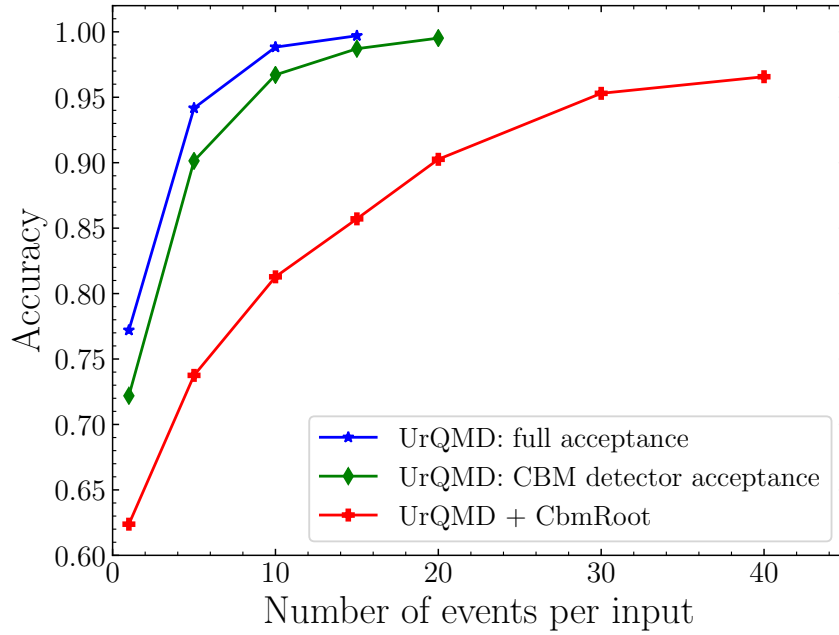


Figure 5.37: Validation accuracy of PointNet models as a function of the number of events combined to create the input. The number of training and validation samples was fixed to 60000 and 20000 respectively for all models, although multiple events were combined to create a sample. While randomly combining events, it was ensured that an event in training sample was never present in a validation sample. The DL models achieved over 99% accuracy with the combination of 15 events in the ideal case, whereas 20 events had to be combined in the presence of an acceptance cut. However, the DL model required a combination of 40 events to achieve about 96% accuracy in a more realistic experimental condition. Note that in all three cases shown in the figure, the hybrid version of UrQMD was used.

accuracy similar to the first case. The models cannot distinguish particles belonging to one event from another. Therefore, it is likely that the unique DL constructed observables are some aggregate quantities, probably within some region of phase space. An acceptance cut could remove some of the information that would otherwise be available (in the first case), and calculating these observables accurately would obviously require more statistics.

In the third dataset, more realistic experimental constraints on acceptance and resolution were introduced. The UrQMD output was passed through the CBM detector simulation and the model was trained on the tracks reconstructed from the particle hits in the MVD and STS detectors of the detector simulation. In this case, the average classification accuracy for single event inputs was only 62.4%. However, after combining 40 events for an input, the accuracy increased again to 96.6%. For this model to achieve a similar performance to the second dataset, the number of events combined to create the input had to be doubled. This model, based on dataset 3 and using 40 events of reconstructed tracks

as input, will be referred to as *Model-1*.

The accuracy of the PointNet models in the three cases as a function of the number of events combined is plotted in figure 5.37. It is clear from the plot that the performance of the DL model is only marginally degraded in the presence of a simple acceptance cut, but there is a large drop in accuracy when a more realistic experimental scenario is considered. This shows that the final state particles have strong features that are characteristic of the macroscopic properties that governed the evolution of the QCD medium. In an experiment, however, these strong features become weaker and more difficult to identify. Uncertainties in the measurements due to detector resolution and randomness in the detected particle spectra due to interactions of particles in the detector reduce the relevant signals in the data. Inefficiencies in reconstruction algorithms and selection cuts also introduce errors into the final data. However, the DL model is able to circumvent these problems by combining more events for decision making. Similar behaviour has also been reported in [214]. Increasing the statistics reduces the stochasticity in the data, thereby improving the predictive power of DL. For example, the global feature used by the PointNet models to classify EoS is the average (given by the average pooling layer) of each feature extracted by the convolution kernels. These averages could be determined more accurately if more sample points were used. In this way, the performance of the PointNet models could be improved by using more events.

It is well known that conventional observables are very sensitive to model parameters such as centrality selection, initial state, freeze-out condition, etc. Therefore, we now investigate in detail the generalisation ability of the PointNet models on these parameters.

Centrality dependence

Model-1, which had an accuracy of 96.6%, was trained on events with impact parameters of 0-7 fm. Although the accuracy is already good enough, the model showed slightly better performance on central events, suggesting a centrality dependence. To see if the accuracy of the model could be increased by selecting a different centrality, a model (*Model-2*) was explicitly trained on events with an impact parameter of 0-3 fm. This model also used the tracks reconstructed by the detector and combined the data from 40 events to form one input. The *Model-2* achieved a prediction accuracy of 99.8% on events with an impact parameter of 0-3 fm: Choosing a smaller centrality bin therefore improved the performance of the model. However, most of the events collected in the experiment will be unusable if we choose only central collisions. To address this issue, a model (*Model-3*) was trained that combined only events with impact parameters 0-3 fm and 3-7 fm separately. The input to this model was a combination of 40 events (reconstructed tracks) from either the 0-3 fm or 3-7 fm impact parameter bin. In addition to this selection of events, the network had 1 additional input to feed the impact parameter bin of the given sample (i.e.; 0 if $b=0-3$ fm and 1 if $b=3-7$ fm). This input is concatenated with other extracted global features and fed into the DNN. The *Model-3* achieved a validation accuracy of about 99.65% for events with impact parameter 0-3 fm and 81.27% for impact parameter 3-7 fm.

The PointNet models can achieve the best performance for central events, assuming they can be accurately identified [288]. However, significant accuracies can also be achieved for peripheral events if they are separated from central events for training.

5.4.2 Dependence on model parameters

We have already shown how PointNet models can be used to correctly classify the nature of the QCD transition with high accuracy over a wide range of centralities or a small range of centralities, depending on the experimental requirements. However, the physical and model parameters were kept constant, i.e. they were assumed to be known exactly. In reality, this is not the case, and to ensure the reliability of the DL model in an experiment, the models must be robust to reasonable changes in the physical parameters of the hydrodynamic event generator. Two such parameters are the starting time of the hydrodynamic evolution (t_{start}), which essentially determines the time at which local equilibrium can be assumed to have been reached, and the particlization energy density (ϵ), which determines the point at which the system begins to fall out of local equilibrium. Since at this energy density particles are emitted from the hydro into the nonequilibrium hadronic rescattering phase, matter below this criterion is effectively not affected by the EoS. To assess the dependence of the DL models on these parameters, the trained PointNet models were tested on events where t_{start} was varied by $\pm 10\%$ and ϵ by $\pm 40\%$ from the training value. The performance of the DL models is shown and compared in figure 5.38. In general, the models seem to achieve an accuracy similar to the validation accuracy as t_{start} or ϵ is decreased. However, the accuracies decrease significantly when t_{start} or ϵ is increased. This effect can be understood by studying the fraction of matter that is below the particlization criterion, and therefore does not carry any information about the EoS, for the different initial and freeze-out conditions. This fraction also varies as a function of the impact parameter, as shown in figure 5.39. The decrease in performance as the duration of the hydrodynamic evolution and the centrality decreases is therefore nicely illustrated by the figure 5.39. It can be seen that as the impact parameter is increased, a smaller fraction of the emitted hadrons experience the dynamics of the phase transition. This explains the higher validation accuracy for *Model-2* compared to *Model-1* and the lower validation accuracy for *Model-3* for events with impact parameters 3-7 fm.

A delayed start time of the hydrodynamic evolution or an increased freeze-out energy density reduces the contribution of the hydrodynamic evolution of the system to the emitted particles and therefore the EoS will have less influence on the final particle spectra. While increasing the duration of the hydrodynamic evolution results in a longer influence of the EoS on the evolution of the medium and thus in a higher accuracy, the decrease in performance may be related to a limitation imposed by the physics, which may not be avoidable.

Similarly, a 40% increase in the freeze-out energy density for $b=0$ fm results in about 50 % of the final particles being emitted before the hydrodynamic evolution even begins. The DL models have to rely on the artefacts left by the EoS in the remaining 50% of the

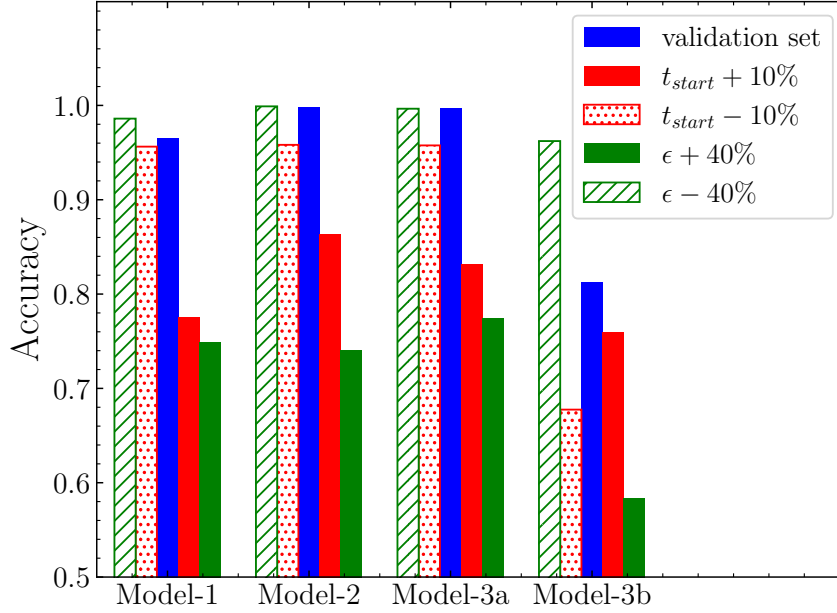


Figure 5.38: Variation in the testing accuracy of the PointNet models with change in t_{start} and ϵ . The blue bars show the validation accuracies of the models, while the other colours represent the testing accuracy on datasets different from the training data. Each testing dataset consisted of 2000 events for each EoS. The *Model-3a* and *Model-3b* are the test results of the *Model-3* on impact parameters 0-3 fm and 3-7 fm respectively.

emitted particles to make a decision. Therefore, the accuracy decreases significantly as the freeze-out energy density increases. However, the decrease in the fraction of emitted particles that undergo hydrodynamic evolution is greater for a 40% increase in the freeze-out energy density than for a 10% increase in t_{start} . Therefore, the drop in accuracy is comparatively smaller when t_{start} is increased by 10%. In short, hadrons from central events with an early start of the hydrodynamic evolution or a reduced freeze-out energy density carry more information about the EoS because they are emitted on average after a longer hydrodynamic evolution.

Results on an unseen EoS

We have shown that the PointNet models can accurately classify the data into one of the two training EoS. However, the actual EoS of the fluid dynamic evolution can be different from those used during training. To understand how the DL model would perform in such a scenario, we tested *Model-1* on an EoS on which it was not trained. On the hadron resonance gas EoS, *Model-1* classified 68% of the samples as crossover and the rest as first order phase transition. As can be seen from figure 5.36, the hadron gas EoS is similar to a crossover EoS. At low energy densities the hadron gas EoS follows the crossover equation of state and at high densities the pressure lies between the phase transition and the crossover

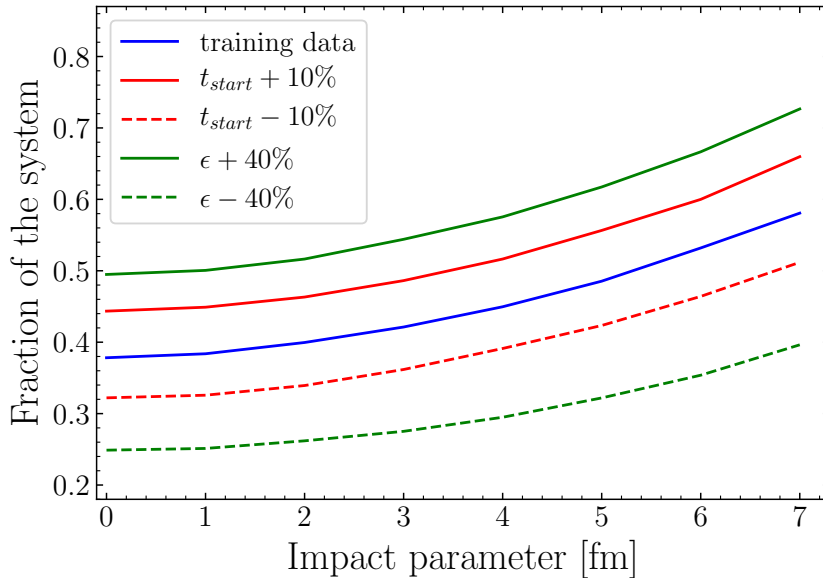


Figure 5.39: Fraction of the medium below the freeze-out energy density at the beginning of hydrodynamics as a function of impact parameter. This is simply the fraction of the medium that does not undergo hydrodynamic evolution. The blue curve represents the initial conditions used to train the model. Curves above the blue curve correspond to initial conditions that reduce the duration of hydrodynamic evolution and vice versa.

equation of state. The hadron gas EoS also doesn't have a plateau-like region of constant pressure, which is characteristic of the phase transition EoS. This explains why the model prefers to predict the hadron gas EoS as a crossover equation of state. The PointNet-based binary classifier of EoS can therefore provide reliable predictions not only for the trained EoS, but also for other similar crossover and phase transition equations of state.

Comparison with a single event classifier

We have shown that the performance of the model can be improved by combining multiple events to train the PointNet models. A recent study [289] pointed out that a single event classifier, when applied to N events, can outperform a classifier trained on combinations of N events if these events are statistically independent. This raises the question of whether an event-by-event EoS classifier, combined over N events, would outperform the combined event models developed in this study. To test this, 20000 validation events from *Dataset-3* were tested using a model trained to classify the EoS of individual events. The final prediction is then defined as the predicted EoS of the majority of events for groups of 40 random events. This procedure achieved an accuracy of 92.01%. At the same time, the *Model-1*, which was trained on combinations of 40 events to make predictions, had an accuracy of 96.6%. So the single event classifier doesn't achieve the accuracy of the combined event classifier. By training the model on combinations of around 25 events, an

accuracy of around 92% can be achieved, whereas the single event classifier needed 40 events to achieve the same accuracy. The superior performance of the PointNet models trained on combinations of multiple events is due to the centrality dependent influence of the EoS on the system. As shown in figure 5.39, a significantly larger fraction of the system is influenced by the provided EoS for a central event, while most of the system is not influenced by the EoS for peripheral events. Therefore, central events contain more information about the EoS that governed their evolution than a peripheral event. When the PointNet is trained on combinations of random events with all centralities, the model can learn to make decisions using the signals from the central events present in the data. A single event classifier, on the other hand, would struggle to correctly classify the peripheral events, which often contain very weak signatures of EoS. This centrality dependent performance bias would further deteriorate the performance of single event classifiers when considering a realistic impact parameter distribution ($P(b) \propto b$) where the central events are rare compared to the peripheral events. Another practical advantage of using combinations of events is that such models can potentially operate on a continuous data stream without event construction or event separation. This can be extremely useful for the CBM experiment, which will require extremely fast analysis methods for the data collected at rates of up to 10 MHz.

Comparison with conventional observations

The PointNet-based models extract global features from the input point cloud using average pooling layers that compute the mean of the per-point feature maps. However, this does not mean that conventional mean observables such as mean transverse momentum ($\langle p_T \rangle$), collective flow (v_2) etc. can be used to classify the EoS as accurately as PointNet models. The above DL models do not require event selection based on centrality, while the traditional observables have a strong centrality dependence. Without centrality selection and high statistics, the traditional observables will not have well-separated boundaries to aid accurate classification. The $\langle p_T \rangle$ and v_2 distributions for 15 events averaged from UrQMD are plotted in figure 5.40. It is clear from the plots that the distributions of these observables, after averaging over only 15 events, overlap significantly and cannot be used to classify the two classes of data as accurately as the PointNet model. We have also checked that simply averaging the different components of the input features in the PointNet does not lead to easily distinguishable distributions either.

In other words, the PointNet model is able to learn unique observables that produce near perfect classification accuracy from only the combined input of 15 random events. The PointNet model is even able to learn such observables from an "experiment-like data" where the reconstructed tracks are the input (*Model-1*). Below we describe a method for interpreting the decision-making process of our PointNet model, which helps to understand why the model outperforms conventional observables.

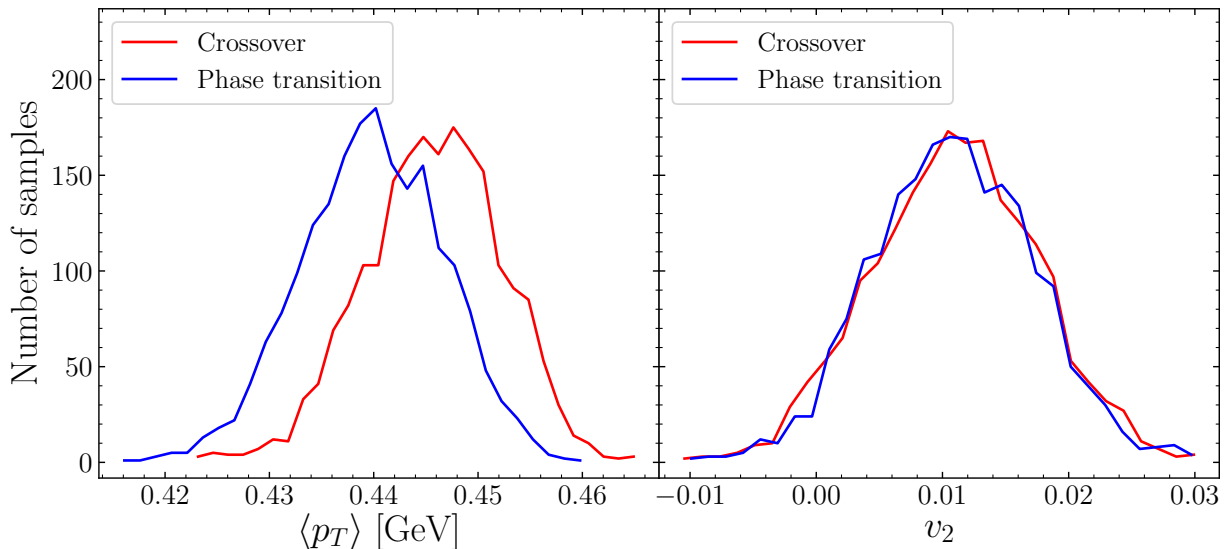


Figure 5.40: Distributions of mean transverse momentum (left) and elliptical flow (right) for crossover and first order phase transitions. The values are averaged over all particles from 15 UrQMD events with $b=0-7$ fm (*Dataset-1*). The distributions have significant overlap such that it is not possible to classify the EoS using these observables, while the DL model with 15 events combined input achieves an accuracy of 99.7%.

5.4.3 Interpreting the PointNet model

It is generally interesting to show how the PointNet model is able to accurately discriminate the QCD transitions even under conditions where the conventional observables fail. However, interpreting the inner workings of a neural network using conventional concepts is not straightforward, especially when the inputs are order-invariant, as in our case. Nevertheless, [182] discusses a method to visualise the critical points of a point cloud. The PointNet architecture consists of several 1-D convolution layers followed by a symmetric function that converts each feature map produced by the last convolution layer into a single number. These numbers, which are considered global features of the point cloud, form the input to a fully connected neural network which classifies the input point cloud. In [182], a max pooling layer is used as the symmetric function to extract the global features. In other words, the feature with the largest numerical value in each feature map given by the last convolution layer becomes the input to the fully connected neural network. Each of these features can be traced back to the original point in the point cloud. Such points are then defined as the critical points of the point cloud, as they directly induce the input to the DNN that classifies the data.

We have extended this method to analyse the decision process of our EoS classifier. Our model generates 512 global features for each point cloud. These global features are then used by a fully connected network to perform the classification. Unlike the method described above, the symmetric function used in our study to generate these features is

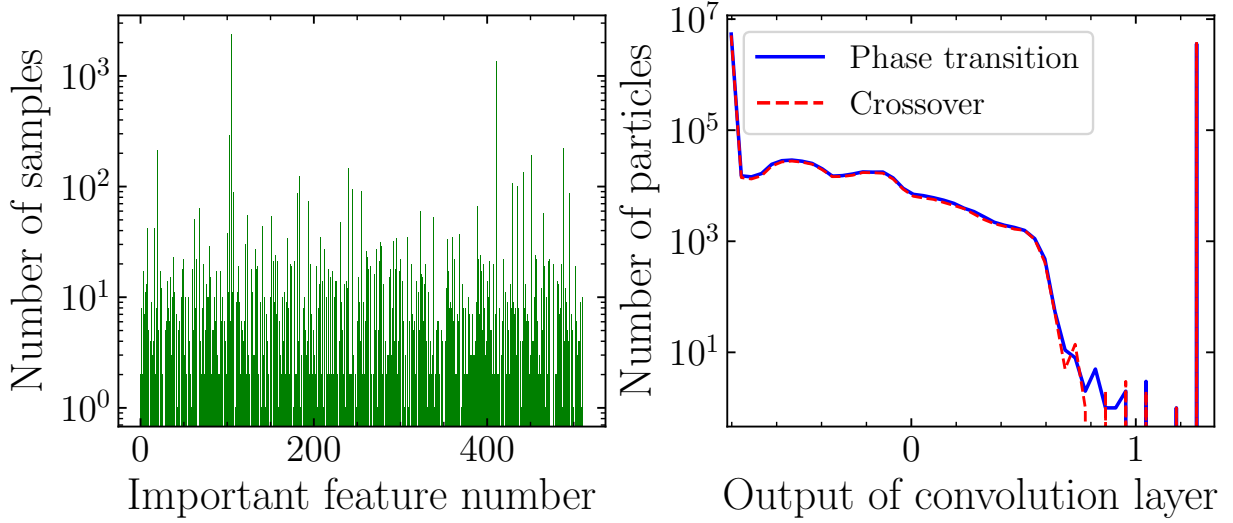


Figure 5.41: Left: Distribution of feature numbers of the most important feature for 10000 pairs of events. An important feature is the global feature that has the largest difference in its values for the two classes. Out of the 512 global features, feature numbers 104 and 410 have the highest frequency, they are the most important feature for about 24% and 14% of the pairs of samples respectively. Right: The output of the convolution layer for global feature 104 (F-104). The plot is generated from about 350 samples for each class whose important feature index is 104.

average pooling. This has serious implications for interpretability, as the average of the feature map, given by the average pooling layer, cannot be uniquely traced back to a single point in the point cloud. However, we can still try to identify the features that seem to be most important for the classification task, and then analyse which properties of the input point cloud affect these features. To do this, we calculate the values of all 512 global features for 20000 samples of the crossover and phase transition events (10000 each). The global feature with the largest difference (in numerical value) is then selected for each pair of crossover and phase transition events. This feature can be considered as an important feature for the given pair of samples. By repeating this for all 10000 pairs, it is possible to find out which global features are the most important global features for most pairs of samples. The distribution of the important features (as defined by their feature number from 0 to 511), within the total 10000 pairs of samples, is shown on the left side of figure 5.41.

It can be seen that for about 2400 pairs of input samples, feature number 104 is an important global feature. The feature map from which feature number 104 is calculated is shown in the right plot of figure 5.41. We can see that the values in the feature map distribution are mostly concentrated in two bins, one around -0.8 and another around 1.25. To reiterate, each particle in the input point cloud contributes to some value in the output convolutional layer. In this case, most particles contribute to either a value around zero

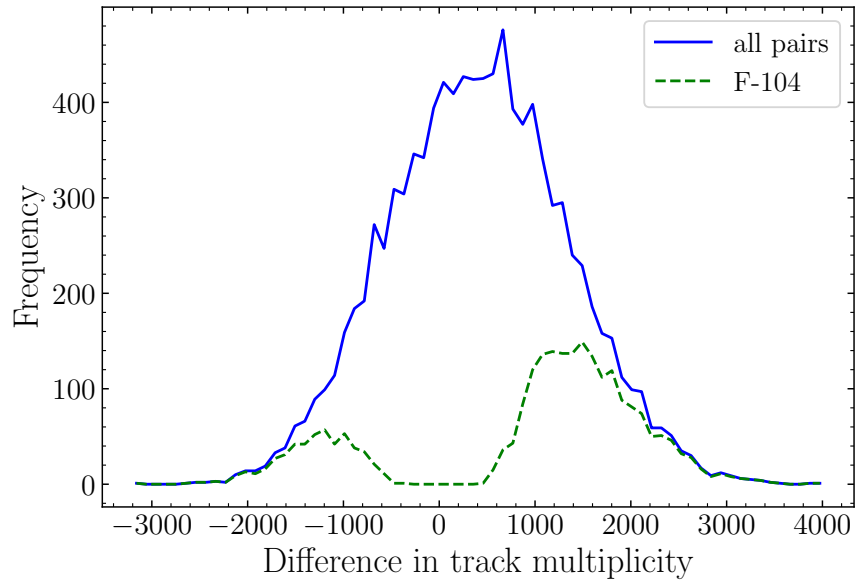


Figure 5.42: Distribution of track multiplicity difference. The difference in the number of tracks is calculated for 10000 pairs of samples (first order phase transition - crossover) and plotted in blue. The green colour represents the multiplicity difference of all sample pairs whose main feature is 104 (F-104). Most of the pairs of events whose main feature is feature number 104 contain a significantly higher number of tracks for first order phase transition samples compared to crossover samples.

or a value around 1.25. The average is then mainly determined by the relative number of particles in the two prominent bins. So we tracked the particles in the two bins and looked at their properties separately. We found that all the particles contributing to the right hand peak in the histogram (around 1.25) were the fake/empty particles (with zeros for the features) that we added to the input data to keep the input dimensions identical for all samples. Most of the real particles formed the peak on the left (around -0.8) and very few particles had a value between the two peaks. Therefore, the global feature -104 is simply a feature that estimates the total track multiplicity in the sample. In other words, track multiplicity is an important feature used to classify the EoS. However, just because track multiplicity is an important global feature learned by the model does not mean that multiplicity alone is sufficient for classification.

Figure 5.42 shows the distribution of the track multiplicity difference (phase transition - crossover) for both classes for all pairs of test samples, as well as for pairs where feature number 104 (i.e. track multiplicity) is the important feature. It is evident that for the pair of samples where feature number 104 (F-104) is the important feature, there is a significant difference in their multiplicities for the two classes. For most of the pairs where this feature is important, phase transition samples contain significantly more particles than a crossover sample with F-104.

Advantages of the DL approach

The PointNet models learn the global features that can classify the EoS despite the uncertainties in the data arising from a discrete particle spectra with final state effects, detector effects and inefficiencies of the reconstruction algorithms. It is noteworthy that the PointNet models can achieve a classification accuracy of up to 96.6% from the reconstructed particle tracks of just 40 collision events. The PointNet models can operate on a wide range of impact parameters, but they achieve best performance when only central collisions are selected for analysis. However, it is also possible to include non-central collisions in the analysis if central collision events are not mixed with non-central collisions. The predictions of the DL models were also robust to some changes in the physical parameters such as the initial condition. The performance of the models was consistent when t_{start} or ϵ was decreased from the training value, while a decrease in performance is observed when these parameters are increased. This is interpreted as a physical consequence of a decreased influence of the hydrodynamic evolution and the EoS on the emitted particles. Nevertheless, the DL models show good performance compared to conventional averaged event features such as $\langle p_T \rangle$ or v_2 , which have similar values for both classes. The values of these features are also very different for different model parameters.

In order for the CBM experiment to fully exploit the high event rates, accurate online event selection and analysis techniques are required. The PointNet-based EoS meter can serve this purpose and can be coupled with other DL-based algorithms (e.g. centrality meter [288]) for comprehensive online event analysis. In fact, we now have a novel method that any future heavy-ion experiment can easily adapt for accurate online determination of the EoS.

Chapter 6

Summary

The properties of strongly interacting matter at high temperatures and/or densities are studied in the laboratory via heavy-ion collisions. The ultimate goal of the experimental programmes is to construct a phase diagram for QCD matter that reveals the phase boundaries, the nature of the transitions at the boundary, and the critical regions. Currently, the focus is mainly on intermediate energy heavy-ion collisions probing QCD matter at high baryon densities in order to search for several interesting structures in the QCD phase diagram, such as a conjectured first- or second-order phase transition and a corresponding critical endpoint. First principle lattice QCD studies at vanishing and small baryon chemical potentials predict a smooth crossover transition from a hot gas of hadronic resonances to a chirally restored phase of strongly interacting quarks and gluons. However, at high net baryon densities, i.e. large chemical potentials, direct lattice QCD simulations are currently unavailable due to the fermionic sign problem. Therefore, QCD motivated effective models as well as direct experimental evidence are used to search for a phase transition or critical endpoint.

The experimental measurements for various conventional observables are compared with expensive model calculations to infer the physics governing the evolution of the matter created in the collisions. However, this comparison is not straightforward. The experimental data must undergo several pre-processing steps, such as track reconstruction, particle identification, event building and centrality selection, before different observables can be calculated. For a consistent comparison of these experimental observables with theoretical model predictions, the model calculations should take into account the phase space acceptance and detector efficiencies of the experiment through simplified acceptance and efficiency cuts or sophisticated detector simulations. The pre-processing algorithms introduce additional uncertainties and biases into the data that can skew the results of the analysis. Furthermore, such methods use iterative algorithms, which can be extremely slow and impractical for future high event rate experiments requiring online processing of experimental data. In addition, to complicate the analysis process, a combined inference based on multiple observables is often necessary to extract the properties of QCD matter

such as the equation of state..

The aim of this work was to develop novel AI-based methods to bridge this gap between theory and experiment. The main focus was on building AI tools that can work directly with detector outputs such as particle hits/tracks measured in intermediate energy heavy-ion collisions. In addition to AI that works directly on detector-level experimental data, methods to consistently compare model predictions for conventional observables with experimental data were also investigated. The CBM experiment at FAIR was used as an example to illustrate the capabilities of the developed DL models, as it is a unique next generation intermediate energy experiment that will measure intermediate energy collisions at unprecedented intensities.

After a brief introduction to QCD, heavy-ion collisions and AI for heavy-ion collisions in chapter 1, various heavy-ion programmes around the world, with particular emphasis on the physics programme at the FAIR accelerator facility and the CBM experiment, were presented in chapter 2. The experimental challenges associated with the analysis of the measured data were also briefly discussed in chapter 2. In chapter 3 different models for the simulation of heavy-ion collisions at intermediate beam energies were discussed. The advantages and limitations of different models for heavy-ion collisions were examined. The emphasis here was on understanding how different models incorporate the EoS, which governs the evolution of the system. In the hydrodynamic description of collisions and in the UrQMD hybrid model, which uses a hydrodynamic intermediate stage for evolution, the EoS enters the model as a free input necessary to solve the hydrodynamic equations of motion. However, the introduction of an equation of state is not straightforward in a transport model such as UrQMD. Non-trivial hadronic interactions can be introduced in UrQMD through the potential energy term, which enters the non-relativistic QMD equations of motion. Thus, an arbitrary EoS can be implemented in the QMD part of UrQMD if the potential energy per baryon is known for the model. This method was used to implement a realistic CMF EoS in UrQMD and to study its influence on the evolution of the bulk properties of the matter produced in the collision. The results were also compared with hydrodynamic simulations using the same EoS to establish the reliability of the method. The bulk density evolution showed good agreement with hydrodynamic simulations when the same EoS is used in both cases. At the same time, the densities obtained are strongly dependent on the EoS used. This suggests that observables sensitive to the initial compression phase and the maximum compression achieved can be used to study the EoS at high baryon densities. However, the non-equilibrium effects cause the temperature of the system in UrQMD to be higher than that obtained in hydrodynamic simulations. Nevertheless, this method employs a consistent treatment of the equation of state throughout the evolution of the system and can be used to study the effects of an EoS in the initial compression phase of the collision at low energies.

The basic principles of AI and different AI methods were introduced in chapter 4. The working of a fully connected neural network and convolution neural networks were explained in detail. The CNN based deep learning models are not optimised for learning from ex-

perimental data. The PointNet based models were introduced as a novel DL method that can be trained directly on hit/track information of particles measured in a detector. The general structure of the PointNet architecture and its functioning were described in detail. The PointNet model is specialised to learn from order-invariant point cloud data, which is a natural representation for detector data. The PointNet model uses 1-D convolution to extract order-invariant per-point feature maps, which are then transformed into a global event feature through symmetric operations. The extracted global event features are fed into a fully connected neural network to regress or classify the target variable. In addition to the PointNet based DL methods, the Bayesian inference technique and its principles have also been explained in this chapter.

Chapter 5 began with a comparative study of the Glauber MC model used by experiments for centrality estimation and the UrQMD transport model. It was found that the centrality determination and the estimated fluctuations of N_{part} suffer from strong model dependencies for Au-Au collisions at 1.23 AGeV. The Glauber MC model used in the experiments to relate the measured track multiplicity to the impact parameter or N_{part} predicts a completely different N_{part} distribution compared to the microscopic transport theory based UrQMD cascade model. This strong model dependence of N_{part} can bias the results of the experimental analysis if the N_{part} used is not consistent throughout the analysis and the final model-data comparison. To demonstrate this effect, the charged pion production and the proton and light nuclei rapidity spectra at $E_{lab} = 1.23A$ GeV were investigated and the results were compared with HADES and STAR measurements. It was found that the pion multiplicity per participant can be highly sensitive to the model used to estimate the underlying N_{part} distribution for a given centrality class. It is suggested that studying observables such as pion multiplicity as a function of centrality instead of N_{part} can partially avoid the explicit model dependence of N_{part} that arises when comparing experimental data with model predictions. Nevertheless, this does not guarantee that the experimental data and the model being compared have a similar distribution of N_{part} .

The model dependence of N_{part} has measurable consequences for the observed rapidity distributions of free protons and light nuclei. Here again, preliminary data from the HADES experiment show a significant reduction in the proton dN/dy compared to UrQMD, consistent with a significantly smaller N_{part} , an effect not observed in data from the STAR experiment. Obviously, understanding these inconsistencies is also important for the interpretation of observables such as pion multiplicity and proton number fluctuations.

Having established the issues with the conventional method for centrality estimation, different AI methods are introduced in chapter 5 for estimation of event centrality and interaction volume. In particular PointNet based models were trained to reconstruct the impact parameter of collisions from the hits and/or reconstructed track of particles in 10 AGeV Au-Au collisions at the CBM experiment. In order to develop models that can be used in experiments, a dataset that closely mimics the experimental data was prepared. To achieve this, the output from UrQMD was passed through a complex pipeline consisting of a GEANT3 based CBM detector simulation that performs particle transport, hit

digitisation and event reconstruction. It was found that the PointNet models can perform accurate reconstruction of the impact parameters in the range 2-14 fm. A model using hits from the MVD detector and tracks reconstructed from hits in the MVD and STS to predict the impact parameter had a validation MSE of about 0.39 fm^2 . Unlike conventional Glauber MC-based centrality selection, which only provides an expected impact parameter distribution for events belonging to a given centrality class, the PointNet models can perform accurate impact parameter reconstruction on an event-by-event basis. The idea of impact parameter reconstruction has also been extended to the PANDA experiment at FAIR. For antiproton-neon collisions at $p_{lab} = 15 \text{ GeV}$, a model trained on the point cloud of the momentum four vector and the final state particle charge had a validation MSE of about 1 fm^2 . A system size dependence of the performance was also observed, where the prediction accuracy decreased with decreasing system size. The PointNet based models were then adapted to determine the N_{part} in collisions. It was found that the models can also perform accurate, event-by-event N_{part} determination for $10 A \text{ GeV}$ Au-Au collisions in the CBM experiment with a validation MAE of about 8.2. For $1.23 A \text{ GeV}$ Au-Au collisions at the HADES experiment, the PointNet models showed an MAE of about 11.6. Nevertheless, the PointNet based models provide event-by-event N_{part} consistent with a theoretical model. This avoids the inconsistent use of Glauber MC predicted N_{part} for event selection when comparing experimental data with a theoretical model such as UrQMD. The PointNet based models can perform fast and accurate event-by-event impact parameter and N_{part} determination in the CBM experiment. Thus, one can essentially replace Glauber MC based centrality selection and event characterisation with the superior DL models. Such models can also be used in experiments for online analysis and event characterisation of free streaming detector output.

One of the main goals of the heavy-ion programmes worldwide is to study the equation of state of hot and dense QCD matter. In the last part of the thesis, AI methods were employed to study the equation of state at high baryon densities. First, a Bayesian inference was performed to constrain the density dependence of the equation of state from the available experimental measurements of the elliptical flow and the mean transverse kinetic energy of mid rapidity protons in intermediate energy collisions. The UrQMD model, extended to include arbitrary potentials (or equivalently the EoSs), was used in this study. Gaussian process models were trained as fast emulators for the UrQMD model to perform fast MCMC sampling. A polynomial parameterisation for the density dependent potential was used and Bayesian inference was performed to construct the joint posterior for the polynomial coefficients. The experimental data constrain the posterior constructed in this way for the EoS for densities up to $4n_0$. However, beyond $3n_0$ the shape of the posterior depends on the choice of observables used. As a result, the speed of sound extracted for these posteriors show obvious differences. The EoS extracted using all available data points is in good agreement with the constraints from BNSMs with a stiff EoS for densities up to $4n_0$ and no phase transition. The inference encounters a tension in the measurements of $\langle m_T \rangle - m_0$ and v_2 at a collision energy of $\approx 4 \text{ GeV}$. This could indicate large uncertainties in the measurements, or alternatively the inability of the underlying model to describe the

observables with a given input EoS. It should be noted that the data come from different experiments and were carried out over different time periods. The differences in acceptance, resolution, statistics and even methods of analysis of the experimental data make it difficult for us to pinpoint the exact sources of these effects.

Bayesian inference can constrain the high-density QCD EoS using experimental data on v_2 and $\langle m_T \rangle - m_0$ of protons. Such an analysis based on HIC data can verify the properties of dense QCD matter extracted from neutron star observations and complements astrophysical studies to extract the finite temperature EoS from BNSM merger signals and constrain its dependence on the symmetry energy. However, tighter constraints and fully conclusive statements on the EoS beyond density $3n_0$ require accurate, high-statistics data in the whole beam energy range of 2-10 GeV, which will hopefully be provided by the beam energy scan programme of STAR-FXT at RHIC, the upcoming CBM experiment at FAIR, and future experiments at HIAF and NICA.

Finally, it was shown that the PointNet based models can also be used to identify the equation of state in the CBM experiment. PointNet based models trained to classify a phase transition EoS from a crossover EoS from the reconstructed track information in the CBM experiment were able to achieve almost perfect prediction accuracy. Despite the uncertainties arising from limited detector acceptance and biases in the reconstruction algorithms, the PointNet based model was able to learn the features that can accurately identify the underlying physics of the collision. The model was also found to be robust to some changes in the model parameters. In short, this demonstrates the flexibility of PointNet based models in the study of heavy-ion collisions. The PointNet based model can not only identify the geometric event features, such as the impact parameter or the N_{part} , but can also extract abstract physical features, such as the EoS, directly from the detector outputs.

6.1 Outlook

In this work, several artificial intelligence techniques to study heavy-ion collisions at high baryon density were developed. The Bayesian analysis to constrain the high density EoS suggests that the flow observables indeed carry valuable information that can tightly constrain the EoS of high density nuclear matter. However, it is noted that when approaching higher beam energies, which would be important to extend the constraints to higher temperatures/densities, the currently used transport model needs to incorporate further finite-temperature and possible partonic matter effects together with relativistic corrections, which has to be investigated in future studies. Further efforts should be made to develop and improve the theoretical models to consistently incorporate different density dependent EoSs for the study of systematic uncertainties. In addition, other observables such as the higher order flow coefficients and v_1 can be included in the Bayesian analysis, if computational constraints allow, for a more comprehensive constraint on the EoS in the future.

PointNet based DL models that can extract very complex universal event features from basic initial event information available from heavy-ion collision experiments were developed in this work. With the use of PointNet based models it is now possible to accurately extract the event specific impact parameter and N_{part} in heavy-ion collision experiments. PointNet based models are even able to classify events by very abstract event features such as the EoS present during the hot and dense phase of the collision, i.e. whether a phase transition was present or not. It is shown for the first time how DL models can be used in heavy-ion collision experiments to identify phase transitions directly from experimental output.

The use of experimental output, such as particle hits, can eliminate possible biases in the data that may appear in later stages of data processing. The point cloud representation of the data requires minimal pre-processing before being fed into the DL model. This allows the model to be used in the experiment for rapid online analysis of experimental data. Due to their ability to detect global features in the input, PointNet based models can also be easily adapted to analyse any other global event feature of heavy-ion collisions. Although the PointNet based models developed in this work have been focused for use in the CBM experiment, the models can be easily extended for use in other experiments.

The use of these DL models in the experiment would also require further investigation into the robustness of the model to the expected detector noise and efficiency. Further studies on the scalability of the prediction speed on multiple GPUs and the possibility of incorporating other selection criteria are also important for the use of PointNet based models for online event characterisation and analysis. The PointNet based EoS meter can be extended in the future by incorporating more equation of states, making it a multi-class classification problem. Such models can be used in experiments as an online, physics based event selection technique. It would also be interesting to study the performance of DL models in a continuous data stream and in the presence of detector noise, event pileup, etc. Studies on training the DL models on low-level detector data, such as the signals from the readout channels, and applying them directly to the detectors using FPGAs is another interesting direction that could be extremely beneficial for the CBM experiment. Such methods can be used for ultra-fast event selection and analysis based on yet unachievable complex event features.

Appendix A

Equations of state

A.1 The hadron resonance gas model

The hadron resonance gas model is an approximation to confined hadronic QCD matter [290]. It is based on the assumption that a gas of interacting hadrons can be described by including all hadron species and their resonances as explicit degrees of freedom in the partition function. This partition function then mimics the fundamental thermodynamic properties of QCD at low temperatures and small densities. The HRG has been shown to successfully describe the properties of lattice QCD thermodynamics below the chiral transition [291–298]. However, due to the lack of many-body and long-range interactions, the model is unable to describe basic features of QCD phenomenology such as a bound nuclear ground state or deconfinement. Several extensions of the model have been developed over the years (for a survey see [299–305]). However, all modifications have similar shortcomings as the few-parameter description of the EoS in the Skyrme model. A comparison of hydro simulations with an HRG equation of state and UrQMD in cascade mode has been used as a reference to study the effects of instantaneous equilibration on the dynamics [48].

A.2 The chiral mean field model

The CMF is a mean-field model that describes several aspects of QCD phenomenology. It has been successfully applied to the analysis of lattice QCD data [306], the description of cold neutron stars [164], and has been used as the EoS in the hydrodynamic simulations of both heavy-ion collisions and binary neutron star mergers [72, 307]. The CMF includes the transition between quarks and hadronic degrees of freedom, the liquid-vapour transition in nuclear matter, and chiral symmetry restoration. Parity doubling introduces heavy parity partners to the baryons of the lowest octet [308, 309]. The baryons and their parity partners interact via mesonic mean fields (attractive scalar σ , ζ and repulsive ω , ρ , ϕ

meson exchanges). The effective masses of the parity partners depend on the chiral fields, so the partners become mass-degenerate as the chiral symmetry is restored. A detailed description of the CMF model and its parameters can be found in [306].

In the model, the effective masses of the ground state octet baryons and their parity partners (assuming isospin symmetry) read [308]:

$$\begin{aligned}
 m_{b\pm}^* &= \sqrt{\left[(g_{\sigma b}^{(1)}\sigma + g_{\zeta b}^{(1)}\zeta)^2 + (m_0 + n_s m_s)^2 \right]} \\
 &\pm g_{\sigma b}^{(2)}\sigma,
 \end{aligned}
 \tag{A.1}$$

where the various coupling constants $g_{*b}^{(*)}$ are determined by vacuum masses and nuclear matter properties. m_0 refers to a bare mass term of the baryons which is not generated by the breaking of chiral symmetry, and $n_s m_s$ is the $SU(3)_f$ -breaking mass term which generates an explicit mass corresponding to the strangeness n_s of the baryon. The single-particle energy of the baryons thus becomes a function of their momentum k and effective masses: $E^* = \sqrt{k^2 + m_b^{*2}}$.

Similar to the effective mass m_b^* , which is modified by the scalar interactions, the vector interactions lead to a modification of the effective chemical potentials for the baryons and their parity partners:

$$\mu_b^* = \mu_b - g_{\omega b}\omega - g_{\phi b}\phi - g_{\rho b}\rho.
 \tag{A.2}$$

Note that the couplings of nucleons and hyperons to the mean fields were fixed to reproduce nuclear binding energies $E_0/B \approx -15.2$ MeV as well as the asymmetry energy $S_0 \approx 31.9$ MeV, and incompressibility $K_0 \approx 267$ MeV.

The CMF EoS along different trajectories of fixed entropy per baryon is shown in Fig. A.1. This plot is useful because one can see several relevant features in the CMF-EoS. First, along the curve at zero entropy per baryon ($T = 0$) a small kink in the pressure is observed, indicating a very weak phase transition around four times the saturation density. This kink disappears at higher entropies per baryon. Secondly, for values of S/A up to 10, the pressure depends very little on the finite temperature and is dominated by the density dependence. Finally, we also show the $T = 0$ EoS in the HRG model as a grey line compared to the corresponding black line of the CMF. The CMF clearly shows a much larger pressure due to the mean field interactions, which will lead to observable effects in the dynamical simulations.

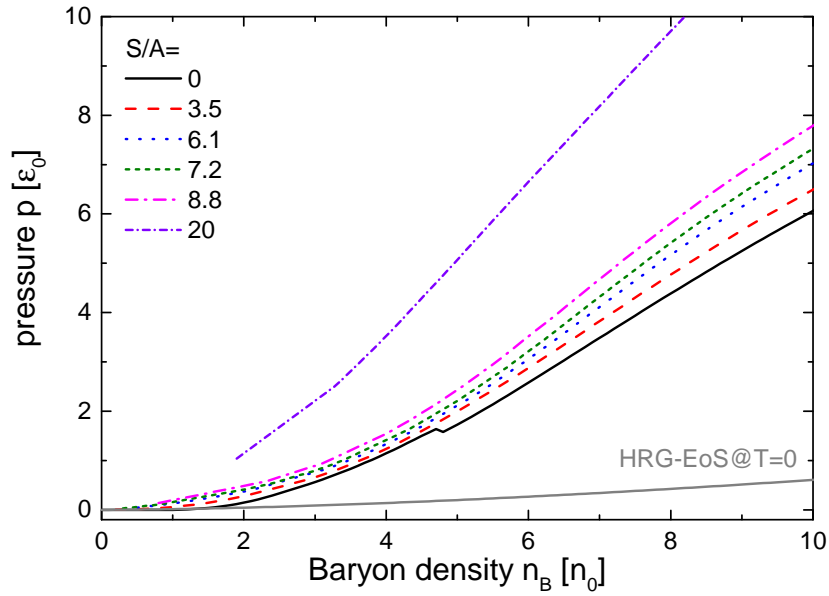


Figure A.1: The CMF equation of state, plotted as pressure as a function of baryon density, for different values of constant entropy per baryon (S/A). The black solid line corresponds to the CMF-EoS at zero temperature, where around $4n_0$ a small kink in the pressure due to the chiral phase transition can be observed. The same relation for the HRG EoS at vanishing temperature is also shown as a grey line. The pressure in the HRG is significantly lower than in the CMF model.

Bibliography

- [1] H. Stoecker and W. Greiner, “High-Energy Heavy Ion Collisions: Probing the Equation of State of Highly Excited Hadronic Matter,” *Phys. Rept.*, vol. 137, pp. 277–392, 1986.
- [2] H. Stoecker, J. A. Maruhn, and W. Greiner, “Collective sideward flow of nuclear matter in violent high-energy heavy ion collisions,” *Phys. Rev. Lett.*, vol. 44, p. 725, 1980.
- [3] H. Kruse, B. V. Jacak, and H. Stoecker, “Microscopic theory of pion production and sideways flow in heavy ion collisions,” *Phys. Rev. Lett.*, vol. 54, pp. 289–292, 1985.
- [4] W. Scheid, H. Muller, and W. Greiner, “Nuclear Shock Waves in Heavy-Ion Collisions,” *Phys. Rev. Lett.*, vol. 32, pp. 741–745, 1974.
- [5] W. Scheid, R. Ligensa, and W. Greiner, “Ion-Ion Potentials and the Compressibility of Nuclear Matter,” *Phys. Rev. Lett.*, vol. 21, no. 21, p. 1479, 1968.
- [6] M. I. Sobel, H. A. Bethe, P. J. Siemens, and J. P. Bondorf, “Shock Waves in Colliding Nuclei,” *Nucl. Phys. A*, vol. 251, pp. 502–529, 1975.
- [7] H. G. Baumgardt, J. U. Schott, Y. Sakamoto, E. Schopper, H. Stoecker, J. Hofmann, W. Scheid, and W. Greiner, “Shock Waves and MACH Cones in Fast Nucleus-Nucleus Collisions,” *Z. Phys. A*, vol. 273, pp. 359–371, 1975.
- [8] J. Hofmann, H. Stoecker, U. W. Heinz, W. Scheid, and W. Greiner, “Possibility of Detecting Density Isomers in High Density Nuclear MACH Shock Waves,” *Phys. Rev. Lett.*, vol. 36, pp. 88–91, 1976.
- [9] H. H. Gutbrod, A. M. Poskanzer, and H. G. Ritter, “PLASTIC BALL EXPERIMENTS,” *Rept. Prog. Phys.*, vol. 52, p. 1267, 1989.
- [10] A. Sandoval *et al.*, “STREAMER CHAMBER EXPERIMENTS,” *Nucl. Phys. A*, vol. 400, p. 365C, 1983.
- [11] J. Barale, “Performance of the Bevalac,” *IEEE Trans. Nucl. Sci.*, vol. 22, pp. 1672–1674, 1975.

BIBLIOGRAPHY

- [12] R. Stock *et al.*, “COMPRESSION EFFECTS IN RELATIVISTIC NUCLEUS NUCLEUS COLLISIONS,” *Phys. Rev. Lett.*, vol. 49, pp. 1236–1239, 1982.
- [13] H. H. Gutbrod, B. W. Kolb, H. R. Schmidt, A. M. Poskanzer, H. G. Ritter, and K. H. Kampert, “A New Component of the Collective Flow in Relativistic Heavy Ion Collisions,” *Phys. Lett. B*, vol. 216, pp. 267–271, 1989.
- [14] K. G. R. Doss *et al.*, “Nuclear Collective Flow as a Function of Projectile Energy and Mass,” *Phys. Rev. Lett.*, vol. 57, pp. 302–305, 1986.
- [15] D. Beavis, S. Y. Chu, S. Y. Fung, W. Gorn, A. Huie, D. Keane, J. J. Lu, R. T. Poe, B. C. Shen, and G. J. VanDalen, “MEASUREMENT OF KINETIC FLOW PARAMETERS FOR RELATIVISTIC COLLISIONS OF Ne ON NaF AND AR ON Pb-30-4,” *Phys. Rev. C*, vol. 27, pp. 2443–2446, 1983.
- [16] S. A. Voloshin, A. M. Poskanzer, and R. Snellings, “Collective phenomena in non-central nuclear collisions,” *Landolt-Bornstein*, vol. 23, pp. 293–333, 2010.
- [17] U. Heinz and M. Jacob, “Evidence for a new state of matter: An assessment of the results from the cern lead beam programme,” *arXiv preprint nucl-th/0002042*, 2000.
- [18] I. Arsene *et al.*, “Quark gluon plasma and color glass condensate at RHIC? The Perspective from the BRAHMS experiment,” *Nucl. Phys. A*, vol. 757, pp. 1–27, 2005.
- [19] K. Adcox *et al.*, “Formation of dense partonic matter in relativistic nucleus-nucleus collisions at RHIC: Experimental evaluation by the PHENIX collaboration,” *Nucl. Phys. A*, vol. 757, pp. 184–283, 2005.
- [20] B. B. Back *et al.*, “The PHOBOS perspective on discoveries at RHIC,” *Nucl. Phys. A*, vol. 757, pp. 28–101, 2005.
- [21] J. Adams *et al.*, “Experimental and theoretical challenges in the search for the quark gluon plasma: The STAR Collaboration’s critical assessment of the evidence from RHIC collisions,” *Nucl. Phys. A*, vol. 757, pp. 102–183, 2005.
- [22] Y. Aoki, G. Endrodi, Z. Fodor, S. D. Katz, and K. K. Szabo, “The Order of the quantum chromodynamics transition predicted by the standard model of particle physics,” *Nature*, vol. 443, pp. 675–678, 2006.
- [23] S. Borsanyi, Z. Fodor, C. Hoelbling, S. D. Katz, S. Krieg, and K. K. Szabo, “Full result for the QCD equation of state with 2+1 flavors,” *Phys. Lett. B*, vol. 730, pp. 99–104, 2014.
- [24] A. Bazavov *et al.*, “Equation of state in (2+1)-flavor QCD,” *Phys. Rev. D*, vol. 90, p. 094503, 2014.
- [25] S. Borsanyi, G. Endrodi, Z. Fodor, A. Jakovac, S. D. Katz, S. Krieg, C. Ratti, and K. K. Szabo, “The QCD equation of state with dynamical quarks,” *JHEP*, vol. 11, p. 077, 2010.

- [26] K. Fukushima and T. Hatsuda, “The phase diagram of dense QCD,” *Rept. Prog. Phys.*, vol. 74, p. 014001, 2011.
- [27] J. B. Kogut, M. Stone, H. W. Wyld, W. R. Gibbs, J. Shigemitsu, S. H. Shenker, and D. K. Sinclair, “Deconfinement and Chiral Symmetry Restoration at Finite Temperatures in SU(2) and SU(3) Gauge Theories,” *Phys. Rev. Lett.*, vol. 50, p. 393, 1983.
- [28] <https://www.gsi.de/work/forschung/theorie/theory-new/hot-and-dense-qcd>. Accessed: 2023-02-16.
- [29] J. Pochodzalla *et al.*, “Probing the nuclear liquid - gas phase transition,” *Phys. Rev. Lett.*, vol. 75, pp. 1040–1043, 1995.
- [30] B. Borderie and M. F. Rivet, “Nuclear multifragmentation and phase transition for hot nuclei,” *Prog. Part. Nucl. Phys.*, vol. 61, pp. 551–601, 2008.
- [31] L. McLerran and R. D. Pisarski, “Phases of cold, dense quarks at large $N(c)$,” *Nucl. Phys. A*, vol. 796, pp. 83–100, 2007.
- [32] D. H. Rischke, “The Quark gluon plasma in equilibrium,” *Prog. Part. Nucl. Phys.*, vol. 52, pp. 197–296, 2004.
- [33] M. G. Alford, K. Rajagopal, and F. Wilczek, “QCD at finite baryon density: Nucleon droplets and color superconductivity,” *Phys. Lett. B*, vol. 422, pp. 247–256, 1998.
- [34] J. N. Guenther, R. Bellwied, S. Borsanyi, Z. Fodor, S. D. Katz, A. Pasztor, C. Ratti, and K. K. Szabó, “The QCD equation of state at finite density from analytical continuation,” *Nucl. Phys. A*, vol. 967, pp. 720–723, 2017.
- [35] M. A. Stephanov, “Non-Gaussian fluctuations near the QCD critical point,” *Phys. Rev. Lett.*, vol. 102, p. 032301, 2009.
- [36] M. A. Stephanov, “On the sign of kurtosis near the QCD critical point,” *Phys. Rev. Lett.*, vol. 107, p. 052301, 2011.
- [37] M. Bluhm *et al.*, “Dynamics of critical fluctuations: Theory – phenomenology – heavy-ion collisions,” *Nucl. Phys. A*, vol. 1003, p. 122016, 2020.
- [38] G. F. Bertsch and S. Das Gupta, “A Guide to microscopic models for intermediate-energy heavy ion collisions,” *Phys. Rept.*, vol. 160, pp. 189–233, 1988.
- [39] H. Kruse, B. V. Jacak, J. J. Molitoris, G. D. Westfall, and H. Stoecker, “VLASOV-UHLENBECK THEORY OF MEDIUM-ENERGY HEAVY ION REACTIONS: ROLE OF MEAN FIELD DYNAMICS AND TWO-BODY COLLISIONS,” *Phys. Rev. C*, vol. 31, pp. 1770–1774, 1985.
- [40] J. Aichelin and H. Stoecker, “Quantum molecular dynamics. A Novel approach to N body correlations in heavy ion collisions,” *Phys. Lett. B*, vol. 176, pp. 14–19, 1986.

BIBLIOGRAPHY

- [41] J. Aichelin, “‘Quantum’ molecular dynamics: A Dynamical microscopic n body approach to investigate fragment formation and the nuclear equation of state in heavy ion collisions,” *Phys. Rept.*, vol. 202, pp. 233–360, 1991.
- [42] J. Aichelin, A. Bohnet, G. Peilert, H. Stoecker, W. Greiner, and A. Rosenhauer, “Quantum Molecular Dynamics Approach to Heavy Ion Collisions: Description of the Model, Comparison With Fragmentation Data, and the Mechanism of Fragment Formation,” *Phys. Rev. C*, vol. 37, pp. 2451–2468, 1988.
- [43] H. Sorge, H. Stoecker, and W. Greiner, “RELATIVISTIC QUANTUM MOLECULAR DYNAMICS APPROACH TO NUCLEAR COLLISIONS AT ULTRARELATIVISTIC ENERGIES,” *Nucl. Phys. A*, vol. 498, pp. 567C–576C, 1989.
- [44] C. Hartnack, R. K. Puri, J. Aichelin, J. Konopka, S. A. Bass, H. Stoecker, and W. Greiner, “Modeling the many body dynamics of heavy ion collisions: Present status and future perspective,” *Eur. Phys. J. A*, vol. 1, pp. 151–169, 1998.
- [45] S. A. Bass *et al.*, “Microscopic models for ultrarelativistic heavy ion collisions,” *Prog. Part. Nucl. Phys.*, vol. 41, pp. 255–369, 1998.
- [46] M. Bleicher *et al.*, “Relativistic hadron hadron collisions in the ultrarelativistic quantum molecular dynamics model,” *J. Phys. G*, vol. 25, pp. 1859–1896, 1999.
- [47] P. F. Kolb and U. W. Heinz, “Hydrodynamic description of ultrarelativistic heavy ion collisions,” *arXiv:nucl-th/0305084*, 2003.
- [48] H. Petersen, J. Steinheimer, G. Burau, M. Bleicher, and H. Stöcker, “A Fully Integrated Transport Approach to Heavy Ion Reactions with an Intermediate Hydrodynamic Stage,” *Phys. Rev. C*, vol. 78, p. 044901, 2008.
- [49] R. J. Glauber, “Cross-sections in deuterium at high-energies,” *Phys. Rev.*, vol. 100, pp. 242–248, 1955.
- [50] R. J. Glauber, “Quantum Optics and Heavy Ion Physics,” *Nucl. Phys. A*, vol. 774, pp. 3–13, 2006.
- [51] <https://home.cern/news/news/experiments/first-lead-ion-collisions-lhc-record-energy>. Accessed: 2023-02-09.
- [52] D. Adamova *et al.*, “Universal pion freezeout in heavy ion collisions,” *Phys. Rev. Lett.*, vol. 90, p. 022301, 2003.
- [53] C. Alt *et al.*, “Omega- and anti-Omega+ production in central Pb + Pb collisions at 40-AGeV and 158-AGeV,” *Phys. Rev. Lett.*, vol. 94, p. 192301, 2005.
- [54] C. Alt *et al.*, “Observation of an exotic $S = -2$, $Q = -2$ baryon resonance in proton proton collisions at the CERN SPS,” *Phys. Rev. Lett.*, vol. 92, p. 042003, 2004.

BIBLIOGRAPHY

- [55] C. Alt *et al.*, “Pion and kaon production in central Pb + Pb collisions at 20-A and 30-A-GeV: Evidence for the onset of deconfinement,” *Phys. Rev. C*, vol. 77, p. 024903, 2008.
- [56] R. Arnaldi *et al.*, “First measurement of the rho spectral function in high-energy nuclear collisions,” *Phys. Rev. Lett.*, vol. 96, p. 162302, 2006.
- [57] L. Kumar, “STAR Results from the RHIC Beam Energy Scan-I,” *Nucl. Phys. A*, vol. 904-905, pp. 256c–263c, 2013.
- [58] G. Odyniec, “The RHIC Beam Energy Scan program in STAR and what’s next ...,” *J. Phys. Conf. Ser.*, vol. 455, p. 012037, 2013.
- [59] C. Liu *et al.*, “Summary of the 3-year Beam Energy Scan II operation at RHIC,” *JACoW*, vol. IPAC2022, pp. 1908–1911, 2022.
- [60] K. C. Meehan, “The fixed-target experiment at STAR,” *J. Phys. Conf. Ser.*, vol. 742, no. 1, p. 012022, 2016.
- [61] C. Pinkenburg *et al.*, “Elliptic flow: Transition from out-of-plane to in-plane emission in Au + Au collisions,” *Phys. Rev. Lett.*, vol. 83, pp. 1295–1298, 1999.
- [62] L. Ahle *et al.*, “An Excitation function of K- and K+ production in Au + Au reactions at the AGS,” *Phys. Lett. B*, vol. 490, pp. 53–60, 2000.
- [63] J. B. Elliott *et al.*, “Constructing the phase diagram of finite neutral nuclear matter,” *Phys. Rev. C*, vol. 67, p. 024609, 2003.
- [64] G. Agakishiev *et al.*, “The High-Acceptance Dielectron Spectrometer HADES,” *Eur. Phys. J. A*, vol. 41, pp. 243–277, 2009.
- [65] G. Agakichiev *et al.*, “Dielectron production in C-12+C-12 collisions at 2-AGeV with HADES,” *Phys. Rev. Lett.*, vol. 98, p. 052302, 2007.
- [66] M. Menzel *et al.*, “First measurement of anti-kaon phase space distributions in nucleus - nucleus collisions at subthreshold beam energies,” *Phys. Lett. B*, vol. 495, pp. 26–32, 2000.
- [67] P. Senger *et al.*, “The KAON spectrometer at SIS,” *Nucl. Instrum. Meth. A*, vol. 327, pp. 393–411, 1993.
- [68] A. Andronic *et al.*, “Excitation function of elliptic flow in Au+Au collisions and the nuclear matter equation of state,” *Phys. Lett. B*, vol. 612, pp. 173–180, 2005.
- [69] W. Reisdorf *et al.*, “Systematics of pion emission in heavy ion collisions in the 1A-GeV regime,” *Nucl. Phys. A*, vol. 781, pp. 459–508, 2007.
- [70] P. Spiller and G. Franchetti, “The FAIR accelerator project at GSI,” *Nucl. Instrum. Meth. A*, vol. 561, pp. 305–309, 2006.

BIBLIOGRAPHY

- [71] P. Spiller *et al.*, “The FAIR Heavy Ion Synchrotron SIS100,” *JINST*, vol. 15, no. 12, p. T12013, 2020.
- [72] E. R. Most, A. Motornenko, J. Steinheimer, V. Dexheimer, M. Hanauske, L. Rezzolla, and H. Stoecker, “Probing neutron-star matter in the lab: Similarities and differences between binary mergers and heavy-ion collisions,” *Phys. Rev. D*, vol. 107, no. 4, p. 043034, 2023.
- [73] B. P. Abbott *et al.*, “GW170817: Observation of Gravitational Waves from a Binary Neutron Star Inspiral,” *Phys. Rev. Lett.*, vol. 119, no. 16, p. 161101, 2017.
- [74] B. P. Abbott *et al.*, “GW190425: Observation of a Compact Binary Coalescence with Total Mass $\sim 3.4M_{\odot}$,” *Astrophys. J. Lett.*, vol. 892, no. 1, p. L3, 2020.
- [75] A. Bauswein, H. T. Janka, K. Hebeler, and A. Schwenk, “Equation-of-state dependence of the gravitational-wave signal from the ring-down phase of neutron-star mergers,” *Phys. Rev. D*, vol. 86, p. 063001, 2012.
- [76] E. R. Most, L. J. Papenfort, V. Dexheimer, M. Hanauske, S. Schramm, H. Stöcker, and L. Rezzolla, “Signatures of quark-hadron phase transitions in general-relativistic neutron-star mergers,” *Phys. Rev. Lett.*, vol. 122, no. 6, p. 061101, 2019.
- [77] M. Omana Kuttan, J. Steinheimer, K. Zhou, A. Redelbach, and H. Stoecker, “A fast centrality-meter for heavy-ion collisions at the CBM experiment,” *Phys. Lett. B*, vol. 811, p. 135872, 2020.
- [78] M. Omana Kuttan, J. Steinheimer, K. Zhou, A. Redelbach, and H. Stoecker, “Deep Learning Based Impact Parameter Determination for the CBM Experiment,” *Particles*, vol. 4, no. 1, pp. 47–52, 2021.
- [79] M. Omana Kuttan, K. Zhou, J. Steinheimer, A. Redelbach, and H. Stoecker, “An equation-of-state-meter for CBM using PointNet,” *JHEP*, vol. 21, p. 184, 2020.
- [80] M. Omana Kuttan, J. Steinheimer, K. Zhou, A. Redelbach, and H. Stoecker, “Extraction of global event features in heavy-ion collision experiments using PointNet,” Proceedings of FAIRness2022 -FAIR next generation scientists - 7th Edition Workshop (Paralia (Pieria, Greece) / 23 - 27 May 2022)(Accepted for publication in Proceedings of Science).
- [81] https://www.gsi.de/en/researchaccelerators/fair/the_machine. Accessed: 2023-02-16.
- [82] I. Augustin, H. H. Gutbrod, D. Kramer, K. Langanke, and H. Stocker, “New Physics at the International Facility for Antiproton and Ion Research (FAIR) Next to GSI,” in *4th International Conference on Fission and Properties of Neutron Rich nuclei*, 4 2008.
- [83] H. Stoecker and C. Sturm, “The facility for antiproton and ion research FAIR cosmic matter in the Laboratory,” *Nucl. Phys. A*, vol. 862-863, pp. 92–97, 2011.

BIBLIOGRAPHY

- [84] M. Durante *et al.*, “All the fun of the FAIR: fundamental physics at the facility for antiproton and ion research,” *Phys. Scripta*, vol. 94, no. 3, p. 033001, 2019.
- [85] B. Friman, C. Hohne, J. Knoll, S. Leupold, J. Randrup, R. Rapp, and P. Senger, eds., *The CBM physics book: Compressed baryonic matter in laboratory experiments*, vol. 814. Lect.Notes Phys., 2011.
- [86] H. Geissel *et al.*, “The Super-FRS project at GSI,” *Nucl. Instrum. Meth. B*, vol. 204, pp. 71–85, 2003.
- [87] C. P. Welsch and J. Ullrich, “FLAIR: A facility for low-energy antiproton and ion research,” *Hyperfine Interact.*, vol. 172, pp. 71–80, 2006.
- [88] A. Lehrach, O. Boine-Frankenheim, F. Hinterberger, R. Maier, and D. Prasuhn, “Beam performance and luminosity limitations in the high-energy storage ring (HESR),” *Nucl. Instrum. Meth. A*, vol. 561, pp. 289–296, 2006.
- [89] T. Stöhlker *et al.*, “APPA at FAIR: From fundamental to applied research,” *Nucl. Instrum. Meth. B*, vol. 365, pp. 680–685, 2015.
- [90] T. Ablyazimov *et al.*, “Challenges in QCD matter physics –The scientific programme of the Compressed Baryonic Matter experiment at FAIR,” *Eur. Phys. J. A*, vol. 53, no. 3, p. 60, 2017.
- [91] V. Friese, “The CBM experiment at GSI/FAIR,” *Nucl. Phys. A*, vol. 774, pp. 377–386, 2006.
- [92] P. Senger, “The CBM experiment at FAIR,” *J. Phys. Conf. Ser.*, vol. 50, pp. 357–360, 2006.
- [93] P. Staszal, “CBM experiment at FAIR,” *Acta Phys. Polon. B*, vol. 41, pp. 341–350, 2010.
- [94] R. Krucken, “The NuSTAR facility at FAIR,” *J. Phys. G*, vol. 31, pp. S1807–S1811, 2005.
- [95] M. F. M. Lutz *et al.*, “Physics Performance Report for PANDA: Strong Interaction Studies with Antiprotons,” *arXiv:0903.3905*, 2009.
- [96] G. Agakishiev *et al.*, “Inclusive dielectron spectra in p+p collisions at 3.5 GeV,” *Eur. Phys. J. A*, vol. 48, p. 64, 2012.
- [97] G. Agakishiev *et al.*, “Baryon resonance production and dielectron decays in proton-proton collisions at 3.5 GeV,” *Eur. Phys. J. A*, vol. 50, p. 82, 2014.
- [98] G. Agakishiev *et al.*, “Lambda hyperon production and polarization in collisions of p(3.5 GeV)+Nb,” *Eur. Phys. J. A*, vol. 50, p. 81, 2014.
- [99] G. Agakishiev *et al.*, “Subthreshold Ξ^- Production in Collisions of p(3.5 GeV)+Nb,” *Phys. Rev. Lett.*, vol. 114, no. 21, p. 212301, 2015.

BIBLIOGRAPHY

- [100] G. Agakishiev *et al.*, “Study of dielectron production in C+C collisions at 1-A-GeV,” *Phys. Lett. B*, vol. 663, pp. 43–48, 2008.
- [101] G. Agakishiev *et al.*, “Measurement of charged pions in C-12 + C-12 collisions at 1A-GeV and 2A-GeV with HADES,” *Eur. Phys. J. A*, vol. 40, pp. 45–59, 2009.
- [102] G. Agakishiev *et al.*, “Dielectron production in Ar+KCl collisions at 1.76A GeV,” *Phys. Rev. C*, vol. 84, p. 014902, 2011.
- [103] G. Agakishiev *et al.*, “Hyperon production in Ar+KCl collisions at 1.76A GeV,” *Eur. Phys. J. A*, vol. 47, p. 21, 2011.
- [104] G. Agakishiev *et al.*, “Deep sub-threshold Xi- production in Ar+KCl reactions at 1.76A-GeV,” *Phys. Rev. Lett.*, vol. 103, p. 132301, 2009.
- [105] J. Adamczewski-Musch *et al.*, “Directed, Elliptic, and Higher Order Flow Harmonics of Protons, Deuterons, and Tritons in Au + Au Collisions at $\sqrt{s_{NN}} = 2.4\text{GeV}$,” *Phys. Rev. Lett.*, vol. 125, p. 262301, 2020.
- [106] J. Adamczewski-Musch *et al.*, “Proton-number fluctuations in $\sqrt{s_{NN}} = 2.4\text{ GeV}$ Au + Au collisions studied with the High-Acceptance DiElectron Spectrometer (HADES),” *Phys. Rev. C*, vol. 102, no. 2, p. 024914, 2020.
- [107] J. Adamczewski-Musch *et al.*, “Sub-threshold production of K_s^0 mesons and Λ hyperons in Au+Au collisions at $\sqrt{s_{NN}} = 2.4\text{ GeV}$,” *Phys. Lett. B*, vol. 793, pp. 457–463, 2019.
- [108] J. M. Heuser, “The Silicon Tracking System of the CBM Experiment at FAIR,” *JPS Conf. Proc.*, vol. 8, p. 022007, 2015.
- [109] M. Deveaux and J. M. Heuser, “The silicon detector systems of the Compressed Baryonic Matter experiment,” *PoS*, vol. Vertex2013, p. 009, 2013.
- [110] J. Adamczewski-Musch *et al.*, “The CBM RICH project,” *Nucl. Instrum. Meth. A*, vol. 845, pp. 434–438, 2017.
- [111] I. Deppner and N. Herrmann, “The CBM Time-of-Flight system,” *JINST*, vol. 14, no. 09, p. C09020, 2019.
- [112] J. de Cuveland and V. Lindenstruth, “A first-level event selector for the CBM experiment at FAIR,” *J. Phys. Conf. Ser.*, vol. 331, p. 022006, 2011.
- [113] N. Abgrall *et al.*, “NA61/SHINE facility at the CERN SPS: beams and detector system,” *JINST*, vol. 9, p. P06005, 2014.
- [114] M. Gazdzicki, “NA49/NA61: results and plans on beam energy and system size scan at the CERN SPS,” *J. Phys. G*, vol. 38, p. 124024, 2011.
- [115] B. B. Abelev *et al.*, “Performance of the ALICE Experiment at the CERN LHC,” *Int. J. Mod. Phys. A*, vol. 29, p. 1430044, 2014.

BIBLIOGRAPHY

- [116] K. Aamodt *et al.*, “The ALICE experiment at the CERN LHC,” *JINST*, vol. 3, p. S08002, 2008.
- [117] P. Cortese *et al.*, “ALICE: Physics performance report, volume I,” *J. Phys. G*, vol. 30, pp. 1517–1763, 2004.
- [118] Z. Sweger, “Recent Results and Future Prospects from the STAR Beam Energy Scan Program,” in *57th Rencontres de Moriond on QCD and High Energy Interactions*, 5 2023.
- [119] K. H. Ackermann *et al.*, “STAR detector overview,” *Nucl. Instrum. Meth. A*, vol. 499, pp. 624–632, 2003.
- [120] X. Sun, “The STAR Forward Detector System Upgrade Status,” *Acta Phys. Polon. Supp.*, vol. 16, no. 1, p. 139, 2023.
- [121] D. H. Rischke, Y. Pürsün, J. A. Maruhn, H. Stoecker, and W. Greiner, “The Phase transition to the quark - gluon plasma and its effects on hydrodynamic flow,” *Acta Phys. Hung. A*, vol. 1, pp. 309–322, 1995.
- [122] H. Stoecker, “Collective flow signals the quark gluon plasma,” *Nucl. Phys. A*, vol. 750, pp. 121–147, 2005.
- [123] M. A. Stephanov, K. Rajagopal, and E. V. Shuryak, “Signatures of the tricritical point in QCD,” *Phys. Rev. Lett.*, vol. 81, pp. 4816–4819, 1998.
- [124] Y. Hatta and M. A. Stephanov, “Proton number fluctuation as a signal of the QCD critical endpoint,” *Phys. Rev. Lett.*, vol. 91, p. 102003, 2003. [Erratum: *Phys.Rev.Lett.* 91, 129901 (2003)].
- [125] M. Omana Kuttan, A. Motornenko, J. Steinheimer, H. Stoecker, Y. Nara, and M. Bleicher, “A chiral mean-field equation-of-state in UrQMD: effects on the heavy ion compression stage,” *Eur. Phys. J. C*, vol. 82, no. 5, p. 427, 2022.
- [126] M. Omana Kuttan, J. Steinheimer, K. Zhou, M. Bleicher, and H. Stöcker, “Model dependence of the number of participant nucleons and observable consequences in heavy-ion collisions,” *arXiv:2303.07919*, 2023.
- [127] J. Steinheimer, M. Omana Kuttan, A. Motornenko, A. Sorensen, Y. Nara, V. Koch, M. Bleicher, and H. Stoecker, “Proton and Λ flow and the equation of state at high density,” *EPJ Web Conf.*, vol. 276, p. 01021, 2023.
- [128] H. Stoecker *et al.*, “VUU and (R)QMD model of high-energy heavy ion collisions,” *Nucl. Phys. A*, vol. 538, pp. 53C–64C, 1992.
- [129] S. R. De Groot, *Relativistic Kinetic Theory. Principles and Applications*. 1980.
- [130] R. L. Workman *et al.*, “Review of Particle Physics,” *PTEP*, vol. 2022, p. 083C01, 2022.

BIBLIOGRAPHY

- [131] L. V. Bravina *et al.*, “Microscopic models and effective equation of state in nuclear collisions at FAIR energies,” *Phys. Rev. C*, vol. 78, p. 014907, 2008.
- [132] J. Steinheimer, M. Bleicher, H. Petersen, S. Schramm, H. Stoecker, and D. Zschesche, “(3+1)-dimensional hydrodynamic expansion with a critical point from realistic initial conditions,” *Phys. Rev. C*, vol. 77, p. 034901, 2008.
- [133] S. Endres, H. van Hees, J. Weil, and M. Bleicher, “Dilepton production and reaction dynamics in heavy-ion collisions at SIS energies from coarse-grained transport simulations,” *Phys. Rev. C*, vol. 92, no. 1, p. 014911, 2015.
- [134] J. P. Boris and D. L. Book, “Flux-corrected transport. I. SHASTA, a fluid transport algorithm that works,” *J. Comput. Phys.*, vol. 11, no. 1, pp. 38–69, 1973.
- [135] D. H. Rischke, S. Bernard, and J. A. Maruhn, “Relativistic hydrodynamics for heavy ion collisions. 1. General aspects and expansion into vacuum,” *Nucl. Phys. A*, vol. 595, pp. 346–382, 1995.
- [136] S. Paiva, Y. Hama, and T. Kodama, “Fluctuation effects in initial conditions for hydrodynamics,” *Phys. Rev. C*, vol. 55, pp. 1455–1462, 1997.
- [137] Y. Hama, T. Kodama, and O. Socolowski, Jr., “Topics on hydrodynamic model of nucleus-nucleus collisions,” *Braz. J. Phys.*, vol. 35, pp. 24–51, 2005.
- [138] S. A. Bass and A. Dumitru, “Dynamics of hot bulk QCD matter: From the quark gluon plasma to hadronic freezeout,” *Phys. Rev. C*, vol. 61, p. 064909, 2000.
- [139] T. Hirano, “Is early thermalization achieved only near mid-rapidity at RHIC?,” *Phys. Rev. C*, vol. 65, p. 011901, 2002.
- [140] T. Hirano and Y. Nara, “Hydrodynamic afterburner for the color glass condensate and the parton energy loss,” *Nucl. Phys. A*, vol. 743, pp. 305–328, 2004.
- [141] T. Hirano, P. Huovinen, K. Murase, and Y. Nara, “Integrated Dynamical Approach to Relativistic Heavy Ion Collisions,” *Prog. Part. Nucl. Phys.*, vol. 70, pp. 108–158, 2013.
- [142] C. Nonaka and S. A. Bass, “Space-time evolution of bulk QCD matter,” *Phys. Rev. C*, vol. 75, p. 014902, 2007.
- [143] K. Werner, I. Karpenko, T. Pierog, M. Bleicher, and K. Mikhailov, “Event-by-Event Simulation of the Three-Dimensional Hydrodynamic Evolution from Flux Tube Initial Conditions in Ultrarelativistic Heavy Ion Collisions,” *Phys. Rev. C*, vol. 82, p. 044904, 2010.
- [144] C. Gale, S. Jeon, and B. Schenke, “Hydrodynamic Modeling of Heavy-Ion Collisions,” *Int. J. Mod. Phys. A*, vol. 28, p. 1340011, 2013.

BIBLIOGRAPHY

- [145] C. Shen, Z. Qiu, H. Song, J. Bernhard, S. Bass, and U. Heinz, “The iEBE-VISHNU code package for relativistic heavy-ion collisions,” *Comput. Phys. Commun.*, vol. 199, pp. 61–85, 2016.
- [146] E. Iancu and R. Venugopalan, “The Color glass condensate and high-energy scattering in QCD,” *arXiv:hep-ph/0303204*, 2003.
- [147] F. Gelis, E. Iancu, J. Jalilian-Marian, and R. Venugopalan, “The Color Glass Condensate,” *Ann. Rev. Nucl. Part. Sci.*, vol. 60, pp. 463–489, 2010.
- [148] J. L. Albacete and C. Marquet, “Gluon saturation and initial conditions for relativistic heavy ion collisions,” *Prog. Part. Nucl. Phys.*, vol. 76, pp. 1–42, 2014.
- [149] H.-J. Drescher, A. Dumitru, A. Hayashigaki, and Y. Nara, “The Eccentricity in heavy-ion collisions from color glass condensate initial conditions,” *Phys. Rev. C*, vol. 74, p. 044905, 2006.
- [150] H. J. Drescher and Y. Nara, “Effects of fluctuations on the initial eccentricity from the Color Glass Condensate in heavy ion collisions,” *Phys. Rev. C*, vol. 75, p. 034905, 2007.
- [151] B. Schenke, P. Tribedy, and R. Venugopalan, “Fluctuating Glasma initial conditions and flow in heavy ion collisions,” *Phys. Rev. Lett.*, vol. 108, p. 252301, 2012.
- [152] M. Rybczynski, G. Stefanek, W. Broniowski, and P. Bozek, “GLISSANDO 2 : GLauber Initial-State Simulation AND mOre... , ver. 2,” *Comput. Phys. Commun.*, vol. 185, pp. 1759–1772, 2014.
- [153] J. S. Moreland, J. E. Bernhard, and S. A. Bass, “Alternative ansatz to wounded nucleon and binary collision scaling in high-energy nuclear collisions,” *Phys. Rev. C*, vol. 92, no. 1, p. 011901, 2015.
- [154] J. Steinheimer, J. Aichelin, M. Bleicher, and H. Stöcker, “Influence of the hadronic phase on observables in ultrarelativistic heavy ion collisions,” *Phys. Rev. C*, vol. 95, no. 6, p. 064902, 2017.
- [155] D. H. Rischke, Y. Pursun, and J. A. Maruhn, “Relativistic hydrodynamics for heavy ion collisions. 2. Compression of nuclear matter and the phase transition to the quark - gluon plasma,” *Nucl. Phys. A*, vol. 595, pp. 383–408, 1995. [Erratum: *Nucl.Phys.A* 596, 717–717 (1996)].
- [156] J. Konopka, . PhD thesis, Goethe University, Frankfurt am Main, Germany, 1996.
- [157] Y. Nara and H. Stoecker, “Sensitivity of the excitation functions of collective flow to relativistic scalar and vector meson interactions in the relativistic quantum molecular dynamics model RQMD.RMF,” *Phys. Rev. C*, vol. 100, no. 5, p. 054902, 2019.

BIBLIOGRAPHY

- [158] Y. Nara, T. Maruyama, and H. Stoecker, “Momentum-dependent potential and collective flows within the relativistic quantum molecular dynamics approach based on relativistic mean-field theory,” *Phys. Rev. C*, vol. 102, no. 2, p. 024913, 2020.
- [159] A. Sorensen and V. Koch, “Phase transitions and critical behavior in hadronic transport with a relativistic density functional equation of state,” *Phys. Rev. C*, vol. 104, no. 3, p. 034904, 2021.
- [160] C. Hartnack, Z. X. Li, L. Neise, G. Peilert, A. Rosenhauer, H. Sorge, H. Stoecker, W. Greiner, and J. Aichelin, “Quantum Molecular Dynamics: A Microscopic Model From Unilac to CERN Energies,” *Nucl. Phys. A*, vol. 495, pp. 303C–320C, 1989.
- [161] J. Steinheimer, A. Motornenko, A. Sorensen, Y. Nara, V. Koch, and M. Bleicher, “The high-density equation of state in heavy-ion collisions: constraints from proton flow,” *Eur. Phys. J. C*, vol. 82, no. 10, p. 911, 2022.
- [162] P. Papazoglou, D. Zschesche, S. Schramm, J. Schaffner-Bielich, H. Stoecker, and W. Greiner, “Nuclei in a chiral SU(3) model,” *Phys. Rev. C*, vol. 59, pp. 411–427, 1999.
- [163] J. Steinheimer, S. Schramm, and H. Stoecker, “An Effective chiral Hadron-Quark Equation of State,” *J. Phys. G*, vol. 38, p. 035001, 2011.
- [164] A. Motornenko, J. Steinheimer, V. Vovchenko, S. Schramm, and H. Stoecker, “Equation of state for hot QCD and compact stars from a mean field approach,” *Phys. Rev. C*, vol. 101, no. 3, p. 034904, 2020.
- [165] M. Omana Kuttan, J. Steinheimer, K. Zhou, and H. Stöcker, “The QCD EoS of dense nuclear matter from Bayesian analysis of heavy ion collision data,” *arXiv:2211.11670*, 2022.
- [166] Y. LeCun, Y. Bengio, and G. Hinton, “Deep learning,” *nature*, vol. 521, no. 7553, pp. 436–444, 2015.
- [167] Y. Taigman, M. Yang, M. Ranzato, and L. Wolf, “Deepface: Closing the gap to human-level performance in face verification,” in *Proceedings of the IEEE conference on computer vision and pattern recognition*, pp. 1701–1708, 2014.
- [168] D. Silver, A. Huang, C. J. Maddison, A. Guez, L. Sifre, G. Van Den Driessche, J. Schrittwieser, I. Antonoglou, V. Panneershelvam, M. Lanctot, *et al.*, “Mastering the game of go with deep neural networks and tree search,” *nature*, vol. 529, no. 7587, pp. 484–489, 2016.
- [169] J. Jumper, R. Evans, A. Pritzel, T. Green, M. Figurnov, O. Ronneberger, K. Tunyasuvunakool, R. Bates, A. Žídek, A. Potapenko, *et al.*, “Highly accurate protein structure prediction with alphafold,” *Nature*, vol. 596, no. 7873, pp. 583–589, 2021.
- [170] <https://openai.com/blog/chatgpt>. Accessed: 2023-01-03.

BIBLIOGRAPHY

- [171] G. Cybenko, “Approximation by superpositions of a sigmoidal function,” *Mathematics of control, signals and systems*, vol. 2, no. 4, pp. 303–314, 1989.
- [172] K.-I. Funahashi, “On the approximate realization of continuous mappings by neural networks,” *Neural networks*, vol. 2, no. 3, pp. 183–192, 1989.
- [173] K. Hornik, M. Stinchcombe, and H. White, “Multilayer feedforward networks are universal approximators,” *Neural networks*, vol. 2, no. 5, pp. 359–366, 1989.
- [174] K. Hornik, “Approximation capabilities of multilayer feedforward networks,” *Neural networks*, vol. 4, no. 2, pp. 251–257, 1991.
- [175] D. P. Kingma and J. Ba, “Adam: A Method for Stochastic Optimization,” *arXiv:1412.6980*, 2014.
- [176] J. Duchi, E. Hazan, and Y. Singer, “Adaptive subgradient methods for online learning and stochastic optimization.,” *Journal of machine learning research*, vol. 12, no. 7, 2011.
- [177] M. D. Zeiler, “Adadelta: an adaptive learning rate method,” *arXiv:1212.5701*, 2012.
- [178] S. Ruder, “An overview of gradient descent optimization algorithms,” *arXiv:1609.04747*, 2016.
- [179] D. E. Rumelhart, G. E. Hinton, and R. J. Williams, “Learning representations by back-propagating errors,” *Nature*, vol. 323, no. 6088, pp. 533–536, 1986.
- [180] L.-G. Pang, K. Zhou, N. Su, H. Petersen, H. Stöcker, and X.-N. Wang, “An equation-of-state-meter of quantum chromodynamics transition from deep learning,” *Nature Commun.*, vol. 9, no. 1, p. 210, 2018.
- [181] A. Kawęcka, W. Bryliński, M. Omana Kuttan, O. Linnyk, J. Pawlowski, K. Schmidt, M. Słodkowski, O. Wszyński, and J. Zieliński, “NA61/SHINE online noise filtering using machine learning methods,” *J. Phys. Conf. Ser.*, vol. 2438, no. 1, p. 012104, 2023.
- [182] C. R. Qi, H. Su, K. Mo, and L. J. Guibas, “Pointnet: Deep learning on point sets for 3d classification and segmentation,” in *Proceedings of the IEEE conference on computer vision and pattern recognition*, pp. 652–660, 2017.
- [183] N. Metropolis, A. W. Rosenbluth, M. N. Rosenbluth, A. H. Teller, and E. Teller, “Equation of state calculations by fast computing machines,” *J. Chem. Phys.*, vol. 21, pp. 1087–1092, 1953.
- [184] C. J. T. Braak, “A markov chain monte carlo version of the genetic algorithm differential evolution: easy bayesian computing for real parameter spaces,” *Statistics and Computing*, vol. 16, pp. 239–249, 2006.
- [185] C. J. Ter Braak and J. A. Vrugt, “Differential evolution markov chain with snooker updater and fewer chains,” *Statistics and Computing*, vol. 18, pp. 435–446, 2008.

BIBLIOGRAPHY

- [186] A. J. Larkoski, I. Moutl, and B. Nachman, “Jet Substructure at the Large Hadron Collider: A Review of Recent Advances in Theory and Machine Learning,” *Phys. Rept.*, vol. 841, pp. 1–63, 2020.
- [187] L. de Oliveira, M. Kagan, L. Mackey, B. Nachman, and A. Schwartzman, “Jet-images — deep learning edition,” *JHEP*, vol. 07, p. 069, 2016.
- [188] G. Kasieczka, T. Plehn, M. Russell, and T. Schell, “Deep-learning Top Taggers or The End of QCD?,” *JHEP*, vol. 05, p. 006, 2017.
- [189] P. Baldi, K. Bauer, C. Eng, P. Sadowski, and D. Whiteson, “Jet Substructure Classification in High-Energy Physics with Deep Neural Networks,” *Phys. Rev. D*, vol. 93, no. 9, p. 094034, 2016.
- [190] H. Qu and L. Gouskos, “ParticleNet: Jet Tagging via Particle Clouds,” *Phys. Rev. D*, vol. 101, no. 5, p. 056019, 2020.
- [191] P. T. Komiske, E. M. Metodiev, and M. D. Schwartz, “Deep learning in color: towards automated quark/gluon jet discrimination,” *JHEP*, vol. 01, p. 110, 2017.
- [192] E. A. Moreno, O. Cerri, J. M. Duarte, H. B. Newman, T. Q. Nguyen, A. Periwai, M. Pierini, A. Serikova, M. Spiropulu, and J.-R. Vlimant, “JEDI-net: a jet identification algorithm based on interaction networks,” *Eur. Phys. J. C*, vol. 80, no. 1, p. 58, 2020.
- [193] G. Kasieczka, S. Marzani, G. Soyez, and G. Stagnitto, “Towards Machine Learning Analytics for Jet Substructure,” *JHEP*, vol. 09, p. 195, 2020.
- [194] P. Baldi, P. Sadowski, and D. Whiteson, “Searching for Exotic Particles in High-Energy Physics with Deep Learning,” *Nature Commun.*, vol. 5, p. 4308, 2014.
- [195] L. de Oliveira, M. Paganini, and B. Nachman, “Learning Particle Physics by Example: Location-Aware Generative Adversarial Networks for Physics Synthesis,” *Comput. Softw. Big Sci.*, vol. 1, no. 1, p. 4, 2017.
- [196] M. Erdmann, J. Glombitza, and T. Quast, “Precise simulation of electromagnetic calorimeter showers using a Wasserstein Generative Adversarial Network,” *Comput. Softw. Big Sci.*, vol. 3, no. 1, p. 4, 2019.
- [197] V. Chekalina, E. Orlova, F. Ratnikov, D. Ulyanov, A. Ustyuzhanin, and E. Zakharov, “Generative Models for Fast Calorimeter Simulation: the LHCb case,” *EPJ Web Conf.*, vol. 214, p. 02034, 2019.
- [198] E. Buhmann, S. Diefenbacher, D. Hundhausen, G. Kasieczka, W. Korcari, E. Eren, F. Gaede, K. Krüger, P. McKeown, and L. Rustige, “Hadrons, better, faster, stronger,” *Mach. Learn. Sci. Tech.*, vol. 3, no. 2, p. 025014, 2022.

BIBLIOGRAPHY

- [199] G. Karagiorgi, G. Kasieczka, S. Kravitz, B. Nachman, and D. Shih, “Machine learning in the search for new fundamental physics,” *Nature Rev. Phys.*, vol. 4, no. 6, pp. 399–412, 2022.
- [200] M. Farina, Y. Nakai, and D. Shih, “Searching for New Physics with Deep Autoencoders,” *Phys. Rev. D*, vol. 101, no. 7, p. 075021, 2020.
- [201] P. Thaprasop, K. Zhou, J. Steinheimer, and C. Herold, “Unsupervised Outlier Detection in Heavy-Ion Collisions,” *Phys. Scripta*, vol. 96, no. 6, p. 064003, 2021.
- [202] D. Bourilkov, “Machine and Deep Learning Applications in Particle Physics,” *Int. J. Mod. Phys. A*, vol. 34, no. 35, p. 1930019, 2020.
- [203] A. Radovic, M. Williams, D. Rousseau, M. Kagan, D. Bonacorsi, A. Himmel, A. Aurisano, K. Terao, and T. Wongjirad, “Machine learning at the energy and intensity frontiers of particle physics,” *Nature*, vol. 560, no. 7716, pp. 41–48, 2018.
- [204] D. Guest, K. Cranmer, and D. Whiteson, “Deep Learning and its Application to LHC Physics,” *Ann. Rev. Nucl. Part. Sci.*, vol. 68, pp. 161–181, 2018.
- [205] L. G. Almeida, M. Backović, M. Cliche, S. J. Lee, and M. Perelstein, “Playing Tag with ANN: Boosted Top Identification with Pattern Recognition,” *JHEP*, vol. 07, p. 086, 2015.
- [206] A. Butter *et al.*, “The Machine Learning landscape of top taggers,” *SciPost Phys.*, vol. 7, p. 014, 2019.
- [207] A. M. Sirunyan *et al.*, “Identification of heavy, energetic, hadronically decaying particles using machine-learning techniques,” *JINST*, vol. 15, no. 06, p. P06005, 2020.
- [208] W. Esmail, T. Stockmanns, and J. Ritman, “Machine Learning for Track Finding at PANDA,” in *Connecting the Dots and Workshop on Intelligent Trackers*, 10 2019.
- [209] R. Haake, “Machine and deep learning techniques in heavy-ion collisions with ALICE,” *arXiv:1709.08497*, 2017.
- [210] D. Samuel and K. Suresh, “Artificial Neural Networks-based Track Fitting of Cosmic Muons through Stacked Resistive Plate Chambers,” *JINST*, vol. 13, no. 10, p. P10035, 2018.
- [211] D. Samuel, A. Samalan, M. Omana Kuttan, and L. P. Murgod, “Machine learning-based predictions of directionality and charge of cosmic muons—a simulation study using the mICAL detector,” *JINST*, vol. 14, no. 11, p. P11020, 2019.
- [212] K. Zhou, G. Endrődi, L.-G. Pang, and H. Stöcker, “Regressive and generative neural networks for scalar field theory,” *Phys. Rev. D*, vol. 100, no. 1, p. 011501, 2019.
- [213] J. Steinheimer, L. Pang, K. Zhou, V. Koch, J. Randrup, and H. Stoecker, “A machine learning study to identify spinodal clumping in high energy nuclear collisions,” *JHEP*, vol. 12, p. 122, 2019.

BIBLIOGRAPHY

- [214] Y.-L. Du, K. Zhou, J. Steinheimer, L.-G. Pang, A. Motornenko, H.-S. Zong, X.-N. Wang, and H. Stöcker, “Identifying the nature of the QCD transition in relativistic collision of heavy nuclei with deep learning,” *Eur. Phys. J. C*, vol. 80, no. 6, p. 516, 2020.
- [215] J. E. Bernhard, J. S. Moreland, and S. A. Bass, “Bayesian estimation of the specific shear and bulk viscosity of quark–gluon plasma,” *Nature Phys.*, vol. 15, no. 11, pp. 1113–1117, 2019.
- [216] D. Everett *et al.*, “Multisystem Bayesian constraints on the transport coefficients of QCD matter,” *Phys. Rev. C*, vol. 103, no. 5, p. 054904, 2021.
- [217] S. Pratt, E. Sangaline, P. Sorensen, and H. Wang, “Constraining the Eq. of State of Super-Hadronic Matter from Heavy-Ion Collisions,” *Phys. Rev. Lett.*, vol. 114, p. 202301, 2015.
- [218] A. Greiner, “Deep Learning based data analysis for the CBM and PANDA experiments,” Master’s thesis, Johannes Gutenberg University Mainz, Germany, 2022.
- [219] T. Reichert, O. Savchuk, A. Kittiratpattana, P. Li, J. Steinheimer, M. Gorenstein, and M. Bleicher, “Decoding the flow evolution in Au+Au reactions at 1.23A GeV using hadron flow correlations and dileptons,” *Phys. Lett. B*, vol. 841, p. 137947, 2023.
- [220] J. Cimerman, I. Karpenko, B. Tomasik, and P. Huovinen, “Next-generation multifluid hydrodynamic model for nuclear collisions at sNN from a few GeV to a hundred GeV,” *Phys. Rev. C*, vol. 107, no. 4, p. 044902, 2023.
- [221] J. Brachmann, S. Soff, A. Dumitru, H. Stoecker, J. A. Maruhn, W. Greiner, L. V. Bravina, and D. H. Rischke, “Antiflow of nucleons at the softest point of the EoS,” *Phys. Rev. C*, vol. 61, p. 024909, 2000.
- [222] L. P. Csernai and D. Rohrich, “Third flow component as QGP signal,” *Phys. Lett. B*, vol. 458, p. 454, 1999.
- [223] A. Ohnishi, Y. Nara, H. Niemi, and H. Stoecker, “Directed Flow in Heavy-ion Collisions and Softening of Equation of State,” *Acta Phys. Polon. Supp.*, vol. 10, p. 699, 2017.
- [224] J. Adamczewski-Musch *et al.*, “Proton, deuteron and triton flow measurements in Au+Au collisions at $\sqrt{s_{NN}} = 2.4$ GeV,” *Eur. Phys. J. A*, vol. 59, no. 4, p. 80, 2023.
- [225] J. Adamczewski-Musch *et al.*, “Centrality determination of Au + Au collisions at 1.23A GeV with HADES,” *Eur. Phys. J. A*, vol. 54, no. 5, p. 85, 2018.
- [226] M. Abdallah *et al.*, “Higher-order cumulants and correlation functions of proton multiplicity distributions in sNN=3 GeV Au+Au collisions at the RHIC STAR experiment,” *Phys. Rev. C*, vol. 107, no. 2, p. 024908, 2023.

BIBLIOGRAPHY

- [227] J. Adamczewski-Musch *et al.*, “Charged-pion production in Au+Au collisions at $\sqrt{s_{NN}} = 2.4$ GeV: HADES Collaboration,” *Eur. Phys. J. A*, vol. 56, no. 10, p. 259, 2020.
- [228] K. Godbey, Z. Zhang, J. W. Holt, and C. M. Ko, “Charged pion production from Au + Au collisions at sNN=2.4 GeV in the relativistic Vlasov-Uehling-Uhlenbeck model,” *Phys. Lett. B*, vol. 829, p. 137134, 2022.
- [229] P. Hillmann, K. Käfer, J. Steinheimer, V. Vovchenko, and M. Bleicher, “Coalescence, the thermal model and multi-fragmentation: the energy and volume dependence of light nuclei production in heavy ion collisions,” *J. Phys. G*, vol. 49, no. 5, p. 055107, 2022.
- [230] H. Liu, “Measurement of Light-nuclei Production in Heavy-ion Collisions by the STAR Experiment,” *Acta Phys. Polon. Supp.*, vol. 16, no. 1, p. 148, 2023.
- [231] H. Schuldes, *Charged kaon and ϕ reconstruction in Au+Au collisions at 1.23 AGeV*. PhD thesis, Goethe U., Frankfurt (main), 2016.
- [232] M. Lorenz, “Recent Results from HADES,” At the 18th International Conference on Strangeness in Quark Matter 2019.
- [233] S. Jeon and V. Koch, “Event by event fluctuations,” *arXiv:hep-ph/0304012*, 2003.
- [234] V. Skokov, B. Friman, and K. Redlich, “Volume Fluctuations and Higher Order Cumulants of the Net Baryon Number,” *Phys. Rev. C*, vol. 88, p. 034911, 2013.
- [235] V. Klochkov and I. Selyuzhenkov, “Centrality determination in heavy-ion collisions with the CBM experiment,” *J. Phys. Conf. Ser.*, vol. 798, no. 1, p. 012059, 2017.
- [236] <https://subversion.gsi.de/cbmsoft/cbmroot/release/OCT19/>. Accessed: 2019-12-01.
- [237] S. A. Bass, A. Bischoff, C. Hartnack, J. A. Maruhn, J. Reinhardt, H. Stoecker, and W. Greiner, “Neural networks for impact parameter determination,” *J. Phys. G*, vol. 20, pp. L21–L26, 1994.
- [238] C. David, M. Freslier, and J. Aichelin, “Impact parameter determination for heavy-ion collisions by use of a neural network,” *Phys. Rev. C*, vol. 51, pp. 1453–1459, 1995.
- [239] S. A. Bass, A. Bischoff, J. A. Maruhn, H. Stoecker, and W. Greiner, “Neural networks for impact parameter determination,” *Phys. Rev. C*, vol. 53, pp. 2358–2363, 1996.
- [240] F. Haddad, K. Hagel, J. Li, N. Mdeidayeh, J. B. Natowitz, R. Wada, B. Xiao, C. David, M. Freslier, and J. Aichelin, “Impact parameter determination in experimental analysis using neural network,” *Phys. Rev. C*, vol. 55, pp. 1371–1375, 1997.

BIBLIOGRAPHY

- [241] J. De Sanctis, M. Masotti, M. Bruno, M. D’Agostino, E. Geraci, G. Vannini, and A. Bonasera, “Classification of the impact parameter in nucleus-nucleus collisions by a support vector machine method,” *J. Phys. G*, vol. 36, p. 015101, 2009.
- [242] F. Li, Y. Wang, H. Lü, P. Li, Q. Li, and F. Liu, “Application of artificial intelligence in the determination of impact parameter in heavy-ion collisions at intermediate energies,” *J. Phys. G*, vol. 47, no. 11, p. 115104, 2020.
- [243] D. Durand, “An event generator for the study of nuclear collisions in the Fermi energy domain (I). Formalism and first applications,” *Nucl. Phys. A*, vol. 541, pp. 266–294, 1992.
- [244] R. J. Charity *et al.*, “Systematics of complex fragment emission in niobium-induced reactions,” *Nucl. Phys. A*, vol. 483, pp. 371–405, 1988.
- [245] M. Belkacem, V. Latora, and A. Bonasera, “Critical evolution of a finite system,” *Phys. Rev. C*, vol. 52, pp. 271–285, 1995.
- [246] C. O. Dorso, V. C. Latora, and A. Bonasera, “Signals of critical behavior in fragmenting finite systems,” *Phys. Rev. C*, vol. 60, p. 034606, 1999.
- [247] R. Brun, F. Bruyant, M. Maire, A. C. McPherson, and P. Zancarini, “GEANT3,” *CERN-DD-EE-84-1*, 1987.
- [248] J. Pochodzalla, “Exploring the potential of antihyperons in nuclei with antiprotons,” *Phys. Lett. B*, vol. 669, pp. 306–310, 2008.
- [249] A. Sanchez Lorente, S. Bleser, M. Steinen, and J. Pochodzalla, “Antihyperon potentials in nuclei via exclusive antiproton–nucleus reactions,” *Phys. Lett. B*, vol. 749, pp. 421–424, 2015.
- [250] J. Pochodzalla, S. Bleser, A. Sanchez Lorente, M. Martínez Rojo, M. Steinen, J. Gerl, J. Kojouharova, and I. Kojouharov, “Many Facets of Strangeness Nuclear Physics with Stored Antiprotons,” *JPS Conf. Proc.*, vol. 17, p. 091002, 2017.
- [251] D. Oliinychenko, A. Sorensen, V. Koch, and L. McLerran, “Sensitivity of Au+Au collisions to the symmetric nuclear matter equation of state at 2 – 5 nuclear saturation densities,” *arXiv:2208.11996*, 2022.
- [252] H. Song and U. W. Heinz, “Causal viscous hydrodynamics in 2+1 dimensions for relativistic heavy-ion collisions,” *Phys. Rev. C*, vol. 77, p. 064901, 2008.
- [253] B. Schenke, S. Jeon, and C. Gale, “(3+1)D hydrodynamic simulation of relativistic heavy-ion collisions,” *Phys. Rev. C*, vol. 82, p. 014903, 2010.
- [254] J. Steinheimer, J. Auvinen, H. Petersen, M. Bleicher, and H. Stöcker, “Examination of directed flow as a signal for a phase transition in relativistic nuclear collisions,” *Phys. Rev. C*, vol. 89, no. 5, p. 054913, 2014.

BIBLIOGRAPHY

- [255] I. Tews, T. Krüger, K. Hebeler, and A. Schwenk, “Neutron matter at next-to-next-to-next-to-leading order in chiral effective field theory,” *Phys. Rev. Lett.*, vol. 110, no. 3, p. 032504, 2013.
- [256] C. Drischler, K. Hebeler, and A. Schwenk, “Chiral interactions up to next-to-next-to-next-to-leading order and nuclear saturation,” *Phys. Rev. Lett.*, vol. 122, no. 4, p. 042501, 2019.
- [257] Y. Wang, C. Guo, Q. Li, A. Le Fèvre, Y. Leifels, and W. Trautmann, “Determination of the nuclear incompressibility from the rapidity-dependent elliptic flow in heavy-ion collisions at beam energies 0.4 A –1.0 A GeV,” *Phys. Lett. B*, vol. 778, pp. 207–212, 2018.
- [258] P. Danielewicz, R. Lacey, and W. G. Lynch, “Determination of the equation of state of dense matter,” *Science*, vol. 298, pp. 1592–1596, 2002.
- [259] J. Molitoris and H. Stoecker, “Stopping power, equilibration, and collective flow in the reactions Ar + Pb and Nb + Nb: A Theoretical analysis,” *Phys. Lett. B*, vol. 162, pp. 47–54, 1985.
- [260] S. Huth *et al.*, “Constraining Neutron-Star Matter with Microscopic and Macroscopic Collisions,” *Nature*, vol. 606, pp. 276–280, 2022.
- [261] D. Adamova *et al.*, “New results from CERES,” *Nucl. Phys. A*, vol. 698, pp. 253–260, 2002.
- [262] L. Adamczyk *et al.*, “Inclusive charged hadron elliptic flow in Au + Au collisions at $\sqrt{s_{NN}} = 7.7 - 39$ GeV,” *Phys. Rev. C*, vol. 86, p. 054908, 2012.
- [263] J. Adam *et al.*, “Flow and interferometry results from Au+Au collisions at $\sqrt{s_{NN}} = 4.5$ GeV,” *Phys. Rev. C*, vol. 103, no. 3, p. 034908, 2021.
- [264] M. S. Abdallah *et al.*, “Disappearance of partonic collectivity in sNN=3GeV Au+Au collisions at RHIC,” *Phys. Lett. B*, vol. 827, p. 137003, 2022.
- [265] L. Ahle *et al.*, “Proton and deuteron production in Au + Au reactions at 11.6/A-GeV/c,” *Phys. Rev. C*, vol. 60, p. 064901, 1999.
- [266] C. Alt *et al.*, “Energy and centrality dependence of anti-p and p production and the anti-Lambda/anti-p ratio in Pb+Pb collisions between 20/A-GeV and 158/A-GeV,” *Phys. Rev. C*, vol. 73, p. 044910, 2006.
- [267] L. Adamczyk *et al.*, “Bulk Properties of the Medium Produced in Relativistic Heavy-Ion Collisions from the Beam Energy Scan Program,” *Phys. Rev. C*, vol. 96, no. 4, p. 044904, 2017.
- [268] Y. Nara, H. Niemi, J. Steinheimer, and H. Stöcker, “Equation of state dependence of directed flow in a microscopic transport model,” *Phys. Lett. B*, vol. 769, pp. 543–548, 2017.

BIBLIOGRAPHY

- [269] T. Reichert, J. Steinheimer, C. Herold, A. Limphirat, and M. Bleicher, “Harmonic flow correlations in Au+Au reactions at 1.23 AGeV: a new testing ground for the equation-of-state and expansion geometry,” *Eur. Phys. J. C*, vol. 82, no. 6, p. 510, 2022.
- [270] C. Currin, T. Mitchell, M. Morris, and D. Ylvisaker, “Bayesian prediction of deterministic functions, with applications to the design and analysis of computer experiments,” *Journal of the American Statistical Association*, vol. 86, no. 416, pp. 953–963, 1991.
- [271] J. Novak, K. Novak, S. Pratt, J. Vredevoogd, C. Coleman-Smith, and R. Wolpert, “Determining Fundamental Properties of Matter Created in Ultrarelativistic Heavy-Ion Collisions,” *Phys. Rev. C*, vol. 89, no. 3, p. 034917, 2014.
- [272] <https://www.pymc.io/projects/docs/en/v4.1.6/api/generated/pymc.DEMetropolisZ.html>. Accessed: 2022-09-01.
- [273] <https://github.com/pymc-devs/pymc/releases/tag/v4.0.0>. Accessed: 2022-09-01.
- [274] M. S. Abdallah *et al.*, “Light nuclei collectivity from $\sqrt{s_{NN}} = 3$ GeV Au+Au collisions at RHIC,” *Phys. Lett. B*, vol. 827, p. 136941, 2022.
- [275] E. Kashirin, I. Selyuzhenkov, O. Golosov, and V. Klochkov, “Directed flow measurement in Pb+Pb collisions at $P_{lab} = 13A$ GeV/c collected with NA61/SHINE at SPS,” *J. Phys. Conf. Ser.*, vol. 1690, no. 1, p. 012127, 2020.
- [276] J. Barrette *et al.*, “Energy and charged particle flow in a 10.8-A/GeV/c Au + Au collisions,” *Phys. Rev. C*, vol. 55, pp. 1420–1430, 1997. [Erratum: *Phys.Rev.C* 56, 2336–2336 (1997)].
- [277] C. Alt *et al.*, “Directed and elliptic flow of charged pions and protons in Pb + Pb collisions at 40-A-GeV and 158-A-GeV,” *Phys. Rev. C*, vol. 68, p. 034903, 2003.
- [278] S. Altiparmak, C. Ecker, and L. Rezzolla, “On the Sound Speed in Neutron Stars,” *Astrophys. J. Lett.*, vol. 939, no. 2, p. L34, 2022.
- [279] S. Soma, L. Wang, S. Shi, H. Stöcker, and K. Zhou, “Reconstructing the neutron star equation of state from observational data via automatic differentiation,” *Phys. Rev. D*, vol. 107, no. 8, p. 083028, 2023.
- [280] M. Leonhardt, M. Pospiech, B. Schallmo, J. Braun, C. Drischler, K. Hebeler, and A. Schwenk, “Symmetric nuclear matter from the strong interaction,” *Phys. Rev. Lett.*, vol. 125, no. 14, p. 142502, 2020.
- [281] Y. Fujimoto, K. Fukushima, L. D. McLerran, and M. Praszalowicz, “Trace Anomaly as Signature of Conformality in Neutron Stars,” *Phys. Rev. Lett.*, vol. 129, no. 25, p. 252702, 2022.

BIBLIOGRAPHY

- [282] O. Savchuk, A. Motornenko, J. Steinheimer, V. Vovchenko, M. Bleicher, M. Gorenstein, and T. Galatyuk, “Enhanced dilepton emission from a phase transition in dense matter,” *arXiv:2209.05267*, 2022.
- [283] P. Li, J. Steinheimer, T. Reichert, A. Kittiratpattana, M. Bleicher, and Q. Li, “Effects of a phase transition on two-pion interferometry in heavy ion collisions at $\sqrt{s_{NN}} = 2.4 - 7.7$ GeV,” *Sci. China Phys. Mech. Astron.*, vol. 66, no. 3, p. 232011, 2023.
- [284] O. Savchuk, R. V. Poberezhnyuk, A. Motornenko, J. Steinheimer, M. I. Gorenstein, and V. Vovchenko, “Phase transition amplification of proton number fluctuations in nuclear collisions from a transport model approach,” *Phys. Rev. C*, vol. 107, no. 2, p. 024913, 2023.
- [285] I. Kisel, “Event reconstruction in the CBM experiment,” *Nucl. Instrum. Meth. A*, vol. 566, pp. 85–88, 2006.
- [286] J. E. Bernhard, J. S. Moreland, S. A. Bass, J. Liu, and U. Heinz, “Applying Bayesian parameter estimation to relativistic heavy-ion collisions: simultaneous characterization of the initial state and quark-gluon plasma medium,” *Phys. Rev. C*, vol. 94, no. 2, p. 024907, 2016.
- [287] P. A. Zyla *et al.*, “Review of Particle Physics,” *PTEP*, vol. 2020, no. 8, p. 083C01, 2020.
- [288] M. Omana Kuttan, J. Steinheimer, K. Zhou, A. Redelbach, and H. Stoecker, “A fast centrality-meter for heavy-ion collisions at the CBM experiment,” *Phys. Lett. B*, vol. 811, p. 135872, 2020.
- [289] B. Nachman and J. Thaler, “Learning from many collider events at once,” *Phys. Rev. D*, vol. 103, no. 11, p. 116013, 2021.
- [290] R. Dashen, S.-K. Ma, and H. J. Bernstein, “S Matrix formulation of statistical mechanics,” *Phys. Rev.*, vol. 187, pp. 345–370, 1969.
- [291] F. Karsch, K. Redlich, and A. Tawfik, “Thermodynamics at nonzero baryon number density: A Comparison of lattice and hadron resonance gas model calculations,” *Phys. Lett. B*, vol. 571, pp. 67–74, 2003.
- [292] P. Huovinen and P. Petreczky, “QCD Equation of State and Hadron Resonance Gas,” *Nucl. Phys. A*, vol. 837, pp. 26–53, 2010.
- [293] S. Borsanyi, Z. Fodor, C. Hoelbling, S. D. Katz, S. Krieg, C. Ratti, and K. K. Szabo, “Is there still any T_c mystery in lattice QCD? Results with physical masses in the continuum limit III,” *JHEP*, vol. 09, p. 073, 2010.
- [294] C. Ratti, S. Borsanyi, Z. Fodor, C. Hoelbling, S. D. Katz, S. Krieg, and K. K. Szabo, “Recent results on QCD thermodynamics: lattice QCD versus Hadron Resonance Gas model,” *Nucl. Phys. A*, vol. 855, pp. 253–256, 2011.

BIBLIOGRAPHY

- [295] P. Alba, R. Bellwied, M. Bluhm, V. Mantovani Sarti, M. Nahrgang, and C. Ratti, “Sensitivity of multiplicity fluctuations to freeze-out conditions in heavy ion collisions,” *Phys. Rev. C*, vol. 92, no. 6, p. 064910, 2015.
- [296] A. Bazavov *et al.*, “Fluctuations and Correlations of net baryon number, electric charge, and strangeness: A comparison of lattice QCD results with the hadron resonance gas model,” *Phys. Rev. D*, vol. 86, p. 034509, 2012.
- [297] P. Huovinen and P. Petreczky, “Hadron resonance gas with repulsive interactions and fluctuations of conserved charges,” *Phys. Lett. B*, vol. 777, pp. 125–130, 2018.
- [298] V. Vovchenko, D. V. Anchishkin, and M. I. Gorenstein, “Hadron Resonance Gas Equation of State from Lattice QCD,” *Phys. Rev. C*, vol. 91, no. 2, p. 024905, 2015.
- [299] J. D. Walecka, “A Theory of highly condensed matter,” *Annals Phys.*, vol. 83, pp. 491–529, 1974.
- [300] M. Dutra, O. Lourenco, J. S. Sa Martins, A. Delfino, J. R. Stone, and P. D. Stevenson, “Skyrme Interaction and Nuclear Matter Constraints,” *Phys. Rev. C*, vol. 85, p. 035201, 2012.
- [301] M. Dutra, O. Lourenço, S. S. Avancini, B. V. Carlson, A. Delfino, D. P. Menezes, C. Providência, S. Typel, and J. R. Stone, “Relativistic Mean-Field Hadronic Models under Nuclear Matter Constraints,” *Phys. Rev. C*, vol. 90, no. 5, p. 055203, 2014.
- [302] V. Vovchenko, D. V. Anchishkin, and M. I. Gorenstein, “Van der Waals Equation of State with Fermi Statistics for Nuclear Matter,” *Phys. Rev. C*, vol. 91, no. 6, p. 064314, 2015.
- [303] V. Vovchenko, M. I. Gorenstein, and H. Stoecker, “van der Waals Interactions in Hadron Resonance Gas: From Nuclear Matter to Lattice QCD,” *Phys. Rev. Lett.*, vol. 118, no. 18, p. 182301, 2017.
- [304] V. Vovchenko, “Equations of state for real gases on the nuclear scale,” *Phys. Rev. C*, vol. 96, no. 1, p. 015206, 2017.
- [305] R. V. Poberezhnyuk, V. Vovchenko, D. V. Anchishkin, and M. I. Gorenstein, “Quantum van der Waals and Walecka models of nuclear matter,” *Int. J. Mod. Phys. E*, vol. 26, no. 10, p. 1750061, 2017.
- [306] A. Motornenko, S. Pal, A. Bhattacharyya, J. Steinheimer, and H. Stoecker, “Repulsive properties of hadrons in lattice QCD data and neutron stars,” *Phys. Rev. C*, vol. 103, p. 054908, 2021.
- [307] F. Seck, T. Galatyuk, A. Mukherjee, R. Rapp, J. Steinheimer, J. Stroth, and M. Wiest, “Dilepton signature of a first-order phase transition,” *Phys. Rev. C*, vol. 106, no. 1, p. 014904, 2022.

BIBLIOGRAPHY

- [308] J. Steinheimer, S. Schramm, and H. Stoecker, “The hadronic SU(3) Parity Doublet Model for Dense Matter, its extension to quarks and the strange equation of state,” *Phys. Rev. C*, vol. 84, p. 045208, 2011.
- [309] G. Aarts, C. Allton, D. De Boni, and B. Jäger, “Hyperons in thermal QCD: A lattice view,” *Phys. Rev. D*, vol. 99, no. 7, p. 074503, 2019.

BIBLIOGRAPHY

Acknowledgements

I would like to express my sincere thanks to everyone who has supported me during this exciting adventure with heavy-ions and AI.

This thesis would not have been possible without the constant support and advice of my supervisor, Prof. Dr. Horst Stöcker. He is a wonderful mentor who has always encouraged me to explore new ideas and to see the bigger picture. In addition to his scientific knowledge, his leadership and teaching skills have always fascinated and inspired me. I am very grateful for the opportunity to complete my PhD under his supervision and for all his efforts to make me a better researcher.

I would like to thank Dr. Jan Steinheimer, one of my co-supervisors, who is a wonderful colleague and a good friend. It wouldn't have been easy to settle in Germany as a foreigner without his help and support. He is also a great teacher who helped me learn a lot about the physics of heavy ion collisions and the UrQMD model. He has always been there to answer any of my questions that I had as a new student in this field. He has also been a great help to me in various projects with the implementation of UrQMD models.

I would also like to thank Dr. Kai Zhou, another co-supervisor for my doctoral studies. Dr. Zhou has been very helpful in various projects, especially in the implementation of various AI methods. He helped me learn a lot about artificial intelligence and its applications in physics. I am very grateful to him for his support during my Ph.D. studies and his continued support in advancing my career.

I am thankful to Prof. Dr. Joachim Stroth for his guidance as a member of my HGS HIRe PhD Committee. His insightful comments during the PhD committee meetings were valuable in improving my research. I am also grateful to HGS HIRe for the soft skills courses and the travel grants that enabled me to attend several international conferences.

I thank PD Dr. Olena Linnyk for her help during my early days at FIAS and for the opportunity to present my research at the NA61 collaboration meeting at CERN. I would also like to thank Prof. Dr. Marcus Bleicher, Prof. Dr. Marek Gazdzicki, Prof. Dr. Marco Durante, Prof. Dr. Christian Graeff, Dr. Lennart Volz, Dr. Andreas Redelbach, Dr. Wojciech Brylinski, Dr. Behruz Kardan, Alexander Greiner and Janik Pawlowski for their collaboration on various projects.

ACKNOWLEDGEMENTS

I am also very grateful to my teachers at the Central University of Karnataka, especially Dr. Deepak Samuel, who was my Master's thesis supervisor at CUK. I thank him for introducing me to the field of AI and high energy physics and for guiding me towards a career in physics research.

I would also like to thank my colleagues and friends at FIAS, especially Dr. Anton Motornenko, Mariia Bilousova, Solomia Motornenko-Bilousova, Shriya Soma, Megha Chakraborty and Pavithran Sakamuri for creating such a nice and friendly working environment. Many thanks to the Seismology and AI Group at FIAS for organising various activities and letting me be a part of them.

I thank Amrutha Samalan for all her love and support throughout this journey. Thank you Shivaraj Mulleria Babu, Rufa Rafeek and Amrutha for all the wonderful holidays we had together.

Finally, I am very grateful to my parents and my brother Hariprasadh without whose support and love I would not have come this far. I dedicate this thesis to the loving memory of my father who always believed in me and encouraged me to follow my dreams.

Manjunath Omana Kuttan

Frankfurt Institute for Advanced Studies
3/204, Ruth-Moufang-Str 1, 60438, Frankfurt
✉ manjunath@fias.uni-frankfurt.de

Education

- 2019- **Goethe Universität, Frankfurt am Main**
PhD student at Frankfurt Institute for Advanced Studies
Member at HGS-HIRe for FAIR
Member at Frankfurt International Graduate School for Science
Anticipated year of PhD: 2023
- 2017-2019 **Central University of Karnataka**
M.Sc Physics
Grade: 80 %
- 2014-2017 **Government College Kasaragod, Kerala**
B.Sc Physics
Grade: 83 %
- 2012-2014 **Thanbeehul I. H. S School, Kerala**
Class 12
Grade: 89 %
- 2011-2012 **M Gregorious Dynesius Boys High School, Kerala**
Class 10
Grade: 90 %

Current research

- Tentative thesis title *Artificial Intelligence in Heavy-Ion Collisions: bridging the gap between theory and experiments.*
- Supervisor Prof. Dr. Horst Stoecker
- Description The final state spectra measured by particle detectors in heavy-ion collision experiments carry information on the properties and dynamics of the QCD matter created in the collision. However, due to the transient and stochastic nature of heavy-ion collisions, extracting the relevant physics signals from observables based on the final state spectra is not trivial. My research focuses on the development of such analysis techniques based on Artificial Intelligence and different statistical methods for heavy-ion collision experiments that could overcome the limitations of conventional methods for physics analyses

Completed

- works
 - ResNet based DL architecture to filter noise clusters from particle hits (online) from raw data in the Time Projection Chambers of CERN NA61 experiment.
 - Centrality-meter for the CBM experiment that can perform accurate, online event-by-event impact parameter determination from raw experimental data.
 - Novel DL model for identifying first order phase transitions at CBM experiment.
 - Study of the dynamical time evolution in transport and fluid dynamical models to extract the properties of strongly interacting matter.
 - Analysis of the uncertainties in MC-Glauber modelling of Heavy-ion Collisions at SIS-18 energies.
 - Constraining the QCD Equation of State at the highest baryon densities from Heavy-ion collision data through bayesian inference.

Ongoing/

Future works

- Generative Modelling of Relativistic Heavy-ion Collisions with Deep Learning.
- Development of deep learning models that can be deployed directly on FPGAs for online event selection/ characterisation.
- Deep Learning based ultra-fast track identification/ reconstruction for heavy-ion collision experiments.
- Development of novel treatment planning methods for heavy-ion arc therapy using machine learning methods.
- DL model to determine the number of participant nucleons in Heavy-ion Collisions.
- Accurate reconstruction of neutrino momentum at the India based Neutrino Observatory - ICAL detector using deep learning methods

Master's Thesis

- Title *Deep Learning techniques for muon momentum reconstruction for the INO-ICAL detector*
- Supervisor Dr. Deepak Samuel
- Description The India-based Neutrino Observatory (INO) will construct a 50 kton magnetised iron calorimeter (ICAL) for the detection and study of neutrino oscillations. The momentum of the neutrino is reconstructed from the momentum of the final state particles namely muons. The kalman filter technique is being currently used for muon momentum reconstruction in ICAL. In my work, I have implemented a deep learning based algorithm to reconstruct the muon momentum, quantified its performance in terms of the computing power required and the achievable accuracy and compared it with the kalman filter technique.

Scientific skills

- Programming C++, Python (5 years+)
- Libraries Geant4, ROOT, Qt, Scikit-learn, Keras, Tensorflow and Pytorch (4 year)
- Data analysis Using Python and ROOT (4 year)
- HIC models UrQMD, MC-Glauber (3+ years)
- Detectors Experience in development, testing and characterisation of Resistive Plate Chambers (2 months)
- GPU Short exercise using OpenACC (1 month)
- OS Proficient in both Linux and Windows based systems
- Others Contributed to development of a Geant4-based simulation software QUIQG4

Awards

- Giersch-Excellence-Grant 2021: for outstanding scientific work in the past years.
- Giersch-Excellence-Grant 2020: for outstanding scientific work in the past years.

Soft skill courses

- Jan 2021 Attended HGS-HIRe Basic Course I: Making an Impact as an Effective Researcher
- Feb 2022 Attended HGS-HIRe Basic Course II: Leading Teams in a Research Environment

Internship

- Summer 2018 **India based Neutrino Observatory, IICHEP**
Fabrication of Resistive Plate Chambers (RPC), setting up test experiments for RPCs, installation of mini-ICAL detector and data analysis of cosmic muon data at Tata Institute of Fundamental Research field station at Madurai

Online courses (credited)

- NPTEL **Physics of Semiconductors**, Prof. H C Verma, IIT Kanpur (Nov 2017)
- MITX **Quantum Information Science - Part I**, Prof. Peter Shor and Prof Isaac Chuang, MIT, USA (Feb 2018)

Conference & workshops

- March 2023 **MAGIC23: Workshop on QCD equation of state in dense matter HIC and astrophysics** Kovalam, Kerala, India
Oral presentation: Bayesian inference of the EoS of dense nuclear matter from heavy-ion collision data
- Dec 2022 **INT Workshop INT-22-84W: Dense Nuclear Matter Equation of State from Heavy-Ion Collisions** Seattle, USA
Oral presentation: The EoS of dense nuclear matter from Bayesian analysis of heavy-ion collision data
- June 2022 **Strangeness in Quark Matter 2022** Busan, Republic of Korea
Poster: PointNet for fast event characterisation in heavy-ion collision experiments

- May 2022 **FAIRNESS2022: FAIR next generation scientists- 7th edition workshop** *Pieria, Greece*
 Oral presentation: Extraction of global event features at the CBM experiment using PointNet
- April 2022 **Quark Matter 2022: 29th International Conference on Ultra-relativistic Nucleus-Nucleus Collisions.** *Krakow, Poland (attended Online)*
 Poster: Deep Learning the physics of heavy-ion collisions at the CBM experiment using PointNet
- March 2022 **DPG Spring conference: Divisions of Hadronic and Nuclear Physics and Plasma Physics as well as the Working Group on Accelerator Physics.** *Online*
 Oral presentation: Classifying the QCD Equation of State in heavy-ion collision experiments with Deep Learning
- Feb 2022 **IDT-UM collaboration meeting** *Online*
 Oral presentation: PointNet for event characterisation at the CBM experiment
- July 2021 **XF-IJRC workshop 2021** *Online*
 Oral presentation: AI/DL for high energy and nuclear physics detectors at large scale research facilities
- May 2021 **IDT-UM collaboration meeting** *Online*
 Oral presentation: Classifying the QCD transition at the CBM experiment with Deep Learning
- Aug 2020 **Workshop on analysis techniques for centrality determination and flow measurements at FAIR and NICA,** *Online*
 Oral presentation: Using machine learning techniques to determine impact parameter of collisions in CBM experiment
- Feb 2020 **CERN NA61/SHINE collaboration meeting,** *CERN, Geneva*
 Oral presentation: Deep learning for fast TPC data processing
- Nov 2019 **Giersch International Symposium: AI for Science,** *Frankfurt Institute for Advanced Studies*
 Participated in the symposium and GIS school: Machine learning applications for science
- Dec 2018 **XXIII DAE-BRNS High Energy Physics Symposium,** *Indian Institute of Technology, Madras*
 Oral presentation: Deep learning techniques for energy reconstruction of cosmic muons in mICAL detector
- Oct 2018 **National Conference on Cosmology and Particle Physics,** *Womens Christian College, Chennai* Assisted in the demonstration of Geant4 based simulation software QUIQG4
- Jan 2018 **Physics Experiments using Python and Open Source Instrumentation,** *Central University of Karnataka*

Publications

- a) **Omana Kuttan, M.,** Zhou, K., Steinheimer, J., Redelbach, A., & Stoecker, H. (2021). *An equation-of-state-meter for CBM using PointNet.* Journal of High Energy Physics, 2021(10), 1-25.
- b) **Omana Kuttan, M.,** Steinheimer, J., Zhou, K., Redelbach, A., & Stoecker, H. (2020). *A fast centrality-meter for heavy-ion collisions at the CBM experiment.* Physics Letters B, 811, 135872.

- c) **Omana Kuttan, M.**, Steinheimer, J., Zhou, K., Redelbach, A., & Stoecker, H. (2021). *Deep Learning Based Impact Parameter Determination for the CBM Experiment*. *Particles*, 4(1), 47-52.
 - d) **Omana Kuttan, M.**, Motornenko, A., Steinheimer, J., Stoecker, H., Nara, Y., & Bleicher, M. (2022). *A chiral mean-field equation-of-state in UrQMD: effects on the heavy ion compression stage*. *The European Physical Journal C*, 82(5), 1-12.
 - e) Samuel, D., Samalan, A., **Omana Kuttan, M.**, & Murgod, L. P. (2019). *Machine learning-based predictions of directionality and charge of cosmic muons—a simulation study using the mICAL detector*. *Journal of Instrumentation*, 14(11), P11020.
 - f) Samuel, D., **Omana Kuttan, M.**, Samalan, A., & Murgod, L. P. (2021). *Deep Learning-Based Energy Reconstruction of Cosmic Muons in mini-ICAL Detector*. In XXIII DAE High Energy Physics Symposium (pp. 787-791). Springer, Singapore.
 - g) Kawęcka, A., Bryliński, W., **Omana Kuttan, M.**, Linnyk, O., Pawlowski, J., Schmidt, K.,... & Zieliński, J. (2023, February). *NA61/SHINE online noise filtering using machine learning methods*. In *Journal of Physics: Conference Series* (Vol. 2438, No. 1, p. 012104). IOP Publishing.
 - h) Steinheimer, J., **Omana Kuttan, M.**, Motornenko, A., Sorensen, A., Nara, Y., Koch, V., ... & Stoecker, H. (2023, June). *Proton and Λ flow and the equation of state at high density*. In *European Physical Journal Web of Conferences* (Vol. 276, p. 01021).
- Under review **Omana Kuttan, M.**, Steinheimer, J., Zhou, K., & Stoecker, H. (2022). *The QCD EoS of dense nuclear matter from Bayesian analysis of heavy ion collision data*. arXiv preprint arXiv:2211.11670.
- Under review **Omana Kuttan, M.**, Steinheimer, J., Zhou, K., Bleicher, M., & Stoecker, H. (2023). *Model dependence of the number of participant nucleons and observable consequences in heavy-ion collisions*. arXiv preprint arXiv:2303.07919.

Online profiles

iNSPIRE-HEP <https://inspirehep.net/authors/1823113>

ORCID <https://orcid.org/0000-0003-1432-9643>

Google Scholar <https://scholar.google.com/citations?user=cZe18xwAAAAJ>

References

Prof. Dr. Dr. h.c. mult. Horst Stoecker,
Senior Fellow
 Frankfurt Institute for Advanced Studies
 Frankfurt am Main-Germany
 stoecker@fias.uni-frankfurt.de

Dr. Jan Steinheimer,
Research Fellow
 Frankfurt Institute for Advanced Studies
 Frankfurt am Main-Germany
 steinheimer@fias.uni-frankfurt.de

Dr. Kai Zhou,
Research Fellow
 Frankfurt Institute for Advanced Studies
 Frankfurt am Main-Germany
 zhou@fias.uni-frankfurt.de

Dr. Deepak Samuel,
Associate professor and Dean, HOD
 Department of physics
 Central University of Karnataka- India
 deepaksamuel@cuk.ac.in